CHRISTIAN-ALBRECHTS-UNIVERSITÄT ZU KIEL

Observational appearance of debris disks

DISSERTATION

zur Erlangung des Doktorgrades
Doktor der Naturwissenschaften (Dr. rer. nat.)
der Mathematisch-Naturwissenschaftlichen Fakultät
der Christian-Albrechts-Universität zu Kiel

vorgelegt von

Minjae Kim

Kiel, 2020

Minjae Kim:
Observational appearance of debris disks © June 2020
Das beobachtbare Erscheinungsbild von Trümmerscheiben © June 2020

Erstprüfer: **Prof. Dr. Sebastian Wolf**

Institut für Theoretische Physik und Astrophysik, Christian-Albrechts-Universität zu Kiel

Zweitprüfer: **Prof. Dr. Bernd Heber**

Institut für Experimentelle und Angewandte Physik, Christian-Albrechts-Universität zu Kiel

Datum der mündlichen Prüfung: 29. 10. 2020

Zum Druck genehmigt: 29. 10. 2020

- gez. **Prof. Dr. Frank Kempken**

“*Somewhere, something incredible is waiting to be known.*”

- Carl Sagan

Abstract

Debris disks are dusty circumstellar disks around main-sequence stars and natural by-products of the planet formation process. With an almost gas-free environment, dust-replenishing parent bodies orbit their host star and most likely continuously supply fine dust through mutual collisions. Thus, debris disks comprise solids ranging from kilometer-sized planetesimals down to micrometer-sized dust. Due to the large surface to volume ratio, dust grains are efficient radiators of thermal re-emission and scatterers of incident radiation from the stellar source. Dust grains are, therefore, readily detectable in a planetary system. Consequently, debris disk observables mainly depend on dust properties and the disk structure, as well as stellar properties.

In this dissertation, an observational appearance of debris disks is investigated. This allows the verification of predictions made concerning the spatial structure, underlying dynamical processes, and optical properties of the dust in the debris disk system. In particular, the potential for multi-wavelength and spatially resolved observations in numerical studies are conducted to constrain the observational appearance of debris disks with the physical properties and dynamics of dust grains. To develop observational strategies of disk observations, a new tool has been developed for analytical modeling of debris disks and the interpretation of results from the collisional approach.

The dependence of the observational appearance of debris disks on essential collisional parameters, such as the eccentricity of the parent belt, the dispersion of the eccentricities of parent belt bodies, and the critical specific energy for fragmentation of dust particles, is investigated. Furthermore, the feasibility of detecting water ice in typical debris disk systems, assuming various ice destruction mechanisms and dust mixtures with various internal structures, is investigated. Additionally, the multi-wavelength modeling of debris disks in η Chameleontis cluster is investigated to constrain the physical parameters and properties of the disks, such as the range of possible radial locations and total dust mass, based on observation from the APEX/LABOCA and the archival Gaia/DR2 data. Finally, a model based on a planetesimal mass distribution function is investigated to discuss the flattening of the spectral energy distribution of HD 107146 at mm wavelength with the NIKA2 observation.

Zusammenfassung

Trümmerscheiben sind zirkumstellare Staubscheiben um Hauptreihensterne und natürliche Begleiterscheinungen des Planetenentstehung. In einer beinahe gasfreien Umgebung umkreisen große Körper ihren Zentralstern und produzieren durch gegenseitige Kollisionen höchstwahrscheinlich ständig feinen Staub. Somit setzen sich Trümmerscheiben aus Festkörpern zusammen, deren Größe von kilometergroßen Planetesimalen bis hin zu mikrometergroßem Staub reicht. Aufgrund ihres großen Oberflächen-Volumen-Verhältnisses streuen diese Staubteilchen einen Großteil des einfallenden Lichts des Sterns und sind gleichzeitig effiziente thermische Strahler. Dadurch sind Staubscheiben trotz ihrer geringen Gesamtmasse relativ einfach zu beobachten. Infolgedessen sind die Beobachtungsergebnisse von Trümmerscheiben hauptsächlich von den Staubeigenschaften und der Scheibenstruktur sowie den stellaren Eigenschaften bestimmt.

In der vorliegenden Dissertation wird das beobachtbare Erscheinungsbild von Trümmerscheiben studiert. Jenes erlaubt die Verifikation von Vorhersagen über die geometrische Struktur, grundlegende dynamische Prozesse sowie die optischen Eigenschaften des Staubs im System der Trümmerscheibe. Besonders wird das Potential von räumlich aufgelösten Beobachtungen in mehreren Wellenlängen in numerischen Studien erforscht, um das Erscheinungsbild von Trümmerscheiben mit den physikalischen Eigenschaften und der Dynamik von Staubpartikeln einzugrenzen. Um Beobachtungsstrategien für Scheibenbeobachtungen zu entwicklen, wurde eine neue Simulationssoftware zur analytischen Modellierung von Trümmerscheiben sowie zur Auswertung der Ergebnisse erarbeitet.

Untersucht wird die Abhängigkeit des Erscheinungsbildes von Trümmerscheiben von grundlegenden Kollisionsparametern, wie etwa der mittleren Exzentrizität und der Exzentrizitätenverteilung der Umlaufbahnen großer Körper und der kritischen spezifischen Fragmentierungsenergie von Staubpartikeln. Außerdem wird die Durchführbarkeit des Nachweises von Wassereis in charakteristischen Trümmerscheibensystemen mit verschiedenen Eiszerstörungsmechanismen und Staubzusammensetzungen geprüft. Darüber hinaus wird mittels Modellierung der Trümmerscheibe im η Chameleontis-Cluster in mehreren Wellenlängen untersucht, ob sich die physikalischen Parameter und Eigenschaften der Scheibe eingrenzen lassen. Ein Beispiel hiefür ist der Versuch den Bereich der möglichen radialen Verteilung und die Gesamtstaubmasse einzugrenzen, auf der Grundlage von Beobachtungen aus dem APEX/LABOCA sowie der archivierten Gaia/DR2-Daten. Abschließend erfolgt eine Modelluntersuchung auf der Grundlage einer planetesimalen Massenverteilungsfunktion, um die Abflachung der spektalen Energieverteilung von HD 107146 bei mm Wellenlänge mit der NIKA2-Beobachtung zu besprechen.

Contents

List of Figures

List of Tables

List of Papers

The following papers are included in this dissertation.

PAPER I:
Impact of planetesimal eccentricities and material strength on the appearance of eccentric debris disks,
M. Kim, S. Wolf, T. Löhne, F. Kirchschlager, A.V. Krivov (2018): A&A 618, A38
DOI: 10.1051/0004-6361/201833061

PAPER II:
Constraining the detectability of water ice in debris disks,
M. Kim, S. Wolf, A. Potapov, H. Mutschke, C. Jäger (2019): A&A 629, A141
DOI: 10.1051/0004-6361/201936014

PAPER III:
The η Chamaeleontis Association: star formation and disk characterization with *Gaia*/DR2 and APEX/LABOCA,
V. Roccatagliata, A. Sicilia-Aguilar, **M. Kim**, S. Wolf et al. in preparation

PAPER IV:
NIKA2 Observations of the debris disk around HD107146,
J. F. Lestrade, **M. Kim**, S. Wolf, and NIKA2 core team et al. in preparation

Physical Constants

Gravitational constant	$G = 6.674\,08 \times 10^{-11}\,\mathrm{m^3 kg^{-1} s^{-2}}$
Speed of Light	$c = 2.997\,924\,58 \times 10^{8}\,\mathrm{m\,s^{-1}}$
Planck constant	$h = 6.63 \times 10^{-34}\,\mathrm{J\,s}$
Bolzmann constant	$k_\mathrm{B} = 1.380\,662 \times 10^{-23}\,\mathrm{m^2\,kg\,s^{-2}\,K^{-1}}$
Parsec	$pc = 3.085\,677\,581\,20 \times 10^{16}\,\mathrm{m}$
Astronomical Unit	$au = 149\,597\,870\,691\,\mathrm{m}$
Solar luminosity	$\mathrm{L}_\odot = 3.846 \times 10^{26}\,\mathrm{W}$
Solar radius	$\mathrm{R}_\odot = 696\,340\,\mathrm{km}$
Solar mass	$\mathrm{M}_\odot = 1.989 \times 10^{30}\,\mathrm{kg}$
Jupiter mass	$\mathrm{M}_\mathrm{J} = 1.898 \times 10^{27}\,\mathrm{kg}$
Earth mass	$\mathrm{M}_\oplus = 5.972 \times 10^{24}\,\mathrm{kg}$

Dedicated to

my mom Jeongsim Lee,
my dad Sunho Kim,
my twin Seojun Kim,
his wife Jisun Kim,
their baby girl Siwon Kim, who will enlighten the world,

and my dear Jihang Bona Han.

Chapter 1

Introduction

1.1 Profound questions

Where do we come from? What are the requirements to form and evolve life-sustaining planets? Are we alone in the Universe? We human beings have been asking these profound questions from the beginning of our history. Since these questions lie at the heart of the general interest of science, they naturally lead us to focus on the multi-disciplinary studies, which fall into two representative categories:

- The formation processes of the Sun and planets
- The understanding of the origin/evolution of organic matters

In particular, the formation of the stars and planets (and thus our solar system) is one of the fundamental questions in astronomy and astrophysics. Furthermore, if we do not know how the Earth itself formed, it is hard to explain how life evolved on Earth as well. Thus, we have to understand and find many clues to help us build the general picture of the star/planet formation process, even though this complex process is not well understood in detail to date. Consequently, it will help us disentangle the connections between profound questions of a human being, and thus allow us to make predictions about where to look for life beyond the solar system.

1.2 The standard paradigm of star/planet formation

The current standard picture of star and planet formation is based on the first proposed theory of our solar system formation by Kant (1755) and Laplace (1808)[1]. In the following, the generally accepted paradigm of T Tauri stars (i.e., a low mass star with $M < 2\ M_\odot$) formation based on young stellar objects (YSOs) classification (Shu and Adams, 1987; Andre, Ward-Thompson, and Barsony, 1993; Andre and Montmerle, 1994; Lada and Wilking, 1984; see also a brief summary with edge-on view picture in Fig. 1.1) is briefly discussed. The original criterion for this classification is based on the slope of the spectral energy distribution from the near-infrared (near-IR) to mid-infrared (mid-IR) $\alpha = \frac{d \log(\lambda F_\lambda)}{d \log \lambda}$, where F_λ is energy flux and λ is the wavelength (Lada and Wilking, 1984). For simplicity, a single isolated star is assumed from this point on, even though the star formation is generally not an isolated process in clusters (e.g., they often form in binaries or larger multiple systems; Duquennoy and Mayor, 1991).

---

[1] They predicted our solar system formed in broadly two steps: First, a slow rotating gaseous cloud collapses under its self-gravity. Next, the infalling material rotates more rapidly as a consequence of the conservation of angular momentum and flattens along the rotation axis, forming a disk, which eventually gives birth to the Sun and planets.

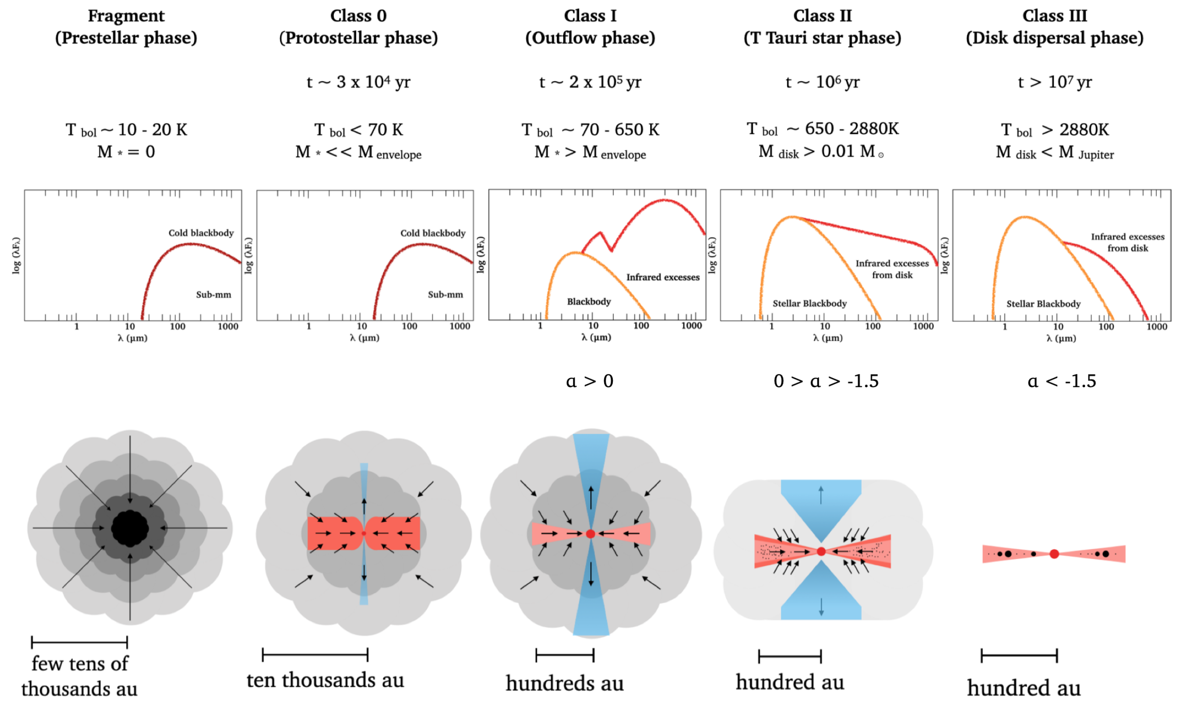

FIGURE 1.1: The current view of star/planet formation and evolution. T_{bol} represents the bolometric temperature that is defined as the temperature of a blackbody having the same flux-weighted mean frequency as the observed continuum spectrum (Krumholz, 2017). M_*, $M_{envelope}$, and M_{disk} represent the mass of the stellar core, envelope surrounding the stellar core, and disk, respectively. The value of α indicates the slope of the spectral energy distribution from the near- to mid-IR, e.g., ~ 2.2 to ~ 20 µm. A more detailed description can be found in Sect. 1.2. Figure is based on Shu and Adams (1987), Andre, Ward-Thompson, and Barsony (1993), Andre and Montmerle (1994), and Lada and Wilking (1984).

1.2.1 Prestellar phase: Collapse phase

Stars born in cold and dense molecular clouds[2] of interstellar gas and dust. These molecular clouds are originally pressure supported by the thermal gas pressure, the rotation, and magnetic fields. In particular, magnetic fields are the greatest supporting pressure to molecular clouds keep from collapsing.

Ions in molecular clouds carry the magnetic field with them, whereas the neutrals are unaffected by the magnetic field. Thus, there is a very slow slippage between the ions (i.e., mostly protons) and neutrals (i.e., the decoupling of neutral particles from plasma, called ambipolar diffusion; also known as "ion-neutral drift"; Mestel and Spitzer, 1956; Mouschovias and Spitzer, 1976; Greaves and Holland, 1999) in the cloud, which results in the slow diffusion of the ions from the magnetic field. Once the magnetic support has been fully removed and turbulences in the cloud create overdensities (i.e., masses larger than the Jeans mass $M_{\rm Jeans}$[3]), cloud finally collapses due to gravitational contraction.

As the cloud contracts, the density of the cloud increases by many orders of magnitude during the free fall process. As long as the density still remains adequately low for the cloud to be transparent (i.e., optically thin), the thermal energy gained by the collapse is radiated into the universe, and thus the temperature remains nearly constant, i.e., isothermal collapse. The Jeans mass $M_{\rm Jeans}$ decreases as the collapse continues. Consequently, different small

---

[2] Molecular clouds have the temperatures in the range of ~ 10 to 50 K, masses in the range of ~ a few $M_\odot$ to 10^6 $M_\odot$, sizes in the range of a few pc to the order of 100 pc, and number densities in the range of ~ 10^3-10^5 cm^{-3} (Arzoumanian et al., 2011). A large number of molecular clouds are found in the spiral arms of the Milky way.

[3] The Virial equation $|E_{\rm grav}| = 2E_{\rm kin}$ can be solved to find the minimum mass a cloud must have if gravity is to overwhelm pressure and thus the cloud to be collapsed, called the Jeans mass $M_{\rm Jeans} = \left(\frac{R_{\rm g}}{\mu G}\right)^{3/2} \left(\frac{3}{4\pi}\right)^{1/2} T^{3/2} \rho^{-1/2} \propto \sqrt{\frac{T^3}{\rho}}$, where $R_{\rm g}$ is the universal gas constant, μ is the mean molecular weight of gas, ρ is the gas density, T is the temperature of the cloud, and G is the gravitational constant (Kippenhahn and Weigert, 1994; Bonnell, Clarke, and Bate, 2006).

regions within the cloud satisfy the Jeans criterion locally and thus lead to the fragmentation of the molecular cloud. This results in many small stellar cores.

1.2.2 Protostellar phase: Class 0 (t < 0.03 Myr)

During the continuous collapse, the density increases to up to $\sim 10^{-13}$g cm^{-3}, which increases the optical depth (i.e., optically thick), resulting in the collapse to be adiabatic rather than isothermal. Thus, energy is not radiating away and gets trapped. Finally, the trapped thermal energy heats the core, which results in the dissociation of the molecular hydrogen H_2 into hydrogen atoms H. This builds up the internal pressure until a hydrostatic equilibrium is reached (i.e., gravity balances pressure) and a protostar is born with a radius of ~ 5 au. As the envelope of the protostar collapses and due to the conservation of angular momentum, the quasi-static protostellar core begins to spin, i.e., the radius of the protostellar core gets smaller, and thus the cloud spins faster. This rapid rotation creates stronger centrifugal forces, which are greatest at the equator. The rotating contracting cloud, therefore, starts to spread out and finally forms a disk, e.g., the small central protostar is being surrounded by a large rotating disk (i.e., circum-protostellar disk) with a radius of ~ a few hundred au and an optically thick infalling envelope, resulting in a deeply embedded protostellar core. Protostar grows by acquiring mass from its surrounding envelope that is composed of interstellar dust and gas. Also, bipolar molecular outflows ("jets") generated by the protostellar core, which is perpendicular to the rotation plane.

The SED of Class 0 objects has a similar to a single temperature blackbody function with a very low temperature (< 70 K); peak in far-infrared (far-IR) to sub-millimeter (sub-mm) range; (see also Fig. 1.1).

1.2.3 Outflow phase: Class I (t ~ 0.2 Myr)

The more evolved protostar has already accreted most of the mass from the enveloping cloud and the accumulated circumstellar material. As the core (protostar) continues to condense and rotation accelerates, leading to a higher mass of the Class I object, and thus the depletion of the surrounding cloud, the angular momentum of the object increases. As a consequence of the conservation of angular momentum, the Class I object thus emits two continuous flows of gas (i.e., polar jets) from the poles of the protostar. Consequently, its envelope loses most of its mass due to bipolar outflows and is heated by the accretion luminosity onto the core of the protostar.

Class I objects show a near-IR emission and are characterized by a slope of the SED α that is flat or rising with increasing wavelength ($\alpha > 0$), whose infrared excess due to the warm envelope peaks in the far-IR. The 10-µm silicate absorption feature, which is typical for these systems, is clearly shown (see also Fig. 1.1).

1.2.4 T Tauri phase: Class II (t ~ 1 Myr)

From this stage on, the protostar has lost its envelope and it is optically visible unless it is obscured by the disk. The central protostar becomes a pre-main sequence star (e.g., a classical T Tauri star) and accretes mass only from the surrounding disk, which is called a protoplanetary disk. During this phase, accretion proceeds through the disk by redistribution of angular momentum. In particular, a small amount of matter eventually carries all the angular momentum outwards, while the rest of the mass is losing angular momentum and falls onto the star (Pringle, 1981; Armitage, 2011). Consequently, the disk is spreading inwards and outwards (Lynden-Bell and Pringle, 1974), depending on the material accretion rate and the angular momentum transport rate, which are responsible for the structure and evolution of the protoplanetary disk. Several mechanisms have been proposed for the gradual loss of angular momentum of the rotating matter and mass in accretion disks, including viscous torques, gravitational torques, and magnetic torques.

Protoplanetary disks are the environment where tiny dust grains that are inherited from the interstellar medium must grow and form planets in the interim. To form a planet, tiny µm size grains need to grow in size by ~ 13 orders of magnitude and in mass by ~ 40 orders of magnitude (see also Sect. 1.2.6).

The dust in a protoplanetary disk absorbs stellar radiation and re-radiates thermally in the infrared wavelength range. This results in Class II objects, e.g., T Tauri stars, in a disk system that is showing an excess of infrared emission, and a decreasing emission in the sub-mm ($0 > \alpha > -1.5$; see also Fig. 1.1).

1.2.5 Disk dispersal phase: Class III (t ≥ 10 Myr)

The final stage of star/planet formation is the disk dispersal phase. As Zuckerman, Kim, and Liu (1995) and Haisch, Lada, and Lada (2001) indicated, the oldest observed gas-rich protoplanetary disks are about a few 10^6-10^7 years old, meaning that the disk must be cleared in this phase. Viscous accretion spreads disk mass, continuously causes accretion onto the star, which is primarily responsible for the removal of the innermost matter (r ≤ 1 au; called 'cavity'). Once a gap is formed, the isolated inner disk accretes onto the star, which results in the inner edge of the outer disk being directly irradiated (Alexander and Armitage, 2007). For the outer regions of disks (r ≥ 1 au), the stellar wind and high energy incident electromagnetic radiation from the young protostar (i.e., photoevaporation to the disk surface; Hollenbach and Adams, 2004) is the dominant mechanism of disk dispersal. As the gas escapes, a pressure gradient drives the unbound gas away from the star as a wind (Clarke, Gendrin, and Sotomayor, 2001). The mass loss continues outwards until the entire gas disk is gone after ~ 10 Myr (Fedele et al., 2010). Consequently, the timescale of disk clearing strongly constrains and affects the architecture and evolution of planetary systems. Once the gas in the protoplanetary disk has been dispersed, the remaining dust disk is called a debris disk. Debris disks may influence the process of terrestrial planet formation that may continue for up to ~ 100 Myr (Kenyon and Bromley, 2006; see also Fig. 1.2), while the formation of giant planets already ceased. Furthermore, debris disks continue evolving collisionally, dynamically, and gravitationally even in mature systems where planet formation has long been completed, like our solar system.

Class III sources show the stellar photosphere in the near- to mid-IR. These sources are either naked stars or debris disks with infrared excesses that peak in the far-IR ($\alpha < -1.5$; see also Fig. 1.1).

1.2.6 Dust evolution

The gas in the disk consists mostly of light elements, the evolution of which is predominantly, most of the processes (e.g., viscous disk accretion and the clearing of the disk) discussed above mainly drive the evolution of the gas in the disk. However, once the gas component in the disk disappeared (almost) completely during the disk dispersal phase (Sect. 1.2.5), the young star is surrounded by a planetary system (e.g., planetesimals and even planets). This means other processes operate on the dust particles in the disk (Sect. 1.2.4). Key to the understanding of the dust evolution is the process of dust growth, even though the current knowledge of the dust growth process is still far from complete.

A very brief description of dust evolution, which comprises mainly three steps, i.e., grain growth, planetesimals growth, and planet formation, is discussed in this section (see also a very brief description in Fig. 1.2).

Grain growth: Even though the full process of grain growth is not well understood, it is generally accepted that grain growth is a multi-step process. Gas dynamics determine dust motion and grain growth in general.

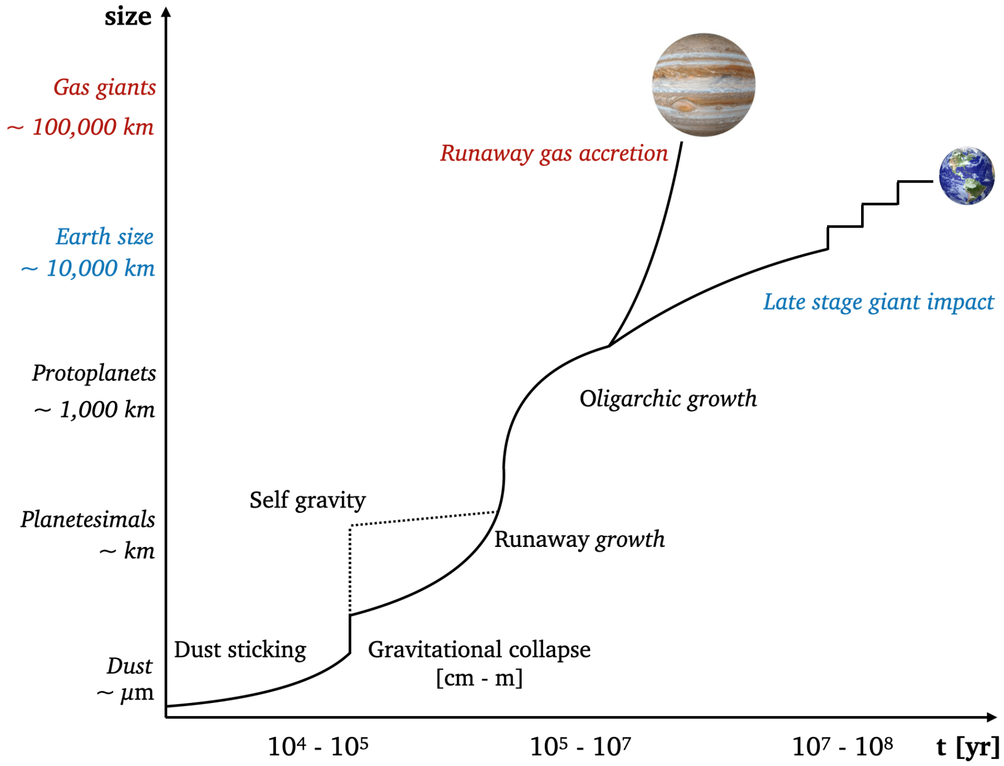

FIGURE 1.2: The current view of dust evolution (i.e., the growth of small dust grains towards the gravitationally bound planetesimals and planets) and its rough timeline. Figure is based on Raymond et al. (2009) and Armitage (2011).

- **Grain growth via sticking**: Tiny grains stick electrostatically by Brownian motion, leading to fractal aggregates, which eventually compacted to form spheroidal grains.
- **Grain growth via settling/collisions**: Due to the vertical component of gravity acting in the disk on the pressure-less dust component, dust grains tend to slowly settle toward the midplane on a time scale of a few hundred thousand years (Dullemond and Dominik, 2004; Dominik et al., 2007). Thus, the likelihood of grain-grain collisions is increased due to an increase in the density of grains, so that grain growth via settling/collisions can proceed more rapidly (Dullemond and Dominik, 2005). There are several possible outcomes of a grain-grain collision, e.g., sticking, bouncing, erosion/cratering, mass transfer, or fragmentation (Windmark et al., 2012; Güttler et al., 2010), depending on the relative velocity of the grains and their chemical and physical properties (Blum et al., 2006). For example, high-speed collisions are more likely to result in shattering, while icy grain surfaces are likely to enhance sticking. Furthermore, collisions of objects moving at the same speed are less destructive than those of objects moving at different speeds.
- **Radial migration**: Once the growing grains have settled to the mid-plane, grains migrate radially towards the star via drift.

Planetesimal growth via accretion: There are two stages of planetesimal growth, i.e., the faster runaway and the slower oligarchic growth.

- **Runaway growth**[4]: Larger bodies grow faster than smaller bodies (called "runaway growth"; Wetherill and Stewart, 1993; Weidenschilling et al., 1997). Their mass accretion rate is a very strong function of the

---

[4] In the case of runaway growth one particle grows rapidly in a swarm of smaller ones, while in the case of orderly growth the whole ensemble has similar particle sizes

gravitational strength of the object $\propto M^{4/3}$, which finally results in the emergence of large protoplanets. The runaway growth eventually ends when the largest bodies are massive enough to increase the random velocities of nearby planetesimals, i.e., when gravitational stirring by protoplanets dominates planetesimal random velocities (Ida and Makino, 1993).

- **Oligarchic growth**: The end of runaway growth leads to the beginning of the "oligarchic growth" regime, where mass accretion grows $\propto M^{2/3}$ (Ida and Makino, 1993; Kokubo and Ida, 1998). Now, the disk is dominated by large adjacent planetary embryos (i.e., protoplanets), which slowly grow due to accretion. Thus, the planetary embryos become large enough to overcome eccentricity damping due to dynamical friction from smaller planetesimals, which leads to embryo-embryo collisions and signals the last stage of accretion of terrestrial planets and giant planet cores (Mandell, 2014). The oligarchic growth ends when they have swept up everything (i.e., when the protoplanets have accreted everything within their gravitational reach; Wetherill and Stewart, 1989). After clearing of the planetesimals, the final mass (called "the isolation mass") increases with surface density and radial direction.

Planet formation: Planet formation falls into two representative categories, i.e., the giant planet formation and the terrestrial planet formation:

- **Giant planet formation**: Giant planets (e.g., Jupiter or Saturn) must have completed their formation before the disappearance of the gas in the disk, i.e., the protoplanetary disks last 3-10 Myr, which corresponds to the global-disk gas depletion timescale (Haisch, Lada, and Lada, 2001; see also 1.2.5). Two competing giant planet models are being discussed (Bodenheimer and Pollack, 1986; Mizuno, Nakazawa, and Hayashi, 1980; Perri and Cameron, 1974), the core accretion model and the gravitational instability model. Both models are competing with each other, nonetheless, it may be that not all giant planets are formed by the same mechanism.

  The core accretion model is an initially slow process, until the quick sweeping up of planetesimals ("Bottom-up process"; D'Angelo, Durisen, and Lissauer, 2010). In the core accretion model, the basic requirement is a solid core of $\sim 10\ M_\oplus$ originating from an accretion of planetesimals. Once the core reaches this critical mass, a hydrodynamic instability is triggered that results in rapid gas accretion (Pollack et al., 1996). The gaseous envelope is accreted in a runaway process (see also Fig. 1.2). This runaway gas accretion is no longer limited by the cooling properties of the gas envelope, but only by the availability of gas in the disk. This means that this rapid growth only ends when the gas dissipates in the disk (Alibert et al., 2005; Hubickyj, Bodenheimer, and Lissauer, 2005). Therefore, a giant planet must form quickly before the dissipation of the gas in the disk.

  The gravitational instability model is initially a rapid process, until the slow sweeping up of planetesimals ("Top-down process"; D'Angelo, Durisen, and Lissauer, 2010). In this model, the disk is unstable due to its own self-gravity, when the Toomre parameter $Q \sim 1$ (Toomre, 1981), which occurs, when the disk is cold and massive. To have fragmentation into bound clumps, the cooling time of the gas needs to be short (Gammie, 2001). Assuming these conditions are met, the disk fragments into planets in just a few orbits. This finally leads to the direct fragmentation of the gas into massive planets (Boss, 1997).

- **Terrestrial planet formation**: The heavier rocky and metallic materials are better suitable for the condensation at higher temperatures. Thus, when rocks and metals orbiting the star move close to one another, they gradually grow larger. This is because collisions of objects moving at a similar speed are less destructive (Blum et al., 2006); thus they stick together more often. Consequently, the planets residing in the inner part of the solar system are made almost entirely of heavier materials (e.g., rock and metal) and form a group called the terrestrial planets. After gas giant planet formation ceased, there are no more mechanisms, which damp the random velocities of the isolated planetary embryos, e.g., gas damping and/or viscous friction. This finally results in gravitational scattering increasing the random velocities. Since the growth of velocity dispersion in the disk is dominated by the protoplanets and gravitational focusing is weak, growth in this regime is very slow. These bodies continue to evolve through a series of giant impacts until they reach a configuration where the spacing leads to long-term stability (Goldreich, Lithwick, and Sari, 2004).

1.3 What are debris disks?

As indicated in the Sect. 1.2.5, after the dispersal/dissipation of gas (removed by accretion onto a protoplanet and/or photo-evaporation), a star at the end of the protoplanetary disk phase is expected to be surrounded by one or all of the following components (Wyatt, 2008; Safronov and Zvjagina, 1969; Wetherill, 1980; Lissauer, 1987): the remnant of the protoplanetary disk (e.g., dust and gas[5]), planetesimal belts in which planetesimals kilometer-sized solid bodies) continue to grow or grind to copious dust, and several planets from Earth-size to Jupiter size. All of these objects, including sub-planetary solids and particles, are called debris disks. Debris disks are observed around main-sequence stars of all ages, although they are more often detected around early-type/young stars due to their higher luminosity (e.g., by the Spitzer and Herschel surveys; Su et al., 2006; Eiroa and Dunes Consortium, 2013)[6].

In particular, due to the large surface to volume ratio, dust grains are efficient radiators of thermal re-emission (grains absorb the optical and ultraviolet light from the central star and then emit/radiate this energy away at the infrared) and scatterers of stellar light. Therefore, they are the most readily detectable in a planetary system and observed around a significant fraction of main-sequence stars older than about 10 Myr. However, this detectable dust in dusty debris disks is thought to be removed by the stellar radiation on a short time scale compared to the system's age (Backman and Paresce, 1993; Artymowicz and Clampin, 1997). This means that dust must be transient and/or more likely continuously replenished. The grain growth is hardly possible in debris disks. This is because the relative velocities are not damped by ambient gas with the almost gas-free environment in debris disks. Thus, the most probable explanation is that dust-replenishing parent bodies (i.e., planetesimals) in debris disks orbit their host star and continuously supply the copious fine dust through mutual collisions. Consequently, stellar radiation directly interacts with the leftovers, which are being ground down to µm sized dust (e.g. Strubbe and Chiang, 2006; Krivov, 2010). This means that detectable dust must be secondary material, which represents the composition of exo-planetary material, e.g., asteroids and meteorites.

A decade before the first detection of an exoplanet around a main-sequence star (51 Pegasi by Mayor and Queloz, 1995), Aumann (1984) reported a serendipitous discovery of circumstellar dust around Vega with an infrared excess (hereafter referred to as "IR-excess"; see Fig. 1.3) above the expected photospheric value by the Infrared Astronomical Satellite (IRAS)[7]. Besides, a scattered-light image of β Pictoris promptly showing that circumstellar dust is accompanied with a disk (Smith and Terrile, 1984). These discoveries of dusty circumstellar disks, that emit much more radiation at wavelengths between 25 and 100 µm, around main-sequence stars were indeed the most notable achievement of the IRAS. Since then, the number of debris disk detections has grown over the last 25 years. So far, there are about tens of very well-resolved, and more than a hundred marginally resolved debris disks imaged in thermal emission or scattered light (Catalog of resolved debris disks[8]; Catalog of Circumstellar Disks[9]).

---

[5] After gas dispersal gas are in general not detected in debris disks (e.g., Moór et al., 2011). However, gas was already detected in several debris disk systems, in particular, either primary gas (e.g., Thi et al., 2014) or secondary gas (e.g., Dent et al., 2014). A more detailed description can be found in Sect. 3.3.3.

[6] Debris disks observations are sensitive to individual disk parameters and the detection threshold, implying that debris disks are probably more ubiquitous below current detection thresholds.

[7] This was first believed to be a protoplanetary disk. However, it is now known to be a debris disk due to the lack of gas in the disk, fractional luminosity from the disk, and the age of the star.

[8] `https://www.astro.uni-jena.de/index.php/theory/catalog-of-resolved-debris-disks.html`

[9] `https://www.circumstellardisks.org/index.php`

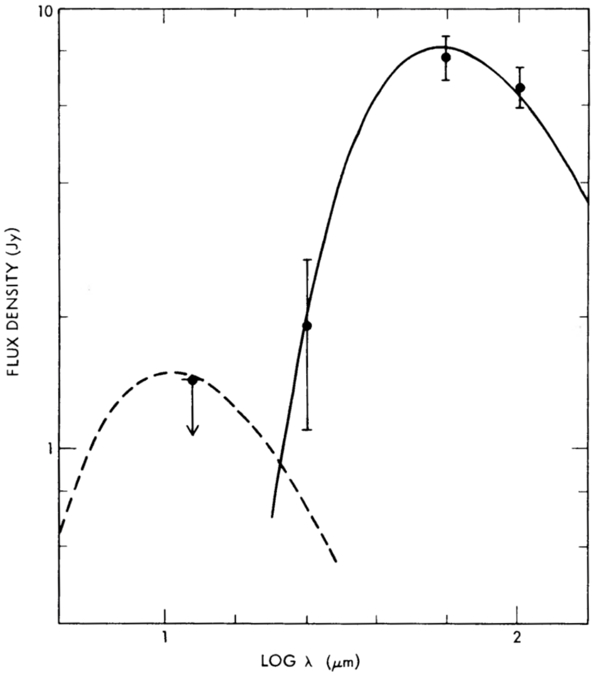

FIGURE 1.3: Spectral energy distribution of the infrared excess from Vega. The solid and dashed lines represent a 85 K and 500 K blackbody spectrums, respectively. Figure credit: Aumann (1984).

To date, 4158 confirmed exoplanets (NASA Exoplanet Archive[10]) have been detected via various methods, e.g., radial velocity techniques (*CARMENES*; Quirrenbach et al., 2016) and the transit technique (*Kepler*; Borucki and Koch, 2010). Interestingly, planets found by these missions show diversity in their properties. Besides, many planetary systems are quite different from our solar system (e.g. Butler et al., 2006). The vast majority are gas giant planets usually far bigger than those of our solar system, while there is a small number (~ 350) of terrestrial planets with Earth-like mass. Among them it is considered that only a handful exists in a habitable zone, allowing for the presence of possible key materials of life signatures, e.g., oxygen, water, and organic matters. However, even with state-of-the-art observations, it is not possible to resolve these exoplanets well enough to search for signs of life or habitability, in particular, detecting low mass planets at tens of au is still far beyond current instrumentation (Dong, Zhu, and Whitney, 2015). Since a definitive understanding of the planet formation process, e.g., how Earth formed, should be accompanied by an answer to the question of the origin of life, it is still difficult to answer the profound questions in Sect. 1.1. We, therefore, need to focus on an alternative way, the environments where they are born, e.g., the circumstellar disks, to understand the origin and characteristics of exoplanets.

In particular, debris disks can tell us a lot about the history and structure of planetary systems (and our solar system), because they are a natural outcome of planet formation processes. In this way, young debris disk system observation, in general, provides various information about the early evolution of planetary systems. Furthermore, planets can interact with the disk system dynamically. Thus, the presence of planets can be inferred from particular disk structures (e.g., Rosotti et al., 2016). Additionally, debris disk observations provide a way to study the outer regions of the planetary system (Marino et al., 2018). Consequently, understanding the spatial information and composition of debris disks is a very crucial step in understanding the origin of exoplanets and determining the potential habitability of terrestrial planets, complementary to the direct/indirect studies on exoplanets and their

---

[10] https://exoplanetarchive.ipac.caltech.edu/cgi-bin/TblView/nph-tblView?app=ExoTbls&config=planets

mother star. Thus, this field of research finally leads us to the proper answers to our profound questions (Sect. 1.1) and is connected to the question about the future of our solar system (Jura et al., 2007; Melis et al., 2010).

1.4 This dissertation

1.4.1 Research Unit FOR 2285 "Debris Disks in Planetary Systems"

This thesis was written as a part of Project P4: Observational appearance of debris disks in the Research Unit FOR 2285 "Debris Disks in Planetary Systems"[11], which is the first large-scale Research Unit to focus on debris disks in Germany and was established in 2015 (now in the second phase). The primary goal of this Research Unit is to explore constraints posed by debris disks onto the architecture, formation, and evolution of planetary systems, and thus better understand debris disks. Combining the theoretical (e.g., analytic and numerical modeling of their collisional/dynamical evolution) and laboratory results (e.g., laboratory studies of the optical properties of dust and its interaction with stellar radiation), the Research Unit provides elaborate models of individual disk systems and thus gives us new insights into a variety of puzzles including the origin of debris disks, the composition of their dust, and their evolution.

1.4.2 Aim of this work

This thesis work is motivated by new major observatories and instruments that will become available in the near future. These will provide high-sensitivity/angular resolution capabilities required for observational debris disk studies. Therefore, the goal of this dissertation is to develop observational strategies, which allow the verification of predictions made concerning the spatial structure, underlying dynamical processes, and optical properties of the dust in the debris disk system. This dissertation investigates the potential of multi-wavelength and spatially resolved observations in numerical studies to constrain the observational appearance of debris disks with physical properties and phenomena, e.g., dust spatial distribution and optical properties of various dust phases, characterized by their size, chemical composition, and internal structure (compact/porous, amorphous/crystalline, single component/multi-layer). A general description of this dissertation is addressed below:

- In Chapter 1, the basic introduction, stellar and planetary evolution is described, beginning with the description of the contraction of a molecular cloud due to ambipolar diffusion up until its last stages of planet formation and evolution, including the dust evolution. Finally, the importance of debris disks studies is discussed.
- In Chapter 2, the comprehensive physics of dust in debris disks (e.g., forces on dust particles in debris disks and irradiated dust particles) is discussed.
- In Chapter 3, the general context of debris disks observations is introduced. Furthermore, observational constraints on dust properties in debris disks and the general description of debris disks structures, showing structural diversity of disk systems, are discussed.
- In Chapter 4, the general description of the debris disk modeling and the simulation tools used in this work are discussed.
- In Chapter 5, the impact of the most frequent phenomena, i.e., collisions between planetesimals, in debris disks on the observational appearance of these systems are addressed. Therefore, studies on planetesimal collisions in debris disks have conducted. The dependence of the appearance of debris disks on essential

---

[11] http://www.astro.uni-jena.de/FOR2285/en/index.php

collisional parameters, such as the eccentricity of the parent belt, the dispersion of the eccentricities of parent belt bodies, and the critical specific energy for fragmentation of dust particles, are investigated.

- In Chapter 6, the feasibility of detecting water ice in typical debris disk systems, assuming various ice destruction mechanisms and dust mixtures with various shapes consisting of amorphous ice, crystalline ice, astrosilicate, and vacuum inclusions, is addressed. For this purpose, the influence of these parameters on the resulting observables of debris disks, e.g., the SED, spatially resolved images, and their radial profiles, is discussed. Finally, the feasibility of detecting water ice in debris disks with future observations is investigated.

- In Chapter 7, a continuum sub-mm survey of the cold material of protoplanetary disks and new debris disks in η Chameleontis cluster with the APEX/LABOCA observations and the archival Gaia/DR2 data are introduced. The multi-wavelength modeling of debris disks in η Chameleontis cluster to constrain the physical parameters and properties of the disks, e.g., the range of possible radial locations and total dust mass based on observation, is investigated.

- In Chapter 8, the NIKA2 observation of debris disk around HD 107146 is introduced. The flattening of the SED of HD 107146 that becomes close to the Rayleigh-Jeans regime at mm wavelength domain is revisited and discussed. In particular, a model based on a planetesimal mass distribution function that includes the perturbed pattern is proposed and investigated.

- In Chapter 9, conclusions and outlooks of this dissertation are presented.

Chapter 2

Physics of debris disks

The interplay between many forces (e.g., collisions and gravitational perturbations) and all the solid components in debris disks, ranging from kilometer-sized (km-sized) planetesimals down to micrometer-sized (µm-sized) dust grains (Sect. 1.3), determines the distribution of dust in debris disks and the spatial structures of the disk system. Thus, the study of the forces on dust particles is directly linked to the unseen planetesimals and planets. Furthermore, dust particles that are heated by and scatter the stellar radiation are visible to us. In this chapter, a brief summary of the effect of physics on dust in debris disks and the observation of irradiated dust particles are presented.

2.1 Forces on dust particles

In this section, forces acting on dust particles in debris disks are briefly addressed (see also Fig. 2.1 as a brief summary). The topics of this section include the stellar gravity and three dominant forces related to stellar radiation: the radiation pressure, inwards the Poynting-Robertson drag, and the stellar wind drag. Additionally, one of the most important and dominant phenomena in debris disks, namely mutual collisions, are considered. Finally, other important factors such as the Lorentz force, the Yarkovsky effect, the sublimation effect, the sputtering effect, and interactions with one or more planets are considered. Due to the scale, the star is treated as a point source for the matter of convenience in this dissertation.

2.1.1 Stellar gravity

The main force keeping dust particles in their orbits is the gravity of the central star. Dust particles with a mass m_{dust} orbiting a star with the mass M_* at a distance r are primarily affected by the inwardly directed gravitational force of the star:

$$\mathbf{F}_{\text{g}} = -\frac{GM_* m_{\text{dust}}}{r^2}\frac{\mathbf{r}}{r}\ , \tag{2.1}$$

where $\mathbf{r}$ is the position vector of the object. At this point, further possible gravitational forces (e.g., induced by planets in the system) are neglected. This force depends on the eccentricity of the particles orbit e[1], particularly. For example, particles on elliptical orbits are gravitationally bound to the system, which is characterized by $0 \leq e < 1$. On the other hand, particles with $e \geq 1$ are unbound and thus leave the system on parabolic or hyperbolic trajectories.

2.1.2 Radiation pressure

The dominant non-gravitational force acting on the dust particles is the radiation pressure, which arises from the photons emitted by the central star. When photons are absorbed by dust particles, the momentum has to be

---

[1] e is derived from parameters of conic sections and determines how much its orbit deviates from a perfect circle (i.e., $e = 0$).

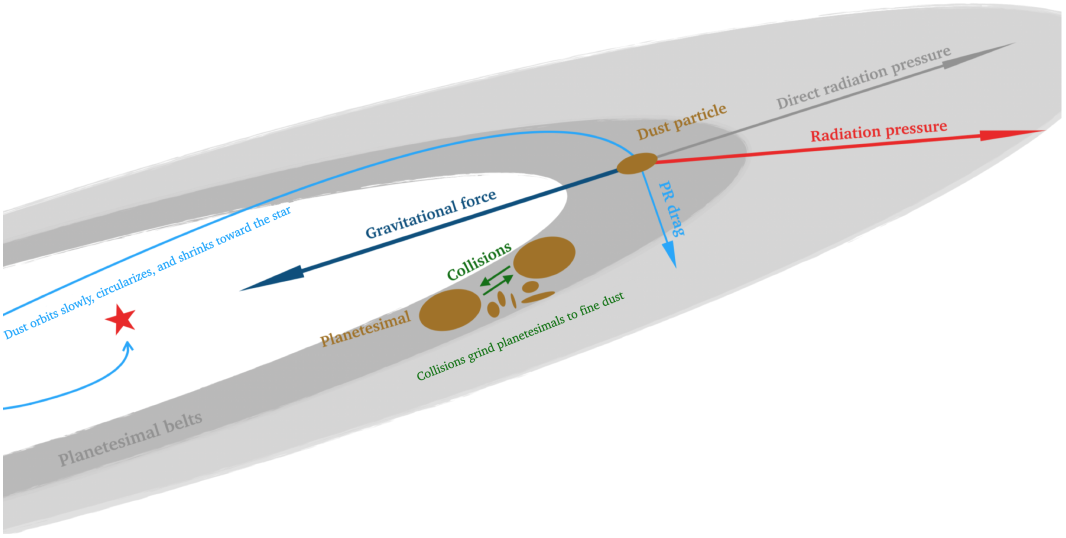

FIGURE 2.1: Brief sketch of the most important forces on dust particles in debris disks. Figure is based on Krivov (2010).

transferred to dust particles due to momentum conservation. By considering the number of photons absorbed per unit time, one easily derives the force on the particle due to radiation pressure. The radiation pressure can be expressed as:

$$\mathbf{F}_{\mathrm{rad}} = \frac{\sigma \int_0^\infty L_*(\lambda)\, Q_{\mathrm{pr}}(a)\, \mathrm{d}\lambda}{4\pi r^2 c} \frac{\mathbf{r}}{r} , \tag{2.2}$$

where σ $(= \pi a^2)$ is the geometrical cross-section of the particle with the size of dust grain a, Q_{pr} is the radiation efficiency of the particle, and c is the speed of light in a vacuum. Furthermore, $L_*(\lambda)$ is the emission of the star, which can be described by its monochromatic luminosity $L_*(\lambda) = 4\pi R_*^2 B_\lambda(T_{\mathrm{eff}})$, where R_* is the radius of the star, T_{eff} is the effective temperature of the star, and $B_\lambda(T_*)$ is the specific spectral radiance described by Planck's law (called Planck function[2]). Like stellar gravitational force, radiation pressure decreases with the distance squared to the star. However, this force is directed opposite to the stellar gravity, i.e., outwards.

Particles are strongly affected by both stellar gravity (Eq. 2.1) and radiation pressure (Eq. 2.2). In this way, one can introduce the combined force from the star the so-called "photogravitational" force F_{pg} (Burns, Lamy, and Soter, 1979; Krivov, 2010). It can be written as:

$$\mathbf{F}_{\mathrm{pg}} = \mathbf{F}_{\mathrm{g}} + \mathbf{F}_{\mathrm{rad}} = -\frac{GM_*(1-\beta)\, m_{\mathrm{dust}}}{r^3} r = (1-\beta)\, \mathbf{F}_{\mathrm{g}} , \tag{2.4}$$

where β is the ratio between radiation pressure and stellar gravity and is given as:

$$\beta = \frac{|\mathbf{F}_{\mathrm{rad}}|}{|\mathbf{F}_{\mathrm{g}}|} = \frac{\sigma \int_0^\infty L_*(\lambda)\, Q_{\mathrm{pr}}(a)\, \mathrm{d}\lambda}{4\pi c G M_* m_{\mathrm{dust}}} = \frac{3}{16\pi} \frac{\int_0^\infty L_*(\lambda)\, Q_{\mathrm{pr}}(a)\, \mathrm{d}\lambda}{c G M_* a \rho_{\mathrm{dust}}} , \tag{2.5}$$

---

[2] The blackbody doesn't emit equal amounts of radiation at all wavelengths, in particular, most of the energy is radiated within a relatively narrow band of wavelengths. The Planck function is the exact amount of energy emitted at a particular wavelength λ and is described by:

$$B_\lambda(T) = \frac{2hc^2}{\lambda^5} \frac{1}{e^{\frac{hc}{\lambda k_{\mathrm{B}} T}} - 1} , \tag{2.3}$$

where T is the temperature of the blackbody, h is Planck's constant, and k_{B} is Boltzmann's constant.

where the dust particle mass can be expressed by $m_{\rm dust} = \frac{4}{3}\pi a^3 \rho_{\rm dust}$ with the assumption of compact grains with spherical shape that are characterized by their bulk density $\rho_{\rm dust}$. This value is no function of the distance from the star; instead it depends on the properties of the dust particle (size a, bulk density $\rho_{\rm dust}$, and radiation pressure efficiency $Q_{\rm pr}$) and the stellar properties (e.g., stellar mass M_* and stellar luminosity $L_{\lambda *}$). With the assumption that the radiation pressure efficiency of an ideal absorber is, $Q_{\rm pr} \approx 1$, the β parameter approximates to (Wyatt et al., 1999):

$$\beta \approx 575 \left(\frac{\rho_{\rm dust}}{\rm kg\,m^{-3}}\right)^{-1} \left(\frac{a}{\rm \mu m}\right)^{-1} \left(\frac{L_*}{\rm L_\odot}\right) \left(\frac{M_*}{\rm M_\odot}\right)^{-1} , \tag{2.6}$$

where $\frac{L_*}{\rm L_\odot}$ and $\frac{M_*}{\rm M_\odot}$ are the stellar luminosity and mass in solar units, respectively.

As the radiation pressure counteracts the stellar gravity, there is a value of β that results in a liberation of the particle from the system. A particle released from a parent body if its kinetic energy is greater than or equal to its potential energy[3](Harwit, 1963; Zook and Berg, 1975). This results in the approximation of the value of β being greater than or equal to 0.5 (Burns, Lamy, and Soter, 1979). Thus, there are several possible orbits of dust particles under the photogravitational force, depending on the value of β (see Fig. 2.2; Krivov, 2010). For example, the system releases fragments into bound elliptical orbits if $0 < \beta < 0.5$ (which corresponds to $0 < e < 1$). The grain orbits are parabolic or hyperbolic and thus unbound[4] if $\beta = 0.5$ or $0.5 < \beta < 1$, respectively (which corresponds to $e = 1$ and $e > 1$, respectively). Also, if $\beta \geq 1$, the grain orbits are on anomalous hyperbola and thus released from the system. Consequently, the ejection condition and thus the cutoff blowout grain size $a_{\rm bo}$ is a strong function of the value of β.

Small particles are affected more strongly by radiation pressure, while the opposite is true for larger particles (see also a quantitative comparison of various forces acting on different dust grain sizes in Rodmann, 2006). This is due to smaller particles having a higher surface area to mass ratio, which increases the stellar incident radiation force on small particles. Small grains affected by radiation pressure in a typical disk are removed on timescales as short as 10-$10^{2.5}$ yr (Hillenbrand, 2008), which is far shorter than timescales for other forces. Thus, the radiation pressure is the dominant mechanism for the removal of small grains ∼ 1 to a few µm. This means that the grains with radii below the cutoff $a_{\rm bo}$ are not expected to be seen in a debris disk. Note that the timescale of radiation pressure is a function of the stellar source and grain properties.

Furthermore, the ejection condition, as well as the β ratio depends on the eccentricity of the parent bodies. A general expression for the β threshold, for which a dust particle is ejected from the eccentric system, can be expressed as follows (Murray and Dermott, 1999):

$$\beta_{\rm eject} \geq \frac{1}{2}\left(\frac{1-e^2}{1+e\cos\phi}\right) , \tag{2.7}$$

where ϕ corresponds to the longitude of the orbit, at which the particle ejected ($\phi = 0$ and $\phi = \pi$ corresponding to periastron and apastron, respectively). More detailed information on the ejection condition and blowout size of the eccentric parent belts can be found in Chapter 5.

2.1.3 Poynting-Robertson effect

The radiation pressure force acts radially on dust particles. However, the direction of the incident radiation (i.e., a tangential component) in the dust particle's reference frame is not perpendicular to the direction of the particle's motion. Thus, radiation pressure force depends on the velocity of the dust particle because the speed of light is

---

[3] This can be expressed by $\frac{m_{\rm dust} v^2}{2} \geq \frac{GM_*(1-\beta)\, m_{\rm dust}}{r}$, with $v^2 = \frac{GM_*}{r}$.

[4] Dust grains in bound and unbound orbits are called α-meteoroids and β-meteoroids, respectively (Zook and Berg, 1975).

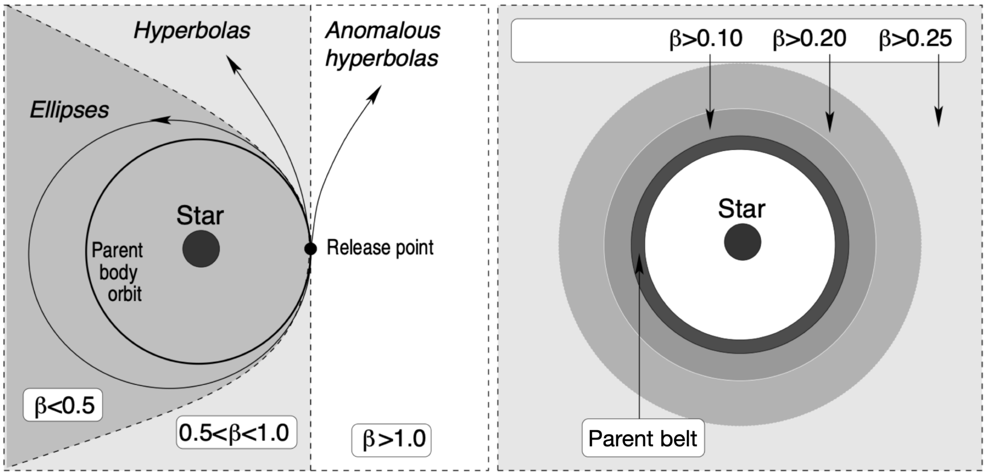

FIGURE 2.2: *Left*: Possible orbits of dust particles under the photogravitational force depending on the β value when grains are assumed to be released from a circular orbit. *Right*: Schematic of a debris disk produced by a parent belt, i.e., planetesimal belt, depending on the β value. Figure credit: Krivov (2010).

finite. The frequencies of photons emitted in the forward direction the particle's motion are relativistically boosted (or blueshifted). Thus, the dust particle loses more momentum in its forward direction as seen in the star's reference frame. As a result, this causes the orbiting dust particles to lose its angular momentum on its orbit around the star and in turn a continuous deceleration of the particle, which forces the particle to spiral inward (see also Fig. 2.1). This effect is called the Poynting-Robertson effect $\mathbf{F}_{\rm PR}$ (hereafter refered to as "PR drag"; Poynting, 1903; Robertson, 1937). The PR drag is given by (Burns, Lamy, and Soter, 1979):

$$\mathbf{F}_{\rm PR} = -\frac{GM_* \, m_{\rm dust}\beta}{r^2}\left(\frac{\mathbf{v}\cdot\mathbf{r}}{\mathbf{c}\cdot\mathbf{r}}\frac{\mathbf{r}}{r} + \frac{\mathbf{v}}{c}\right) , \tag{2.8}$$

where $\mathbf{v}$ is the particle velocity vector. As can be seen from Eq. 2.8 above, this effect is equivalent to a friction. Furthermore, particles can be trapped into resonances (Sect. 2.1.10) as they drift. The timescale for a dust grain to fall onto the star (i.e., spiral from a given distance r to the star) $t_{\rm PR}$ is given by (Burns, Lamy, and Soter, 1979; Gustafson, 1994; Wyatt, 2005; van Lieshout et al., 2014):

$$t_{\rm PR}(r) = -\frac{c\,r^2}{4GM_*\beta} . \tag{2.9}$$

In a typical debris disk, this happens on a timescale of $10^{5.5}$-$10^{7.5}$ yr (Hillenbrand, 2008). The PR drag is particularly effective on micrometer-sized grains, moving in Keplerian ellipses with reducing semimajor axes a and eccentricities e (Wyatt and Whipple, 1950; Breiter and Jackson, 1998). This is because larger dust grains are more likely to collide with each other long before the PR drag can have an effect on them. Thus, for low-density disks such as our solar system, the PR drag makes particles migrate inward before they are destroyed by collisions (Wyatt, Clarke, and Booth, 2011). Wyatt (2005) argues that for most currently detectable extrasolar debris disks, the densities are too high for the PR drag to be significant. This force, therefore, might be only important for systems around early-type stars.

2.1.4 Stellar winds drag

The electromagnetic radiation from the star gives rise to radiation pressure forces, while particulate radiation (e.g., charged particles rather than photons) from the star causes stellar wind forces. The total stellar wind force can also be decomposed into direct stellar wind pressure and stellar wind drag, similar to how total stellar radiation that can be decomposed into direct stellar radiation and PR drag. For most stars, the momentum carried by the stellar wind is $\sim$ several orders of magnitude smaller than the momentum carried by photons. Thus, the stellar wind pressure force may be negligible. However, stellar wind drag may not be ignored (Burns, Lamy, and Soter, 1979; Krivov, 2010). This is because the stellar wind velocity $v_{\rm sw}$, which is $\approx$ 300 to 800 km $\rm s^{-1}$ in the solar system (Allen and Penston, 1973), is much smaller than the speed of light and thus leads to greater forces, when replacing c in Eq. 2.8[5].

Gustafson (1994) indicated that the stellar wind drag is approximately 30% of the PR drag in the solar system. Furthermore, previous studies (e.g., Plavchan, Jura, and Lipscy, 2005; Strubbe and Chiang, 2006; Reidemeister et al., 2011), indicated that this stellar wind is not negligible for debris disks around late-type stars and becomes even more effective in this case.

2.1.5 Collisions

Since the lifetime of the dust particle $t_{\rm dust}$ ($\approx$ 1 Myr; Artymowicz and Clampin, 1997) is much shorter than that of the stellar source, dust in debris disks must be continuously produced, and thus replenished. Therefore, disruptive (or alternatively, destructive, fragmenting, or catastrophic) collisions have to be a dominant process acting on the almost gas-free environment in debris disks. For collisions to be disruptive, a sufficiently high relative velocity between large particles (e.g., km-sized planetesimals) is necessary (Krivov, 2010; Löhne et al., 2017). Thus, debris disks must be stirred to initiate a "collisional cascade".

The ignition of the collisional cascade: stirring mechanisms

Below, presently proposed stirring mechanisms on how a collisional cascade of planetesimals can be initiated in debris disks are presented:

- **Pre-stirring**: In a protoplanetary disk, relative velocities of solids are set by turbulences, Brownian motion, differential settling, and differential radial migration/drift (see Sect. 1.2.5), even though these relative velocities are mostly damped by dense ambient gas. This "pre-stirring" phenomenon results in particles being expected to have their eccentricities and inclinations $e \approx i \approx 0.001$ (Wyatt, 2008; Brauer, Dullemond, and Henning, 2008), which is far smaller than in typical debris disks (Brauer, Dullemond, and Henning, 2008). Solids are expected to preserve a low-velocity dispersion that they get by primordial gas removal.

- **Delayed stirring**: Planetesimal stirring takes longer and thus is delayed (i.e., it occurs later) from the gas dispersal (i.e., the stirring of disks may still proceed some time after the birth of the star). It is, therefore, referred to as "delayed stirring" (Dominik and Decin, 2003). This stirring could be due to the external events of stellar flybys with energetic collisions, which may be possible during the early phase of the debris disk evolution in a young cluster, though such events are statistically rare (Kenyon and Bromley, 2002). One obvious prediction of the delayed stirring models is an increase of the disk's outer radius with age (Wyatt, 2008).

- **Self-stirring**: At later times, it is expected that the planetesimals grow large enough for stirring (e.g., bigger than $\sim$ a thousand to a few thousands of km, i.e., Pluto-sized). At this point, the disk is stirred by the gravitational perturbations that excite the remaining smaller bodies within the planetesimal belt. This

---

[5] The stellar winds drag $\mathbf{F}_{\rm sw\,drag}$ is given by (Burns, Lamy, and Soter, 1979; Krivov, 2010):

$$\mathbf{F}_{\rm sw\,drag} = -\frac{GM_* \, m_{\rm dust}\beta}{r^2}\left(\frac{\mathbf{v}\cdot\mathbf{r}}{\mathbf{v}_{\rm sw}\cdot\mathbf{r}}\frac{\mathbf{r}}{r} + \frac{\mathbf{v}}{v_{\rm sw}}\right). \tag{2.10}$$

mechanism is called "self-stirring" (Kenyon and Bromley, 2008; Kenyon and Bromley, 2010; Kennedy and Wyatt, 2010). Kenyon and Bromley (2008) predicted that Pluto-sized objects can grow quickly enough to explain the dust production starting at the ages of several hundreds of Myr. This excitation depends strongly on their orbital periods, and thus the distance to the star, as well as on the surface density of solid material (e.g., planetesimals). Recently, Krivov and Booth (2018) found that self-stirring by mid-sized planetesimals can be more efficient than thought previously. Furthermore, this efficiency strongly depends on the (initial) total disk mass. The self-stirring mechanisms occur at delayed time scales as well, this is, therefore, considered as a subset of the delayed stirring mechanism.

- **Planetary stirring**: The self-stirring model is the most comprehensive model so far. However, the effect of the formation of massive planets in the disk is ignored in that model. Kalas et al. (2008) indicated that large numbers of massive planets exist within debris disks systems. The effect of a massive planet, therefore, cannot be ignored. Mustill and Wyatt (2009) showed that a planetesimal belt at several tens of au can be stirred by an eccentric (e.g., $e \approx 0.2$-0.4) "giant planet" (e.g., 2-3 $\mathrm{M_J}$[6]) located close to the inner edge at only a few au on timescales of typically several tens of Myr. The timescale of these secular perturbations may be shorter than the timescale of the self-stirring for systems where the planet orbits close to the inner edge of the disk.

The radial structure of the debris disk can provide valuable information for distinguishing between different interpretations/methods of stirring (Wyatt, 2008). The self-stirring and planetary stirring include an inner planet/planetary object and assume the "inside-out process", i.e., the collisional cascade is ignited in the inner disk first and propagates outwards. Consequently, these mechanisms may result in an increase of the surface density profile (Kennedy and Wyatt, 2010), which is confirmed by ALMA observations (e.g., AU Mic and HD 107146; MacGregor, 2014; Ricci et al., 2015a).

The collisional cascade

Once a disk is sufficiently stirred, planetesimals participate in a collisional cascade. A collisional cascade grinds the solid material (e.g., planetesimals) down to dust size until the smallest fragments with $\beta \gtrsim 0.5$ are blown out from the disk by stellar radiation pressure (see Sect. 2.1.2). Typical eccentricities of grain orbits are in the same order as their β ratio (e.g., Burns, Lamy, and Soter, 1979; Murray and Dermott, 1999; see also Eq. 2.7), meaning that the radiation pressure ensures the impact velocities to be sufficiently high. Consequently, stirring mechanisms are no longer required for the dust-sized particles. In addition, β-meteoroids (Zook and Berg, 1975) with hyperbolic orbits (see Sect. 2.1.2) may be energetic enough to trigger a self-sustained cascade (called "dust avalanche"; Artymowicz and Clampin, 1997; Krivov, Mann, and Krivova, 2000; Grigorieva, Artymowicz, and Thébault, 2007).

A steady-state collisional cascade[7] produces a grain size distribution numbers $n(a)$ that is usually described by a power-law or by a combination of power-laws with different exponents for different size ranges:

$$n(a) \propto a^{\gamma} \ , \tag{2.11}$$

where $n(a)\,\mathrm{d}a$ is the number of planetesimals of size between a and $a + \mathrm{d}a$. Under the assumptions of an equilibrium collisional cascade without additional forces acting on the dust particles, Dohnanyi (1969) predicted that collisions produce a simple analytical solution with γ = - 3.5 for the differential size distribution of dust grains. Due to the steep slope of the power-law, the grain size distribution is heavily weighted towards small grains, meaning that most

---

[6] $\mathrm{M_J}$ = 1 Jupiter mass = 1.898×10^{27} kg = 317.8 $\mathrm{M_\oplus}$

[7] A steady-state implies a balance between the dust production by the collisional cascade and its losses by the stellar radiation pressure.

of the cross-section, i.e., emitting surface area budget, is in the small particles, while most of the mass budget is in the larger planetesimals. This classical solution is expected to result in a good agreement with very massive debris disks, where collisions dominate the dynamics of the dust, while it is not satisfied with less massive disks, where PR drag becomes more significant (Sect. 2.1.3).

However, the collisional cascade does not extend down to arbitrarily small particles, i.e., in reality, a collisional cascade proceeds only up to some smallest fragments corresponding to $\beta \gtrsim 0.5$, since particles with $a < a_{\rm bo}$ are being quickly removed by radiation forces (see also Sect. 2.1.2). In addition, the non-gravitational forces acting on grains, particularly in the range of tens to hundreds of micrometers in diameter, may further modify the size distribution, i.e., it is strongly affected by dust grain dynamics in debris disks (Krivov, Mann, and Krivova, 2000; Thébault and Augereau, 2007; Löhne et al., 2017). Thus, the size dependency of the critical specific energy for fragmentation (e.g., disruption and/or dispersal), which is necessary to disrupt a particle, must be considered.

The kinetic energy of the projectile per unit target mass is called critical specific energy $Q^*_{\rm D}$. This is the conventional definition of the threshold between partial disruptive collisions (called cratering), which results in the target retains at least half of its original mass, and disruptive collisions, which results in the largest remnant containing half of the original target mass $m_{\rm largest} = 0.5\, m_{\rm t}$, where $m_{\rm t}$ is the mass of the target (see e.g., Paolicchi, Verlicchi, and Cellino, 1996; Durda, Greenberg, and Jedicke, 1998; Benz and Asphaug, 1999; Thébault and Augereau, 2007). For smaller solids, $Q^*_{\rm D}$ for disruption of the target (called shattering) is determined solely by the material strength $Q_{\rm s}$ and decreases with increasing target size because of a decreased effective strength with increasing size of the target asteroid. On the other hand, for larger solids (> 100 m), the value of $Q^*_{\rm D}$ for the disruption of the target (called dispersion) is determined by the gravitational binding energy $Q_{\rm g}$ and increases with increasing target size because of the increasing role of self-gravity (Durda, Greenberg, and Jedicke, 1998; Benz and Asphaug, 1999; Stewart and Leinhardt, 2009). Consequently, $Q^*_{\rm D}$ can be described by the sum of two power-laws with different slopes, in particular, the gravitational strength $Q_{\rm g}$ shows a much steeper slope than that of material strength $Q_{\rm s}$ (see Fig. 2.3; Holsapple, 1994; Paolicchi, Verlicchi, and Cellino, 1996; Durda, Greenberg, and Jedicke, 1998; Benz and Asphaug, 1999; Kenyon and Bromley, 2004; Stewart and Leinhardt, 2009). Furthermore, $Q^*_{\rm D}$ is a strong function of the composition and porosity of the solid (Collins et al., 2019). For example, the value of $Q^*_{\rm D}$ of an icy material is smaller (weaker material; tends to be shattered easily) than that of rocky material. Consequently, the $Q^*_{\rm D}$ value is a very important quantity in the collisional evolution that can be expressed approximately as:

$$Q^*_{\rm D} = Q_{\rm s}\left(\frac{a_{\rm t}}{1{\rm m}}\right)^{-b_{\rm s}} + Q_{\rm g}\left(\frac{a_{\rm t}}{1{\rm km}}\right)^{b_{\rm g}} , \tag{2.12}$$

where $a_{\rm t}$ represents the target radius and the subscripts of s and g stand for the strength and gravity regime, respectively. The values of $Q_{\rm s}$ and $Q_{\rm g}$ lie in the range $\sim 10^5$-10^7 erg g^{-1}, $b_{\rm s}$ is between 0 and 0.5, and $b_{\rm g}$ between 1 and 2 (Benz and Asphaug, 1999). The critical energy reaches a minimum ($\sim 10^4$-10^6 erg g^{-1}) at sub-km sizes. Since very small dust sizes have never been probed experimentally, true values still remain unknown, and thus, Eq. 2.12 is assumed to extrapolate only $\sim 10^8$ erg g^{-1} towards small target radii. From the definition of the critical specific energy $Q^*_{\rm D}$, the minimum mass of a projectile that destroys the target satisfies the equation below:

$$\frac{m_{\rm t}\, m_{\rm crit}}{m_{\rm t} + m_{\rm crit}} \frac{{v_{\rm imp}}^2}{2} = m_{\rm t}\, Q^*_{\rm D}\left(m_{\rm t}\right) + m_{\rm crit}\, Q^*_{\rm D}\left(m_{\rm crit}\right) , \tag{2.13}$$

where $m_{\rm crit}$ and $m_{\rm t}$ are the minimum mass of the shattering projectile and the mass of the target, respectively, and $v_{\rm imp}$ is the impact velocity. With the assumption of $m_{\rm crit} \ll m_{\rm t}$, Eq. 2.13 can be simplified to:

$$\frac{m_{\rm crit}\, {v_{\rm imp}}^2}{2} \approx m_{\rm t}\, Q^*_{\rm D}\left(m_{\rm t}\right) . \tag{2.14}$$

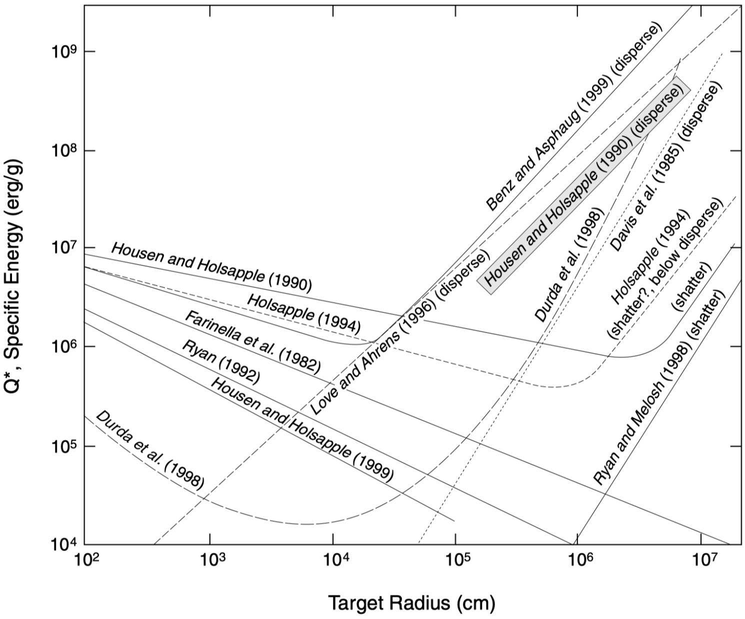

FIGURE 2.3: Various critical specific energy Q^*_D values with shattering and dispersion, as presented by various authors. Note that these results are for rocky bodies only, and not for porous bodies. Figure credit: Holsapple et al. (2002).

Consequently, both colliders are disrupted if their relative velocity v_rel exceeds (Krivov, Sremčević, and Spahn, 2005):

$$v_\mathrm{crit} = \sqrt{\frac{2(m_\mathrm{t} + m_\mathrm{p})^2}{m_\mathrm{t}\, m_\mathrm{p}} \, Q^*_\mathrm{D}} \, , \tag{2.15}$$

where m_p is the mass of the projectile. Overall, lower Q^*_D means lower v_crit, so that the relative velocity v_rel for a disruption collision between both colliders is decreased, i.e., a more violent collisional environment (see Chapter 5). With the assumption of the sizes of projectile and target to be similar, one can get v_crit is about $\sqrt{8Q^*_\mathrm{D}}$, meaning that $v_\mathrm{crit} \approx$ several hundred m s^{-1} (Krivov, 2010). Furthermore, detailed analyses in simulational studies (Thébault and Augereau, 2007; Krivov, 2010; Löhne et al., 2017) show that two outcomes are expected to play a crucial role in debris disks: complete disruption and cratering. In particular, the cratering is responsible for making a wavy grain size distribution at larger sizes. Thus, this effect substantially enhances the maximum of the grain size distribution at smaller sizes (see also Sect. 4.2.1).

If planetesimal belts are more dynamically excited, the number density is decreased in general. Thus, the ring widths are different and so are the peak densities. The dynamical excitation (level of stirring) is, therefore, also one of the important parameters for collisions. A more detailed discussion about the influence of the collisions, e.g., planetesimal eccentricities, dynamical excitation, and material strength, on the observational appearance of debris disks can be found in Chapter 5.

Wyatt (2005) indicated that the densities of most known debris disks are too high for the PR drag (see also Sect. 2.1.3) to be significant, meaning the dust grains are more likely to be destroyed by mutual grain-grain collisions. Therefore, the collisional activity has a rather short typical timescale (e.g., < 10^4-$10^{5.5}$ yr; Hillenbrand, 2008).

2.1.6 The Lorentz force

The forces discussed in the previous sections influence dust grains that carry a positive charge due to the photoemission of electrons; their motion is influenced by electromagnetic forces (Goertz, 1989). This means these dust grains are subject to be affected by the Lorentz force $F_{\rm L}$ in the environment of the interplanetary magnetic field of the star, which acts mainly along the vertical direction (i.e., perpendicular to the disk), and thus rapidly changes the direction and inclination of a particle's orbit (Gustafson, 1994; Rodmann, 2006). However, this effect becomes significant for grains less than several nanometers in size, which makes only a minor contribution to both the mass budget and the total cross-section area of the dust disk. Assuming the charge on a grain surface to be proportional to its size a, and the ratio of Lorentz force to stellar gravity is then given by Rodmann (2006):

$$\frac{\mathbf{F}_{\rm L}}{\mathbf{F}_{\rm g}} \propto \frac{q\,\mathbf{B}}{m_{\rm dust}/r^2} \propto \frac{a/r}{a^3/r^2} = \frac{r}{a^2} \,, \tag{2.16}$$

where q is electric charge and $\mathbf{B}$ is a magnetic field. Thus, the Lorentz force is of relevance only for small grains far away from the star. These small grains are blown away by the radiation pressure (see Sect. 2.1.2). Furthermore, larger solids (e.g., planetesimals) are neutral. Consequently, the Lorentz force is not included in most of debris disk modeling.

2.1.7 The Yarkovsky effect

An object that is illuminated by a stellar source absorbs stellar radiation non-isotropically, which leads to an uneven temperature distribution of the surface of the object. This results in the "afternoon" hemisphere of the object being warmer than the "morning" hemisphere (Burns, Lamy, and Soter, 1979). The resulting reaction force may speed up or slow down the orbital motion of meter-sized objects, depending on the object's spin axis. This effect is called the Yarkovsky effect $F_{\rm Y}$. However, it only acts on large (meter-sized and larger), rotating bodies (Burns, Lamy, and Soter, 1979). Thus, this effect is often neglected as well, as long as the steep grain size distribution is considered (i.e., the contribution of larger grains are neglected) in the debris disk modeling.

2.1.8 Sublimation

Refractory dust grains in orbits around a star spiral into the star due to the PR drag (2.1.3). Because the particles lose their mass during sublimation, the β value for each particle increases. As a result, their radial-drift rates decrease and the particles pile up at the outer edge of their sublimation zone. These grains sublimate in the immediate vicinity of the star (e.g., Mukai and Yamamoto, 1979; Burns, Lamy, and Soter, 1979; Kobayashi et al., 2011). Therefore, the formation of a dust ring due to the sublimation of dust particles is a common process for radially drifting particles due to the PR drag. This effect gradually reduces the sizes of dust grains, which makes this process an efficient way of dust depletion of small grains in debris disks. In addition, the fact that the gas pressure in debris disks is very low in contrast to protoplanetary disks, sublimation, therefore, occurs at lower temperatures, e.g., water ice sublimates at $\sim$ 100-110 K (Lecar et al., 2006; Kobayashi et al., 2011). A more detailed discussion about the influence of the sublimation effect on the observational appearance of debris disks can be found in Chapter 6.

2.1.9 Sputtering

Since debris disks are very optically thin, i.e., transparent to the stellar radiation, even highly energetic photons such as ultraviolet (UV) photons can penetrate debris disks out to very far distances. Individual UV photons absorbed by an ice grain do not only dissociate water molecules but can cause OH to be directly desorbed from the surface of the ice grain. This effect is called UV photosputtering (Grigorieva et al., 2007). It is currently believed that these dust particles are destroyed by sputtering erosion. Grigorieva et al. (2007) predicted that UV photosputtering efficiently destroys ice even far beyond the ice sublimation line. A more detailed discussion about the influence of the sputtering effect on the observational appearance of debris disks can be found in Chapter 6.

2.1.10 Interaction with planets

Dynamical/gravitational interactions with one or more nearby planets, which strongly impact the structure and evolution of debris disks, can lead to representative morphological features in debris disks. These can be used to identify unseen planets in disks because each process has its own characteristic signatures and effects on the dust dynamics (Wyatt, 2003).

The secular perturbation: Pluto-sized planets (and/or massive planets) can stir the disk (Kenyon and Bromley, 2008; Mustill and Wyatt, 2009; see Sect. 2.1.5), which results in higher dynamical excitation, and thus launches a collisional cascade. Eccentric planets cause tightly wound spirals and an offset ring center. In particular, even the outer disk can be stirred by planets close to the star, depending on its initial inclination and if the planet's orbit is eccentric in a sufficiently old system (Wyatt, 2005; Mustill and Wyatt, 2009; Pearce, Wyatt, and Kennedy, 2014). These secular structures are already observed, e.g., HD 141569A (Clampin et al., 2003), Fomalhaut (MacGregor et al., 2016), and β Pictoris (Golimowski et al., 2006).

Resonances: Planets decrease the particle density within their orbits in a debris disk system (Kenyon and Bromley, 2002), which may significantly sculpt the spatial distribution of the dust and planetesimals, e.g., by the formation of gaps (Bryden and Lin, 1999; Bryden et al., 2000; Kley, 2000) or inner holes in the spatial distribution (Wyatt, 2003), preventing dust grains from moving inwards due to PR drag. In particular, if the dust particle's orbital period is a fraction of the planet's period, the interaction of the two bodies (e.g., a planet and a dust particle) orbiting a central star induces a resonance. The orbital periods $T_{\mathrm{orb}\,1,\mathrm{orb}\,2}$ of an these bodies, are connected to their mean angular velocities $n_{1,2}$ by the relation $n_{1,2} = 2\pi/T_{\mathrm{orb}\,1,\mathrm{orb}\,2}$. This type of resonance is, therefore, called "mean motion resonance", which follows the equation (Murray and Dermott, 1999):

$$\frac{T_{\mathrm{orb}\,1}}{T_{\mathrm{orb}\,2}} = \frac{n_2}{n_1} = \frac{p}{p+q}, \tag{2.17}$$

where p and q are integers with $p > 0$ and $p + q \geq 1$. For example, for $p = 2$ and $q = 1$ (i.e., the particle being in the 2:3 resonance), the dust particle completes two orbits for every three orbits of the planet (see Fig. 2.4). Note that the angular velocity on a given orbit does not only depend on the central mass but also the precession of the orbit due to the gravitational perturbations on small particles, meaning that a dust particle and a planet on the same orbit might not have the same angular velocity, and thus not be in resonance (Ertel, 2012). A well-known example of a mean-motion resonance is the asteroid belt and Kuiper belt in the solar system. For example, the Hilda group and Koronis family in asteroids belt are in a 3:2 and 5:2 resonance with Jupiter, respectively. In addition, Twotinos and Plutinos in the Kuiper Belt are in a 2:1 and 3:2 resonance with Neptune, respectively (e.g., Jewitt, Trujillo, and Luu, 2000; Chiang and Jordan, 2002). Furthermore, similar structures exist in other debris disk systems, e.g., ϵ Eridani, Fomalhaut, and Vega (Holland et al., 1998; Holland et al., 2003; Wilner et al., 2002).

The scattering process: Based on the disk architecture, solids in debris disks can be scattered by inner/outer planets (e.g., Davies et al., 2014). In the solar system, this is the dominant process governing the evolution of solids and comets that are from the Kuiper belt. For example, Kuiper belt objects scattered in by outer giant planets may have become short-period Jupiter-family comets (Levison and Duncan, 1997), while Oort cloud objects were probably scattered out from Kuiper belt, possibly during the formation of outer planets or through interactions with Neptune

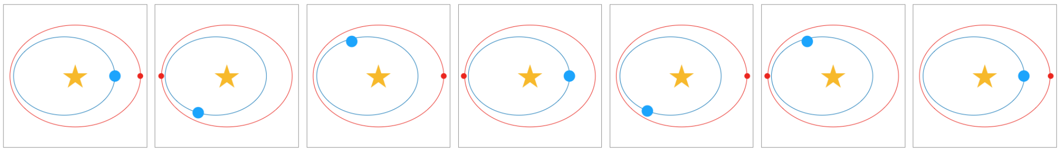

FIGURE 2.4: An example of the orbital motion in 2:3 mean motion resonance, i.e., for $p = 2$ and $q = 1$. The star indicates the yellow star-shape in the center, the blue dot indicates the planet, and the small red dot indicates the small body (e.g., an asteroid or a dust grain). Figure is based on Rodmann (2006).

(Morbidelli, Emel'yanenko, and Levison, 2004). Bonsor and Wyatt (2012) indicated, for a system packed with planets between 1-30 au and an outer belt, the minimum distance to which comets can be scattered depends on the planet mass. Consequently, the planetary scattering process causes migration and depletion of solids in debris disks.

2.2 Irradiated dust particles

When stellar radiation hits a dust particle, the radiation and the particle interact. This process either changes the direction of the photons due to reflection, refraction, or diffraction, which is called 'scattering' or it is absorbed. As a consequence, the dust particle re-emits its absorbed radiation again, which is called 'thermal re-emission'. The non-interacting transmitted intensity, though, decreases exponentially with the optical thickness of the material the light is passing through. The emergent observables, e.g., the spectral energy distributions (SEDs) and spatially resolved images, are then determined by scattering, absorption & re-emission of stellar radiation, which is addressed in the following section based on several assumptions below:

- Since debris disks are optically (and geometrically) thin, the dust configuration is optically thin along any line of sight for both the stellar and re-emitted radiation by the dust. Furthermore, the effects of multiple scattering, the self-extinction (e.g., self-scattering), and the additional grain heating by dust re-emission are completely neglected (i.e., each dust grain is heated only by the stellar radiation). This finally leads to a significant simplification of the radiative transfer equations. For example, the dust temperature distribution is solely determined by stellar radiation, the distance to the star, and the optical properties (which is, in turn, a function of chemical composition and the individual grain sizes).

- Observed circumstellar disks have higher densities and larger-sized particles than the interstellar medium (ISM). This is either caused by the sticking together of small particles and/or the disruption of larger bodies through mutual collisions. Not only grains smaller than a few µm can be affected by stellar radiation, and thus been blown away (see Sect. 2.1.2), but also the dust re-emission varies on short timescales, and thus there is no equilibrium temperature for very small grains (~ 1 nm), as Kruegel (2003) indicated. Consequently, dust grains are assumed to be large enough ($\gg 1$ nm; i.e., with large size parameters x) to rule out stochastic heating, so that they are in a state of thermal equilibrium with the ambient radiation field.

- The dust grains are assumed to be compact and spherical objects with homogeneous physical, chemical, and mineralogical properties.

2.2.1 Optical properties

When an electrically insulating material or a very poor conductor of electric current such as silicate (i.e., the representative dust particle in debris disks) is placed in an electric field $\vec{E}$, electric charges do not flow through the material, i.e., there is practically no current, but they shift slightly from their average equilibrium positions, which causes dielectric polarization. This results in positive charges being displaced in the direction of the field and negative charges shifting in the direction opposite to the field and creating an internal electric field that reduces the overall field within the electrical insulator (called dielectric) itself. The response of the material to the electrical field $\vec{E}$ (i.e., a measure of how much the material opposes the external electric field) can be characterized by the dielectric function ϵ $(= \epsilon' + \epsilon'')$, called the permittivity of a non-magnetic material, which is a direct result of the Maxwell equations. This dielectric function is linked to the complex refractive index $m = \sqrt{\epsilon/\epsilon_0} = n + ik$, where ϵ_0 is the dielectric function in vacuum, n is the real part of the refractive index, and k is the imaginary part of refractive index. Here, the real part n determines the phase velocity, while the imaginary part k (also called the extinction coefficient) determines the amount of attenuation an electromagnetic wave experiences when it propagates through the material. Both n and k are wavelength dependent.

2.2.2 Mie theory

The interaction of a dust particle with the incident stellar radiation can be described by Mie theory (Mie, 1908). Here only three parameters are used to govern this interaction, i.e., the incident radiation wavelength λ, the size of the dust particle a (and thus the dimensionless size parameter $x = 2\pi a/\lambda$), and the complex refractive indices n and k (Sect. 2.2.1). The main objective of this theory is to calculate the scattering and absorption cross-sections at a given wavelength, for a particle of a given size and thus size parameter. Important quantities that are used to describe the effects on a photon when scattering is introduced in this section. A more detailed description of the Mie scattering solution can be found in Van de Hulst and Twersky (1957), Deirmendjian (1969), Bohren and Huffman (1983), and Wolf and Hillenbrand (2003).

To describe the electromagnetic radiation, a set of time averages of the parallel and perpendicular components of the electric field, called the Stokes vector **I**, can be used. Each element of the Stokes vector (i.e., I: total flux density, Q: the difference between flux density transmitted by a linear polarizer oriented parallel to the horizontal direction and one oriented parallel to the vertical direction, U: the difference between flux density transmitted by a linear polarizer oriented 45° to the x-axis and one oriented at 135°, and V: the difference between flux density transmitted by a right-circular polarizer and a left-circular polarizer) is a measurable quantity and is defined as follows:

$$\mathbf{I} = \begin{bmatrix} I = \langle E_{\mathrm{x}}^2 \rangle + \langle E_{\mathrm{y}}^2 \rangle = \langle E_{\mathrm{a}}^2 \rangle + \langle E_{\mathrm{b}}^2 \rangle = \langle E_{\mathrm{l}}^2 \rangle + \langle E_{\mathrm{r}}^2 \rangle \\ Q = \langle E_{\mathrm{x}}^2 \rangle - \langle E_{\mathrm{y}}^2 \rangle \\ U = \langle E_{\mathrm{a}}^2 \rangle - \langle E_{\mathrm{b}}^2 \rangle \\ V = \langle E_{\mathrm{l}}^2 \rangle - \langle E_{\mathrm{r}}^2 \rangle \end{bmatrix}, \tag{2.18}$$

where the subscripts refer to three different bases, the standard Cartesian basis $(\hat{x}, \hat{y})$, a Cartesian basis rotated by 45° $(\hat{a}, \hat{b})$, and a circular basis $(\hat{l}, \hat{r})$ in terms of the time averages (i.e., these intensities are temporally and spatially averaged; denoted by $\langle . \rangle$). The circular basis is defined such that $\hat{l} = (\hat{x} + i\hat{y})/\sqrt{2}$. Furthermore, the Stokes vector **I** represents the most general state of polarization of a light wave with its total intensity I, polarization degree $p = \frac{\sqrt{Q^2+U^2+V^2}}{I}$ (linear polarization degree $p_{\mathrm{L}} = \frac{\sqrt{Q^2+U^2}}{I}$), and the shape parameters of the polarization ellipse. Fully polarized light satisfies $I^2 = Q^2 + U^2 + V^2$, while partially polarized light and unpolarized light satisfy $I^2 > Q^2 + U^2 + V^2$ and $Q = U = V = 0$, respectively.

The scattering of stellar radiation by a dust particle can be described by the 4 x 4 real Müller matrix **S** (or scattering matrix), which provides the complete description of a medium's response to passing light with respect to the change of the polariazation state of the light. The wavelength λ and the scattering angle θ (i.e., the angle between the directions of incident and scattered radiation) dependent Müller matrix **S** fully characterizes the optical properties of the sample by the interaction of polarized light with matter in the absence of non-linear effects and can be described as:

$$\mathbf{S}(\lambda,\theta) = \begin{bmatrix} S_{11}(\lambda,\theta) & S_{12}(\lambda,\theta) & S_{13}(\lambda,\theta) & S_{14}(\lambda,\theta) \\ S_{21}(\lambda,\theta) & S_{22}(\lambda,\theta) & S_{23}(\lambda,\theta) & S_{24}(\lambda,\theta) \\ S_{31}(\lambda,\theta) & S_{32}(\lambda,\theta) & S_{33}(\lambda,\theta) & S_{34}(\lambda,\theta) \\ S_{41}(\lambda,\theta) & S_{42}(\lambda,\theta) & S_{43}(\lambda,\theta) & S_{44}(\lambda,\theta) \end{bmatrix}. \tag{2.19}$$

Although all 16 matrix elements for an ensemble can be non-zero and different, symmetry reduces the number of matrix elements (i.e., in case the light is scattered off by a spherical particle). Consequently, the scattering process, including the scattering matrix for a rotationally and mirror symmetric ensemble, has the form:

$$\begin{bmatrix} I_{\mathrm{s}} \\ Q_{\mathrm{s}} \\ U_{\mathrm{s}} \\ V_{\mathrm{s}} \end{bmatrix} \propto \begin{bmatrix} S_{11} & S_{12} & 0 & 0 \\ S_{12} & S_{11} & 0 & 0 \\ 0 & 0 & S_{33} & S_{34} \\ 0 & 0 & -S_{34} & S_{33} \end{bmatrix} \begin{bmatrix} I_{\mathrm{i}} \\ Q_{\mathrm{i}} \\ U_{\mathrm{i}} \\ V_{\mathrm{i}} \end{bmatrix}. \tag{2.20}$$

Now, the Müller matrix $\mathbf{S}$ of a sample is defined by the linear relationship $\mathbf{I}_{\mathrm{s}}\,(\lambda,\theta) = \mathbf{S}(\lambda,\theta)\,\mathbf{I}_{\mathrm{i}}\,(\lambda)$, where $\mathbf{I}_{\mathrm{i}}\,(\lambda)$ and $\mathbf{I}_{\mathrm{s}}\,(\lambda,\theta)$ are the Stokes vectors of the incident (before scattering) and the scattered beam, respectively.

Based on the size parameter x and the refractive index m of the dust material, one can be calculated for the complex Mie coefficients, which determine the complex amplitude functions in turn. These quantities finally define the individual elements of the Müller matrix $\mathbf{S}_{\mathrm{ik}}$ (Eq. 2.19; Van de Hulst and Twersky, 1957; Bohren and Huffman, 1983; Wolf and Voshchinnikov, 2004). Furthermore, the important parameters that describe the optical properties of dust particles, e.g., the scattering efficiency Q_{sca}, the absorption efficiency Q_{abs}, and the radiation pressure efficiency Q_{pr}, can be calculated via the complex Mie coefficients.

The absorption cross-section C_{abs} (= $\sigma \cdot Q_{\mathrm{abs}}$[8]) and scattering cross-section C_{sca} (= $\sigma \cdot Q_{\mathrm{sca}}$) indicate how efficient dust grains can absorb and scatter the stellar radiation compared to perfect absorption or scattering (i.e., $Q_{\mathrm{abs}} = Q_{\mathrm{sca}} = 1$), respectively. In the Rayleigh scattering regime (i.e., the size of the dust grain is smaller than the wavelength; $x \ll 1$; see Fig. 2.5), depending on the wavelength, dust grain size, and chemical composition, Q_{abs} and Q_{sca} approximately follow $\propto \frac{1}{\lambda}$ and $\frac{1}{\lambda^4}$, respectively, if m is a weak function of the wavelength. Thus, the absorption and scattering cross-section typically show relatively high values at visible to mid-IR wavelengths and decreases gradually and steeply toward longer wavelengths, respectively. In the geometric scattering regime (i.e., the size of dust grain is larger than the wavelength; $x \gg 1$; see Fig. 2.5), grains act like blackbodies, thus, Q_{abs} and Q_{sca} are close to ≈ 1. The extinction cross-section C_{ext} (= $C_{\mathrm{sca}} + C_{\mathrm{abs}}$) is the sum of two cross-sections, i.e., C_{abs} and C_{sca}. Thus, this value indicates the total extinction cross-section encountered by the radiation passing the medium.

The radiation pressure cross-section C_{pr} (= $\sigma \cdot Q_{\mathrm{pr}}$) = C_{abs} + (1 - g) C_{sca}, where g is the scattering asymmetry parameter (or "mean cosine of scattering angle" $\langle \cos\theta \rangle$), which indicates the intensity-weighted average of the cosine of the scattering angle[9], can be calculated via Mie theory as well. The Q_{pr} value is varying with 0 (for perfect transmitters), 1 (for perfect absorbers), and 2 (for perfect backscatterers). This value, therefore, controls the fraction of the momentum transferred from the infalling radiation to the grain. In case of an anisotropic forward scattering (i.e., $g \approx 1$), the Q_{pr} value gets close to the Q_{abs} value.

---

[8] The cross-sections C are of area dimension, while the efficiency factors Q are dimensionless.

[9] The value of g can be calculated via the integration of the element S_{11} of the Müller matrix $\mathbf{S}$ ($g = \frac{\int_0^\pi S_{11} \cos\theta \sin\theta \, d\theta}{\int_0^\pi S_{11} \sin\theta}$) and varies between -1 and 1, with -1 (backward scattered like a mirror), 0 (symmetric scattering; $x \ll 1$), and 1 (purely forward scattering; $x \approx 1$). Therefore, g represents the distribution of the scattered radiation in the forward/backward direction (Wolf and Voshchinnikov, 2004).

Based on these efficiencies, the dust albedo Λ[10] can be calculated as well. These quantities are necessary to describe the interaction of a dust particle with the stellar radiation as discussed in the following sections (Sect. 2.2.3 and 2.2.4).

A numerical implementation of the Mie theory is *miex* (Wolf and Voshchinnikov, 2004), which allows considering arbitrary size parameters with broad grain size distributions and a very wide wavelength range of the interacting radiation. Single particles, as well as particle ensembles consisting of several components and particle size distributions, can be considered.

2.2.3 Scattering of stellar radiation

Scattering is the redirection of radiation due to interactions with matter, e.g., molecule and particle - dipoles, which are composed of discrete electrical charges. A single dust particle can be considered as a tiny dipolar antenna that is driven to radiate in response to an incident oscillating electric field. This induces the dust particle to emit its own waves in reaction to the incoming waves. Therefore, the resulting total wave is the superposition of the incident and scattered electromagnetic waves. Scattering by a coherent array of antennas depends on the dust properties such as the geometry (e.g., its size, shape, observation angle, and scattering angle) and the composition (e.g., the response of the individual antennas), as well as the polarization state of the incident wave. In the UV, visible (VIS) and near-IR, scattering is the dominant atmospheric source of radiation along any line of sight (Buenzli and Schmid, 2009); Mie scattering is the dominant process based on the grain size distribution that is considered (see Sect. 2.1.5) in this study (see Fig. 2.5). Furthermore, initially unpolarized light scattered off of dust is generally linearly polarized. Thus, a high degree of (linear) polarization is expected when assuming a characteristic orientation that is (at least radially) symmetric with respect to the source of the illumination in the optically thin case (Kruegel, 2003). In the solar system, the intensity and polarization state, in particular, the degree of polarization of scattered light is a key diagnostic for the grain properties, e.g., grain size, shape, composition, physical structure, and alignment of individual grains and their distribution along the line of sight (Graham, Kalas, and Matthews, 2007).

The stellar radiation can be considered to be unpolarized (i.e., $Q_\mathrm{i} = U_\mathrm{i} = V_\mathrm{i} = 0$) because of the isotropic incident radiation (Schwarz, 1986). Furthermore, the multiple scattering can be neglected in optically thin debris disks. The Stokes vectors of the incident radiation can, therefore, be written as $\mathbf{I}_\mathrm{i} = [\mathrm{I}_\mathrm{i}, 0, 0, 0]^\mathrm{T}$. Consequently, the scattered (linearly polarized) radiation by a dust particle $\mathbf{I}_\mathrm{s}$ and $\mathbf{Q}_\mathrm{s}$ can be simplified to:

$$\mathbf{I}_\mathrm{s} = S_{11}(\theta)\,\mathbf{I}_\mathrm{i}, \tag{2.21}$$

and

$$\mathbf{Q}_\mathrm{s} = S_{12}(\theta)\,\mathbf{I}_\mathrm{i}. \tag{2.22}$$

The photons emitted by the central star are not isotropically scattered by the dust grains, which is one of the main differences between scattering and thermal re-emission of dust, which occurs isotropically. A scattering process is in general occurring unevenly in all directions (also inducing linear polarization), and is azimuthal direction independent and symmetric with respect to the plane perpendicular to the incident radiation. Thus, the direction is always given by two angles, the (first) scattering angle θ and the "azimuthal angle ϕ" as the second scattering angle (Li, 2008; Brunngräber, 2018). The probability for a scattered photon to have a scattering angle in the range $[\theta, \theta + \mathrm{d}\theta]$ at wavelength λ is given by $\mathrm{S}_{11}(\theta)\,\mathrm{d}\theta$ from Eq. 2.20, while the probability for the azimuthal angle ϕ to be in

---

[10] The albedo $\Lambda = Q_\mathrm{sca}/Q_\mathrm{ext}$ is the fraction of scattering to total extinction, i.e., the ratio of the scattering cross-sections/efficiency to the sum of the scattering and absorption cross-sections/efficiencies.

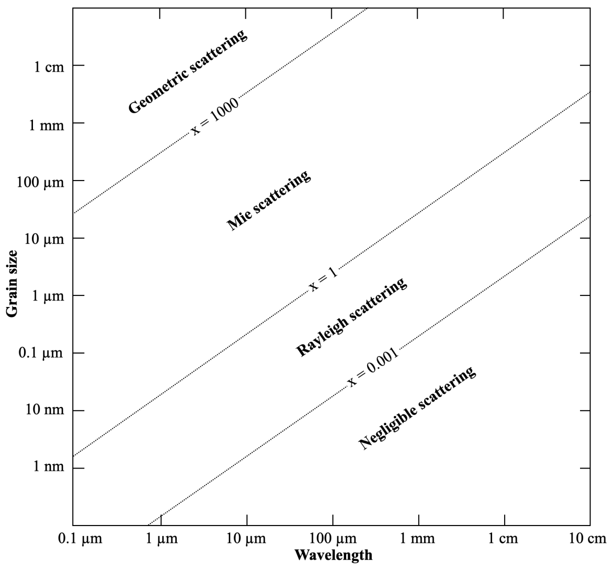

FIGURE 2.5: Three different scattering regimes, i.e., Rayleigh scattering (x ≪ 1), Mie scattering (x ≈ 1), and geometric scattering (x ≫ 1), depending on the particle size, wavelength, and refractive index. This plot considers only single scattering by spheres, which is a good approximation for debris disks. A more detailed description can be found in Sect. 2.2. Note that multiple scattering and scattering by non-spherical objects result in many complex values. Figure is based on Bohren and Huffman (1983) and Mölders and Kramm (2014).

the range $[\phi, \phi + \mathrm{d}\phi]$ is constant and given by $\frac{\mathrm{d}\phi}{2\pi}$. Consequently, the angle-dependent scattered radiation F_{sca} and linearly polarized scattered radiation $F_{\mathrm{pol-sca}}$ at a given wavelength λ in the direction between θ and $\theta + \mathrm{d}\theta$, and between ϕ and $\phi + \mathrm{d}\phi$ of a dust particle can be expressed as (Brunngräber, private communication):

$$F_{\mathrm{sca}}(\lambda)\,\mathrm{d}\theta\,\mathrm{d}\phi = L_*(\lambda)\,\pi\,Q_{\mathrm{sca}}(a)\,\frac{\pi a^2}{4\pi r^2}\,\frac{S_{11}(\lambda,\theta,\phi)\,\mathrm{d}\theta\,\mathrm{d}\phi}{d^2\,2\pi\int_0^{\pi} S_{11}\sin\theta\,\mathrm{d}\theta}\,, \tag{2.23}$$

and

$$F_{\mathrm{pol-sca}}(\lambda)\,\mathrm{d}\theta\,\mathrm{d}\phi = L_*(\lambda)\,\pi\,Q_{\mathrm{sca}}(a)\,\frac{\pi a^2}{4\pi r^2}\,\frac{S_{12}(\lambda,\theta,\phi)\,\mathrm{d}\theta\,\mathrm{d}\phi}{d^2\,2\pi\int_0^{\pi} S_{11}\sin\theta\,\mathrm{d}\theta}\,, \tag{2.24}$$

where $\sigma_{\mathrm{geo}} = \pi a^2$ indicating the integration over the dust particle's surface (i.e., a projected geometrical cross-section), r is the distance from the star to dust particles (thus $4\pi r^2$ in the numerator is strictly from geometrical considerations), d is the distance to the observer, and the additional π in the stellar emission comes from the integration over one hemisphere (radiant exitance definition from Lambertian reflectance law). The term with $2\pi\int_0^{\pi} S_{11}\sin\theta\,\mathrm{d}\theta$ ($=\frac{4\pi^2 C_{\mathrm{sca}}}{\lambda^2}$; Kruegel, 2003) in denominator indicates the integrated S_{11} over all direction for the normalization.

From Eq. 2.23 & 2.24, the degree of polarization can be computed:

$$p = \frac{F_{\mathrm{pol-sca}}(\lambda)\,\mathrm{d}\theta\,\mathrm{d}\phi}{F_{\mathrm{sca}}(\lambda)\,\mathrm{d}\theta\,\mathrm{d}\phi} = \left|\frac{S_{12}}{S_{11}}\right|. \tag{2.25}$$

More detailed information can be found in Brunngräber (2018) and Wolf and Hillenbrand (2003).

2.2.4 Absorption, thermal re-emission, and dust temperature

In addition to scattering, dust particles also absorb stellar radiation and re-emit radiation again. As mentioned previously, the effects of additional grain heating by dust re-emission can be neglected in debris disks. In the mid-IR, far-IR, and sub-millimeter/millimeter (mm), thermal re-emission is the dominant source of radiation along any line of sight (Coupeaud et al., 2010).

The total flux absorbed $F_{\rm abs}(\lambda)$ and re-emitted $F_{\rm re-rm}(\lambda)$ at given wavelength λ by a dust grain can be expressed as (Brunngräber, private communication):

$$F_{\rm abs}(\lambda) = L_*(\lambda)\, Q_{\rm abs}(a)\, \frac{\pi a^2}{4\pi r^2}\ , \tag{2.26}$$

and

$$F_{\rm re-em}(\lambda) = 4\pi^2 a^2\, Q_{\rm abs}(a)\, B_\lambda(T_{\rm dust})\ , \tag{2.27}$$

where $B_\lambda(T_{\rm dust})$ is the Planck function (Eq. 2.3) of the dust particles, on the assumption that a spherical grain absorbs starlight over a projected cross-section. Using the energy conservation law with both equations 2.26 and 2.27, one can derive an expression for the radial distance from the star, which is a function of the equilibrium temperature of dust particles $T_{\rm dust}$ (Backman and Paresce, 1993; Voshchinnikov and Semenov, 2000; Wolf and Hillenbrand, 2003). The resulting equation, which is based on the assumption of the star is radiating like a blackbody with temperature T_* and radius R_*, can be expressed as:

$$r(T_{\rm dust}) = \frac{R_*}{2}\sqrt{\frac{\int_0^\infty Q_{\rm abs}(a) B_\lambda(T_*) {\rm d}\lambda}{\int_0^\infty Q_{\rm abs}(a) B_\lambda(T_{\rm dust}) {\rm d}\lambda}}\ . \tag{2.28}$$

Consequently, the dust temperature is solely determined by stellar radiation, the distance to the star, and the optical properties (which are, in turn, a function of the chemical composition and the individual grain size). This means that the radiative transfer equation has a simple solution that allows one to derive the distance from the star at which the dust has a certain temperature and it shows, that small grains are hotter, and thus located farther from the star, while larger grains are colder, and thus located closer to the star.

More detailed information can be found in Brunngräber (2018) and Wolf and Hillenbrand (2003).

Chapter 3

Observations of debris disks

Observations of debris disks can give us basically two main pieces of information. The statistical information of debris disk observations provides correlations between various stellar and debris disk parameters, e.g., stellar age, spectral type, metallicity vs. disk mass, disk luminosity, disk size, dust temperature, detection rate around a main-sequence star, and even planet detection rate in the disk system. More importantly, debris disk observations provide information about individual architecture/properties of disk systems. The visibility and observables of debris disks mainly depend on dust properties and stellar properties as well as the disk structure. In this chapter, the general context of debris disk observations is introduced. Furthermore, observational constraints on dust properties and the general description of debris disks structures, showing structural diversity of disk systems are discussed. Additionally, the brief description of the current and (near) future observations of debris disks depending on the wavelength, i.e., from visual to mm, can be found in the Appendix A.

3.1 Observational methods of debris disks

Debris disk observations fall into two different categories: by the IR-excess in spectral energy distribution (i.e., spatially unresolved objects appear as a point of light to the observer) and spatially resolved image (i.e., the observer can determine the shape and size of a resolved object). Depending on the observing wavelength, both categories can be again divided into three regimes, i.e., the thermal re-emission, the scattered radiation, and the polarized scattered radiation.

3.1.1 Spectral energy distribution

By observing of disk systems at multiple wavelengths with continuous spectra, e.g., the shape of the continuum called a spectral energy distribution (SED), the IR-excess (see Fig. 1.3) expected from the star itself reveals the presence of the debris disk. The IR-excess is characterized by the disk's fractional luminosity $f_{\rm disk}$ at the wavelength of the peak of the dust emission. This can be defined with the ratio of infrared luminosity of the disk to that of the star as (Wyatt et al., 2007; Wyatt, 2008; Pawellek et al., 2014):

$$f_{\rm disk} = \frac{L_{\rm ir}}{L_*} = \left(\frac{F^{\rm disk}_{\nu,\,\rm max}}{F^*_{\nu,\,\rm max}}\right)\left(\frac{\lambda^*_{\rm max}}{\lambda^{\rm disk}_{\rm max}}\right) , \tag{3.1}$$

where $F^{\rm disk}_{\nu,\,\rm max}$ and $F^*_{\nu,\,\rm max}$ are the peak fluxes of the disk and star, respectively, and $\lambda^{\rm disk}_{\rm max}$ and $\lambda^*_{\rm max}$ are the wavelengths at the flux peak from the dust emission and stellar emission, respectively. The fractional luminosities of debris disks $f_{\rm disk}$ are smaller than $\sim$ a few times 10^{-3} (e.g., Bryden et al., 2009; Hughes, Duchêne, and Matthews, 2018). This is contrary to the optically thick protoplanetary disks around young Herbig Ae/Be and T Tauri stars, which are dominated by gas dynamics and have higher fractional luminosities. For example, even the brightest debris disks have fractional luminosity that are two orders of magnitudes lower than those of protoplanetary disks (Greaves,

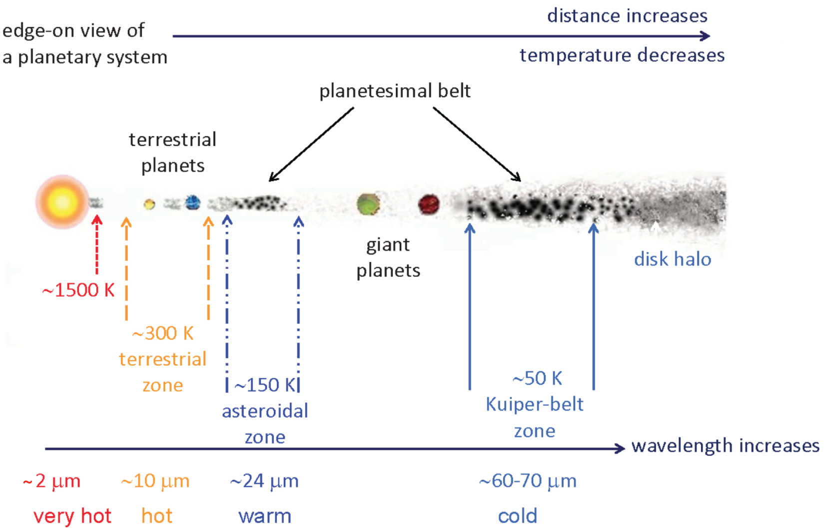

FIGURE 3.1: The five characteristic zones of the dust emission observed in debris disks and the corresponding typical temperatures observed at those locations. Note that not all zones are detected in every disk. Figure credit: Su et al. (2014).

Wyatt, and Bryden, 2009; Lagrange and Chauvin, 2012). Besides, several useful information such as the dust temperature $T_{\rm dust}$ and radial distance of the location of the dust emission to the star, can be inferred with the shape of the IR-excess in the SED on the assumption that the stellar photosphere and dust behave like a blackbody (i.e., dust particles reach an equilibrium temperature at which the energy they absorb from stellar flux equals the energy they radiate). The dust temperature $T_{\rm dust}$ can be derived with Wien's displacement law (Wien, 1897; Wyatt, 2008; Pawellek and Krivov, 2015; Torres, 2017):

$$T_{\rm dust}\,[\mathrm{K}] = \frac{5100\,\mu\mathrm{m}}{\lambda_{\rm max}^{\rm disk}}\ , \tag{3.2}$$

The estimation via this method tells us that the dust temperature in debris disks is ranging from ∼ a few tens up to a few hundreds K. If a disk is comprised of multiple components at a range of distances from the star, then observations at different wavelengths can probe the different components at different distances. Based on Eq. 3.2, the radial distance from the star r in au can be derived (Wyatt, 2008; Su et al., 2014):

$$r\,[\mathrm{au}] = \left(\frac{278\,\mathrm{K}}{T_{\rm dust}}\right)^2 \left(\frac{L_*}{\mathrm{L}_\odot}\right)^{0.5}\ . \tag{3.3}$$

Fig. 3.1 shows the five characteristic zones of the dust emission observed in debris disks and the corresponding observing wavelengths. For example, materials close to the inner region of the disk can be traced by shorter wavelengths, while larger dust grains in the outer region of the disk, where the detected thermal re-emission dominates, can be probed by longer wavelengths (Su et al., 2014). Furthermore, the size of debris disks can be inferred from SEDs. For example, smaller debris disks are warmer, while larger debris disks are colder in the case of unresolved debris disks (Booth et al., 2013). Additionally, the Rayleigh-Jeans's tail of the SED, i.e., the slope of the SED (called the spectral index), can provide a wealth of information on the emitting grain size distribution and their radial distribution in the disk. It is directly related to the grain size distribution of large grains in the disk. More detailed information can be found in Sect. 3.2.1.

More importantly, the SED provides mineralogical information through emission and/or absorption lines. For example, the Spitzer/IRS instrument observed in the mid-IR show spectral features, which may be indicating Fe-rich sulfide, (possibly) water ice, and other compounds (e.g. Chen, 2006). Consequently, the SED has been not only the primary way to characterize the fractional excess luminosity of the disk over the stellar photosphere, but it has also been used to infer the dust properties of debris disks.

However, there have only been significant studies on the grains' thermal emission that are based on the SED. This is because the star overwhelms the light scattered by the dust in debris disks at visual and near-IR wavelengths, where scattering dominates. Thus, it is challenging to get meaningful data for scattered-light at short wavelengths in SED observations.

Furthermore, for small grains cooling is difficult and thus they attain a warmer temperature than perfect blackbodies, which arises from the fact that the radiation of wavelengths much larger than their own size is inefficient. Larger grains, though, with a radius comparable to or larger than the observing wavelength behave like blackbodies, which results in correspondence between their temperature and their obtained radial distance to the star. Thus, Eq. 3.1 & 3.3 are a rather rough approximation and dust grains would be inferred to be closer to the star than they actually are.

Additionally, debris disk SED observation (and/or SED modeling) is hampered by a fundamental degeneracy between the disk geometry, e.g., the disks' inner/outer radius, and grain properties like their sizes (Wolf and Hillenbrand, 2003; Chen et al., 2005; Moro-Martín et al., 2005). For example, smaller dust grain sizes and a higher dust mass in debris disks can mislead to inner-filled and larger debris disks, respectively. One way to circumvent the problem of the blackbody assumption and break the fundamental degeneracy is to invoke information from spatially resolved images, as they show directly where most of the emitting dust is actually located. The comparison between the observed disk radius and expected temperature based on the SED contains information about how overheated the smallest and populous dust grains with thermal emission in the disk are (Booth et al., 2013; Hughes, Duchêne, and Matthews, 2018). Consequently, even though the SED is a powerful diagnostic, the shortcomings of this method emphasize the importance of multi-wavelength broadband resolved photometry.

3.1.2 Spatially resolved image of debris disks

The spatially resolved observations of debris disks (i.e., the angular resolution of a telescope is small compared to the disk's angular extent in the sky[1]) can circumvent the aforementioned problem of the SED (Sect. 3.1.1), and thus break some of the degeneracies by providing geometrical constraints, e.g., by measuring the disk size directly.

The dust particle, which emits the most efficient, has a size that is comparable to the observing wavelength (A more detailed description can be found in Sect. 3.2.1). This results in resolved images of the same disk at different wavelengths that will look differently (Müller, Löhne, and Krivov, 2010). For example, debris disk observations at longer wavelengths trace larger grains, because they are cooler. Thus, parent planetesimal belts and resonances with fewer effects from stellar radiation can be traced easier at longer wavelength observations (e.g., the thermal emission at mid-IR/far-IR to sub-mm/mm). However, the radius of debris disks $r\,[\mathrm{au}]$ can be resolved up to a distance of $\sim 10\, r\, D/\lambda$ in pc, which is defined through the diffraction limit full width half maximum (FWHM). Thus, nearby disks with large telescopes are required for higher resolution observations at longer wavelengths. For example, James Clerk Maxwell Telescope (JCMT; Holland et al., 2017) and Herschel Space Observatory (HSO; Eiroa and Dunes Consortium, 2013) can resolve Kuiper belt-sized disks out to only 18 pc and 10 pc, respectively, meaning that only a small number of the nearest disks were imaged in any detail. For this reason, only a few tens of debris disks had

---

[1] An object can only be resolved if its angular size (i.e., how large it appears in the sky) is larger than the angular resolution limit of the telescope Θ, which is defined as:

$$\Theta\,[\mathrm{rad}] \approx 1.22 \times \frac{\lambda}{D}\,, \tag{3.4}$$

where D is the diameter of the telescope and 1.22 is derived from a calculation of the position of the first dark circular ring surrounding the central Airy disk of the diffraction pattern.

been resolved before two decades ago. However, the combination of far-IR surveys (e.g., Spitzer MIPS, AKARI, and Herschel PACS; Su et al., 2004; Eiroa and Dunes Consortium, 2013; Liu, Wang, and Jiang, 2014; Matthews et al., 2014) and the advent of interferometry in the sub-mm/mm (e.g. SMA and ALMA; Hughes et al., 2011; ALMA Partnership et al., 2015; Booth et al., 2017; Booth et al., 2019) made such observations now possible. Thus, the number of resolved systems has increased rapidly in the past few years and allowed to trace larger particles in the system and to determine the temperature of the dust due to their thermal emission. To date, many 100s of debris disks have been resolved at various wavelengths from the optical to the (sub-)mm observations (Pawellek et al., 2014).

On the other hand, smaller grains are probed at shorter wavelengths, because they are warmer. Since small grains are easily affected by stellar radiation (see Sect. 2.1.2), the same disk appears featureless and much more extended at shorter wavelengths compared to that of longer wavelength observation (Krivov et al., 2008; Müller, Löhne, and Krivov, 2010). Furthermore, higher resolution images can be achieved at short wavelength observation (e.g., the scattered light at optical/near-IR). They highlight and probe regions where small grains dominate down to a few au. Small grains are subject to radial migration induced by radiation forces (and/or PR drag; Burns, Lamy, and Soter, 1979). Thus, short-wavelength observations are not only very efficient in revealing the vertical structure (e.g., if the disk is seen as edge-on; Graham, Kalas, and Matthews, 2007) and radial density profile/distribution of debris disks, but also the central holes (e.g., if the disk is seen as face-on; Kalas, Graham, and Clampin, 2005) and structures induced by planet-like objects. The scattering of dust has dependencies on the grain size, shape, and composition (see Sect. 2.2.3). Thus, this can also give us information about the grains themselves. For example, the dust composition can be inferred by the change of grain albedo with wavelength. However, the light scattered by the dust in debris disks at these wavelengths is overwhelmed by the light of the central star (Sect. 3.1.1). To overcome this challenge, a coronagraphic observation to occult the stellar light is strongly desired (Graham, Kalas, and Matthews, 2007), thereby as it increases the sensitivity of debris disk observations, which is required to perform high contrast imaging. Furthermore, the reduction of the inner working angle for achieving a better contrast is important, since occulting spot partly hides the inner part of debris disks. Even though the coronagraph suppresses much of the starlight, nonetheless, a fraction of the stellar light leaks through the disk system. Therefore, it must be subtracted from the data by post-processing techniques, in particular, an accurate on-axis point spread function (PSF; the response of an imaging system to a point source) subtraction is mandatory.

3.2 Observational constraints on dust properties

More precisely, debris disks observables mainly rely on a vast number of dust and disk parameters and assumptions. Even though most of them are poorly known, the properties of the observable dust, e.g., temperature (and location), chemical composition, physical shape including the size, and dust mass (and their number density), should be studied, because the debris disk observations are sensitive to the cross-sectional area of the dust. In this section, observational constraints on various dust parameters, e.g., dust grain size distributions, dust composition, and dust mass are presented.

3.2.1 Observational constraints on the dust grain size distribution

· **Characteristic grain size**: To describe the infrared excess emission properly, Backman and Paresce (1993) proposed the modified blackbody for thermal emission by dust grains with a two-parameter (i.e., λ and β), where λ is the wavelength and β is the dust opacity index, on the assumption of a constant absorption efficiency Q_{abs} (a, λ) = 1 up to a critical wavelength λ_0. For wavelengths larger than λ_0, the absorption efficiency decreases with $(\lambda/\lambda_0)^{-\beta_{\text{mod}}}$, where $\beta_{\rm mod}$ is the modified opacity index, due to small particles being inefficient emitters. The absorption efficiency is described as:

$$Q_{\rm abs}(a, \lambda) = \begin{cases} 1 & \lambda \leq \lambda_0 \\ (\lambda/\lambda_0)^{-\beta_{\rm mod}} & \lambda > \lambda_0. \end{cases} \tag{3.5}$$

The characteristic wavelength λ_0 can be linked to the characteristic grain size and is a strong function of the grain optical properties (Backman and Paresce, 1993), i.e., $\lambda_0 = 2\pi a$ for strongly absorbing materials, $\lambda_0 = a$ for moderately absorbing materials, and $\lambda_0 = a/2\pi$ for weakly absorbing materials. Consequently, dust grains only emit efficiently at wavelengths shorter than their physical size with a steep decline in emission efficiency at longer wavelengths. Another piece of information on dust particle can be inferred from the parameter $\beta_{\rm mod}$. For example, previous studies (e.g., Witt, 1989; Planck Collaboration et al., 2015) indicated that typically the value of $\beta_{\rm mod}$ is typically higher for crystalline materials (~ 2) compared to amorphous materials (~ 1). Furthermore, the ISM dust has a value of $\beta_{\rm mod} \approx 1.5$-$2.0$ (Boulanger et al., 1996; Planck Collaboration et al., 2015). Due to the presence of larger grains, the value of $\beta_{\rm mod}$ in debris disks are expected to be rather lower (Draine, 2006).

· **Grain size distribution**: Draine (2006) indicated that the value of γ in the dust grain size distribution (Eq. 2.11) is related to the value of $\beta_{\rm mod}$ via the equation:

$$\beta_{\rm mod} = (\gamma - 3)\beta_{\rm s} \ , \tag{3.6}$$

where $\beta_{\rm s}$ is a long wavelength emissivity of small particles (i.e., much smaller than the observing wavelength) in the Rayleigh-Jeans limit. For example, most astronomical dust compositions have similar values of $\beta_{\rm s} \approx 1.6$-$2$ (Draine, 2006) and recent long-wavelength observations show (e.g., Sibthorpe et al., 2018) that typical values for $\beta_{\rm mod}$ are ≈ 1. This implies a grain size distribution power-law index of about $\gamma \approx 3.5$. In addition, γ can be calculated from the observed sub-mm/mm spectral index $\alpha_{\rm mm} = \left|\frac{\log(F_{\nu_1}/F_{\nu_2})}{\log(\nu_1/\nu_2)}\right|$ using the equation (MacGregor et al., 2017):

$$\gamma = \frac{\alpha_{\rm mm} - \alpha_{\rm Planck}}{\beta_{\rm s}} + 3 \ , \tag{3.7}$$

where $\alpha_{\rm Planck}$ is the spectral index of the Planck function, given the inferred temperature of the disk in the Rayleigh-Jeans limit $\alpha_{\rm Planck} \approx 2$ (Ricci et al., 2015a). Consequently, by measuring the millimeter spectral index $\alpha_{\rm mm}$ and inferring $\alpha_{\rm planck}$, it is possible to know the slope of the grain size distribution γ, i.e., the $\beta_{\rm mod}$ is directly linked to γ value of the grain size distribution, and thus also to the spectral index $\alpha_{\rm mm}$.

The grain size distribution (including the estimate for γ) can also be deduced and analyzed from the broadband/narrowband disk spectrum. For example, Mittal et al. (2015) analyzed the mid-infrared silicate emission to estimate the value of γ of the grain size distribution assuming that µm-sized grains show weaker and broader spectral features compared to smaller grains. They indicated that the inferred values of γ obtained via spectral analyses of the mid-infrared silicate feature lie in the range of ~ 3.2-4.2.

Overall, previous studies imply that the simple analytical solution with steady-state collisional models by Dohnanyi (1969) is in good agreement with current observations, even though this is the simplest model possible. Consequently, observations of debris disk evolution can be reasonably explained with collisional timescales that are shorter than the system age over which the cascade has been evolving (Wyatt, 2008; Wyatt, Clarke, and Booth, 2011; see also Sect. 2.1.5).

Besides, the different spectral decomposition gives us a piece of information about the relative number of different grain sizes, and thus, provides a constraint on γ in the small grain limit using a simple method (e.g., Eq. 3.5;

a single characteristic grain size depending on the grain structure; Backman and Paresce, 1993). For example, dust grains with radii on the order of hundreds of µm are indicated by sub-mm/mm fluxes (Zuckerman and Becklin, 1993). However, this method is restricted only to larger dust grains. This is because the smallest detectable dust grains dominate the thermal emission at any given wavelength. On the other hand, only the µm-sized grains can contribute to scattered light observations, i.e., grains much smaller than the observing wavelength are expected to scatter rather isotropically compared to larger grains, which are strongly preferred to show forward scattering. Thus, given the steep slope of the size distribution, the angular distribution of light intensity scattered by dust particles at a given wavelength (i.e., called the scattering phase function) provides a meaningful constraint on the minimum dust grain size as well as the slope of the grain size distribution in the small grain regime (Hughes, Duchêne, and Matthews, 2018).

Another method to estimate dust grain sizes is the spatial/wavelength-dependent scattered polarized radiation. Voshchinnikov and Krügel (1999) modeled the polarimetric image of the β Pictoris debris disks system in the optical wavelength regime and assumed a general power-law grain size distribution, whereas Krivova, Krivov, and Mann (2000) assumed a cutoff to the power-law below a few µm, and were able to obtain a more detailed fit to the optical polarimetric observations of the β Pictoris debris disks system. This can be explained by the shorter lifetime of small particles by the radiation pressure (see Sect. 2.1.2).

Note that the nongravitational forces acting on grains particularly in the range of tens to hundreds of micrometers in diameter (Krivov, Löhne, and Sremčević, 2006; Thébault and Augereau, 2007; Löhne et al., 2017). This may results in further modifing the grain size distribution. A more detailed investigation of constraining the grain size distribution of debris disks can be found in Chapter 5 and Chapter 8.

3.2.2 Observational constraints on the dust composition

Since debris disks are a by-product of star formation, one can assume that they have the same chemical composition as the ISM dust. For example, astronomical silicate is a composite material that reproduces the features seen in the interstellar medium (hereafter "astrosil"; Draine and Lee, 1984; Draine, 2003). Recent observations (e.g., Spitzer) showed many robust conclusions about the dust components in debris disks, which are dominated by "standard" silicates with a broad range of crystallinity fractions ~ 1-95% (e.g., Mittal et al., 2015; Olofsson et al., 2012). This is inconsistent with that of the ISM materials, which reaches only ~ a few percents (Li, Zhao, and Li, 2007). Furthermore, observations indicated non-negligible amounts of refractories (and ices) with an aggregate-type structure with significant degrees of porosity (Hughes, Duchêne, and Matthews, 2018), which is similar to one in the solar system. Additionally, previous debris disk modeling included dust mixtures with organic carbon materials, water ice, and even vacuum (and thus porosity), which resulted in a better fit to observations compared to ones with compact astrosil only (e.g. Graham, Kalas, and Matthews, 2007; Lebreton et al., 2012; Rodigas et al., 2015; Olofsson et al., 2016; Ballering et al., 2016). All these findings indicate a clear trend: the intrinsic diversity of dust properties in debris disks might come from dust evolution in debris disks. Thus, the assumption of the same chemical composition as the ISM does not hold.

Since dust significantly emits in the near-IR/mid-IR to far-IR, where the prominent emission features of crystalline and amorphous silicates, water ice, amorphous carbon, metal sulfides, silica, SiO and organic materials are, one must investigate the composition of the dust through spectroscopic observations in these wavelength regimes (Sect. 3.1.1).

In scattered light, dust composition primarily influences the surface brightness of debris disks. However, it is nearly impossible to distinguish and establish a difference between low-albedo (e.g., carbon-rich dust) and high-albedo (e.g., silicate or ice-rich dust). This is because the albedo is degenerate with the total dust mass in optically thin disks. Consequently, the interpretation of these analyses is subject to several caveats due to the degeneracy of nearly featureless spectra, indicating the difficulty to constrain dust properties; there will be no unique solution. Depending on the dust composition, additional information such as the dominating grain size (see Sect. 3.2.1) can be gained from scattered light and polarimetric observation (Graham, Kalas, and Matthews, 2007; Hinkley et al., 2009; Maness et al., 2009).

In thermal emission, the dust composition is probed by the presence and shape of solid-state spectral features in the spectrum, which gives mineralogical information (Dutrey et al., 2014; Pontoppidan and Blevins, 2014). For example, the 10 µm silicate feature enables one of the most promising diagnostics for the dust composition and size, whose presence requires grains with an approximate radius of $\approx$ 1.5 µm (i.e., characteristic grain size $\lambda/2\pi$; Backman and Paresce, 1993; see Sect. 3.2.1). However, due to the strong dependency between the blow-out dust grain size and the stellar luminosity, less luminous later-type stars generally have these silicate features with excess at 10 µm, while only a few A stars with 10 µm excess exhibit silicate features (Aumann and Probst, 1991; Chen, 2006). Other silicate features, that are observed at far-IR, are only excited for grains larger than $\sim$ 10 µm and heated to a minimum of 150-200 K. Thus, this mineralogy study of the silicate feature is rather limited to small grains in the warm/hot components, emitting in the mid-IR, in debris disks. Also, the different physical status of silicates (e.g., amorphous and crystalline silicates) can be identified, with the latter typically displaying shaper features. Besides the silicate features, the 69 µm forsterite feature can be present at lower temperatures (de Vries et al., 2012). Furthermore, many non-silicate dust particles have spectral features in the mid-infrared that can be used to infer their presence in debris disks (Olofsson et al., 2012).

A more detailed investigation of the feasibility of detecting various dust components (e.g., ice-dust aggregates) in debris disks can be found in Chapter 6.

3.2.3 Observational constraints on the dust mass

At sub-mm wavelengths, where $h\nu \ll kT$, the Planck function B_λ can be approximated by $2kT/\lambda^2$ (Bulger et al., 2013; i.e., the intensity is only linearly proportional to the dust temperature in the Rayleigh-Jeans limit; Eq. 2.3). Thus, the inferred grain mass is not sensitively dependent on the grain temperature compared to the short wavelength regimes and is only showing a weak dependence for the dust particles with radii smaller than the observing wavelength (Hildebrand, 1983). Consequently, the dust mass is approximately proportional to the sub-mm dust re-emission flux in the optically thin case. Thus, it is reasonable to use sub-mm observation to derive the dust mass in a debris disk system, providing relevant constraints on dust opacity and determination of the dust mass for sizes of up to $\sim$ 1 mm. For example, Roccatagliata et al. (2009) derived the dust mass M_{dust} from the observed 850 µm fluxes obtained by using the SCUBA-2 instrument with the following equation (e.g., Zuckerman and Becklin, 1993; Zuckerman, 2001; Wyatt, 2008):

$$M_{\text{dust}} = \frac{F_\nu d^2}{\kappa_\nu B_\nu(T_{\text{dust}})} , \tag{3.8}$$

where $\kappa_\nu = \kappa_0 \left(\frac{\nu}{\nu_0}\right)^\beta$ is the mass absorption coefficient with β, indicating the frequency dependence of κ_ν, and F_ν is the observed flux at the frequency ν. Furthermore, previous studies (e.g.,Zuckerman and Becklin, 1993; Pollack et al., 1994; Dent et al., 2000) indicated that the normalized value of κ_0 is 0.17 m^2 kg^{-1} at 850 µm and scale with $\beta = 1$, which is adopted for direct comparison with previous studies (e.g., Sylvester, Dunkin, and Barlow, 2001; Wyatt, 2003; Najita and Williams, 2005).

If the disk is a ring-like structure, i.e., without a huge deviation in the temperature calculation of dust grains from the blackbody assumption, the dust re-emission in the disk is reproduced by varying the location of the ring, as well as the total disk mass, quantities that are related in the optically thin case. Thus, the mass of the ring can be calculated and the range of possible radial locations can be constrained based on an infrared excess detection and its upper limits. A more detailed investigation of constraining the dust mass in the ring-like structure of debris disks can be found in Chapter 7.

3.3 Observational structures of debris disks

Recent observations show debris disks with great diversity, such as a wide range of disk sizes (e.g., the radii of debris disks scale from a few tens up to a few thousand au) and various shapes of disks (e.g, the radial, the azimuthal structure, and the vertical structure). This diversity mainly comes from the different combinations of disk components (e.g., dust, planetesimal belts in which planets continue to grow or are being ground down to dust, and planets ranging from Earth-size to Jupiter-size, and even gas), located at different radial distances (e.g., Fig. 3.1; however some radial locations could be almost empty). This finally results in the different structures of debris disks based on the specific disk evolution, which results from the balance between radiation pressure force, gravity, PR drag, and collisions. For example, a planet can easily affect a disk system. It scatters onto a highly eccentric orbit that repeatedly approaches a narrow ring, and thus ignites collisional cascades in the disk structure (Beust et al., 2014; Pearce, Wyatt, and Kennedy, 2014; see also Sect. 2.1.5) and/or broadens narrow rings.

The main questions in this section are whether these fundamentally different shapes of disks of underlying planetesimal populations/different stages of the debris disk evolution can be traced. In addition to that, two more interesting objects are discussed: (i) exozodiacal dust due to its rarity and proximity to the star and (ii) gas in debris disks due to the uncertain origin.

3.3.1 Structural diversity in debris disks

In this section, the morphological diversity of debris disks depending on the geometry and observing angle, in particular: (a) the radial structure, (b) azimuthal structure, and (c) vertical structure of disk systems are presented (see Fig. 3.2).

a. Radial structure

Narrow or broad ring/Multiple rings with the gap: Besla and Wu (2007) argue that the detection of the narrow dust rings may indicate the presence of leftover gas, i.e., not the secondary gas. This implies that the dust is produced at the location of the parent planetesimals, which are confined to narrow and thin ring-like structures[2] (Telesco et al., 2000; Schneider et al., 2009). Then dust decays by collisional erosion and moves from its birthplace through processes such as radiation pressure and PR drag, and thus the ring may broaden. Narrow rings or broad rings are quite commonly found in debris disks, e.g., Fomalhaut (Kalas, Graham, and Clampin, 2005), HD181327 (Schneider et al., 2006), and HR4796 (Schneider et al., 2009; Rodigas et al., 2015). Furthermore, recent high-contrast imaging techniques can spatially resolve a substructure (e.g., two-belt structure), in the radial dust distribution such as multiple rings with one or more gaps, e.g., HD 07146 (Ricci et al., 2015a), HD 107146 (Marino et al., 2018), HD 131835 (Feldt et al., 2017), and HD 120326 (Bonnefoy et al., 2017). Broad as well as shallow gaps can be explained by the planet-sculpting scenarios since debris disks may be very sensitive to even very low-mass planets and thus

---

[2] What makes a ring narrow and/or broad disk is still a very exciting open question. Wyatt (2005) indicated the evolution from transition disks to debris disks involves a few steps. First, they carve a hole and gap in the protoplanetary disks and remove mm-sized dust, thus decreasing the flux in the sub-mm region (e.g., HD 100546). And they start to clear the dust from the inner regions (e.g., HD 141569). Next, they remove CO, and finally, they concentrate planetesimals into a ring.

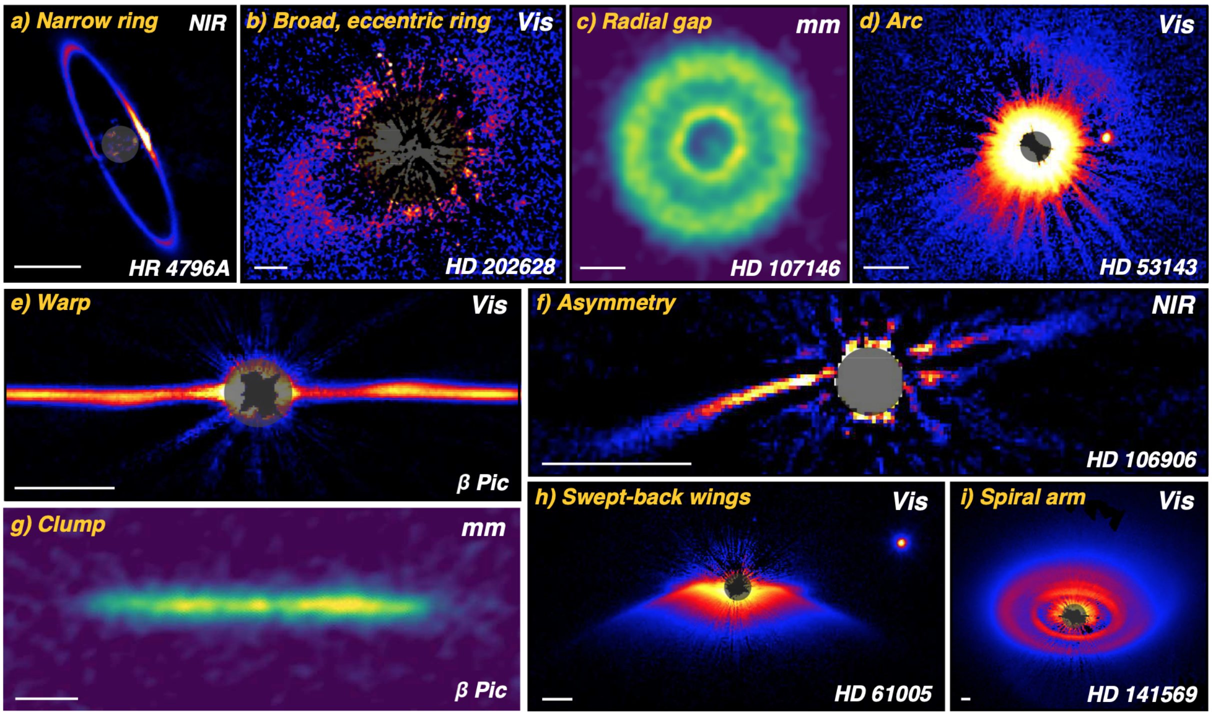

FIGURE 3.2: The structural diversity of debris disks is shown with the white scale bars, representing 50 au. Figure credit: Hughes, Duchêne, and Matthews (2018) and references therein.

easily open a gap (Ricci et al., 2015a).

Halos: In scattered light images of debris disks around Vega, an extended large outer radius (called "halo") shows (Su, 2005; Su et al., 2006). This feature is easily understood as a result of the smallest grains (i.e., the blow-out grains) being blown away by stellar radiation pressure (and/or a stellar wind) from their parent planetesimal belt. The halo phenomenon is not particularly limited to luminous stars, as the debris disk around M stars such as AU Mic can also show an extended scattered light halo (Kalas, Graham, and Clampin, 2005). Such a configuration has also been showing in previous modelings (e.g., Strubbe and Chiang, 2006; Löhne et al., 2017), which emphasizes the importance of collisions and radiation pressure for small dust grains. Furthermore, these modelings found that PR drag may be populated by grains, which spiral inwards. On the other hand, an mm wavelength observation, which traces the larger grains, shows that this extended emission is not well pronounced (e.g., Löhne et al., 2017).

Spiral arms and arcs: Debris disks around HD 141569 and HD 53143 show other unusual complex morphologies such as a spiral pattern and arcs at larger stellocentric distances (Konishi et al., 2016; Schneider et al., 2014). These might be caused by transitional objects that were influencing the system between the protoplanetary and debris disk phases (de Boer et al., 2016; Monnier et al., 2019).

b. Azimuthal structure

Eccentricity: Recent spatially resolved debris disk observations show the azimuthal asymmetries in the surface brightness (e.g., Kalas, Graham, and Clampin, 2005; Stark et al., 2014; Olofsson et al., 2016; Pan, Nesvold, and Kuchner, 2016; MacGregor et al., 2017), which are the result of narrow eccentric belts with some offset between the belt center and the star. Secular perturbations by as yet undiscovered planets probably cause these offsets (Wyatt

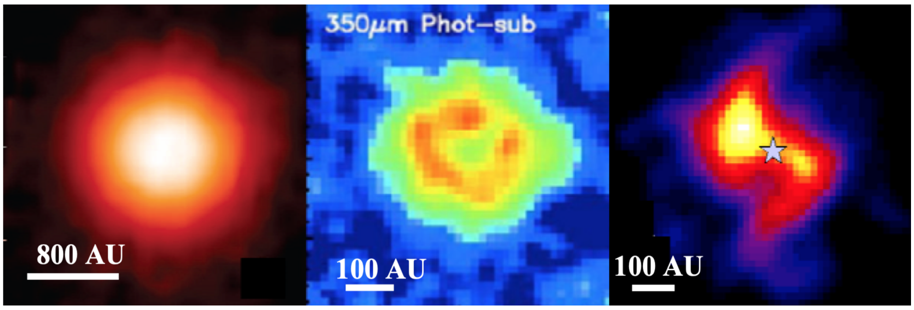

FIGURE 3.3: *Left*: Vega debris disks at 70 μm with Spitzer (Su, 2005), *middle*: Vega debris disks at 350 μm with CSO (Marsh et al., 2006), and *right*: Vega debris disks at 850 μm with JCMT (Holland et al., 1998). Figure credit: Holland et al. (2010).

et al., 1999; Wyatt, 2005; Faramaz et al., 2019; see also Sect. 2.1.10). Thus, the interpretation of these observations may allow one to constrain the parameters of the alleged planets. However, other mechanisms are proposed, e.g., the interaction between the disk's dust particle and gas of the ISM in different configurations (Maness et al., 2009). In scattered light observations, debris disks exhibit a brightness enhancement at the periastron, close to the star with higher temperature, which therefore glows brighter ("pericenter glow"; Wyatt et al., 1999). In thermal emission observations, their flux is becoming insensitive to their temperatures, but the number density gets more important (Sect. 3.2.3). Dust grains on eccentric orbits at the apocenter, however, lead to the opposite phenomenon ("apocenter glow"; Pan, Nesvold, and Kuchner, 2016). A more detailed discussion about azimuthal asymmetries of the surface brightness in eccentric debris disks can be found in Chapter 5.

Clumps: Planets/planetary objects imprint clumpy structures on the disk system. Two possible mechanisms explaining the presence of clumps have been proposed: either dust grains can be trapped into resonances by the PR drag (Sect. 2.1.3 & 2.1.10; Kuchner and Holman, 2003) or resonant planetesimals and grains can be swept along during planet migration (Wyatt, 2003; Reche et al., 2008). In any case, clumps due to mean-motion resonances must be enhanced to be observable. In this manner, a far-IR to sub-mm/mm wavelengths observation (e.g., Holland et al., 2010) is strongly required to trace the perturbation of unseen objects (e.g., distant planets), while observations at a short-wavelength trace emission of small dust grains, that are dynamically scattered by stellar radiation, and thus these observations smooth over and erase clumpy structures (Wyatt et al., 1999; Marsh et al., 2006; Holland et al., 2017). In particular, the comparison between multi-wavelength observations provides a very powerful way of determining the physical characteristics of the perturbing planet. For example, Fig. 3.3 shows that the clumpy structure can be seen at the sub-mm observation, while the far-IR observation traces a more smooth structure, which depends on the mass of the solids, e.g., planet(s)/planetesimal(s) (Su, 2005; Marsh et al., 2006; Holland et al., 1998). Also, ϵ Eridani is surrounded by a narrow ring of dust that contains some bright spots (e.g., Lestrade and Thilliez, 2015; Booth et al., 2017), which is suggestive of interactions with a Neptune-like planet that is shaping the inner and outer edges of the ring.

Swept-back wings: The "swept-back wings" features are often found at scattered light observations of debris disks, e.g., HD 61005 (Esposito et al., 2016), HD 32297 (Debes, Weinberger, and Kuchner, 2009), and HD 30447 (Soummer et al., 2014). This morphology has so far been interpreted as interactions with the ISM (Maness et al., 2009) or torque-based method for invoking the asymmetry (Esposito et al., 2016). A simulational study (e.g., Lee and Chiang, 2016) indicated that morphological features such as a wing-like feature (e.g., HD 61005; (Esposito et al., 2016) might be invoked by a planet.

c. Vertical structure

Warps: The presence of warps in debris disks (i.e., a warped inner disk) was clearly shown in the β Pictoris debris disk system in the scattered light images (Golimowski et al., 2006). This specific disk feature can be explained well as a planet indicator (Lagrange et al., 2010). However, Lee and Chiang (2016) indicated that a single planet may not be enough to produce sustained observable warps, suggesting that multiple planets and/or even different mechanisms may be necessary to explain warped inner disks.

Recent observations of debris disks (e.g., AU Mic and β Pictoris; Golimowski et al., 2006; Fitzgerald et al., 2007; Graham, Kalas, and Matthews, 2007; Thébault, 2009) show that the vertical extent of the debris disk is narrow and relatively flat (i.e., a projected FWHM perpendicular to the disk major axis that is almost constant; a few au to a few tens of AU) or decreases inside a parent belt, which is located at a small radial distance to the star. However, due to the degeneracy between the radial and vertical structure at intermediate inclinations, the measurement of the vertical structure of debris disks is obviously inclination-dependent as well as observing angle-dependent. Thus, an unambiguous investigation is limited to the regime of an edge-on view of a disk system.

3.3.2 Exozodiacal dust

Numerous studies (e.g., Ballering et al., 2013; Pawellek et al., 2014) in the last few years suggest that the majority of debris disks contains two populations of dust with distinct temperatures, (i) the cold component at tens of K and (ii) the warm/hot dust with hundreds to thousands of K (see Fig. 3.4 & 3.1; Kirchschlager et al., 2018; Su et al., 2014). Some debris disk systems substantially exhibit their dust thermal emission with warm dust in the mid-IR and the combination of thermal emission and scattered light with hot dust in the near-IR, respectively, called exozodiacal dust (hereafter as "exozodi"). However, these objects may not follow the standard collisional scenario (Sect. 2.1.5; Payne et al., 2009; Wyatt et al., 2010; Absil et al., 2010; Marion et al., 2014; Nuñez et al., 2017; Ertel et al., 2020). In analogy to our zodiacal dust in the solar system, exozodi is located in (or near) the habitable zone (HZ) of the debris disk system, down to the sublimation line of dust. The presence of exozodi could hamper detections of Earth-like planets in the HZ, thus its structures might point towards dynamical interactions with planets (Stark and Kuchner, 2008). Therefore, the understanding of the origin of exozodi is crucial for the understanding of the evolution of planetary systems and Earth-like planets close to the HZ. It can finally have vast potential as a source of information on planetary systems, complementary to the direct studies on exoplanets and their host stars.

To date, the measurement in SED (Fig. 3.4) is one of the main methods to detect exozodi because of the current space-based telescopes cannot spatially resolve the exozodi from the central star. However, this warm dust with its specific mid-IR emission has been detected by space-based observatories (e.g., Lisse et al., 2008; Lawler et al., 2009) only with an extremely low occurrence rate. Besides, the zodiacal dust in our solar system is too faint to be detected (e.g., by Spitzer) due to the photometric calibration uncertainty ($\sim$ a few percents of the total flux of the system). Thus, making detection is quite challenging. Furthermore, the Wide-Field Infrared Survey Explorer (WISE) detected debris disk systems photometrically in the mid-IR with excesses of only the brightest warm exozodi dust level, while hot exozodis are harder to detect due to the brighter photosphere in the near-IR (Patel, Metchev, and Heinze, 2014). Instead, making the coronagraphic observation is also quite limited, since the larger inner working angle compared to an angular distance of the exozodi to the star is too large and thus would block the region where the warm and hot exozodi are.

To perform an exozodi observation, it is important to separate the stellar emission from the dust emission, i.e., high angular resolution is required. One possible remaining solution is, therefore, the near- or mid-IR interferometry (e.g., CHARA/FLUOR and VLTI/PIONIER; Ertel et al., 2020), measuring the visibility and using a suitable set of

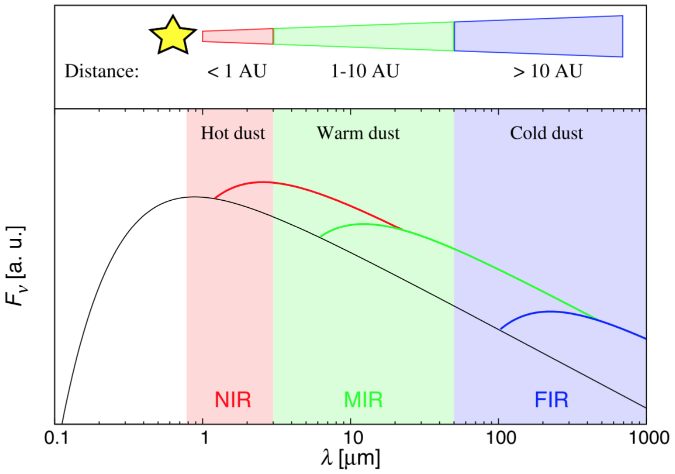

FIGURE 3.4: An illustration of the individual contributions from hot, warm, and cold dust to different parts of the spectral energy distribution of debris disks around a solar-type star, which is represented by a black solid line. Figure credit: Kirchschlager et al. (2018).

baseline configurations. The presence of spatially resolved dust material and beyond its sublimation distance can be inferred from a significant deficit of the interferometric visibility at low spatial frequencies, which enables a direct determination of the flux ratio between the exozodi and the central star (Di Folco et al., 2004). Consequently, a near- or mid-IR interferometric observation allows us to detect exozodi in the system through a signature in a spatially resolved observation (e.g., Smith, Wyatt, and Haniff, 2012; Liu et al., 2005; Stock et al., 2010; Mennesson et al., 2014; Defrère et al., 2015; Kral et al., 2017; Ertel et al., 2020; Defrère et al., 2011; Ertel et al., 2014; Marion et al., 2014; Absil et al., 2009; Absil et al., 2013; Nuñez et al., 2017; Defrère et al., 2018; Mennesson et al., 2011). This will potentially allow to constrain the parameters of exozodi, and thus help to give shed light on details of its origin. Even the recent observations cannot explain clearly the connection between the two species of exozodi, i.e., hot dust and warm dust, and the difference might be large. Thus, most key questions concerning the exozodi in debris disk systems are related to their own origins and characteristics.

3.3.3 Gas in debris disks

Since the primordial gas dispersal timescales are shorter than 10 Myr (Sect. 1.2.5; Hillenbrand, 2008), debris disks are expected to have no gas or to be at least extremely gas-poor compared to gas-rich protoplanetary disks. However, little amounts of gas have been detected (e.g., β Pictoris, 49 Ceti, Sigma Her, HD 32297; Moór et al., 2017; Cavallius et al., 2019) in tens of young debris disks so far. For this reason, the understanding of the gas component in debris disks is a popular subfield of debris disk studies that have advanced very rapidly in recent years. Here, a brief discussion and summary of the current understanding/observations of the gas are shown.

The most fundamental question is the origin of the gas in debris disk systems, i.e., is it primordial material that survived longer in the outer disks than usually assumed (Krivov et al., 2009), indicating that gas and dust evolve on different timescales, or is it second-generation material that may have formed or been released recently. The latter case would be a result of either photon-induced desorption from solids and grain-grain collisions (Chen et al., 2007; Czechowski and Mann, 2007), released via a collision between icy planetesimals/migration into warmer regions (Moór et al., 2011), or from comet evaporation, which might provide insights into the composition of icy bodies in distant planetary systems (e.g. Beust and Valiron, 2007). Recently, Booth et al. (2019) confirmed that the level of gas present in the disk around HD 95086 is inconsistent with the presence of primordial gas and is consistent with the second generation, which is produced through a collisional cascade.

Several methods have been used to determine the composition of the gas in debris disks, i.e., absorption and emission lines of atomic and molecular gas by using the spectrum to study the material along a single line of sight. Absorption lines are the main method to study of the atomic/molecular content of debris disks, e.g., C, O, and CO (e.g., Roberge et al., 2000; Brandeker et al., 2004). However, this method is restricted to a narrow range of inclination angles, in particular, the disk system must be seen close to edge-on with the line of sight from the observer to the debris disks. Furthermore, lines from the interstellar medium in the same spectrum can be misunderstood as lines from debris disks. Emission lines are also used to study the composition and spatial distribution of debris disks at high angular resolution. This is possible with far-IR and sub-mm/mm facilities, which require only minutes to detect gas emission from debris disks, even though the line fluxes are still low compared to those of a protoplanetary environment. Thus, this method is also limited because it is less sensitive to small gas quantities, which is one of the main reasons for lack of information on gas in debris disks, so far. CO is the only molecular species detected with an emission line method in debris disks, which was observed in the extremely bright and nearby β Pictoris system (Olofsson, Liseau, and Brandeker, 2001; Lieman-Sifry et al., 2016; Higuchi et al., 2017), while C and O are the only atomic species that have been detected with an emission line method in debris disks (Zagorovsky, Brandeker, and Wu, 2010).

Chapter 4

Modeling of debris disks & simulation tools used in this work

The evolutionary state of a debris disk (e.g., the age) can be deduced by the fractional luminosity f_{disk} and its temperature (Sect. 3.1.1), which are derived from the blackbody assumption with the spherical grains in thermal equilibrium (Kalas et al., 2007). However, as can be seen in the previous chapter (e.g., Sect. 3.1.1), this assumption may result in a significantly deviating outcome due to the cancellation of the grain radius dependency of the grain's emission spectrum (see, e.g., Sect. 3.1.1 & Sect. 3.2.1). This implies that a radial distance from the star by a blackbody fit to the SED is not a function of grain size. Thus, the real size of the disk is much larger than predicted (Booth et al., 2013), which is a consequence of the large abundance of 'poor emitters' (i.e., small dust grains) in the disk system. Consequently, this approach yields little information on grains and poorly predicted. Furthermore, an estimated of the disk mass relies on an assumed opacity that hides the information of the properties of the grains (e.g., composition and size). In conclusion, simple blackbody radii are the lower limit or a good approximation of the flux from a narrow ring-like disk structure only (i.e., the temperature of dust grains is nearly constant). Thus, one needs to reformulate the equations with individual grain emissivity as a function of the dust grain size and its composition to calculate the thermal emission of grains properly (e.g., Eq. 2.28). This is the essential reason for a more accurate SED modeling of debris disks.

Besides, to derive several constraints from SED observation and modeling alone, which provide in general only weak and ambiguous constraints on dust properties due to the fundamental degeneracy between model parameters, e.g., disk geometry and dust grain size (Sect. 3.1.1), the modeling of spatially resolved debris disks is preferred as it breaks the degeneracy, and thus allows us to understand the grain/disk properties in detail.

Furthermore, detailed modeling of the dust spatial distribution and grain properties (e.g., the chemical composition, the physical shape of the dust grains, the grain size distribution including grain dynamics) can help in understanding and deducing the properties/composition of hidden planetesimals (and/or planets) to get a comprehensive map of planetary systems. Additionally, the comparison of various modelings with the complexity of multiple wavelengths can be used to overcome the limitations of a single observational data set, which is providing rather ambiguous constraints to their properties. Consequently, to extract the complete set of information about a debris disk, several complementary modeling approaches are required.

In this chapter, a general context of the different approaches of debris disk modeling, e.g., analytical modeling and collisional modeling, and simulation tools used in this work are presented.

4.1 Debris disk modeling with an analytical approach

To interpret the debris disk observations, modeling of debris disks with the classic approach, which is based on analytical functions to describe the dust distribution (e.g., Briggs, 1962; Dohnanyi, 1969), is often used. In particular, analytical modeling of debris disks (e.g., Augereau et al., 1999; Wolf and Hillenbrand, 2005; Thébault and Wu, 2008; Ertel et al., 2011) parameterizes power-law distributions with the radial brightness profile, which is extracted from the resolved disks, and the size distribution, which is set by the assumption of a collisional equilibrium. For example, the simplest applied radial density profile in the disk and grain size distribution follows a power-law, i.e., $n(r) \propto r^{\alpha}$, where α determines the radial slope of density distribution (e.g., $\alpha = 1$ represents debris disks with no perturbations by embedded planets and no additional assumptions about dust production processes; Wolf and Hillenbrand, 2003). Furthermore, dust models are considered with a grain size distribution $n(a) \propto a^{\gamma}$, where γ determines the slope of grain size distribution (Eq. 2.11). Thus, the relevant parameters of the analytical modeling are the radial extent of the disk (e.g., inner/outer radius), the slopes of the radial distribution α, the lower/upper grain sizes, the slopes of the size distribution γ, and the dust mass.

In such models, a key strategy is to explore large and complex parameter space and adapt the model parameters to disk observables, and thus understanding allows to study of dust emission in debris disks in a relatively short time.

4.1.1 *DMS*: Debris disks around Main-sequence Star

The *DMS* tool is based on an analytically described optically thin disk model and is based on the same assumptions as described in Sect. 2.2, which leads us to have significantly simplified radiative transfer equations. In particular, this tool has been developed to compute debris disk observables (e.g., SEDs and spatially resolved images), and thus deepen and widen our view of a debris disk with regard to the understanding of many stellar/dust parameters. The development of this tool is based on the previous codes, e.g., *debris* (Ertel et al., 2011), *MODUST* (Rodmann, 2006), and *modim* (Ertel, Wolf, and Rodmann, 2012). This tool's main program is written in **Fortran 90**.

To compute images with high efficiency in a grid of pixels (e.g, the Cartesian grid of pixels, which has been assigned the intensity in *DMS* with a three-dimensional structure), an adaptive grid is used. For example, the temperature of the inner region of a disk system is drastically changing (i.e., the computation of pixels in regions where the intensity distribution is changing significantly on small spatial scales), and thus the spatial resolution has to be high enough, the opposite is true for the outer region of debris disks (i.e., a low spatial resolution is enough) for an analytical density distribution. To utilize grids at different levels of resolution, an adaptive mesh refinement (AMR) method, adapting the accuracy of a solution within a certain sensitivity, is used in the *DMS* code. The AMR method allows high sampling rates without increasing the over-all spatial resolution (pixel number), i.e., only a specific part that needs high sampling rates computed with an increased spatial resolution. Consequently, an AMR method can simultaneously use multiple spatially unconnected grids at a given level of refinement, compared to the fixed resolution (uniform meshes) of a static grid approach. It starts with a coarse grid first and identifies regions that need finer resolution. Then, this method superimposes finer sub-grids only in those regions.

In the *DMS*, the initial pixel is divided iteratively into 8 adjacent sub-pixels covering the original pixel within the region, where the density distribution is defined, i.e., the edges of the pixel are all inside or all outside the region, until they meet one of the following criteria related to input parameters of the AMR method. For example, an iteration stopped when the maximum temperature difference within one given pixel is smaller than maximum difference chosen as an input parameter with ΔT in *DMS* or the chosen maximum number of iterations of splitting one three-dimensional pixel $N_{\text{subvolume}}$ to sample the dust emission has been performed in *DMS*.

Furthermore, in the context of simulating debris disk observables (e.g., SEDs and images) of spatial dust distributions produced by *ACE* tool (Sect. 4.2.1), spatial dust particle distributions mode is applied in *DMS* tool. In the case of this mode, the sampling is given by the position of the particles (and/or the number density, if needed), thus the individual particle with different grain sizes is used directly to compute its emission.

Depending on the size parameter x and refractive index m (i.e., the real and imaginary parts of the refractive index n and k, respectively), the optical properties (e.g., Q_{abs}, Q_{sca}, S_{11}, and S_{12}; see Sect. 2.2.2) of the dust grain/size distribution are computed with *miex* (Wolf and Voshchinnikov, 2004), which is directly included in *DMS*. Several effective medium theories for the optical behaviors with the inhomogeneous dust mixture (e.g., the Maxwell-Garnett mixing rule and the Bruggeman rule; Maxwell Garnett, 1904; Bruggeman, 1936) are also included in *DMS*. Based on stellar parameters and optical properties such as, values of Q_{abs}, *DMS* calculates dust temperature distribution via Eq. 2.28. To create images from the dust distributions with disk parameters, the thermal reemission and the polarized/scattered stellar light at the center of each sub-pixel are computed via Eqs. 2.27, 2.23, and 2.24 and, subsequently, integrated overall sub-pixels corresponding to one pixel along the line of sight. This process is repeated for the all chosen observing wavelengths.

The general descriptions and main features of the numerical implementation in *DMS* (i.e., a *DMS* flowchart) are given in Fig. 4.1.

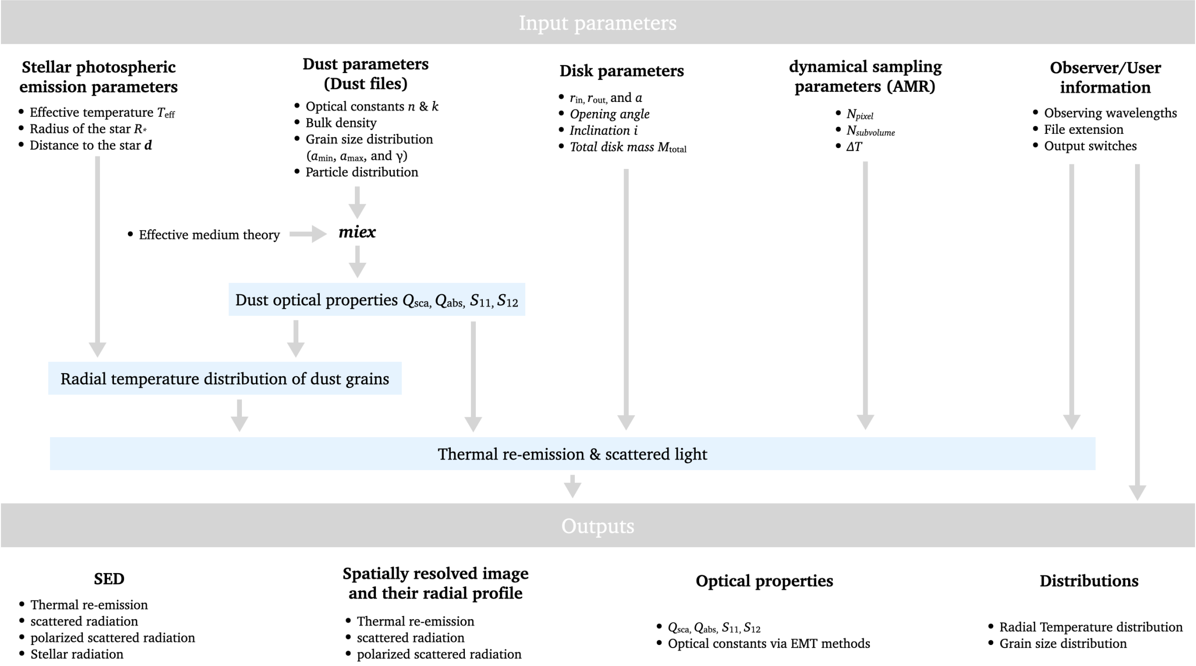

FIGURE 4.1: DMS Flowchart. Figure is based on Kim et al. (2018).

DMS tests

The *DMS* code has passed several tests that are described in the following. The analytical distribution mode and the dust particle distribution mode have been tested with different tools separately. Errors in all tests are below by only a few percents compared when using reasonable sampling parameters, e.g., the radial extent of the disk of ∼ a few au to few hundreds of au, the grain size distribution of ∼ a few hundreds of nm to a few mm, the temperature of ∼ a few K to few hundreds of K, and the dust mass of 10^{-6} to 10^{-12} $M_\odot$.

- The stellar emission spectra with a blackbody assumption have been tested against the *DDS* (Wolf and Hillenbrand, 2005).
- The analytical distribution mode: Edge-on oriented and narrow disks have been tested with respect to the radial temperature distribution, the SEDs, and the spatially resolved images (and their radial profiles) of the thermal reemission, scattered light, and polarized scattered light for single grain sizes against the results of optically thin disks from *Polaris* (Reissl, Wolf, and Brauer, 2016).
- The dust particle distribution mode: The face-on oriented and extended disks have been tested with respect to the optical dust properties, the radial temperature distribution, the SEDs and the spatially resolved images (and their radial profiles) of the thermal reemission, scattered light, and polarized scattered light for grain size distribution against the results from *ACE* (Löhne et al., 2017).

4.2 Debris disk modeling with a collisional approach

Although the classical approach with an analytical model (e.g., *DMS*) can produce and explore a huge parameter space in a relatively short time, they do not cover physical mechanisms/processes that drive the collisional evolution between whole solids, ranging from planetesimals down to dust grains. Thus, it is impossible to deduce directly the information of planetesimal parameters (e.g., their mass, number density, location, and orbital eccentricities) via classical modeling. To model the subsequent collisional evolution of planetesimals, an alternative modeling approach with an initial distribution of planetesimals, following a collisional cascade evolution, is used. Since the planet formation processes might leave a couple of narrow planetesimal belts orbiting the star, which collides at sufficiently high velocities for those bodies to be destroyed, the modeling of the collisional evolution connects particle dynamics and collisions with the coupled size and spatial distributions for the whole population in debris disks. This method, therefore, can constrain the properties of planetesimals as well as infer the architecture of a planetary system, compared to the classical approach with an analytical model, which can only analyze the dust emission and properties to infer the existence of planetesimals. Although collisional modeling provides a more comprehensive picture, the numerical complexity (and thus computation time) is so expensive that only a limited number of parameter space can be explored.

The collisional modeling has been developed in two ways. Many previous studies used a combination of N-body simulations[1] and particle-in-a-box models and focused purely on the gravitational model of planet-disk interactions and forces (e.g., Lecavelier Des Etangs, Vidal-Madjar, and Ferlet, 1996; Thébault, 2009; Kuchner and Stark, 2010; Kral, Thébault, and Charnoz, 2013), which aim at following the trajectories of individual objects by integrating their equations of motion numerically. However, the number of particles in debris disks is orders of magnitude beyond the scope of pure N-body simulations (Matthews et al., 2014). On the other hand, statistical methods effectively replace discrete particles with their distribution on appropriate phase space and mesh of several variables comprising, for instance, their mass, distance, velocity, and/or orbital elements (e.g., Kenyon and Bromley, 2008; Thébault and Augereau, 2007; Thébault and Wu, 2008; Krivov, Sremčević, and Spahn, 2005; Krivov, Löhne, and Sremčević, 2006; Löhne et al., 2017; Sende and Löhne, 2019). The number of particles in each bin of the mesh at successive time instants is computed by solving equations that describe gain and loss of objects by collisions and other physical processes. Therefore, statistical codes are more accurate in handling collisional evolution.

---

[1] The widely used N-body method is a numerical tool to simulate a dynamical system of particles under the influence of the gravity and is used to investigate the dynamics of few-body systems to understand the evolution of the resulting large-scale structures (e.g., planets, stars, or galaxies in the universe).

4.2.1 *ACE*: Analysis of Collisional Evolution

In this section, the basic idea of the numerical modeling of collisional cascades in the code *ACE* (**A**nalysis of **C**ollisional **E**volution; Krivov, Sremčević, and Spahn, 2005; Löhne et al., 2017) is addressed, starting with an initial distribution of planetesimals and modeling its subsequent collisional evolution by calculating the time-dependent production and loss of material.

Phase space & master equation of the kinetic code *ACE*

The collisional code *ACE* numerically solves the Boltzmann-Smoluchowski equation to evolve a broad range of solids (e.g., from sub-μm to hundreds of km), orbiting on (nearly) Keplerian orbits and undergoing a collisional evolution. *ACE* follows the orbit-averaged approach[2], e.g., particles are grouped according to their orbits. Each group populates a given ellipse with a particle density that is uniform across mean anomalies, i.e., uniform in time. Discrete orbits are fixed throughout the simulations and parameterized by orbital elements.

The recent version of the *ACE* tool allows the azimuthal distribution to be non-uniform (Löhne et al., 2017; Sende and Löhne, 2019), i.e., the phase space spans an additional dimension that covers the orientations of object orbits, parameterized by the longitude of periapsis ϖ (= $\Omega + \omega$), which is defined as the sum of the longitude of the ascending node (Ω) and the argument of periapsis (ω). The debris disk evolution is, therefore, described as the discretized distribution of material and is represented by bins with a four-dimensional phase space distribution, i.e., the masses of the individual particles m, the pericenter distances q (instead of the semi-major axis because the belt and the halo have similar pericenter distances, whereas the semi-major axes differ widely), the eccentricities e, and the longitudes of periapsis ϖ. Collisions between pair-wise combinations of bins are possible at up to two distinct points, defined by the colliders' q, e, and ϖ values. Collision velocities, rates, and outcomes follow directly Krivov, Sremčević, and Spahn (2005) and Krivov, Löhne, and Sremčević (2006). *ACE* calculates secular perturbations[3] using the transport equation. The phase space density $n(x)$ at the position changes, depending on the velocity $v(x)$ = 0, $\dot{q}(x)$, $\dot{e}(x)$, and $\dot{\varpi}(x)$ at this point (Löhne et al., 2017; Sende and Löhne, 2019):

$$\dot{n}(x) = -\left[\frac{\partial}{\partial q}\,n(x)\,\dot{q}(x) + \frac{\partial}{\partial e}\,n(x)\,\dot{e}(x) + \frac{\partial}{\partial \varpi}\,n(x)\,\dot{\varpi}(x)\right] \tag{4.1}$$

The discretized master equation, which originates from Eq. 4.1 and which has to be integrated over time and solved is given by:

$$\dot{n}_{\mathrm{i}} = \sum_{\mathrm{jk}} G_{\mathrm{ijk}}\,n_{\mathrm{j}}\,n_{\mathrm{k}} - \sum_{\mathrm{j}} L_{\mathrm{ij}}\,n_{\mathrm{i}}\,n_{\mathrm{j}} + \sum_{\mathrm{j}} T_{\mathrm{ij}}\,n_{\mathrm{j}}\ , \tag{4.2}$$

where n_{i} is the number of objects in the bin specified by multi-index i = $(i_{\mathrm{m}}, i_{\mathrm{q}}, i_{\mathrm{e}}, i_{\varpi})$, coefficients G_{ijk} denote the gain (the specific rates at which objects of type i are formed in collisions between objects of types j and k), L_{ij} denote the loss (the specific rate at which objects of type i are removed in collisions with j), and T_{ij} denotes the transport to cell i from neighbouring cell j (Reidemeister et al., 2011; Löhne et al., 2017).

A more detailed description of this simulation tool can be found in previous studies (e.g., Krivov, Sremčević, and Spahn, 2005; Krivov, Löhne, and Sremčević, 2006; Krivov et al., 2008; Löhne, Krivov, and Rodmann, 2008; Löhne

---

[2] A major difficulty to this approach is the sampling due to numerical complexity. There are two main different way of particle grouping, e.g., 'time-resolved' and 'orbit-averaged'.

[3] Asymmetric structures of debris disks can be plausibly explained by the gravitational field of the (hidden) embedded planet(s) and/or planetesimal(s) in a debris disk (see also Sect. 2.1.5 & 2.1.10). To consider collisions with secular perturbations, the *ACE* tool adds the gravitational influence of a single perturbing planet.

et al., 2012; Löhne et al., 2017; Sende and Löhne, 2019).

Collisional outcomes

This section summarizes the collisional prescription and algorithm used in the *ACE* code. A collision between at least two colliders, i.e., a projectile and a target with the masses m_p and m_t, respectively, occurs with a specific impact velocity v_imp. The total mass and the reduced mass are given by $M_\mathrm{total} = m_\mathrm{p} + m_\mathrm{t}$ and $\mu = \frac{m_\mathrm{p} m_\mathrm{t}}{m_\mathrm{p}+m_\mathrm{t}}$, respectively. The specific impact energy (i.e., the kinetic energy of the projectile per unit target mass) is defined as $Q_\mathrm{imp} = \frac{E_\mathrm{imp}}{m_\mathrm{t}} = \frac{m_\mathrm{p} v_\mathrm{imp}^2}{2 m_\mathrm{t}}$ (Movshovitz et al., 2016). The most important quantity in the collisional evolution of the *ACE* code is the specific energy for the catastrophic disruption threshold Q^*_ij, which is defined as the normalized energy at which the mass of the largest fragment has half of the original target mass (Benz and Asphaug, 1999; see also Eq. 2.12). This quantity follows the definition from Löhne et al. (2012), which assumes a size dependence described by Benz and Asphaug (1999), together with the reformulation by Stewart and Leinhardt (2009), regarding the reduced and the total masses of the colliders and is given by:

$$Q^*_\mathrm{ij} = \left[Q_\mathrm{s}\left(\frac{s_\mathrm{ij}}{1\,\mathrm{m}}\right)^{-b_\mathrm{s}} + Q_\mathrm{g}\left(\frac{s_\mathrm{ij}}{1\,\mathrm{km}}\right)^{b_\mathrm{g}}\right]\left(\frac{v_\mathrm{imp}}{3\,\mathrm{km/s}}\right)^{0.5} + \frac{3G\,(m_\mathrm{i}+m_\mathrm{j})}{5\,s_\mathrm{ij}}\,, \tag{4.3}$$

where the subscripts s and g stand for the material strength and the gravity regime, respectively. The quantity Q_s is relevant for describing the shock disruption in the strength regime, while Q_g is the corresponding specific energy in the gravity regime, both scaled by the impact velocity v_imp. The equivalent radii of the spheres are s_i and s_j, with $s_\mathrm{ij} \equiv (s_\mathrm{i}^3 + s_\mathrm{j}^3)^{1/3}$ as the combined volume of the colliders. The last term of Eq. 4.3 approximates the specific energy required to overcome self-gravity, which is important only for radii ≥ 30 km in the simulations. $Q_\mathrm{s} = Q_\mathrm{g} = 5 \times 10^2$ J/kg, $b_\mathrm{s} = 0.37$, and $b_\mathrm{g} = 1.38$ (Benz and Asphaug, 1999) are set as a reference values in *ACE*. A more detailed description can be found in Chapter 5.

Since gas is already removed and the planet formation concludes during the debris disk stage, i.e., a few Myrs after the birth of the star, cratering collisions and completely disruptive collisions become the dominating collision types. Depending on the colliders' masses m_p and m_t and their specific impact energy Q_imp, several different collisional possibilities between two colliders, i.e., projectile and target, are possible:

- If the Q_imp is sufficient to overcome the threshold Q^*_ij (i.e., the material strength and the combined gravitational potential of the colliders), the largest fragment's mass is smaller than half of the target's mass. This collision type is called a disruptive collision (or alternatively, destructive, fragmenting, or catastrophic collision; see Sect. 2.1.5).
- If Q_imp is smaller than the threshold Q^*_ij, i.e., the energy of the projectile is not sufficient to destroy the target (or the projectile is destroyed while the target is cratered), the target retains at least half of its original mass. This collision type is called a cratering collision.
- If the projectile and target stay intact and are separated again and if the impact velocity v_imp is greater than $\approx$ 10 m/s. This collision type is called bouncing collision.
- If their relative velocities are very low ($\lesssim$ 1-10 m/s), the projectile and target are bound together. This is called sticking collision. However, such low collision velocities are very rare in debris disks.

A more detailed description of collisional outcomes can be found in previous studies (e.g., Löhne et al., 2017) and in Chapter 5.

Chapter 5

Impact of collisions on the appearance of eccentric debris disks

This chapter presents the results published in Kim et al. (2018), which is a follow-up study of Löhne et al. (2017). The author of this dissertation performed the simulated observations of the results from the collisional modeling and made major contributions to the write-up and interpretation of the results. The collisional modeling is performed by Torsten Löhne and other parts of this study were done in collaboration with Sebastian Wolf, Torsten Löhne, Florian Kirchschlager, and Alexander V. Krivov.

Spatially resolved images of many debris disks show azimuthal asymmetries of surface brightness (e.g., Kalas, Graham, and Clampin, 2005; Olofsson et al., 2016; Pan, Nesvold, and Kuchner, 2016; MacGregor et al., 2017). In (sub)-mm wavelength observations, which trace large grains and so the dust parent bodies, such disks often appear as narrow eccentric belts with some offset between the belt center and the star. The most likely explanation for the eccentricities and offsets is secular perturbations by as yet undiscovered planets (e.g., Wyatt et al., 1999; Faramaz et al., 2014). Therefore, interpretation of debris disk observations may allow one to constrain parameters of the alleged planets.

Another goal of the analysis of debris disk observations is to reconstruct the hidden planetesimal populations that produce the observed dust by collisions. Unlike planetesimals, dust is subject to stellar radiation forces that make its distribution different from that of the parent planetesimals. To summarize, in order to constrain parameters of the putative planets and dust parent planetesimals, one has to understand combined effects of the dust-producing collisions in the dynamically perturbed belts and stellar radiation forces exerted on dust.

The link between the dust distributions and observable quantities is also important. What is actually observed is radiation scattered or re-emitted by dust, rather than dust itself. Observations of debris disks at a given wavelength are primarily sensitive to dust particles of a comparable size and to certain dust locations — those at which dust emission at this particular wavelength is the strongest. As a result, the observational appearance of debris disks does not directly reflect the underlying dust distributions, and the same disk may reveal dissimilar structure and shape when viewed at different wavelengths. All this further complicates the analysis.

In recent years, many studies have been focused on collisions and radiation pressure effects in debris disks (e.g., Dominik and Decin, 2003; Wyatt, 2005; Kenyon and Bromley, 2005; Thébault and Augereau, 2003; Thébault and Augereau, 2007; Stark and Kuchner, 2008; Stark and Kuchner, 2009; Kuchner and Stark, 2010; Thébault, 2012; Kral, Thébault, and Charnoz, 2013; Nesvold et al., 2013; Thebault, Kral, and Augereau, 2014; Kral et al., 2015; Nesvold and Kuchner, 2015b; Nesvold and Kuchner, 2015a; Esposito et al., 2016). For these studies, N-body codes have been used that follow the trajectories of individual particles by numerically integrating their equations of motion. In this work, the kinetic approach of statistical physics, which is based on the continuity-like equation for the distribution of dust in an appropriate phase space, and model the evolution of the phase space distributions of the material (Krivov, Löhne, and Sremčević, 2006) is used.

The goal of the current study is to answer following questions: What are the impact of selected collisional parameters on the wavelength-dependent observational appearance of debris disks? Is it possible to constrain selected collisional parameters based on specific observational quantities of debris disks? Based on the work by Löhne et al. (2017), studies on planetesimal collisions in debris disks have conducted and the dependence of the appearance of debris disks on essential collisional parameters, such as the eccentricity of the parent belt, dynamical excitation of the system (i.e., the dispersion of the eccentricities of parent belt bodies), and the critical specific energy for fragmentation (i.e., material strength) of dust particles are investigated.

This Chapeter is organized as follows: Section 5.1 describes the underlying physical process of collisions in the debris disks. In Section 5.2, the applied tools: the collisional code ACE and the code *DMS* for the simulation of observations are briefly introduced. In Section 5.3, impacts of the collisional evolution on observables, in particular, their SEDs and brightness asymmetries in spatially resolved images are quantified and discussed. The findings of this work are summarized in Section 5.4.

5.1 Collisional physics in debris disks

The probability of two spherical objects on Keplerian orbits to collide can be expressed as the product of the overlap of the two orbits, the number density of grains at the desired location in the space of orbital elements, the relative velocity and the collisional cross section (Krivov, Löhne, and Sremčević, 2006). In addition, the collisional outcome depends on many other factors, such as the impact angle, dust species, porosities of dust grains, and hardnesses of projectile and target (Blum and Wurm, 2008). Furthermore, debris disks with larger typical orbital eccentricities can significantly increase the geometrical probability of collision and the collisional velocities (Krivov, Löhne, and Sremčević, 2006; Queck et al., 2007), resulting in an increased efficiency of the collisional cascade.

5.1.1 Influence of eccentric belts on collisions

Various previous studies discussed the brightness asymmetry in eccentric debris disks, for example, ϵ Eridani (Greaves et al., 1998; Greaves et al., 2005; Hatzes et al., 2000; Poulton, Greaves, and Collier Cameron, 2006; Pan, Nesvold, and Kuchner, 2016), HR4796 A (Wyatt et al., 1999; Schneider et al., 2009; Thalmann et al., 2011; Lagrange and Chauvin, 2012), Fomalhaut (Stapelfeldt et al., 2004; Kalas, Graham, and Clampin, 2005; Pan, Nesvold, and Kuchner, 2016; MacGregor et al., 2017), HD 181327 (Schneider et al., 2006), HD 15115 (Kalas et al., 2007), HD 202628 (Krist et al., 2012), HD 115600 (Currie et al., 2015), HD 106906 (Kalas et al., 2015), and HD 61005 (Olofsson et al., 2016), as a result of two competing effects: higher temperatures at the pericenter and higher densities at the apocenter. If the increased emission at short wavelengths at the pericenter exceeds the increased flux due to the over-density at the apocenter, the so-called pericenter glow phenomenon is observed. This effect was detected for the first time in Fomalhaut, a 133 au ring offset by 15 au implying a forced eccentricity of 0.11 (Kalas, Graham, and Clampin, 2005).

On the other hand, Pan, Nesvold, and Kuchner (2016) calculated the lowest order in the time-averaged linear number density of particles as a function of longitude, f, in a mild eccentric disks ($e \ll 1$) ring along the orbit as

$$l_{\text{single}}(f) \propto 1 - e \cos f. \tag{5.1}$$

Using a different approach, Marsh et al. (2005) found a similar enhancement at the apocenter. In summary, since particles orbit faster at periastron than at apastron, their number density in Keplerian orbits decreases at the pericenter and increases at the apocenter by the same fractional amount.

The ejection condition can be derived from the ratio between the radiation pressure of the stellar radiation-field to the gravitational force, β ($\equiv \frac{|F_{\rm rad}|}{|F_{\rm g}|}$; see also Sect. 2.1.2). A general expression for the β threshold, for which a dust particle is ejected from the system, can be expressed as follows (Murray and Dermott, 1999):

$$\beta_{\rm eject} \geq \frac{1}{2}\left(\frac{1-e^2}{1+e\cos\phi}\right), \tag{5.2}$$

where ϕ corresponds to the longitude of the orbit, at which the particle ejected ($\phi = 0$ and $\phi = \pi$ correspond to periastron and apastron, respectively). Apparently, the β-ratio, and thus the ejection condition and blowout size, depend on the eccentricity of parent belts.

The gravitational impact of large planetesimals can be observed, for instance, as higher dynamical excitation (Kenyon and Bromley, 2004). Dynamical excitation, which can be characterized by the width of the typical eccentricity e and inclination i, determines the relative velocities at which orbits cross. Even though the exact level of stirring in debris disks remains unknown, previous studies of debris disk have shown that stirring models are consistent with observations if a dynamical excitation of up to ~ 0.1 is assumed (e.g., Wyatt et al., 2007; Löhne, Krivov, and Rodmann, 2008; Thébault and Wu, 2008; Kennedy and Wyatt, 2010; Müller, Löhne, and Krivov, 2010; Wyatt et al., 2012; Löhne et al., 2012).

5.1.2 Influence of material strength on the outcome of collisions

The second key parameter which determines the outcome of collisions in debris disks is the catastrophic disruption threshold $Q_{\rm D}^*$ that is the impact energy per unit of target mass, which is defined as the normalized energy at which the mass of the largest fragment has half of the original target mass (Benz and Asphaug, 1999). While for smaller objects this quantity is determined by the material strength, the gravitational binding energy dominates in the case of larger objects ($\geq$ 1km). Thus, the catastrophic disruption threshold $Q_{\rm D}^*$ is described by the sum of two power-laws (Davis et al., 1985; Holsapple, 1994; Paolicchi, Verlicchi, and Cellino, 1996; Durda and Dermott, 1997; Durda, Greenberg, and Jedicke, 1998; Benz and Asphaug, 1999; Kenyon and Bromley, 2004; Stewart and Leinhardt, 2009). This work follows the definition from Löhne et al. (2012) and assumes a size dependence described by Benz and Asphaug (1999), together with the reformulation by Stewart and Leinhardt (2009), regarding the reduced and the total masses of the colliders:

$$Q_{\rm D}^* = \left[Q_{\rm s}\left(\frac{s_{\rm ij}}{1\rm m}\right)^{-b_{\rm s}} + Q_{\rm g}\left(\frac{s_{\rm ij}}{1\rm km}\right)^{b_{\rm g}}\right]\left(\frac{v_{\rm imp}}{3\rm km/s}\right)^{0.5} + \frac{3G(m_{\rm i}+m_{\rm j})}{5s_{\rm ij}}. \tag{5.3}$$

Here, the subscripts s and g stand for the material **s**trength and the **g**ravity regimes, respectively. The quantity $Q_{\rm s}$ is relevant for describing shock disruption in the strength regime, while $Q_{\rm g}$ is the corresponding specific energy in the gravity regime, both scaled by the impact velocity $v_{\rm imp}$. Note the equivalent radii of the spheres, $s_{\rm i}$ and $s_{\rm j}$, with $s_{\rm ij} \equiv (s_{\rm i}^3 + s_{\rm j}^3)^{1/3}$ as the combined volume of the colliders. The last term of Equation (3) approximates the specific energy required to overcome self-gravity, which is important only for radii $\geq$ 30 km in the simulations (Löhne et al., 2012). It is chosen that $Q_{\rm s} = Q_{\rm g} = 5\times10^2$ J/kg, $b_{\rm s} = 0.37$, and $b_{\rm g} = 1.38$ (Benz and Asphaug, 1999) in this work as a reference.

Depending on the masses and the impact energy of the colliders, following outcomes are expected: If the energy is sufficient to overcome both the material strength and the combined gravitational potential of the colliders, disruption and dispersal occur. Collisions with specific energies below this threshold are depicted as cratering if the target retains at least half of its original mass. In both cases, a cloud of smaller fragments is produced from the remnants (Löhne et al., 2017). If both colliders stay intact, they are assumed to separate again, unless the impact velocities are below 10 m/s. Only for very low relative velocities ($\leq$ 1-10 m/s) sticking and hence growth may occur (Poppe, Blum, and Henning, 2000). However, such low collision velocities are very rare. A more detailed description can be found in Sect. 4.2.1.

5.2 Numerical models

5.2.1 Dynamical modeling

As discussed in previously, most of the previous studies focused on purely gravitational models of planet-disk interactions and forces using the N-body simulations. Following the trajectories of individual objects is useful when the dynamics are complex, whereas any collisional event is assumed to simply eliminate both colliders (Lecavelier Des Etangs, Vidal-Madjar, and Ferlet, 1996). Even though this method is hardly applicable in the case of a sufficiently large number of objects to cover a broad range of particle masses, a superparticle-method is applicable in the case of shorter collisional timescales or more violent collisional events (e.g., Nesvold et al., 2013; Kral, Thébault, and Charnoz, 2013).

The kinetic method of statistical physics is more suitable for particle distributions and long-term collisional evolution. The kinetic method introduces a multidimensional phase-space distribution of dust (e.g., a distribution of grain sizes, coordinates, and velocities, and the supply, loss, and transport of dust grains). The collisional code *ACE* (Löhne et al., 2017), which allows the simulation of the dust production and removal in the planetesimal belt as well as the dynamical evolution of the whole disk, is applied in this work. *ACE* derives the velocity distribution in particle ensembles with the Boltzmann equation and the size distribution using the Smoluchowski equation for describing the evolution of the solids, including disruptive and cratering collisions. The code allows the implementation of a three-dimensional kinetic model with masses, semi-major axes, and eccentricities as phase-space variables. Thus, the resulting equation can be solved for the phase-space distribution as a function of time, from which mass, size, and spatial distributions can be calculated (Krivov, Löhne, and Sremčević, 2006; Krivov et al., 2008; Krivov, 2010; Löhne et al., 2017). Collisional outcomes are calculated with size-dependent scaling laws for fragmentation and dispersal in both the strength and the gravity regime as mentioned in Section 5.1.2. A more detailed description of this simulation tool can be found in previous studies (e.g., Krivov, Sremčević, and Spahn, 2005; Krivov, Löhne, and Sremčević, 2006; Krivov et al., 2008; Krivov, 2010; Löhne, Krivov, and Rodmann, 2008; Löhne et al., 2012; Löhne et al., 2017) and Sect. 4.2.1.

5.2.2 Simulated observations

The results of the dynamical calculations provide the basis for the simulation of the observational appearance of the considered disk models. For this purpose, newly developed code *DMS*, which allows us to calculate the SED, wavelength- and inclination dependent scattered light images, and polarization maps as well as thermal re-emission maps, is applied in this work. It is based on the approach outlined by Ertel et al. (2011) and Ertel, Wolf, and Rodmann (2012). To spatially resolve the local density and temperature distribution sufficiently well, an adaptive mesh refinement method in Cartesian coordinates is used. The optical properties of the dust grains are computed using the tool *miex* (Wolf and Voshchinnikov, 2004) which is based on Mie1908 theory (Mie, 1908).

In the current study, the density distribution is provided by *ACE* in a tabular form. Thermal re-emission and scattered radiation maps are computed at different observing wavelengths for each dust particle location and dust property. A more detailed discussion of the *DMS* code can be found in Sect. 4.1.1.

5.2.3 Model parameters

The basic debris disk model applied in this study is described in Löhne et al. (2017). In the following, the basic characteristics of that model are summarized in brief. To quantify and identify the specific influence of collisions on the appearance of debris disks, a fiducial idealized typical debris disk system around a Fomalhaut-like star that is an A3V main-sequence star (see Table 5.1) is modeled. The stellar photospheric emission is described by the corresponding PHOENIX/NextGen grid models (Hauschildt et al., 1999).

The particles are assumed to be composed of generic astrosilicates (Draine, 2003) and ice (Li and Greenberg, 1998) in equal volume fractions, with a bulk density of $2.35\,\mathrm{g\,cm^{-3}}$. The effective medium theory (Bruggeman 1935) to calculate the optical properties is used. Since eccentric debris disks in the model is considered, the blowout limit varies between two extreme orbital points that is periastron and apastron (see Eq. 2). For the given photospheric spectrum and an eccentricity $e_\mathrm{b} = 0.4$, the blowout limit amounts to $\sim 3\,\mu$m and $6\,\mu$m at periastron and apastron, respectively. Asymmetries are most easily identified where narrow belts are resolved, which correspond to narrow volumes in the space of orbital elements (Löhne et al., 2017). The relative radial width $\Delta q_\mathrm{b}/\, q_\mathrm{b}$ at apastron $q_\mathrm{b} = a_\mathrm{b}(1 + e_\mathrm{b})$ can be estimated from

$$\frac{\Delta q_\mathrm{b}}{q_\mathrm{b}} = \sqrt{\left(\frac{\Delta a_\mathrm{b}}{a_\mathrm{b}}\right)^2 + \left(\frac{\Delta e_\mathrm{b}}{1+e_\mathrm{b}}\right)^2}, \tag{5.4}$$

where a_b and e_b are varied independently. Here, the quantities a_b and e_b are the semi-major axes of a perturbed belt object and average belt eccentricity, respectively. The quantity Δe_b denotes the dispersion of the eccentricities of parent belt bodies (i.e., dynamical excitation of the system). A more detailed description of the model setup can be found Löhne et al. (2017).

Four different eccentricities of the parent belt, $e_\mathrm{b} = 0.0$ (circular), 0.1, 0.2, and 0.4, respectively, are considered. In addition, three different levels of dynamical excitation, $\Delta e_\mathrm{b} = 0.05$, 0.1, and 0.2 are considered. The dispersion is defined by the range of eccentricity values. It is parameterized by the maximum and minimum orbital eccentricities that planetesimal belts have at the onset of the collisional cascade. Furthermore, five different values of the material strength Q_s, which is the strength component of the catastrophic disruption threshold Q_D^*, ranging from "very high" to "very low" (see Table 5.1) are considered. These are related to the reference value for Q_s by $Q_\mathrm{s} = \alpha \times$ reference value of Q_s, with $\alpha = 25$, 5, 1, 1/5, and 1/25, respectively. Thus, this parameter is spanning a range of $5^4 \sim 625$ in the simulations. Note that Q_D^* can be as small as $10^{-2} \sim 10^{-4}$ J/kg for meter-sized bodies without self-gravity (Bukhari Syed et al., 2017; Whizin, Blum, and Colwell, 2017)

For each run, the system is evolved for 10^7yr. Although many debris disks are much older, this value as a steady-state is achieved within this time (Thébault and Augereau, 2007) is chosen. For the simulation of observations, all grains up to a maximum grain size of around 1 mm are considerd. The contribution of larger particles to the observable quantities is negligible. Surveys at sub-mm wavelengths have shown that for most debris disks mass is typically ranging from $\sim 10^{-9}$ to several 10^{-7} $\mathrm{M}_\odot$ (e.g., Greaves 2005, and references therein). Thus, a collisionally evolved steady-state disk with 0.7×10^{-8} $\mathrm{M}_\odot$ is considered.

TABLE 5.1: Model parameters for simulation of the dynamical evolution.

Parameter	Value
Stellar type	A3V
Mass of the star M_*	1.92 $M_\odot$
Luminosity of the star L_*	16.6 $L_\odot$
Effective temperature T_*	8590 K (Mamajek et al., 2012)
Radial extension	$5\,\mathrm{au} \leq \mathrm{R} \leq 600\,\mathrm{au}$
Number of grid points in radial direction	694
Azimuthal extension	$0 \leq \phi < 2\pi$
Number of grid points in azimuthal direction	6284
Size of dust grains and planetesimals s	[0.264 µm, 48.6 km]
Initial size distribution $n(s)$	$n(s) \propto s^{-3.66}\, T_{\mathrm{orbit}}/T_0$
Belt eccentricities e_b	e_b = 0.0, 0.1, 0.2, and 0.4
Dynamical excitation Δe_b	Δe_b = ± 0.05, 0.1, and 0.2
Catastrophic disruption threshold Q_D^* (material strength Q_s)	"very high" ($Q_\mathrm{s} = 1.25 \times 10^4$ J/kg), "high" ($Q_\mathrm{s} = 2.5 \times 10^3$ J/kg), "reference" ($Q_\mathrm{s} = 5 \times 10^2$ J/kg), "low" ($Q_\mathrm{s} = 1 \times 10^2$ J/kg), "very low" ($Q_\mathrm{s} = 0.2 \times 10^2$ J/kg)
Dust composition and references of corresponding optical data	Homogeneous mixture of astrosilicate (Draine, 2003) and water ice (Li and Greenberg, 1998)
Bulk density of dust ρ_bulk	$2.35\,\mathrm{g\,cm^{-3}}$
Distance to the debris disk system	8 pc

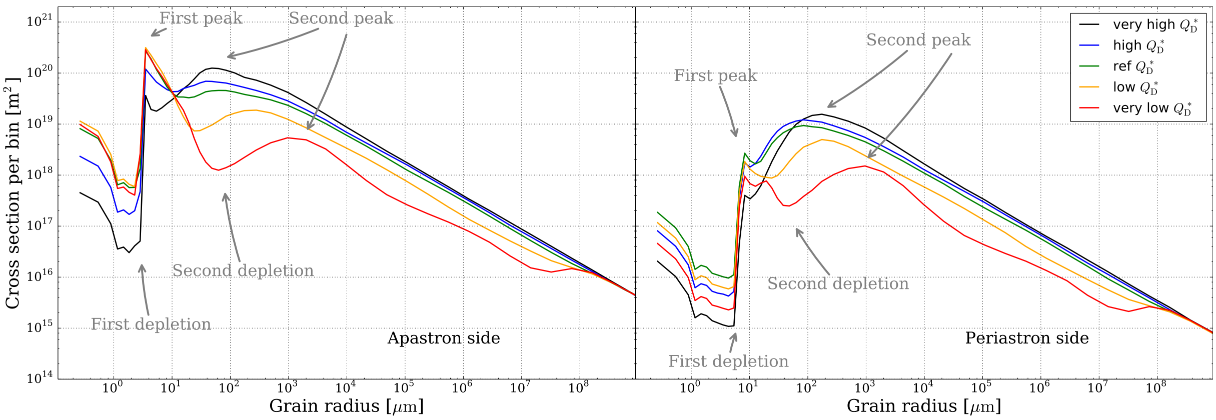

FIGURE 5.1: The grain size distribution at the apastron (left) and periastron side (right) of debris disks with a belt eccentricity of e_b = 0.4 for different material strengths.

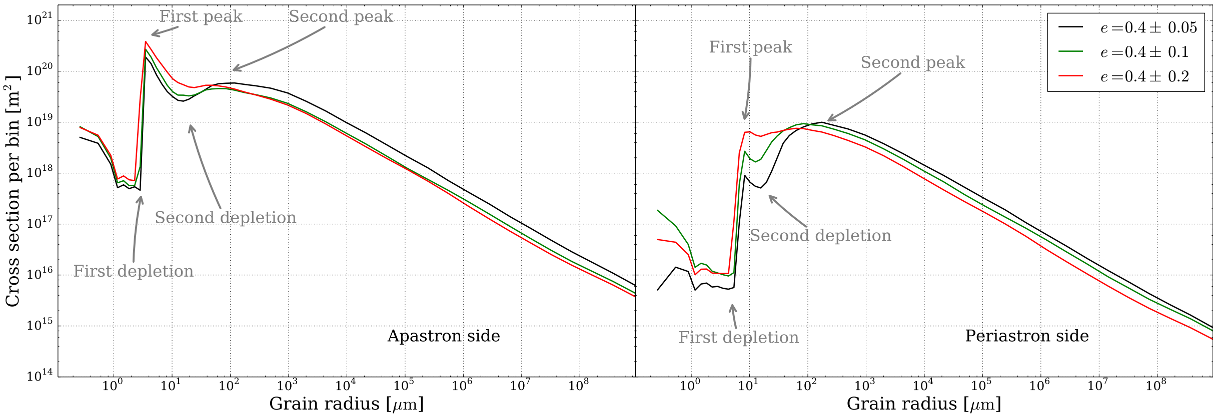

FIGURE 5.2: The grain size distribution at the apastron (left) and periastron side (right) of debris disks with a belt eccentricity of e_b = 0.4 for different levels of dynamical excitation (Δe_b = 0.05, 0.1, and 0.2).

5.3 Results

In the following, impacts of the eccentricity e_b, dynamical excitation Δe_b, and the catastrophic disruption threshold Q_D^* on the observational appearance of the considered debris disks are analyzed. For this purpose, impacts of these parameters on the resulting particle size distribution (Section 5.3.1) are discussed. Subsequently, he corresponding SED (Section 5.3.2) and spatially resolved observations (Section 5.3.3) are analyzed. Studies on the comparison between the periastron and the apastron side of the disk (Section 5.3.4) is considered to constrain the collisional parameters.

5.3.1 Particle size distribution

First the dust grain size distributions at periastron and apastron of debris disks with different material strengths are investigated. As the geometrical cross section of the dust grain is a proxy for the emitted and scattered light, it is shown as a function of the grain size in Figs. 5.1 & 5.2.

In Fig. 5.1, the dust grain size distributions at the periastron and apastron of debris disks a belt eccentricity of e_b = 0.4 (with dynamical excitation Δe_b = 0.1) for different material strengths are investigated. Since the radiation pressure has a strong influence on the cutoff in the grain size distribution at smallest sizes, the wavy patterns of the grain size distributions start around the smallest bound grains. Note that the blowout size can be increased with particle porosity and increasing stellar temperature (Burns, Lamy, and Soter, 1979; Kirchschlager and Wolf, 2013; Brunngräber et al., 2017). One finds different characteristic wavy patterns in the grain size distributions starting with the depletion of grains with radii below the blowout radius $a_{\rm bo}$, which are caused by the lack of $\beta > 0.5$ dust grains (Thébault and Augereau, 2003), depending on different collisional evolutions (Figs. 5.1 & 5.2). For grains with radii $\sim 3\,\mu$m at the apastron side and grains with radii $\sim 6\,\mu$m at the periastron side, a strong wavy pattern develops. This depletion leads to an over-density of slightly larger grains ("first peak") because grains with radii $a < a_{\rm bo}$ are depleted and thus can no longer contribute efficiently to the destruction and erosion processes anymore. The overabundance of grains with radii around the first peak ($\sim 1.5\,a_{\rm bo}$) in turn induces another depletion of grains with radii around the "second depletion" ($\sim 4 - 40\,a_{\rm bo}$) that is caused by small high-β grains originating inside the disks. Thus, an efficient destruction is responsible for the deep depletion of objects with radii of up to $\sim\ 4 - 40\,a_{\rm bo}$. Qualitatively, this first wavy pattern is less pronounced in the size distribution of higher material strengths, where the impact velocities and thus their rate of destructive collisions is significantly lower. A strong depletion for lower material strengths is found for grains with radii $\sim 60\,\mu$m, while the depletion in the case of higher material strengths is valid for radii $\leq 10\,\mu$m (Fig. 5.1). This depletion eventually leads to an over-density of grains with radii around the "second peak". The overabundance of these grains is shifted from $\sim 100\,\mu$m (high material strength) to $\sim 1000\,\mu$m (very low material strength).

These successive domino effects (Thébault and Augereau, 2007) propagate the local maximum in the grain size distribution toward bigger sizes and leave a unique characteristic wavy size distribution with a pronounced succession of over-densities and depletions (e.g., Campo Bagatin et al., 1994; Thébault and Augereau, 2003; Krivov, Löhne, and Sremčević, 2006; Thébault and Augereau, 2007). Finally, the amplitude of the depletion of sub-mm grains reaches its maximum for the lowest material strength. As a result, the wavy pattern of the grain size distribution becomes deeper and broader for low material strengths. These results resemble the finding of Krivov, Löhne, and Sremčević (2006) and Thébault and Augereau (2007).

In Fig. 5.2, the dust grain size distributions at the periastron and apastron of debris disks with different levels of dynamical excitation ($\Delta e_{\rm b}$ = 0.05, 0.1, and 0.2) are investigated. Again, one finds that the size distribution converges toward a quasi steady-state wave pattern, whose characteristics depend on the collisional evolution. However, note that these size distributions (Fig. 5.2) do not converge toward the same large grain radii (~ 0.1 km) for different levels of dynamical excitation $\Delta e_{\rm b}$ as for varying the material strength (Fig. 5.1). If planetesimal belts are more dynamically excited, the number density is – on average – decreased. Thus, the ring widths are different and so are the peak densities.

One finds that the wavy grain size distribution in highly dynamically excited disks, for instance, in the $\Delta e_{\rm b} = 0.2$ regime, becomes shallower and narrower (see Fig. 5.2). For the high-excitation case (broad dispersion of the eccentricities of parent belt bodies that is higher $\Delta e_{\rm b}$) the depletion of small grains is less pronounced. However, it is propagated to larger grain sizes. Thus, the depletion of sub-mm grains in the case of highly dynamical excited disks is more pronounced which is similar to the case of the low material strength. In contrast, for the low-excitation case (narrow dispersion of the eccentricities of parent belt bodies that is lower $\Delta e_{\rm b}$), the depletion of small grains is even more pronounced. Thus, the depletion of sub-mm grains is less pronounced similar to the case of the high material strength. Smaller size particles are strongly affected by the stellar radiation force, which makes their orbits eccentric and their collisional velocities higher. As a result, the collisional lifetimes of small dust grains only weakly vary with the level of dynamical excitation. Thus, the role of destructive collisions for smaller particles becomes less important (Thébault and Augereau, 2007; Thébault and Wu, 2008).

Note that this effect results in the second peak in the grain size distribution which is shifted toward larger grains corresponding to a low-excitation case (Thébault and Wu, 2008). Thus the second peak is shifted toward larger grain sizes for smaller values of $\Delta e_{\rm b}$ (Fig. 5.2). In contrast, the rate at which large grains are produced by impacts between much larger planetesimal-sized objects strongly depends on the level of dynamical excitation. Thus, a high dynamical excitation leads to a depletion of grains with radii $> 40\ \mu$m and an increased overabundance of smaller grains close to the blowout size (see Fig. 5.2). Consequently, the final size distribution reflects both effects: a more pronounced depletion of sub-mm grains and a shift of the second peak toward smaller grain sizes with increasing dynamical excitation Δe_b.

The stirring level in the planetesimal belt and material strength of grains determine the degree of "destructiveness" of collisions (Matthews et al., 2014). Thus, these parameters strongly affect the grain size distribution. Decreasing the material strength has a stronger impact on the grain size distribution than an increased dynamical excitation Δe_b (see Figs. 5.1 & 5.2).

In addition, at large grain sizes around 0.1 km, a change in the slope ("knee") of the size distribution is expected (Campo Bagatin et al., 1994; Durda, Greenberg, and Jedicke, 1998; O'Brien and Greenberg, 2005; Thébault and Augereau, 2007). This is due to the transition from the strength-dominated regime, where the resistance of colliders to impacts decreases with increasing grain size, to the gravity-dominated regime, where the resistance quickly increases with increasing grain size (Durda & Dermott 1997). In the simulations, that knee is only pronounced in very destructive circumstances that is for the lowest material strength considered (at $a \sim 0.4$ km; see Fig. 5.1). For higher material strengths, the evolution time of 10 Myr was too short to sufficiently converge the size distribution to a steady state.

Since the cratering effect was not included in previous models (e.g., Krivov et al., 2007; Löhne, Krivov, and Rodmann, 2008), wavy patterns were present that were much more pronounced compared to the results from this study. Thus, one can deduce that the cratering impact smoothens wavy patterns. Also, a large fraction of the sub-mm grain depletion is due to cratering impacts (see also Thébault and Augereau, 2003; Thébault and Augereau, 2007; Müller, Löhne, and Krivov, 2010). Indeed, small grains of a few µm cannot directly break-up objects larger than ~ 1mm (around the second peak), even with their increased impact velocities. However, the results show that they can gradually erode much bigger grains efficiently.

5.3.2 SED

The influence of different geometries and collisional factors on the resulting SED is investigated. The infrared to the sub-mm wavelength range is chosen because the offset from the stellar photospheric SED is largest in this region.

1. Dependence on the eccentricity and dynamical excitation Löhne et al. (2017) found that the eccentricity of parent belts affects their SED only weakly. Similarly, one finds only a weak influence of the combination of the geometrical offset and collisions on the overall SED for different eccentricities, assuming the reference material strength ($Q_\mathrm{s} = 5 \times 10^2$ J/kg; see Fig. 5.3). The most noticeable change of the SED is the slight increase of the scattered flux with increasing eccentricity in the near-IR wavelength range. Around a wavelength of 10 µm, the difference of fluxes between eccentricities $e_\mathrm{b} = 0.0$ and $e_\mathrm{b} = 0.4$ reaches its maximum because smaller grains can survive at the apastron side in highly eccentric disks (the different blow-out limits on periastron and apastron side; see Eq. 2). However, the circumstellar dust is hardly detectable through photometric measurements because the stellar photosphere is brighter by a factor of 10^5 to 10^7. At wavelengths of ~ 30-50 µm, the thermal re-emission of the dust exceeds the direct stellar radiation, increasing by up to 30% with increasing eccentricity of parent belt.

Fig. 5.3 also depicts the influence of different levels of dynamical excitation Δe_b. The most noticeable change of the SED is the increase of the scattered flux with increasing the level of dynamical excitation in the near to mid-IR wavelength range. However, again it is hardly detectable through photometric measurements in this wavelength range. Increasing the level of dynamical excitation of eccentric parent belts the disk emission increases by up to

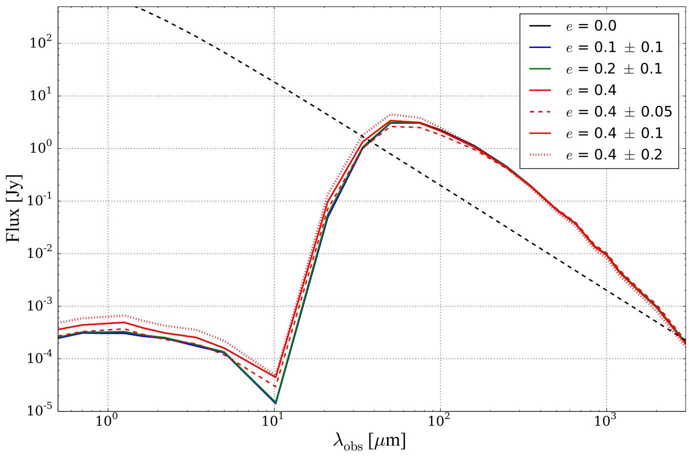

FIGURE 5.3: The spectral energy distribution for systems with different eccentricities (e_b = 0.0, 0.1, 0.2, and 0.4) and dynamical excitations (Δe_b = 0.05, 0.1, and 0.2). The dashed black line represents the photospheric emission of the central star

TABLE 5.2: A total surface area of the dust S_{total} in three different size bins resulting from the collisional evolution for different material strengths.

Q_D^* regime	$\frac{S_{total}\ (a_{dust}[\mu m] < 6)}{S_{total}\ (a_{dust}[\mu m] < 1000)}$	$\frac{S_{total}\ (15 < a_{dust}[\mu m] < 200)}{S_{total}\ (a_{dust}[\mu m] < 1000)}$	$\frac{S_{total}\ (200 < a_{dust}[\mu m] < 1000)}{S_{total}\ (a_{dust}[\mu m] < 1000)}$
very high	39.6 [%]	8.6 [%]	11.0 [%]
high	67.8 [%]	4.1 [%]	6.7 [%]
ref	72.1 [%]	2.4 [%]	4.9 [%]
low	78.9 [%]	0.5 [%]	2.3 [%]
very low	81.6 [%]	0.2 [%]	0.7 [%]

56% at 30-50 μm.

These results are easily explained from the dynamical point of view. Higher eccentricities and an increasing level of dynamical excitation increase the mutual collisional velocities. The efficiency of the collisional cascade is increased resulting in a higher dust production rate. Consequently, the disk appears brighter in those regions where the above effect is strongest.

2. Dependence on the material strength Fig. 5.4 depicts the influence of the combination of geometrical offset and collisions on the overall SED for different the catastrophic disruption threshold Q_D^* (material strengths $Q_s = 1.25 \times 10^4$, 2.5×10^3, 5×10^2, 1×10^2, and 0.2×10^2 J/kg, fixed eccentricity $e_b = 0.4$). In comparison to the results shown in Fig. 5.3, variations of the material strength have a more pronounced effect on the SED than the variation of the eccentricity. The flux at optical to mid-IR wavelengths increases with decreasing material strength. Thus the more destructive collisional systems show higher fluxes at wavelengths ≤ 80 μm. In contrast, the flux at sub-mm wavelengths decreases with decreasing material strength. The deeper and broader wavy pattern of the grain size distribution for low material strengths (see Fig. 5.1) results in the slope of the SED in this range becomes flatter. However, the SEDs in these wavelength ranges have similar spectral indices which makes it hardly possible to constrain the material strength from the analysis of the SED alone.

To analyze this finding, the contributions of the dust within different size ranges to the resulting SED, which is relevant for the optical appearance (see Table 5.2) are compared. One finds a larger surface fraction of grains with radii < 6 μm that is grains which mostly contribute to the SED at optical to mid-IR wavelengths, with decreasing material strength (second column in Table 5.2). For lower material strengths, the increased production of small

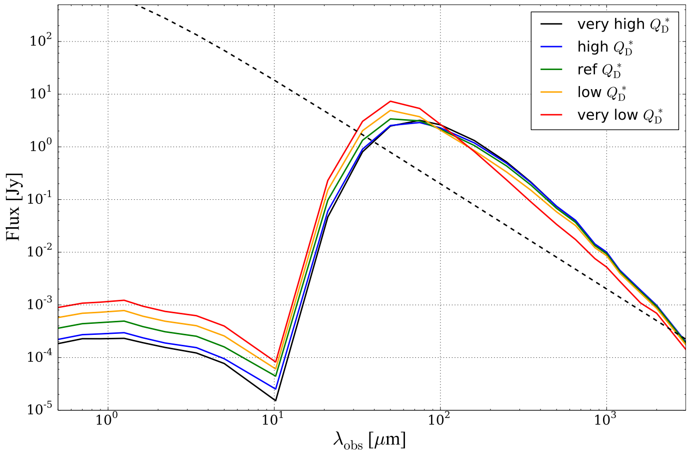

FIGURE 5.4: The spectral energy distribution for systems with different material strengths. The dashed black line represents the photospheric emission of the central star.

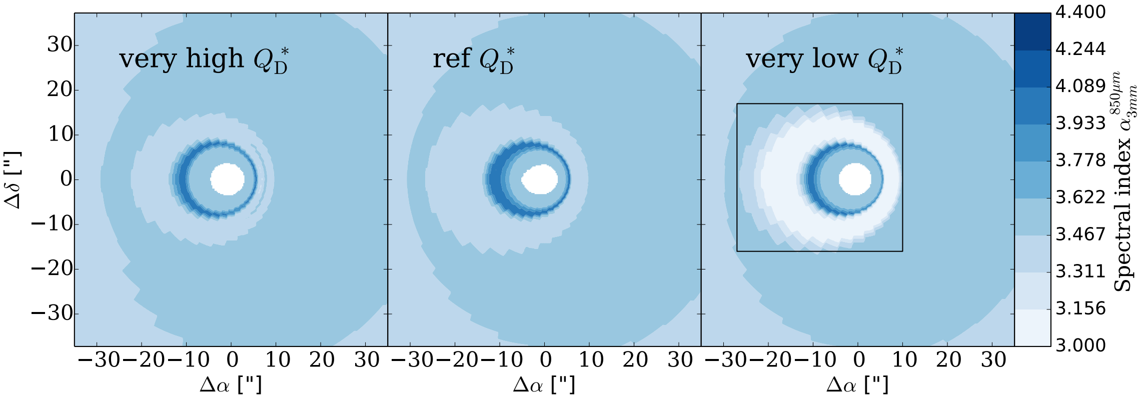

FIGURE 5.5: The spectral index $\alpha_{3\text{mm}}^{850\mu\text{m}}$ map for different material strengths ($e_b = 0.4$). Note the low spectral index in the birth ring close to the central star (black square box) in the case of the very low material strength.

grains result in an increase of the SED at these wavelengths. However, note that surface fraction differences between other collisional regimes are getting smaller because the small grains are more easily affected by stellar radiation. For grains of intermediate size (15 µm < a_{dust} < 200 µm; third column in Table 5.2) that is grains which mostly contribute to the SED at far-IR to sub-mm wavelengths one finds the opposite trend. Less destructive collisional systems, corresponding to the higher material strengths, result in higher fluxes in this wavelengths regime. However, because of the marginal change of the slope of the SED in this range, it is not possible to quantify the material strength from pure photometric measurements. The net surface fraction of dust grains with radii > 200 µm is sufficiently large to not to be affected by the stellar radiation pressure (fourth column in Table 5.2). Thus, collisions become more important here.

The second most obvious difference of the SEDs of disks with different material strengths is the change of the location of their maximum. They are not only shifted from 50 µm for very low material strengths toward ~ 70 µm for very high material strengths (i.e., for the systems with fewer destructive collisions). They also show an increase of the peak flux with decreasing material strength.

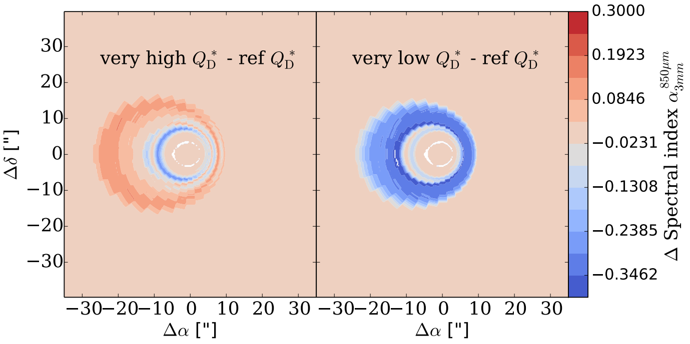

FIGURE 5.6: Differences between the spectral index $\alpha_{3\text{mm}}^{850\mu\text{m}}$ maps for the very high material strength (left) and the very low material strength (right) and the reference case (see Figure 5 for comparison).

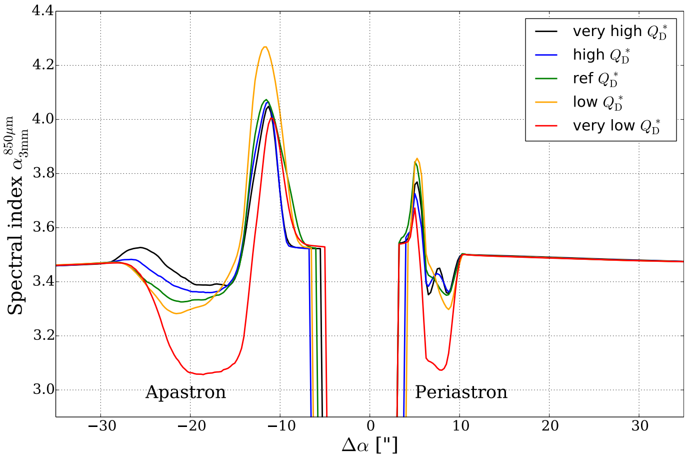

FIGURE 5.7: The radial cut of the spectral index $\alpha_{3\text{mm}}^{850\mu\text{m}}$ map for different material strengths ($e_\text{b} = 0.4$) along $\Delta\delta = 0$ (see Figure 5 for comparison). The left and right side of this figure indicates apastron and periastron side of the disks.

5.3.3 Spatially resolved observations

In Sect. 5.3.2, the dependence between the SED and the varying collisional parameters, for example, dynamical excitation Δe_b and material strength Q_s is discussed. However, as the SED is a representation of net fluxes integrated over the entire disk, now spatially resolved images and derived quantities, which potentially provide a wealth of additional information, are investigated.

Spectral index map

The analysis with the sub-mm spectral index $\alpha_{3\text{mm}}^{850\mu\text{m}}$, based on the fluxes at 850 µm and 3 mm of the observed disks as a function of the material strength for a fixed belt eccentricity $e_\text{b} = 0.4$ (see Fig. 5.5 & 5.7) is considered. In addition, Fig. 5.6 depicts the difference between the spectral index $\alpha_{3\text{mm}}^{850\mu\text{m}}$ for the very low and very high material strengths, which indicates the location where large grains (small grains) are more abundant than in the reference case.

One finds that the spectral index at larger distances hardly depends on the material strength. Radiation pressure is acting most efficiently on small grains, pushing them to larger distances. Therefore, one finds a relatively large fraction of small particles in the outer regions. Consequently, the spectral index is higher at larger distances than around periastron and apastron. Different blowout limits (see Eq. 2), depending on the different locations under which grains are launched from different sites along the parent belts (e.g., around periastron and apastron), shape the local size distributions and eventually result in the asymmetries seen in the halos (Lee and Chiang, 2016; Löhne

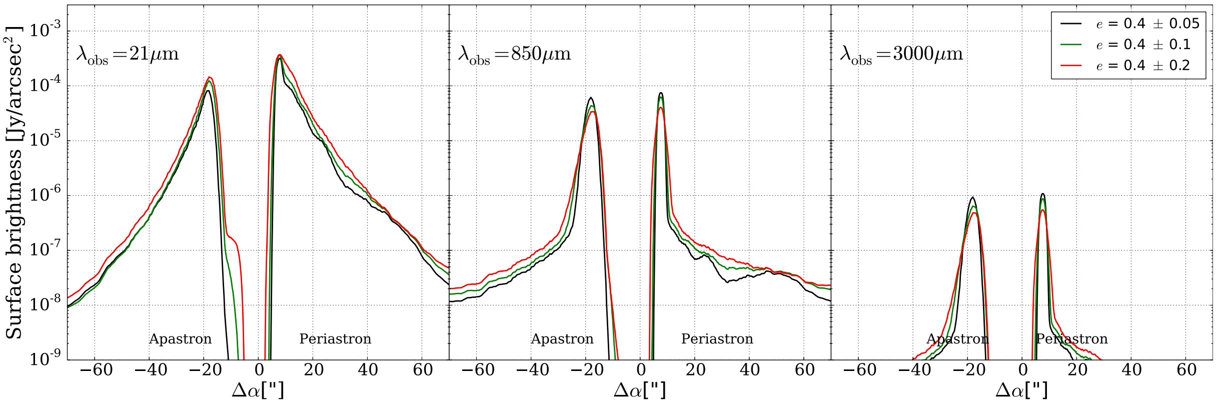

FIGURE 5.8: The radial surface brightness profile as a function of dynamical excitations (Δe_{b}) at wavelengths λ_{obs} = 21 μm, 850 μm, and 3000 μm.

et al., 2017). In consequence, the halo of the periastron side is much more extended than the halo of the apastron side (see Fig. 5.5 & 5.7). However, the halo is typically too faint to allow measuring its (sub-)mm spectral index (Löhne et al., 2017).

In contrast, the spectral index in the region around the parent belt strongly depends on the material strength. Fig. 5.7 illustrates the radial cut of the spectral index around apastron (at right ascension $\Delta\alpha \sim$ -20", declination $\Delta\delta \sim 0$") and periastron (at $\Delta\alpha \sim 8$", $\Delta\delta \sim 0$"). One would expect an increased amount of smaller grains in the case of smaller material strengths. However, Fig. 5.5 (right plot), Fig. 5.6 (right plot), and see Fig. 5.7 (red line) show the opposite behavior that is a lower spectral index in the case of a very low material strength. At λ_{obs} = 850 μm, the radiation is dominated by grains with a characteristic grain size (Backman and Paresce, 1993) $a_{\mathrm{c}} \approx \lambda_{\mathrm{critical}}/2\pi \approx 145$ μm ($\beta \approx 0.0146$), while grains with $a_{\mathrm{c}} \approx 450$ μm ($\beta \approx 0.0047$) dominate the emissions at λ_{obs} = 3000 μm. Fig. 5.1 shows that grains with radii ~ 450 μm are overabundant by a factor of 1.5 compared to grains with radii ~ 145 μm in the case of the very low material strength, eventually causing the observed lower spectral index in the case of the very low material strength.

Spatially resolved disk images

In this section, impacts of collisional parameters, for instance, eccentricities e_{b}, dynamical excitation Δe_{b}, and the material strength Q_{s} on spatially resolved images and their radial surface brightness profiles from near-IR to sub-mm wavelengths are discussed.

1. Dependence on the belt eccentricity and dynamical excitation The panels in Fig. B.1 show simulated observations of spatially resolved disks at different belt eccentricities (e_{b} = 0.2 and 0.4), different levels of dynamical excitation (Δe_{b} = 0.05, 0.1, and 0.2) for the reference material strength Q_{s} at wavelengths λ_{obs} = 2.2 μm, 21 μm, 160 μm, 850 μm, and 3000 μm. Both scattered and thermal re-emission radiation are considered. Grains which contribute to the near-IR flux are the smallest within the entire distribution and thus most sensitive to the strong radiation pressure from the central star. Consequently, debris disks are featureless in this wavelength range. In contrast, the larger grains which are dominating the appearance (emission) at sub-mm wavelengths are only weakly affected by radiation pressure allowing the parent ring to be traced in this wavelength range.

In Fig. 5.8, radial surface brightness profiles are shown for different levels of dynamical excitation (Δe_{b} = 0.05, 0.1, and 0.2) of belt eccentricities e_{b} = 0.4 at wavelengths λ_{obs} = 21 μm, 850 μm, and 3000 μm, assuming the

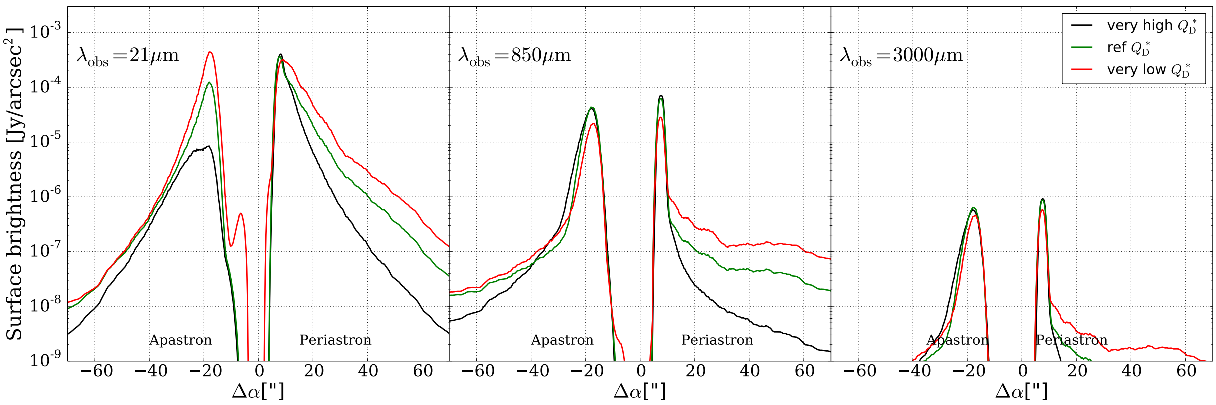

FIGURE 5.9: The radial surface brightness profile as a function of the material strength; belt eccentricity $e_b = 0.4$; $\lambda_{obs} = 21$ µm, 850 µm, and 3000 µm; $\Delta\delta = 0$.

reference material strength. As outlined in Section 5.3.3, the abundance of the smaller particles on the periastron side is reduced. Therefore, the surface brightness is dominated by the large grains on the periastron side, whereas on the apastron side the smaller grains are the dominant population. Thus, if there are more destructive collisions, for instance, due to higher eccentricities or higher dynamical excitations, the production rate of small particles is increased on the apastron side (see Fig. 5.2). This situation is depicted in the simulated surface brightness profile at $\lambda_{obs} = 21$ µm. In the case of a higher dynamical excitation ($\Delta e_b = 0.2$) a brighter apastron side is observed than at lower dynamical excitation ($\Delta e_b = 0.05$).

The abundance of small dust grains is also subject to further forces and effects, including Poynting-Robertson effect and stellar drag forces (e. g., Wyatt et al., 1999; Löhne et al., 2017). For example, disks with a higher dynamical excitation show a higher production rate. Furthermore, smaller particles are most efficiently affected by Poynting-Robertson drag. Consequently, the inner regions of dynamically excited debris disks appear more empty if observed at larger wavelengths as compared to observations at shorter wavelengths (tracing these smaller particles). In addition, Fig. 5.8 also shows that the higher dynamical excitation of the planetesimal belt come along with the increased overall brightness of the halo.

2. Dependence on the material strength The panels in Fig. B.2 show simulated observations of spatially resolved disks as a function of the material strength Q_s at wavelengths $\lambda_{obs} = 2.2$ µm, 21 µm, 160 µm, 850 µm, and 3000 µm ($e_b = 0.4$). Both scattered and thermal re-emission radiation are considered. The different appearances are due to the different spatial and size distribution of the dust resulting from simulated collisional evolutions with different material strengths (Fig. 5.1).

As the periastron side of disks is closer to the star, one could expect that it is always brighter than the apastron side due to the higher dust temperatures and a higher rate of scattered radiation. However, as the particles travel more slowly and hence spend more time at the apocenter, an eccentric disk should be denser in this region (see Eq. 1). Furthermore, a very low material strength amplifies the increased rate of dust production. Thus, destructive collisions may reverse the situation of "pericenter glow" to an "apocenter glow". This can indeed be seen in Figs. 5.9, 5.10, and 5.11, where the brightness of the apastron side increases toward low material strengths. At sub-mm wavelengths ($\lambda_{obs} \geq 0.5$ mm), far from the wavelength of the maximum emission, the impact of the dust temperature on the brightness distribution of the disk is reduced. Consequently, the effect of the pericenter glow is reduced. Instead, the impact of the dust number density on the surface brightness becomes more important. A complementary effect has been recently studied by Pan, Nesvold, and Kuchner (2016) and MacGregor et al. (2017). They found that azimuthal temperature asymmetries, due to disk offset, could be compensated by azimuthal asymmetries in the dust

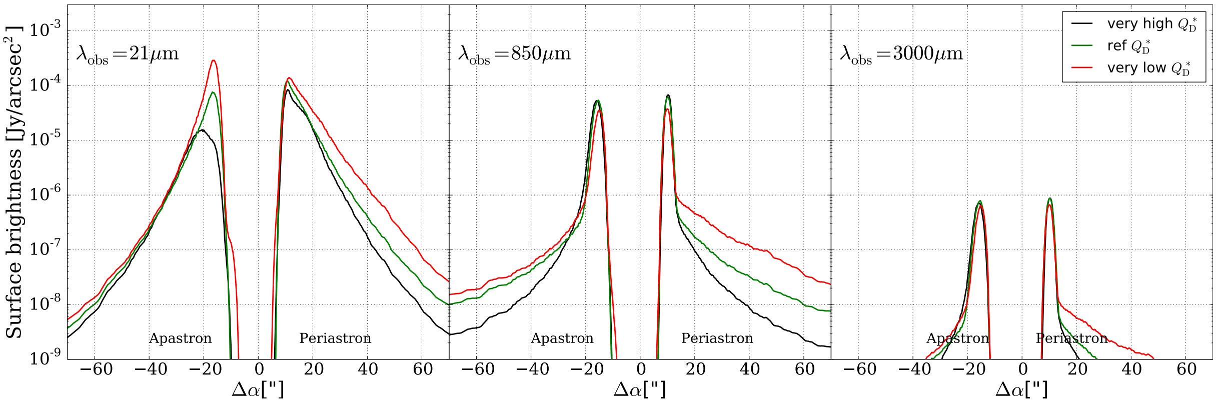

FIGURE 5.10: The radial surface brightness profiles as a function of material strength; belt eccentricity $e_b = 0.2$; $\lambda_{obs} = 21$ µm, 850 µm, and 3000 µm; $\Delta\delta = 0$.

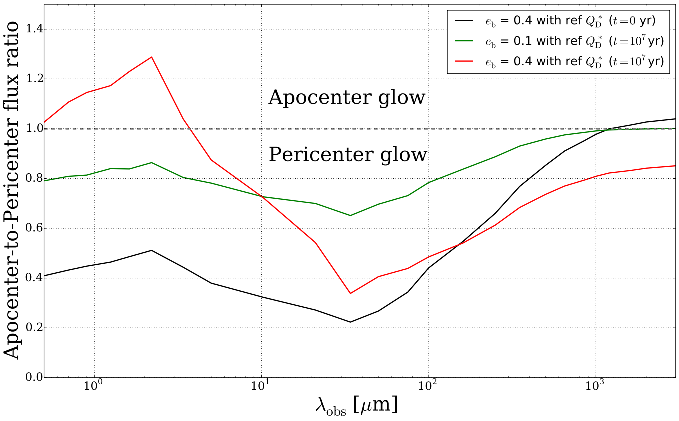

FIGURE 5.11: The wavelength-dependence of the apocenter-to-pericenter flux ratio as a function of eccentricity. Black line: no collisions (t = 0 yr) with $e_b = 0.4$, ; green line: collisional evolution (t = 10^7 yr) $e_b = 0.1$; red line: collisional evolution (t = 10^7 yr) $e_b = 0.4$.

density.

In contrast, in the case of an increase of the material strength, the grain size distribution is critically changed by collisions (see Fig. 5.1). Thus, for very high material strengths, the surface brightness differences (asymmetries) are increased. Consequently, the pericenter glow phenomenon is even more pronounced for higher material strengths.

At shorter observing wavelengths λ_{obs}, different material strengths Q_S seem only to result in a change of the brightness distribution at the apocenter (see Fig. 5.9), while the brightness distribution at the pericenter remains almost unchanged. However, the comparison at large distances that is the halo, different material strengths result in a significant change of the brightness distribution in the halo on the periastron side. At longer observing wavelengths λ_{obs}, the impact of collisions becomes less important. Only the halo regions show differences in the brightness distribution. This behavior is in agreement with the findings outlined in Section. 5.3.3: higher collisional rate results in an increased overall brightness of the halo.

At shorter observing wavelengths (see e.g., left panel of Fig. 5.9) one finds again that smaller particles are abundant in the inner regions of the apastron sides due to the Poynting-Robertson drag force. In contrast, at longer observing wavelengths, inner regions appear void. In conclusion, one finds that the higher collisional activity is responsible for symmetrizing their halo, changing the asymmetry of the peak of parent belts and even filling inner regions with a large fraction of smaller grains.

Fig. 5.10 shows the wavelength-dependent radial brightness profiles for different collisional evolutions for a belt eccentricity $e_b = 0.2$ at wavelengths λ_{obs} = 21 µm, 850 µm, and 3000 µm. One finds that the effects observed for

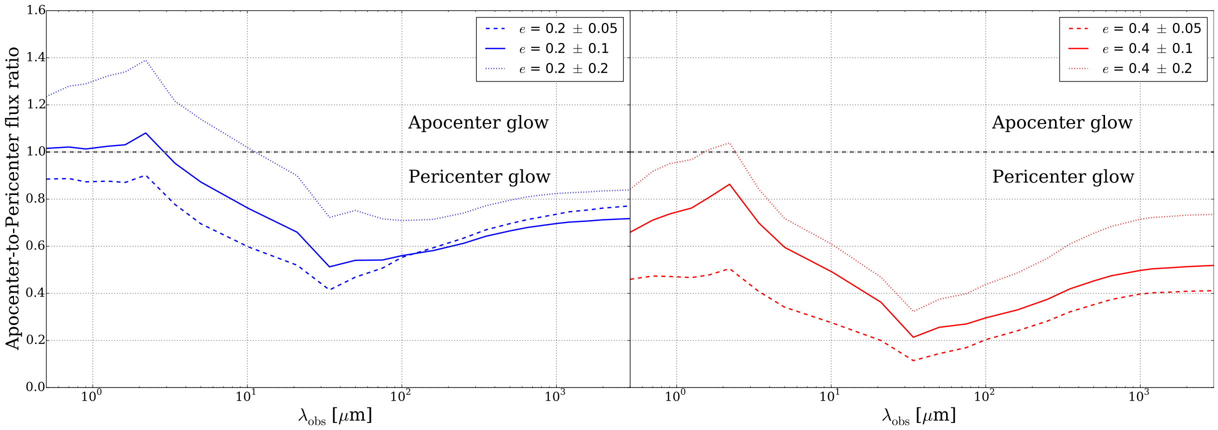

FIGURE 5.12: The wavelength-dependence of the apocenter-to-pericenter flux ratio as a function of dynamical excitation (Δe_b = 0.05, 0.1, and 0.2) for eccentricities e_b = 0.2 (left) and e_b = 0.4(right)

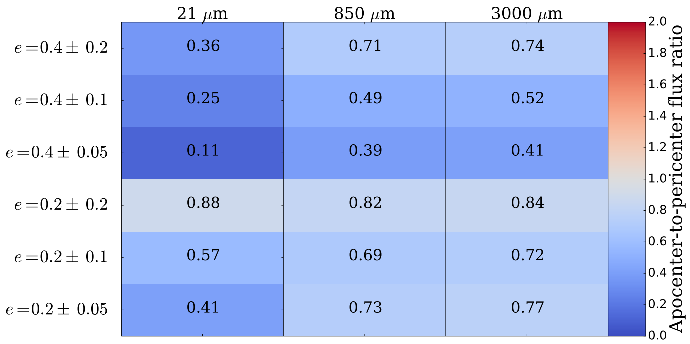

	21 μm	850 μm	3000 μm
e =0.4± 0.2	0.36	0.71	0.74
e =0.4± 0.1	0.25	0.49	0.52
e =0.4± 0.05	0.11	0.39	0.41
e =0.2± 0.2	0.88	0.82	0.84
e =0.2± 0.1	0.57	0.69	0.72
e =0.2± 0.05	0.41	0.73	0.77

FIGURE 5.13: The apocenter-to-pericenter flux ratio for different observing wavelengths λ_{obs} (21 µm, 850 µm, and 3000 µm) as a function of dynamical excitation Δe_b (reference material strength). The number in each box indicates the apocenter-to-pericenter flux ratio.

the belt eccentricity e_b = 0.4 and lower material strength, for instance, the apocenter glow, are still present and more pronounced in the disk with a belt eccentricity e_b = 0.2 and lower material strength.

5.3.4 Constraining collisional parameters from observational quantities

In this section, the potential to constrain the collisional parameters from the observational quantities of debris disks is summarized.

1. Belt eccentricity e_b Fig. 5.11 depicts the apocenter-to-pericenter flux ratio as a function of wavelength for systems before and after the collisional evolution. One finds that collisions have the potential to reduce the pericenter glow at shorter wavelengths. Furthermore, azimuthal asymmetries in the surface brightness at sub-mm wavelengths, which result from an increased dust density at the apastron side (Pan, Nesvold, and Kuchner, 2016; MacGregor et al., 2017), are decreased due to collisions.

For two different belt eccentricities (e_b = 0.1 and 0.4) but the same level of dynamical excitation (Δe_b = 0.1), the situation is more complicated. The apocenter-to-pericenter flux ratio in the case of e_b = 0.1 is nearly constant for all wavelengths. In contrast, the apocenter-to-pericenter flux ratio for e_b = 0.4 is varying, which is due to the different size distributions at the apocenter and pericenter. For e_b = 0.1 the grain size distribution at periastron and apastron is much shallower and broader than for e_b = 0.4. This is not only due to the large number of smaller dust grains that survive at the apastron side of debris disks. It is also because more destructive collisions lead to an over-density of smaller particles and a depletion of larger particles. As a result, the pericenter glow phenomenon is

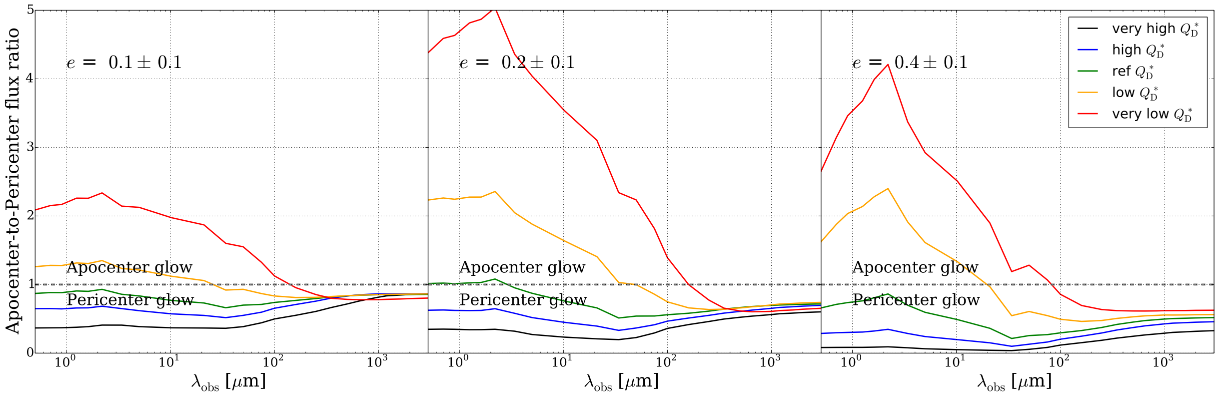

FIGURE 5.14: The wavelength-dependence of the apocenter-to-pericenter flux ratio as a function of eccentricity e_b and material strength Q_s.

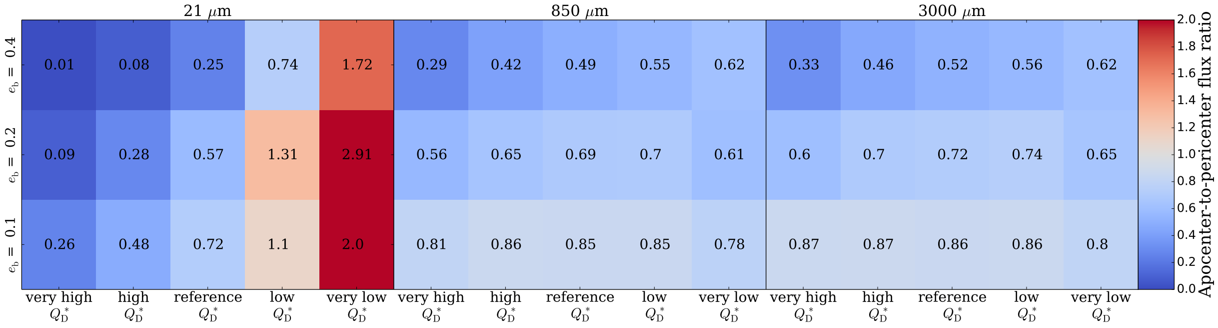

	21 μm					850 μm					3000 μm				
	very high $Q_{\rm D}^*$	high $Q_{\rm D}^*$	reference $Q_{\rm D}^*$	low $Q_{\rm D}^*$	very low $Q_{\rm D}^*$	very high $Q_{\rm D}^*$	high $Q_{\rm D}^*$	reference $Q_{\rm D}^*$	low $Q_{\rm D}^*$	very low $Q_{\rm D}^*$	very high $Q_{\rm D}^*$	high $Q_{\rm D}^*$	reference $Q_{\rm D}^*$	low $Q_{\rm D}^*$	very low $Q_{\rm D}^*$
e_b = 0.4	0.01	0.08	0.25	0.74	1.72	0.29	0.42	0.49	0.55	0.62	0.33	0.46	0.52	0.56	0.62
e_b = 0.2	0.09	0.28	0.57	1.31	2.91	0.56	0.65	0.69	0.7	0.61	0.6	0.7	0.72	0.74	0.65
e_b = 0.1	0.26	0.48	0.72	1.1	2.0	0.81	0.86	0.85	0.85	0.78	0.87	0.87	0.86	0.86	0.8

FIGURE 5.15: The wavelength-dependence of the apocenter-to-pericenter flux ratio for selected values of the eccentricity e_b and material strength Q_s. The number in each box indicates the apocenter-to-pericenter flux ratio. The case of the apocenter-to-pericenter flux ratio > 1 is discussed as the apocenter glow phenomenon in Sect. 5.3.4

reduced at shorter observing wavelengths and increased at longer observing wavelengths in debris disks with higher belt eccentricities (e.g., $e_b = 0.4$).

2. Dynamical excitation Δe_b Fig. 5.12 & 5.13 depict the wavelength-dependent apocenter-to-pericenter flux ratio for different levels of dynamical excitation ($\Delta e_b = 0.05$, 0.1, and 0.2) of different belt eccentricities ($e_b = 0.2$ and 0.4). For the case of $e_b = 0.2$, one finds the apocenter glow phenomenon at shorter wavelengths in the case of the reference and higher dynamical excitation level ($\Delta e_b = 0.1$ and 0.2). The main reasons for this behavior are the proximity of the star to the apastron side and a higher rate of dust production due to higher relative velocities compared to the case of lower dynamical excitation level. For the case of $e_b = 0.4$, the minimum of the apocenter-to-pericenter flux ratio is smaller than in the case of the disk with $e_b = 0.2$ disks that is the more eccentric belt shows a stronger pericenter glow. The temperature dependence due to the proximity to the star is dominating this behavior over the higher production rate of smaller particles.

At short wavelengths, one finds again a decrease of the pericenter glow phenomenon with increasing Δe_b (see also Fig. 5.8). At long wavelengths, the basic trend is similar but one finds that the spread in observed flux ratios is much narrower. In the less dynamically excited case, for instance, $\Delta e_b = 0.05$ for $e_b = 0.2$, higher densities on the apastron sides can weaken the pericenter glow phenomenon. In conclusion, collisional parameters can be best constrained through observations of highly eccentric belts at short wavelengths

3. Material strength Q_s Figs. 5.14 & 5.15 show the wavelength-dependent apocenter-to-pericenter flux ratio for different material strengths Q_s and different belt eccentricities ($e_b = 0.1$, 0.2, and 0.4). First of all, one finds that the material strength and eccentricity are degenerate to a large degree. For all eccentric parent belts ($e_b = 0.1$, 0.2, and 0.4), one finds that a decrease of the pericenter glow phenomenon with the decreasing material strength. As described in 5.3.4, the pericenter glow phenomenon is replaced by the apocenter glow phenomenon in the case of the lower material strengths.

Furthermore, the influence of the material strength is strongest at short wavelengths. The mid-IR images show the apocenter glow phenomenon as long as the material strength is below its reference value. Thus, it is clear that a smaller material strength results in the higher asymmetry in surface brightness and density. In contrast, the pericenter glow phenomenon is increased for the higher material strengths with decreasing eccentricity of the parent belts. At longer wavelengths (sub-mm/mm), the dominating grains are not significantly affected by the stellar radiation pressure anymore that is the apocenter-to-pericenter flux ratio becomes insensitive to details of the underlying collisional evolution.

5.4 Summary

Impacts of collisional parameters, for instance, belt eccentricity e_{b}, dynamical excitation Δe_{b}, and the material strength Q_{s}, on the observational appearance of eccentric debris disks, are studied. We have found surface brightness asymmetries that are caused by the combined effects of collisions and radiation pressure. The key results are as follows:

1. An increasing belt eccentricity of the debris disk system leads to the survival of a large number of smaller dust grains on the apastron side. Thus the "pericenter glow" phenomenon is reduced with decreasing material strength at shorter observing wavelengths. However, the geometrical parameters describing the debris disks system that is the proximity of the star to the apastron side, must be considered as well.
2. An increasing level of dynamical excitation in the eccentric parent belt of the debris disk system leads to a higher production rate of smaller particles and depletion of sub-mm grains. Consequently, the "pericenter glow" is reduced.
3. A decreasing material strength results in a higher production rate of smaller particles, which reduces the surface brightness differences between periastron and apastron. For very low material strengths, the pericenter glow phenomenon is reduced and eventually even replaced by the opposite effect, the apocenter glow in the near to mid-IR wavelength range. In contrast, an increasing material strength results in an increase of asymmetries in the surface brightness distribution.
4. The wavelength-dependent apocenter-to-pericenter flux ratio at short wavelengths is increased in the case of a higher efficiency of destructive collisions, caused by increasing dynamical excitation of the belt or decreasing material strengths. This effect is less pronounced at sub-mm wavelengths. Within the considered parameter space, the impact of the material strength Q_{D}^{*} on the appearance of the disk is stronger than that of dynamical excitation of the belt.
5. The SED alone does not provide unique constraints on the collisional parameters considered. Thus, deriving unique constraints for the impact of considered collisional parameters based on the SED alone is hardly possible.

Chapter 6

Constraining the detectability of water ice in debris disks

This chapter presents the results published in Kim et al. (2019). The author of this dissertation performed the simulated observations of the results and made major contributions to the write-up and interpretation of the results. Other parts of this study were done in collaboration with Sebastian Wolf, Alexey Potapov, Harald. Mutschke, and Cornelia Jäger.

Water ice (hereafter referred to as "ice") is assumed to play an important role during planet formation (Thommes and Duncan, 2006; Min et al., 2011). The ice is thought to immediately sublimate in the hot inner regions of circumstellar disks, therefore it is expected to be present only beyond the ice sublimation front, the so-called snow line. Consequently, the formation of the planetary core in the core formation or gas capture scenario is significantly affected by the freeze-out of water onto dust grains (Stevenson, 1982; Hubickyj, Bodenheimer, and Lissauer, 2005). Furthermore, at later stages of the formation and early evolution of planetary systems, icy planetesimals, icy pebbles, or cometary objects may deliver water to rocky planets (Morbidelli et al., 2000; Raymond, Quinn, and Lunine, 2004; Nagasawa et al., 2007; Woitke, Kamp, and Thi, 2009; Woitke et al., 2009) and also to the innermost part of the remaining disk (Eisner, 2007). Understanding the origin and transport of water to Earth finally is of key importance for deciphering the conditions during the early evolution of life.

The OH stretching vibrational modes are active for cation-bonded hydroxyl groups within H_2O molecules (and minerals at the surface of refractory grains) around 3 µm, which is active when H_2O is present as ice (Beck et al., 2011; Whittet et al., 1996). The observation of the 3 µm ice feature therefore is the main target for ice detection in astrophysical environments. In addition, transverse optical and longitudinal acoustic vibrational modes are active around 44 µm and 62 µm, respectively (Bertie and Whalley, 1967; Omont et al., 1990; Smith et al., 1994; Dartois et al., 1998). An observation of these ice features, for instance, 44 µm and 62 µm, would therefore provide crucial evidence and possible constraints for the presence and properties of ice as well.

In various protoplanetary disks, the ice features at 3 µm, 44 µm, and 62 µm have been detected and analyzed (Pontoppidan and Dullemond, 2005; Terada et al., 2007; Honda et al., 2009; Schegerer and Wolf, 2010; Aikawa et al., 2012; Molinari et al., 1999; Malfait et al., 1999; McClure et al., 2012; McClure et al., 2015). However, only the detection of the 62 µm ice feature has so far been inferred in debris disks (Chen, Fitzgerald, and Smith, 2008). An observational understanding of the spatial distribution of icy grains is therefore in its infancy, and even the presence of ice in debris disks is hardly established observationally.

Next-generation observatories are expected to allow making significant progress on the understanding of the ice distribution in debris disks. Combined observations of JWST/NIRCam (James Webb Space Telescope/Near Infrared Camera; aiming for observations at wavelengths from 0.6 µm to 5 µm, STScI, 2017) and ELT/METIS (Extremely

Large Telescope/The Mid-Infrared E-ELT Imager and Spectrograph; aiming for observations at wavelengths from 3 µm to 20 µm, Brandl et al., 2018) are expected to play a leading role in confirming the presence (or absence) of ice in debris disks. In addition, SPICA/SAFARI (Space Infrared telescope for Cosmology and Astrophysics/SpicA FAR-infrared Instrument; aiming for observations at wavelengths from 34 µm to 230 µm, Jellema et al., 2017) will potentially contribute to the understanding of ice in debris disks.

The goal of this study is to answer the key question of the observational requirements either to constrain the detectability of ice in debris disks or to provide useful limits for the existence, properties, and spatial distribution of ice in debris disks. For this purpose, a numerical feasibility study assuming various fractional ratios of ice, porosities, and shapes of aggregates of icy dust mixtures in debris disks have conducted. Subsequently, whether selected instruments or observatories that will become available in the near future, such as the JWST/NIRCam and SPICA/SAFARI, will indeed allow contributing to answering this question is investigated.

This Chapter is organized as follows: In Section 6.1 the underlying physics related to ice depletion in debris disks is described. In Section 6.2 the typical reference debris disks model in this work is depicted. In Section 6.3 the influence of icy dust parameters on the resulting SEDs and spatially resolved images of debris disks system is investigated. In addition, the boundary of the ice reservoir that is referred to as the "ice survival line" in the following (in contrast to the term "snow line", which is used to characterize the region where gas begins to freeze out onto dust grains in gas-rich protoplanetary disks) is predicted. Finally the detectability of icy dust grains with future observatories is evaluated and constrained. The findings in this work are summarized in Section 6.4.

6.1 Depletion of ice in debris disks

Sublimation If icy grains (at least partially) drift radially inward due to the PR drag (Poynting, 1903; Robertson, 1937), they pile up and form a ring: their inward drift is suppressed by stellar radiation pressure when the ratio of radiation pressure to stellar gravity, that is, $\beta \equiv \frac{|F_{\mathrm{rad}}|}{|F_{\mathrm{g}}|}$ (see also Sect. 2.1.2), on them increases during their sublimation phases as a result of decreasing particle mass loss (Kobayashi et al., 2010; see also Sect. 2.1.8). Eventually, ice immediately sublimates when its temperatures reach the sublimation temperature. Ice sublimation is therefore considered as a possible explanation for the presence of central clearing in debris disks (Jura et al., 1998). The sublimation temperature depends on the gas pressure, which itself is a function of the evolutionary state of circumstellar disks (Fraser et al., 2001; Collings et al., 2004; Brown and Bolina, 2007; Feistel and Wagner, 2007). In addition, mixing of ice with dust grains can alter the kinetics of ice desorption (Potapov, Jäger, and Henning, 2018). The sublimation temperature is independent of dust sizes, therefore small hotter grains sublimate before cooler large grains do (Kobayashi et al., 2008).

Jura et al. (1998) reproduced the IR emission detected in the HR 4796 system by 110 K blackbody grains. In addition, Spitzer IRS spectra around A, B, and F stars with IR excesses were analyzed and fit with a single-temperature (110 - 120 K) blackbody by Chen, Fitzgerald, and Smith (2008). This absence of warmer grains could be interpreted as the result of the ice sublimation in the inner region. Golimowski et al. (2006) interpreted the observed color change beyond 120 au in the archetypal β Pic disks as a possible indication of ice sublimation, which may result in larger average grain sizes, that is, cooler grains, beyond the sublimation zone. Kobayashi et al. (2010) indicated that the flat radial profile of the dust flux at 10 - 50 au and at 5 - 15 au derived from in situ dust impacts measured with the Voyager and Pioneer spacecrafts, respectively, may be caused by ice sublimation.

UV photosputtering Individual UV photons absorbed by an ice grain do not only dissociate water molecules, but can cause OH to be directly desorbed from the surface of ice grain. Alternatively, the molecule recombines. This process is known as UV photosputtering (Artymowicz and Clampin, 1997; Dominik et al., 2005; Grigorieva et al.,

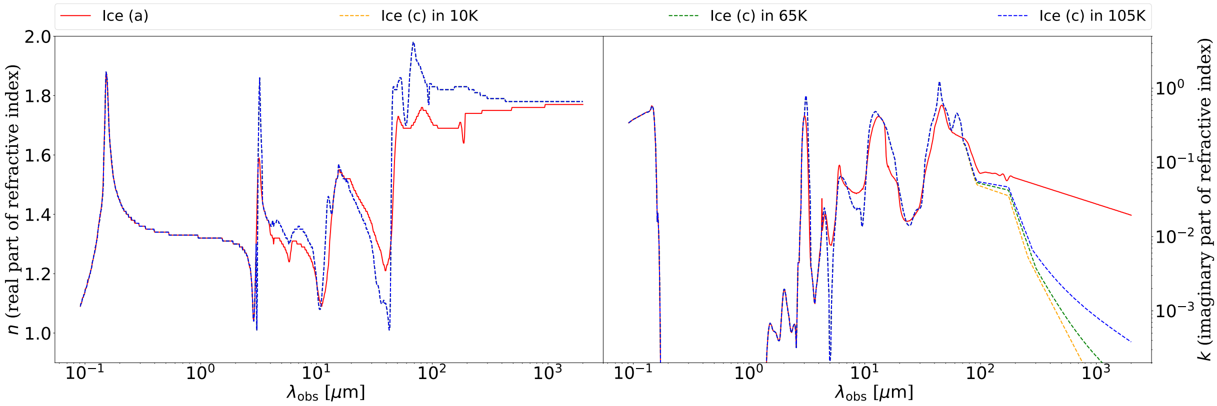

FIGURE 6.1: Optical constants n and k, i.e., the real and imaginary part of the refractive index, of pure amorphous ice and crystalline ice depending on the temperature. Ice (a) and ice (c) indicate amorphous ice (solid line) and crystalline ice (dashed line), respectively. Optical constants n of ice (c) and k of ice (c) in 0.1 µm to 62 µm show the same regardless of the temperature. However, k of ice (c) at $\sim$ 62 µm to 1000 µm shows differences that sensitively depend on the temperature. A more detailed description can be found in Sect. 6.2.

2007; see also Sect. 2.1.9). Because debris disks are transparent to the stellar radiation, energetic UV photon can efficiently penetrate the disks out to very large distances. Brown, Lanzerotti, and Johnson (1982) indicated that the UV photosputtering rate becomes higher than the sublimation rate beyond 5 AU in the solar system. In addition, Oka et al. (2012) found that far-UV photosputtering radiation depresses the ice-condensation front toward the mid-plane and pushes the surface ice snow line significantly outward. These studies imply that ice can be destroyed outside the sublimation distance as well.

Grigorieva et al. (2007) predicted that UV photosputtering efficiently destroys ice in optically thin disks, even far beyond the ice sublimation line. This means that UV photosputtering is responsible for the internal structure, thereby further increasing the effective grain size. Löhne et al. (2012) estimated UV photosputtering lifetimes compared to collisional lifetimes of objects, so that this rough comparison shows that UV photosputtering cannot be a negligible removal mechanism for ice grains with radii smaller than a few tens of µm. Furthermore, the analysis of *Herschel* observations shows that the resolved cold debris disks around HD 61005, HD 104860, and HD 107146 require a minimum grain $a_{\rm min}$ about five times larger than the blow-out size grains $a_{\rm BO}$ (Morales et al., 2016). This observation is indicative for an increase of the effective grain size in debris disks system through grain depletion by UV photosputtering. On the other hand, Honda et al. (2016) detected a shallow 3 µm ice feature that might be caused by the UV photosputtering in Herbig Be HD 100546 disk scattered light spectra. This would mean that UV photosputtering is responsible for the strength of the ice feature as well.

Johnson (1989) predicted that porosity of interstellar and circumstellar grains can significantly lower the photosputtering yield. In addition, recent laboratory experiments have demonstrated trapping of water molecules on porous silicate grains at 200 K (above the desorption temperature of H_2O ice; Potapov, Jäger, and Henning, 2018; Potapov et al., 2018). First experiments on the UV photosputtering of water ice molecules from the surface of porous silicate and carbon grains by UV photons showed an influence of the surface properties on the photosputtering yield, in particular in the monolayer regime (Potapov, Jäger, and Henning, 2019).

6.2 Model description

Debris disk and central star In the following, the basic characteristics of the reference debris disk model are briefly summarized (see also Table 6.1). A fiducial idealized typical debris disk system around a β Pic-like star (A6

TABLE 6.1: Model parameters for the simulation of the reference debris disk model. For the references of optical data, see Sect. 6.2

Parameter	Value
Stellar type	A6 V (Gray et al., 2006)
Mass of the star M_*	1.75 $M_\odot$ (Kervella et al., 2003)
Radius of the star R_*	1.8 $R_\odot$ (Crifo et al., 1997)
Effective temperature T_*	8052 K (Gray et al., 2006)
Distance to the debris disk system d	19.3 pc
Inner radius of the debris disk system $R_{\rm in}$	3 au
Outer radius of the debris disk system $R_{\rm out}$	150 au
Radial density distribution $n(r)$	$n(r) \propto r^{-1.5}$ (Krivov, Löhne, and Sremčević, 2006)
Disk inclination	0 ° (face-on disk)
Size range modeling $n(a)$	[0.1 µm, 1000 µm] with $n(a) \propto a^{-3.5}$ (Dohnanyi, 1969)
Dust composition and	Amorphous ice
References of corresponding optical data	Crystalline ice
	Astrosil
Fractional ratio of ice $\mathcal{F}_{\rm ice}$ in icy dust mixtures	0 (pure Astrosil), 0.25, 0.5, 0.75, and 1 (pure ice)
Porosity of grains $\mathcal{P}$	0 (compact), 0.25, 0.5, 0.75
Sublimation temperature	100 K: Pure amorphous ice
(Brown et al., 2006; Kobayashi et al., 2010)	105 K: Pure crystalline ice
	100 K: Amorphous ice in dust aggregates
	105 K: Crystalline ice in dust aggregates

V main-sequence star) is considered. For the inner radius of debris disks 3 au is considered, which is motivated by the region close to the sublimation line of pure ice. Note that the direct observation of a spatially resolved inner radius of the debris disk system is limited by the fixed occulting spot size, for instance, 0.6" in HST observation. Alternatively, the analysis of debris disks SEDs allows constraining the inner radius as well, but is limited by uncertainties of the optical properties of dust grains. For the outer radius of debris disks 150 au is considered, which is motivated by spatially resolved observations of debris disks[1].

Optically thin debris disks are assumed to approximately cover the range of radial density profiles $n(r) \propto r^{-1.0\sim-2.5}$ (Smith and Terrile, 1984; Artymowicz, Burrows, and Paresce, 1989; Kalas and Jewitt, 1995; Pantin, Lagage, and Artymowicz, 1997; Gor'kavyi et al., 1997; Krivov, Löhne, and Sremčević, 2006; Strubbe and Chiang, 2006). Therefore a radial density profile of the disk of $n(r) \propto r^{-1.5}$ (Krivov, Löhne, and Sremčević, 2006; Strubbe and Chiang, 2006) is considered.

Surveys at submm wavelengths have shown that the dust mass of most debris disks typically ranges from $\sim 10^{-9}$ to several 10^{-7} $M_\odot$ (e.g., Greaves et al., 2005, and references therein). Therefore consider a dust mass in debris disks of 10^{-8} $M_\odot$ is considered.

Chemical composition of the dust The chemical composition of the dust is considered to be similar to that of the dust in the interstellar medium, mainly consisting of silicates (astronomical silicate, hereafter referred to as astrosil) and carbonaceous grains, but also of ice (Henning and Salama, 1998; Draine, 2003). To study the influence of ice parameters, two basic types of ice with different physical states: amorphous and crystalline ice are considered. Note that the sublimation temperature for both forms of ice depends on their physical state as well, for example, 100 K for amorphous ice and 105 K for crystalline ice (Fraser et al., 2001; Brown et al., 2006; Brown and Bolina, 2007;

---

[1] https://www.astro.uni-jena.de/index.php/theory/catalog-of-resolved-debris-disks.html
http://circumstellardisks.org

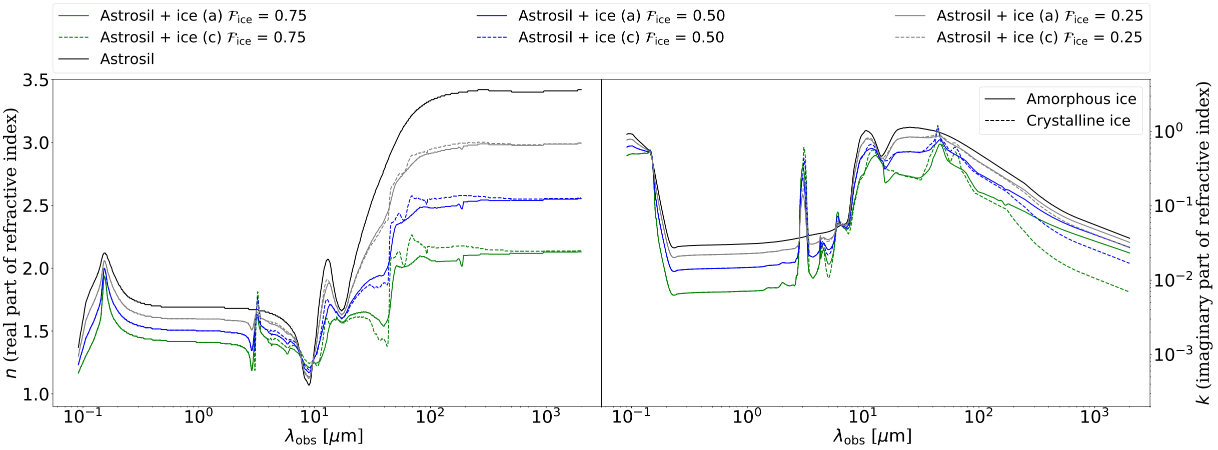

Figure 6.2: Optical constants n and k, i.e., the real and imaginary part of the refractive index, of icy-astrosilicate aggregate depending on the fractional ratio of ice $\mathcal{F}_{\text{ice}}$. Ice (a), ice (c), and astrosil indicate amorphous ice (solid line), crystalline ice (dashed line), and astrosilicate, respectively.

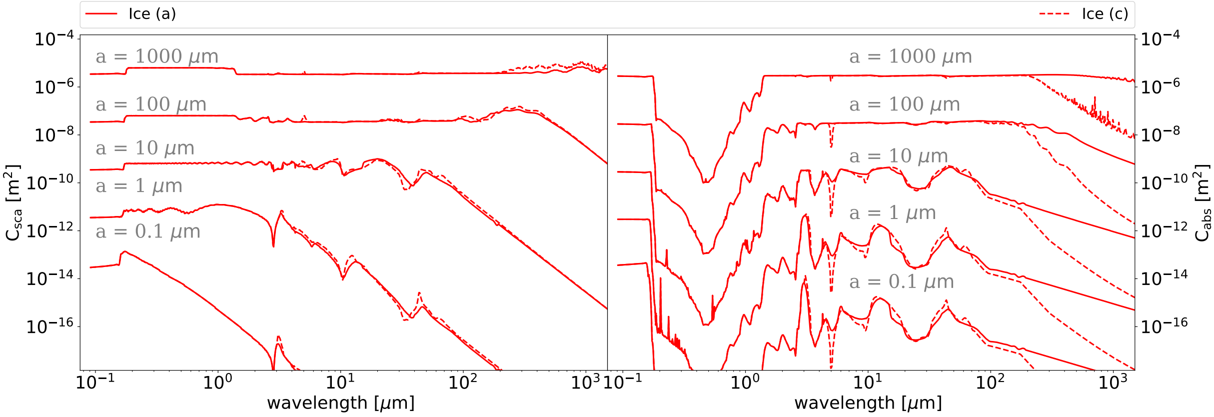

Figure 6.3: Assumed scattering and absorption cross sections (C_{sca} and C_{abs}, respectively) of amorphous ice (solid lines) and crystalline ice (dashed lines) for different grain sizes. The individual grain size is indicated in each plot. For reference to the underlying complex refractive indices, resulting from laboratory measurements, see Table 6.1.

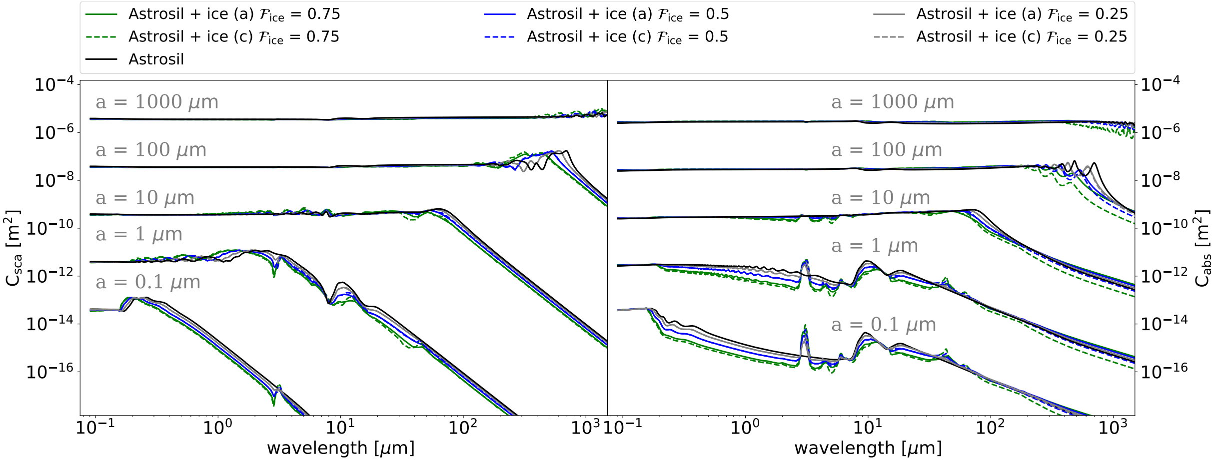

Figure 6.4: Assumed scattering and absorption cross sections (C_{sca} and C_{abs}, respectively) of ice-astrosilicate aggregates depends on the fractional ratio of ice $\mathcal{F}_{\text{ice}}$ for different grain sizes. Ice (a), ice (c), and astrosil indicate amorphous ice (solid line), crystalline ice (dashed line), and astrosilicate, respectively. The individual grain size is indicated in each plot. For reference to the underlying complex refractive indices, resulting from laboratory measurements, see Table 6.1.

Kobayashi et al., 2011). In addition, the sublimation temperature does not change notably for the ice-dust mixture (Kobayashi et al., 2011; Potapov, Jäger, and Henning, 2018). Therefore 100 K for amorphous ice dust aggregates and 105 K for crystalline ice dust aggregates are considered. In this model, the astronomical silicates as the dust material is considered.

The chemical composition of the icy dust aggregates is defined by the fraction of the total ice volume $\mathcal{F}_{\rm ice} = 0$ (corresponds to a pure astrosilicate grain), 0.25, 0.5, 0.75, and 1 (corresponding to pure ice), resulting in bulk densities from 3.5-0.25 g/cm^3 (Draine, 2003; Kobayashi et al., 2010). In addition, for porous ice particles, volume fractions of vacuum inclusions $\mathcal{P} = 0$ (corresponding to compact ice grains), 0.25, 0.5, and 0.75, where $\mathcal{P}$ = 1 - $V_{\rm ice} / V_{\rm total} = V_{\rm vacuum} / V_{\rm total}$ are considered.

Inhomogeneous mixtures and fluffy structure There are indications that interstellar and interplanetary dust grains have an inhomogeneous and fluffy structure. The effective medium theory (EMT) to describe the optical properties of composite material resulting from the optical properties and relative fractions of its components is applied. The code **emc** (effective medium calculator; Ossenkopf, 1991) to compute the effective refractive index, that is, the scattering and extinction behaviors, using rules of the effective medium approximations (i.e., Maxwell-Garnett rule Maxwell Garnett, 1904) for several types of inclusions with different bulk materials, is used. The optical properties of dust aggregates with various shapes, such as a spherical shape of ice inclusion-astrosilicate matrix particles (hereafter inclusion-matrix particles), ice mantled-astrosilicate core particles (hereafter core-mantle particles), porous ice particles, and particles with a platelet shape of ice inclusion-astrosilicate matrix (hereafter platelet-shape particles), are investigated.

Optical data and properties of dust In the following, the optical data of dust components that is used in this work are described briefly. In particular, these are the real and imaginary parts of the complex refractive index (n and k, respectively) for pure amorphous ice, crystalline ice, and astrosilicate (see Figs. 6.1 & 6.2). The real and imaginary parts of the complex refractive index are fundamental parameters that determine the scattering and absorption properties of dust particles. Based on these, the wavelength-dependent scattering and absorption cross sections $C_{\rm sca}$ and $C_{\rm abs}$, respectively, and corresponding scattering and absorption efficiencies $Q_{\rm sca}$ and $Q_{\rm abs}$ (see Figs. 6.3 & 6.4) are derived. These optical properties also play a key role in the dynamical evolution of dust particles by modifying their lifetime thorugh the P-R effect. One finds that $C_{\rm sca}$ and $C_{\rm abs}$ increase with increasing grain size at long wavelengths, regardless of their specific chemical composition. In addition, the strength of various characteristic features decreases with increasing grain size.

For the optical data of crystalline ice in the VIS to near-IR range, that is, at 0.1 μm to 2 μm, the data from Li and Greenberg (1998) is used. In the near-IR to far-IR range, that is, at 2 μm to 94 μm, the optical constants that were obtained from transmission spectra of pure crystalline ice by Potapov et al. (2018) and Curtis et al. (2005) are extrapolated and incorporated. In the far-IR to sub-mm range, i.e., at 94 μm to 1000 μm, a new set of data of crystalline ice from Reinert et al. (2015), Häßner et al. (2018), and Warren (1984) is extrapolated and derived. Note that the slope of the imaginary part of refractive index k sensitively depends on the temperature with increasing wavelength ˘ from 175 ± 6 μm, i.e., getting steeper at a lower temperature (Mishima, Klug, and Whalley, 1983; Reinert et al., 2015; Häßner et al., 2018; see Fig. 6.1).

For the optical data of amorphous ice in the VIS/near-IR to far-IR/sub-mm range, i.e., at 0.1 μm to 2 μm and at 200 μm to 1000 μm, the optical constants from Li and Greenberg (1998), which are based on the data from Hudgins et al., 1993 with power-law extrapolation in the sub-mm range, is used. In the near to far-IR range, i.e., at 2 μm to 200 μm, the transmission spectra of pure amorphous ice from Potapov et al. (2018) and Curtis et al. (2005)) is used. For the optical data of silicate in the optical to sub-mm range, that is, at 0.1 to 1000 μm, the data from Draine (2003) is used.

Grain size distribution In a steady-state grain size distribution, $n(a)$ follows the power-law distribution $n(a) \propto a^{-3.5}$ (Dohnanyi, 1969; see also Eq. 2.11), which represents an approximation for grains around the blow-out size up to planetesimal size, resulting from a collisional cascade (e.g., Thébault and Augereau, 2003; Krivov, Löhne, and Sremčević, 2006; Thébault and Augereau, 2007; Krivov et al., 2008). In summary, grain sizes from 0.1 to 1000 µm with the above steady-state grain size distribution are considered. Note that the nongravitational forces acting on grains particularly in the range of tens to hundreds of micrometers in diameter may further modify the size distribution (Krivov, Mann, and Krivova, 2000; Krivov, Löhne, and Sremčević, 2006; Plavchan, Jura, and Lipscy, 2005; Löhne et al., 2017; Kim et al., 2018). However, this effect has not been taken into account in the current study.

Ice destruction mechanisms Using the approach and results from Grigorieva et al. (2007), ice destruction mechanisms through UV photosputtering and collisions are considered. In particular, they found that only > 5 mm grains can retain their ice at ~ 80 au. Therefore ice grains with radii 5 mm and 80 au as the smallest dust grain size and inner radius of debris disks in case of UV photosputtering in the model are considered. However, ice grains with radii 20 µm and 40 au as the smallest dust grain size and inner radius of debris disks in case of UV photosputtering and collisions are considered. This is because Grigorieva et al. (2007) showed that the collisional activity increases the abundance of smaller ice grains in the inner region of debris disks.

In addition, sublimation of ice was considered. The sublimation radius was derived from the sublimation temperature of each considered dust or ice species and the corresponding radial temperature distribution. The latter was calculated on the basis of the optical properties of the dust or ice (which are in turn a function of the complex refractive index, the shape, and internal structure of the considered dust or ice species). At the inner part of the debris disk system, where only astrosilicate is present as a result of ice sublimation, the optical properties of porous astrosilicate with the same shape of dust aggregate are applied. Thus, the chemical composition of astrosilicate is defined by the fraction of the vacuum inclusions $\mathcal{P} = V_{\text{vacuum}} / V_{\text{total}}$, which is equal to the fractional ratio of sublimated ice.

The simulation of observables of debris disks a newly developed software tool DMS (Kim et al., 2018; see also Sect. 4.1.1), which is optimized for simulating observables of debris disks, or in other words, optically thin systems, is used. In particular, it allows us to simulate scattered light and thermal dust reemission images, the continuum SED, and scattered light polarization images. The optical properties of the dust grains were computed using the tool **miex** (Mie, 1908; Wolf and Voshchinnikov, 2004). The stellar photospheric emission corresponding to the chosen stellar parameters was taken from the **PHOENIX/NextGen** database (Hauschildt et al., 1999).

This study is the simulation approach to implement the temperature-dependent optical data (Omont et al., 1990; Robinson, Smith, and Hyland, 1992; see Fig. 6.1) of crystalline ice laboratory data from Reinert et al. (2015) and Häßner et al. (2018). In the first step, the radial temperature distribution is used. For this purpose, the optical data measured at a temperature of 55K, that is, the optical data corresponding to a median temperature, is applied. However, to calculate observable quantities (SEDs, images, and polarization), the optical data corresponding to the temperature distribution calculated before, is then applied.

6.3 Results

In the following, the effects of dust parameters and various ice destruction mechanism that were discussed in Section 2 on the resulting SED (Section 6.3.1) and spatially resolved images (Section 6.3.2) are discussed and analyzed. In addition, the corresponding ice survival line of debris disks (Section 6.3.3) is predicted. Finally constraining the detectability of ice in debris disk systems with future observation by the JWST/NIRCam and SPICA/SAFARI (Section 6.3.4) is considered.

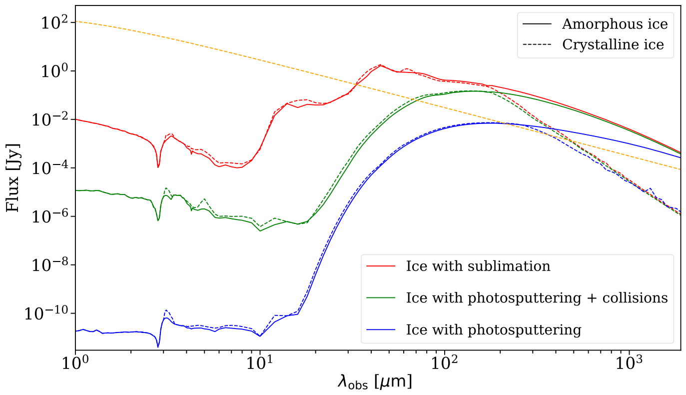

FIGURE 6.5: Effect of ice destruction mechanisms on the resulting SED. UV photosputtering and mutual collisions are considered in addition to ice sublimation. The dashed yellow line represents the photospheric emission of the central star. The solid and dashed lines indicate amorphous ice and crystalline ice with $\mathcal{F}_{\rm ice}$ = 1, respectively.

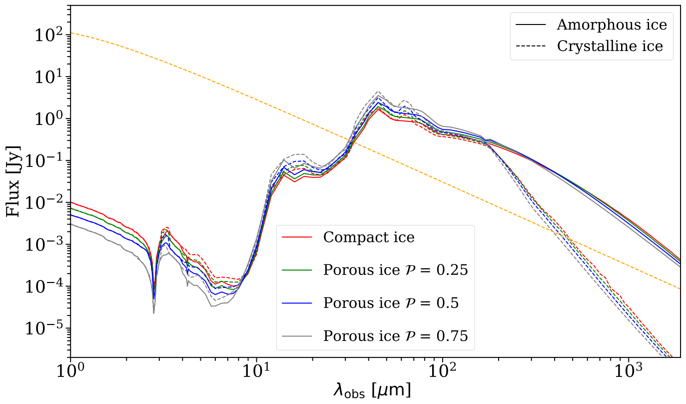

FIGURE 6.6: Effect of ice porosity on the resulting SED. $\mathcal{P}$ indicates the porosity of ice grains. The dashed yellow line represents the photospheric emission of the central star. The solid and dashed lines indicate amorphous ice and crystalline ice, respectively.

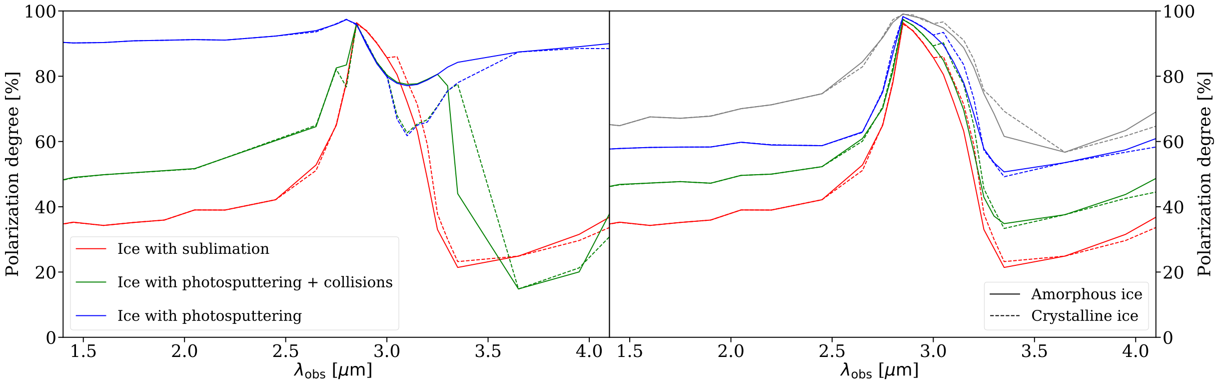

FIGURE 6.7: Effect of the ice destruction mechanism (left) and porosity (right) on the wavelength-dependent polarization degree at near-IR to mid-IR wavelengths. Ice (a) and ice (c) indicate amorphous (solid line) and crystalline ice (dashed line) with $\mathcal{F}_{\rm ice}$ = 1, respectively.

6.3.1 SED

First the influence of individual dust parameters, that is, the fractional ratio of ice $\mathcal{F}_{\rm ice}$, the different shapes of the aggregates, and porosity of ice, on the resulting SED are investigated. In addition, the ice grain survival by quantitatively exploring the role of UV photosputtering and mutual collisions in addition to the sublimation mechanism are investigated. The IR to sub-mm wavelengths is chosen because the offset from the stellar photospheric SED is largest in this wavelength region. The specific absorption or scattering features are reflected in the corresponding features of the resulting SED (see Figs. 6.3 & 6.4).

Pure ice In Fig. 6.5 the SED of debris disks composed of pure ice ($\mathcal{F}_{\rm ice} = 1$) considering three different mechanisms of ice destruction: UV photosputtering, mutual collisions and sublimation, is shown. First, one finds that UV photosputtering is responsible for the destruction of small ice grains; thus, scattered radiation from the ice is significantly decreased in the near-IR to mid-IR wavelength range. Consequently, UV photosputtering reduces the flux in near-IR to mid-IR wavelengths by about eight orders of magnitude compared to the case in which only sublimation is considered. Even if the collisional activity is taken into account, the flux is still decreased by about 2 orders of magnitude. Furthermore, one finds that UV photosputtering (and collisions) are responsible for the strength of the ice features, for instance, the shallow 3 μm feature, which is in good agreement with previous studies (Kamp et al., 2018; Honda et al., 2016).

UV photosputtering (and collisions) significantly contribute to the erosion of the decreased flux far beyond the sublimation-imposed ice survival line as well. This is reflected by the decreased flux at far-IR wavelengths. Consequently, this results in a weakened ice features around 20-30 μm and the shift of the location of the maximum of the dust reemission flux from ≤ 40 μm for sublimation toward ≤ 200 μm (≤ 100 μm for collisions). One also finds a decrease of the peak flux in the case of UV photosputtering (and collisions). In contrast to the previous finding of a shallow 3 μm feature, other ice specific features, for instance, the 44 μm and 62 μm of crystalline ice and 44 μm of amorphous ice, disappear when UV photosputtering (and collisions) are considered.

In the case of the largest grains, UV photosputtering (and collisions) can no longer contribute efficiently to destruction and erosion processes. Therefore, the effect of UV photosputtering (and collision) of sub-mm wavelengths is weaker, or in other words, less pronounced. Consequently, the SED in this wavelength range has a similar spectral index, regardless of the destructive mechanisms that make it hardly possible to constrain the mechanisms of ice destruction from the analysis of the SED alone. In addition, because the absorption coefficient, for example, $C_{\rm abs}$ of crystalline ice, is lower than that of amorphous ice (see Fig. 6.3), their spectral index also becomes significantly lower than that of amorphous ice.

In Fig. 6.6 the SED of debris disks is shown as a function of ice grain porosity, that is, for $\mathcal{P} = 0$ (pure compact ice), 0.25, 0.5, and 0.75. Similar to Brunngräber et al. (2017), one finds only a weak influence of the porosity on the resulting SED. Highly porous ice grains show a higher peak flux in the 10 μm to 80 μm range, but a lower peak flux at shorter or longer wavelengths. This is because the different contribution from individual grain size in each wavelength range, for instance, highly porous grains with radii of about tens of a micron have a high absorption cross-section at far-IR wavelengths.

Scattered-light polarization: While spectropolarimetric observations have shown enhanced polarization levels in the 3 μm ice band for molecular clouds where the increased absorption efficiency is of importance (Hough et al., 1989; Greenberg and Vandebult, 1984; reference therein), it remains to be shown whether the feature is also of importance in scattered light. This is relevant for optically thin debris disks.

One finds that the various mechanisms of ice destruction significantly affect the polarimetric signal. UV

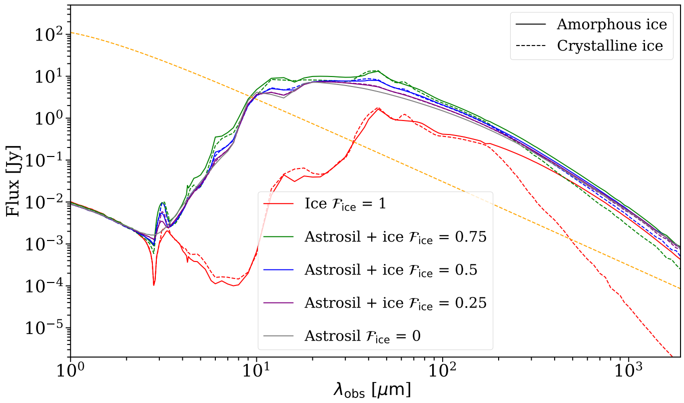

FIGURE 6.8: Effect of the fractional ratio of ice $\mathcal{F}_{\rm ice}$ on the resulting SED. The dashed yellow line represents the photospheric emission of the central star. Ice (a), ice (c), and astrosil indicate amorphous ice (solid line), crystalline ice (dashed line), and astrosilicate, respectively.

photosputtering in particular results in a very high polarization degree at near-IR to mid-IR wavelengths (see the blue line in the left plot of Fig. 6.7), while it is decreased when collisions or sublimation were taken into account (see the green and red lines in the left plot of Fig. 6.7). Overall, the polarization degree is higher for smaller grains at near-IR wavelengths, with a maximum around the 3 µm ice feature. In addition, one finds that highly porous ice grains tend to produce high polarization degrees at near-IR wavelengths (see the right plot of Fig. 6.7).

Icy-astrosilicate dust aggregates In Fig. 6.8 the SED of debris disks that are composed of icy dust aggregates depends on the fractional ratio of ice $\mathcal{F}_{\rm ice}$ is illustrated. Astrosilicate clearly dominates the emissivity (see. Fig. 6.4) even if its relative fraction is as low as 10 %. It is therefore expected that the SED of a mixture of ice and astrosilicate is similar to that of astrosilicate alone (Fig. 6.8). In addition, the sublimation temperature of astrosilicate is significantly higher than the two different physical states ice, that is, crystalline ice and amorphous ice. Consequently, they show a clear difference to the major fraction of warmer dust grains around near-IR to mid-IR on the resulting SED. This results in an increase of the SED in the corresponding wavelength range, which shifts the flux maximum on the SED at wavelengths of about 10 µm.

Finally, the effect of the fractional ratio of ice $\mathcal{F}_{\rm ice}$ on the observation of ice features is investigated. The prominent 3 µm ice feature can be found even in ice-poor aggregates, that is, for a lower fractional ratio of ice $\mathcal{F}_{\rm ice}$. In contrast, the ice features at 44 µm and 62 µm remain only in ice-rich aggregates, that is, in grains with higher fractional ratios of ice $\mathcal{F}_{\rm ice}$. Interestingly, the usually very prominent 10 µm astrosilicate feature disappears for most of the considered icy dust mixtures.

Scattered-light polarization: Fig. 6.9 shows the wavelength-dependent polarization degree at near-IR to mid-IR wavelengths as a function of the fractional ratio of ice $\mathcal{F}_{\rm ice}$. One finds that dust grains with a higher ice fractional ratio of water $\mathcal{F}_{\rm ice}$ tend to produce higher polarization degrees, for example, a polarization degree of pure ice of about 85 %, at 3 µm. However, the polarization degree is lower for pure astrosilicate grain. In the sub-mm range, this effect is less pronounced. Consequently, the measurement of the wavelength-dependent polarization degree potentially allows constraining the composition, that is, porosity of ice $\mathcal{P}$ or the fractional ratio of ice $\mathcal{F}_{\rm ice}$, of icy dust grains (see Figs. 6.7 & 6.9). The polarization was calculated for a scattering angle of 90°. This case corresponds to spatially resolved polarization observations of debris disks seen in face-on orientation.

Different shape of icy dust aggregates In Fig. 6.10 the SED of debris disks that are composed of the icy dust of various shapes, that is, inclusion-matrix particles and core-mantle particles with spherical shape, inclusion-matrix

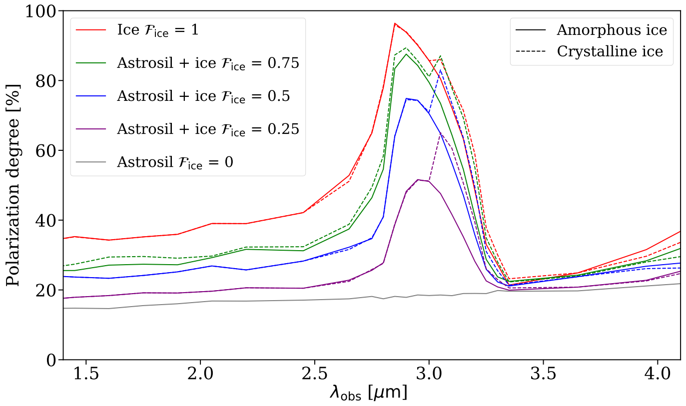

FIGURE 6.9: Effect of the fractional ratio of ice $\mathcal{F}_{\mathrm{ice}}$ on the wavelength-dependent polarization degree at near-IR to mid-IR wavelengths. Ice (a), ice (c), and astrosil indicate amorphous ice (solid line), crystalline ice (dashed line), and astrosilicate, respectively.

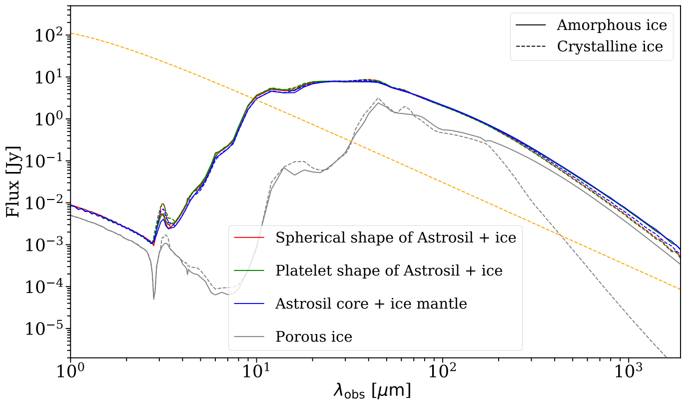

FIGURE 6.10: Effect of the shape of dust aggregates on the resulting SED. Inclusion-matrix particles and core-mantle particles with spherical shape, inclusion-matrix particles with platelet shapes, and porous ice, with the same fractional ratio of ice ($\mathcal{F}_{\mathrm{ice}}$ = 0.5) are considered. The dashed yellow line represents the photospheric emission of the central star. Ice (a), ice (c), and astrosil indicate amorphous ice (solid line), crystalline ice (dashed line), and astrosilicate, respectively.

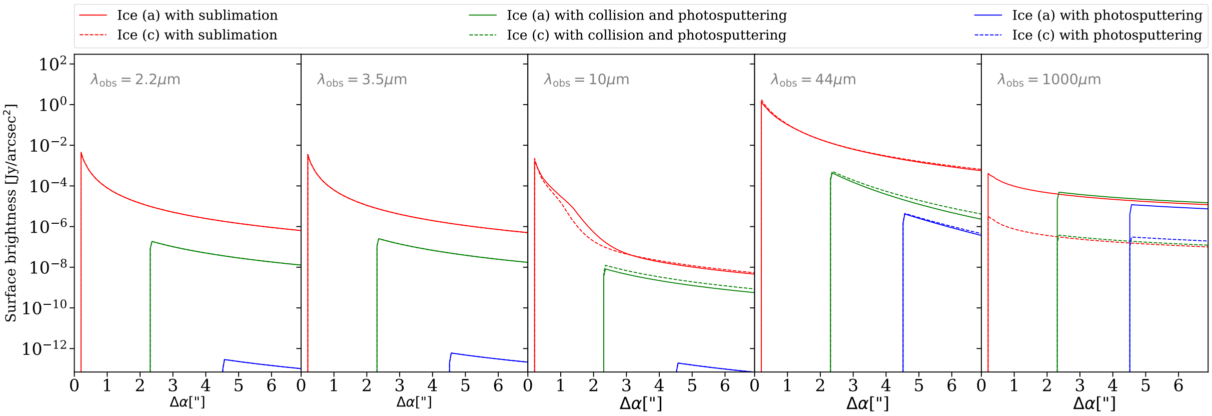

FIGURE 6.11: Effect of the ice destruction mechanisms on the radial surface brightness profile at ˘$_{\mathrm{obs}}$ = 2.2 μm, 3.5 μm, 10 μm, 44 μm, and 1000 μm.

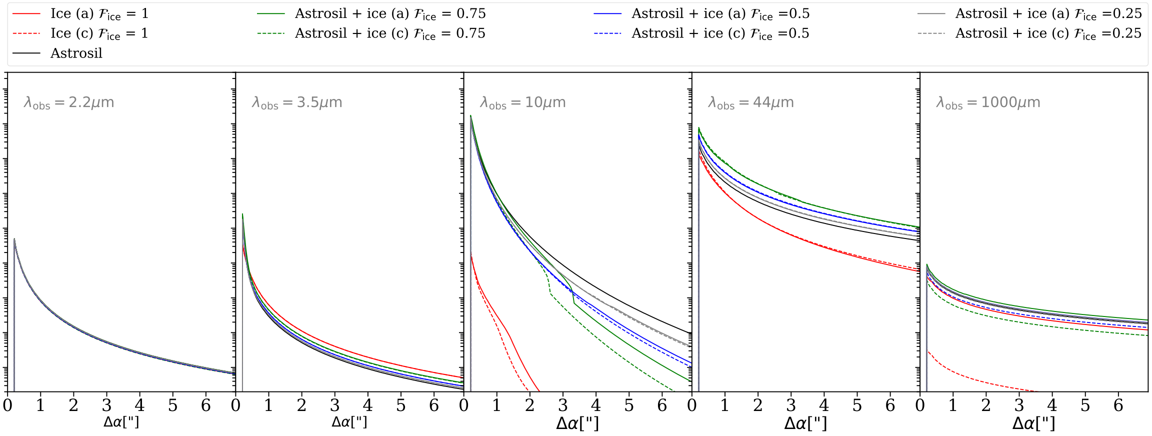

FIGURE 6.12: Effect of the fractional ratio of ice $\mathcal{F}_{\rm ice}$ on the radial surface brightness profile at $˘_{\rm obs}$ = 2.2 µm, 3.5 µm, 10 µm, 44 µm, and 1000 µm.

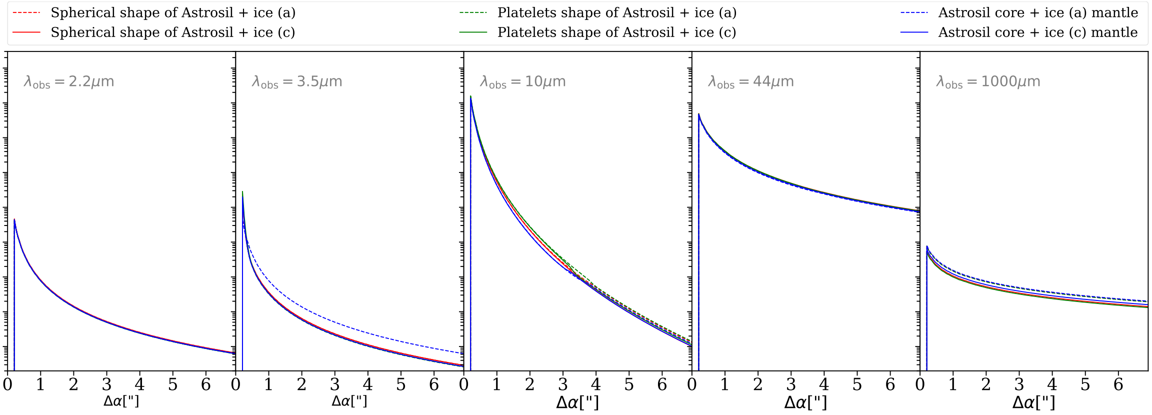

FIGURE 6.13: Effect of the shape of aggregates (with same $\mathcal{F}_{\rm ice}$ = 0.5) on the radial surface brightness profile at $˘_{\rm obs}$ = 2.2 µm, 3.5 µm, 10 µm, 44 µm, and 1000 µm.

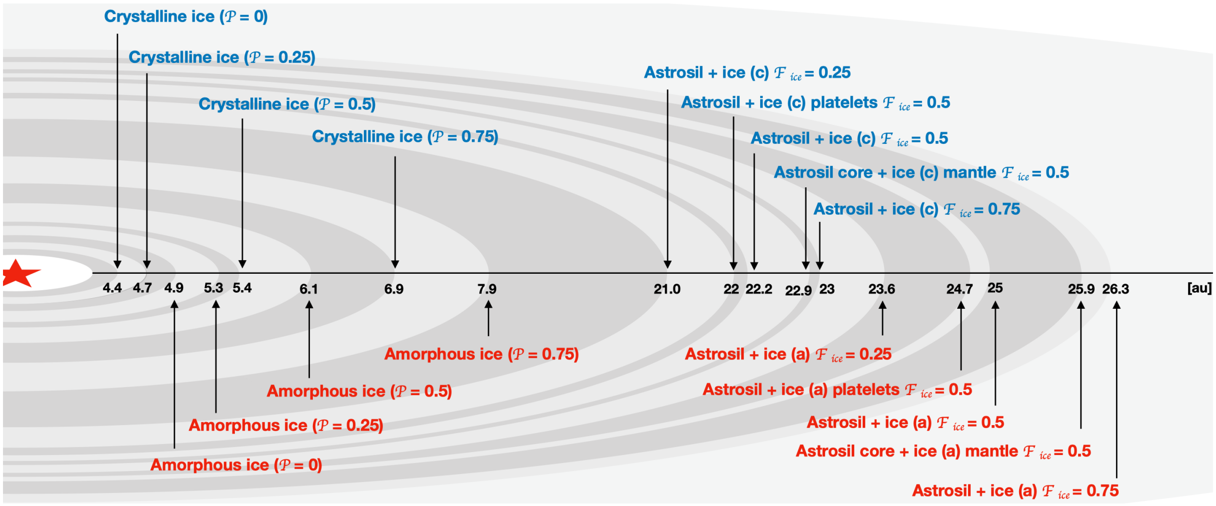

FIGURE 6.14: Prediction of the location of the ice survival line for grains of blowout size in the considered β Pic-like debris disk system. The dependence on the chemical component, shape, and physical state (amorphous vs. crystalline) of the icy dust aggregates is shown.

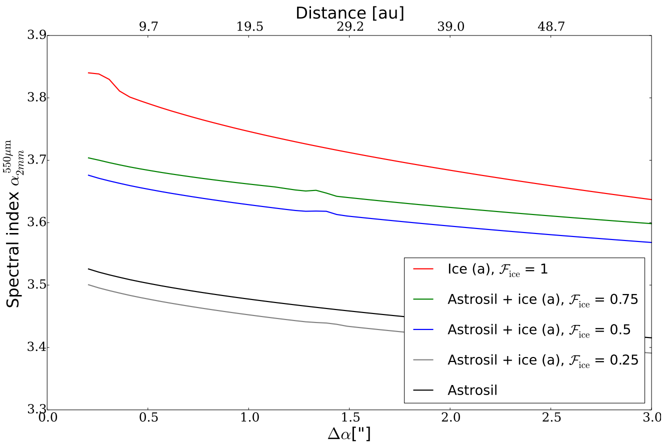

FIGURE 6.15: Radial cut of spectral index $\alpha_{2mm}^{550\mu m}$ maps for models using the different fractional ratio of ice $\mathcal{F}_{ice}$ (0 to 1). Ice (a) and astrosil indicate amorphous ice and astrosilicate, respectively.

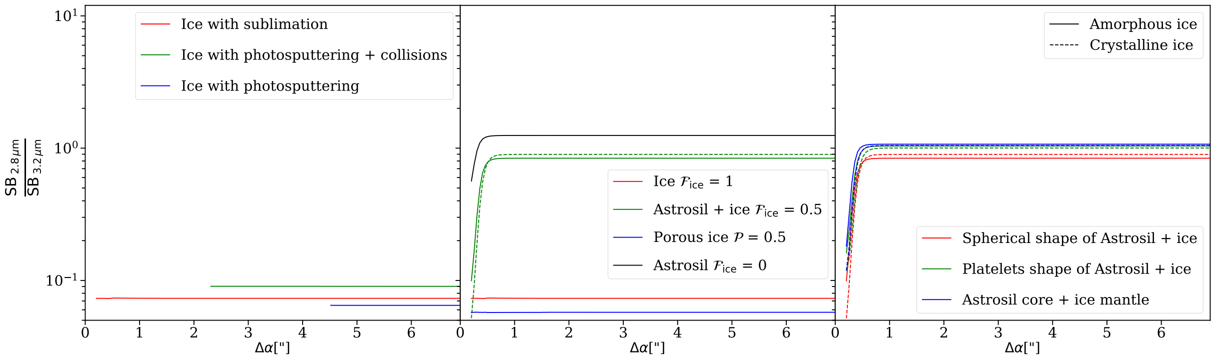

FIGURE 6.16: Ratio between the surface brightness (SB) of debris disks assuming different mechanisms of ice destruction, chemical components, and shapes of icy-astrosilicate mixture at 2.8 µm (i.e., outside of the 3 µm ice feature) and 3.2 µm (i.e., inside of the 3 µm ice feature). The solid line and the dashed line indicate amorphous ice and crystalline ice, respectively.

particles with platelet shapes, and porous ice, assuming the same fractional ratio of ice ($\mathcal{F}_{ice}$ = 0.5) is shown. One finds that the considered shapes affect the SED only weakly, except for the porous ice. However, the shape of icy dust aggregates matters for the strength of the ice features. Moreover, the ice features around 3 µm, 44 µm,

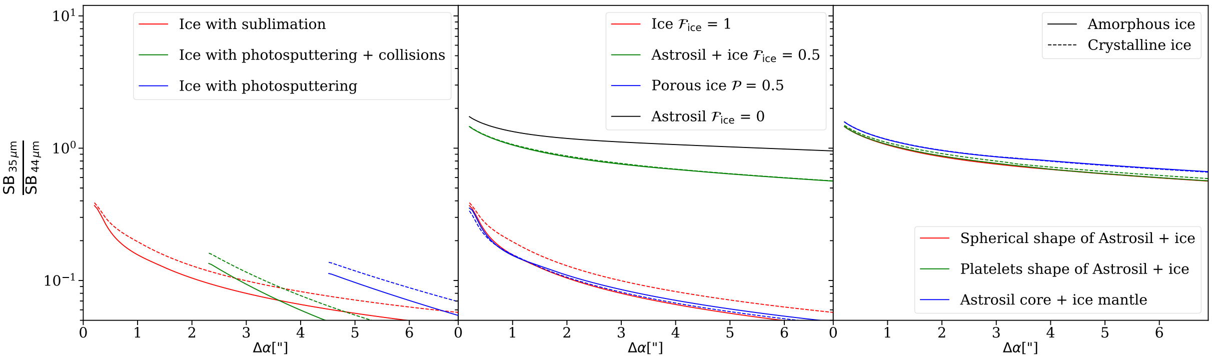

FIGURE 6.17: Ratio between the surface brightness (SB) of debris disks assuming different mechanisms of ice destruction, chemical components, and shapes of icy-astrosilicate mixture at 35 µm (i.e., outside of the 44 µm ice feature) and 44 µm. The solid and dashed line indicate amorphous ice and crystalline ice, respectively.

and 62 µm as well as the astrosilicate feature 10 µm are weakly pronounced only in the case of core-mantle and inclusion-matrix particles.

6.3.2 Spatially resolved images

Now the influence of individual dust parameters and destruction of ice grains on scattered light to thermal reemission observations, that is, on wavelength-dependent spatially resolved images and their radial profiles from near-IR to sub-mm wavelengths (at wavelengths ˇ$_{\text{obs}}$ = 2.2 µm, 3.5 µm, 10 µm, 44 µm, and 1000 µm) is now discussed. Finally the feasibility of constraining the spatial distribution of the smallest grains in the innermost warm disk regions by using the prominent ice and astronomical silicate features in the near-IR to mid-IR bands and the cold disk regions using corresponding features in the far-IR bands is analyzed and quantified.

Pure ice Fig. 6.11 shows radial profiles of simulated observations of spatially resolved disks considering different destructive mechanisms of crystalline and amorphous ice, that is, sublimation, collisions, and UV photosputtering (see the panels in Fig. C.1 for simulated observations of spatially resolved disks). When UV photosputtering is assumed, the surface brightness of debris disks is dominated by the large grains in the outermost cold disk regions. This is because energetic UV photons efficiently penetrate the disks out to very large distances, which critically decreases the abundance of the smaller particles by UV photosputtering. At 44 µm, that is, at the crystalline ice features, the flux density for crystalline ice slightly exceeds that of amorphous ice. This trend is drastically changed at sub-mm wavelengths, which is due to the lower emissivity of crystalline ice (see Fig. 6.3). At sub-mm wavelengths, one finds that the surface brightness of the outer parts are even slightly brighter if UV photosputtering is considered instead of sublimation only (and/or collisions; see the right columns in Figs. 6.11 & 6.12). This is because UV photosputtering (and/or collisional effect) can no longer contribute efficiently to the destruction of larger grains (see Sect. 6.3.1). In addition, collisional activity again clearly improves the situation for smaller and warmer ice survival in the inner region of debris disks.

Icy-astrosilicate dust aggregates Fig. 6.12 shows the radial profiles of simulated observations of spatially resolved disks considering different fractional ratios of crystalline and amorphous ice $\mathcal{F}_{\rm ice}$ in the icy-astrosilicate dust aggregates (see the panels in Fig. C.2 for simulated observations of spatially resolved disks). In the inner part of the debris disk system, where only astrosilicate grains are present because of the ice sublimation (i.e., the porous astrosilicate grain), the surface brightness between debris disks with icy-astrosilicate dust mixtures and pure astrosilicate show a smaller difference. However, this difference increases toward the outer regions, where both astrosilicate and ice are present. This effect is more pronounced at 10 µm observations, where one finds an abrupt transition of the surface brightness around 40-60 au (see Fig. 6.14). This can be understood as a consequence of ice sublimation. In addition, one also finds that the location of the change in surface brightness depends on the different physical state of icy-astrosilicate aggregates. This is due to the slight difference in the sublimation temperatures of both ice modifications in icy-astrosilicate aggregates (see Table 6.1.). On the other hand, one finds that the effect of the different fractional ratio of ice $\mathcal{F}_{\mathrm{ice}}$ on the surface brightness of debris disks at short wavelengths, that is, 2.2 µm and 3.5 µm, and at sub-mm wavelengths is weaker. This is because of the similar scattering and absorption cross section (C_{sca} and C_{abs}) of ice and astrosilicate in the corresponding wavelength regime (see Figs. 6.3 & 6.4). The surface brightness of debris disks with pure crystalline ice at the sub-mm wavelength is only significantly decreased due to their very different emissivity (see Figs. 6.1 & 6.3).

Different shape of icy dust aggregates Fig. 6.13 shows the radial profiles of simulated observations of spatially resolved disks considering different shapes of dust aggregates, that is, inclusion-matrix particles and core-mantle particles with spherical shape, and inclusion-matrix particles with platelet shapes with the same fractional ratio of ice, that is, $\mathcal{F}_{\mathrm{ice}} = 0.5$ (see the panels in Fig. C.3 for simulated observations of spatially resolved disks). The optical properties of ice-dust aggregates depend on size, shape, and physical states (amorphous vs. crystalline) of the dust grains. However, these differences are hardly noticeable in the flux density. Consequently, the spatially resolved disks images are hardly influenced by the different shape of the considered dust mixtures.

6.3.3 Prediction of ice reservoir location

Based on the finding from Sect. 6.3.2, the location of the ice survival line, focusing on grains of blowout size, is investigated. Moreover, the radial position of the ice survival line as a function of various grain parameters such as physical state, the porosity of astrosilicate and ice, fractional ratio of ice $\mathcal{F}_{\mathrm{ice}}$, and shape of the dust aggregates, is studied. Note that the ice survival line also depends on the stellar luminosity.

Prediction of ice reservoir location, the ice survival line In Fig. 6.14 the predicted location of the ice survival line for grains of blowout size is shown. Depending on the chemical composition of dust aggregates with different fractional ratios of ice $\mathcal{F}_{\mathrm{ice}}$, the physical state of ice (amorphous or crystalline), its porosity, and the shape of the aggregates, one finds that the ice survival line is located at about 4.4 (for pure ice)-26.3 (for icy-silicate aggregates) au from the host stars. This result is in good agreement with the previous study by Moerchen (2008), who found that the ice survival line of A-type star is located at about 20 au.

The dependence on the physical state is due to the different emissivities (see also Fig. 6.3). Concerning the fractional ratio of ice $\mathcal{F}_{\mathrm{ice}}$, one finds that the ice survival line is shifted toward the central star if the fractional ratio of ice $\mathcal{F}_{\mathrm{ice}}$ is decreased. Furthermore, thermal conductivity mainly depends on porosity. This means that larger porous dust grains are hotter than compact grains (Krause et al., 2011; Kirchschlager and Wolf, 2013; Pawellek and Krivov, 2015; Brunngräber et al., 2017). Consequently, for grains of a given size, porous grains are located farther out than compact grains. This moves the ice survival line to larger radii when the porosity is increased (see Fig. 6.14). In contrast to these findings, the shape of aggregates affects the location of ice survival line only weakly.

Spectral index $\alpha_{2\mathrm{mm}}^{550\mu\mathrm{m}}$ The snow line causes a radial discontinuity in the spectral index profile (Banzatti and Pontoppidan, 2015). It imprints a strong signal on the dust thermal emission in the protoplanetary disks. Thus, one would expect to observe a similar phenomenon in debris disks. In Fig. 6.15 the spectral index, that is, $\alpha_{2\mathrm{mm}}^{550\mu\mathrm{m}}$, derived from spatially resolved simulations of the brightness profile of disks with ice with varying fractional ratios $\mathcal{F}_{\mathrm{ice}}$ is shown. One finds a dependence of the discontinuity of the spectral index $\alpha_{2\mathrm{mm}}^{550\mu\mathrm{m}}$ on the fractional ratio of ice $\mathcal{F}_{\mathrm{ice}}$. It is located between about 1.3 to 1.5 " (i.e., 25 to 30 au) from the star. A higher fractional ratio of ice $\mathcal{F}_{\mathrm{ice}}$ results in a slightly broader ring with a higher value of $\alpha_{2\mathrm{mm}}^{550\mu\mathrm{m}}$ (see Fig. 6.15). This is because a change in average grain size with a simultaneous change of composition from ice-astrosilicate aggregates to pure astrosilicate, resulting from the ice sublimation. Such particles show different absorption and emission behaviors than cold particles with ice. In addition, one finds a similar phenomenon in the case of pure ice (red line in Fig. 6.15) at the inner part of debris disks. On the other hand, one finds very different spectral indices in the case of the pure crystalline ice (the spectral slope is much steeper), resulting from the very low emissivity of pure crystalline ice (see see Figs. 6.1, 6.3, and 6.5).

6.3.4 Evaluating the detectability of ice dust grains in future observations

Finally, the spatially resolved images and radial profiles (Sect. 6.3.2) to predict the feasibility of detecting the spatially resolved characteristic structures with future observations such as the JWST/NIRCam and SPICA/SAFARI is used.

3 µm H_2O ice band The NIRCam at the JWST, operating in the 0.6 to 5 µm wavelength range, consists of two modules (short-wavelength channel; 0.6-2.3 µm and long-wavelength channel; 2.4-5.0 µm) that point to adjacent fields of view on the sky. The strong scattering feature of ice at around 2.8 µm is located at this wavelength range (local minimum; see Figs. 6.1 & 6.2). In addition, the dependence on the particle phase is particularly high at about 3.5 µm (local maximum; see Figs. 6.1 & 6.2), which indicates possible candidate wavelengths to be compared.

Fig. 6.16 shows the ratio between surface brightness of debris disks with a different mechanism of ice destruction (left figure), chemical component (middle figure), and shape of icy dust mixture (right figure) inside and outside the 3 µm ice feature. One finds that the ratio is affected by the fractional ratio of ice $\mathcal{F}_{\mathrm{ice}}$. Ice-poor aggregates show a higher surface brightness ratio. The surface brightness is higher in the inner part of debris disks at 3.2 µm (and in the outer part of debris disks at 2.8 µm) in the case of the icy-astrosilicate mixture and pure astrosilicate. An extreme increase in surface brightness ratio is therefore expected in the inner region (see the middle plot of Fig. 6.16). However, one finds that the surface brightness ratio is almost constant and shows similar values in the case of pure ice for different ice destruction mechanisms (see the left plot of Fig. 6.16). This means that the ratio is no longer affected by the various depletion mechanisms. In addition, the porosity of ice (see the middle plot of Fig. 6.16) and the shape of the dust (see the right plot of Fig. 6.16) do not significantly affect the surface brightness ratio. Consequently, this comparison study allows constraining the existence of ice and even the fractional ratio of ice $\mathcal{F}_{\mathrm{ice}}$.

44 µm H_2O ice band The SAFARI at SPICA will cover the far-IR window that extends from ~ 34 µm to ~ 230 µm with a field of view of 2’ × 2’ (Roelfsema et al., 2018). Thus, it will be possible to perform observations with medium spectral resolution over the solid-state ice features at ~ 44 µm and 62 µm (see Figs. 6.1 & 6.2). These far-IR features will be useful for ice detection because the far-IR ice bands (broad features due to intermolecular lattice vibrations) are not confused with other solid-state features of less abundant species (unlike the mid-IR features, e.g., stretching, bending, or twisting of intramolecular bonds; Goicoechea et al., 2011).

Fig. 6.17 shows the ratio between surface brightness of debris disks with a different mechanism of ice destruction (left figure), chemical component (middle figure), and shape of the icy dust mixture (right figure) inside and outside of 44 µm ice feature. One finds that the fractional ratio of ice determines the surface brightness ratio, for example, the existence of ice-poor aggregates causes a lower surface brightness ratio. In particular, the surface brightnesses in the two bands are nearly identical, that is, the ratio is close to 1 over the entire disk in the case of icy-astrosilicate aggregates and pure astrosilicate. However, because of the higher flux at the 44 µm ice feature, this effect is less pronounced in the case of pure ice. The ratio is below 1 and decreases significantly with increasing radial direction from the star. In addition, similar to the finding from Sect. 6.3.1, the different shapes of dust and the porosity of ice hardly affect the surface brightness ratio.

6.4 Summary

The feasibility of detecting water ice in typical debris disk systems assuming ice destruction mechanisms (sublimation of ice, dust production through planetesimal collisions, and photosputtering by UV bright central stars) and dust mixtures with various shapes consisting of amorphous ice, crystalline ice, astrosilicate, and vacuum inclusions is investigated. For this purpose, first the influence of these parameters on the resulting the SED (Section 6.3.1), spatially resolved images, and their radial profile (Section 6.3.2), is discussed. Subsequently, the location of the ice survival line as a function of these parameters (Section 6.3.3) is estimated and analyzed. Finally, the feasibility of detecting ice in debris disks in future observations (Section 6.3.4) is discussed. The key results in this work are summarized below.

1. The sublimation of icy dust grains, collisions between planetesimals, and photosputtering due to UV sources clearly affect the observational appearance of debris disk systems. At near-IR to mid-IR wavelengths, the scattered radiation is significantly decreased by the destruction of small ice grains by UV photosputtering or collisions. At far-IR wavelengths, the thermal radiation from the dust is also significantly decreased because of the erosion of ice by UV photosputtering or collisions even far beyond the ice survival line. At submm wavelengths the effect of UV photosputtering/collision is weaker. However, the physical state of ice shows a strong effect on the spectral index of the SED. Furthermore, UV photosputtering and collisions determine the strength of the ice features.
2. The IR flux in the range of about 10 μm to 80 μm increases with increasing porosity. In contrast, flux decreases with increasing porosity at shorter or longer wavelengths.
3. One finds enhanced scattered-light polarization levels in the 3 μm ice band for ice-rich aggregates, that is, a high fractional ratio of ice or highly porous ice. This means that the measurement of the wavelength-dependent polarization degree allows constraining the existence of ice or even the composition of icy dust grains.
4. The optical properties of dust grains depend on size, shape, and physical states (amorphous vs. crystalline) of the dust grains. However, these differences are hardly noticeable in the surface brightness scale of spatially resolved observations at K and L bands. At 10 μm, one finds the abrupt transition of surface brightness as a consequence of ice sublimation, which depends on the fractional ratio of ice $\mathcal{F}_{\text{ice}}$. At the submm wavelength, the surface brightness of debris disks with pure crystalline ice is only significantly decreased as a result of their very different emissivity.
5. The radial position of the ice survival line depends on various grain parameters such as grain size, physical states, the porosity of ice, the chemical component with the different fractional ratio of ice, and the different shapes of aggregates. In the considered model, it covers a range from about 4.4 to 26.3 au.
6. Approaches to detect water ice grain with future observations with instruments operating in the near- to mid-IR (JWST/NIRCam) and far-IR (SPICA/SAFARI) are discussed.

Chapter 7

The η Chamaeleontis Association: disk characterization with *Gaia*/DR2 and APEX/LABOCA

This chapter presents the results in Roccatagliata, V., Sicilia-Aguilar, A., Kim, M., Wolf, S., et al. in preparation. The author of this dissertation performed the simulated observations of debris disks in the η Chamaeleontis association and made major contributions to the write-up and interpretation of these results. Major contributions to the simulated observations of protoplanetary disks in the η Chamaeleontis association, write-up, and interpretation of these results are done by Veronica Roccatagliata and Aurora Sicilia-Aguilar, which are not be included in this dissertation. Other parts of this study were done in collaboration with Sebastian Wolf.

The isolated open cluster η Chamaeleontis (hereafter "η Cha") is one of the youngest ($\sim$ 8 Myr; Sicilia-Aguilar et al., 2009) stellar aggregates in the solar neighborhood (Murphy, Lawson, and Bessell, 2010). As it still contains a large population of disks for its age, it allows us to study of coeval protoplanetary disks. Furthermore, η Cha is one of the closest cluster (94.3 pc; Murphy, Lawson, and Bessell, 2010). Thus, they are ideal to study a complete sample of pre-main-sequence stars (PMS) and the protoplanetary disks down to late M-type stars.

The observation of dust and gas at different ages in associations provides information about the disk evolution including their clearing timescales and physical properties/constraints, which allows us to build up a broad picture of disk evolution. For example, the lifetime of protoplanetary disks allows us to constrain the planet formation theories (Pessah and Gressel, 2017) since the protoplanetary disks provide the inventory material to form a planet.

The evolution of protoplanetary disks is observed to dissipate their dust and gas within a few million years after the commencement of the star formation (Fedele et al., 2010; see Sect. 1.2.5), which dissipation timescale depends on the number of high mass stars in the cluster (Roccatagliata et al., 2011). For example, the IR-excess fraction for stellar source, showing close to 100% in the youngest clusters (e.g., $\sim$ 1Myr), declines dramatically with their age and is typically 10% (or less) for ages of $\sim$ 5 Myr (e.g., Haisch, Lada, and Lada, 2001) as most young cluster members have stopped accreting material at a significant rate. Consequently, the lifetime of protoplanetary disks is inferred to be a few $\sim$ Myr, with order-of-magnitude scatter (Alexander et al., 2014).

The η Cha showed both an excess of stars with accretion and stars with detectable disks compared to clusters of similar age (e.g., Haisch, Lada, and Lada, 2001). For example, some members (e.g., the low-mass stars) in η Cha still retain detectable amounts of gas in their disks (e.g., Sicilia-Aguilar et al., 2009; Murphy et al., 2011; Woitke et al., 2011; Murphy, Lawson, and Bessell, 2012; Simon et al., 2012; Riviere-Marichalar et al., 2015), implying that disk clearing process might be delayed or inefficient. On the other hand, some objects retain enough dust in their disks with a large inner hole to produce a mid-IR-excess (Sicilia-Aguilar et al., 2009). The mechanism responsible for these two different time-scales is still uncertain (Fedele et al., 2010). Consequently, η Cha is one of the most important nearby groupings of PMS stars to enhance our understanding of PMS star evolution.

The main aim of this chapter is to detect the cold material in protoplanetary disks and new debris disks to understand which physical mechanism is the main responsible of the disk dissipation. This chapter is organized as follows: In Section 7.1 the new APEX/LABOCA observations, data reduction, and the results, as well as the archival Gaia/DR2 data and the high-resolution spectroscopic FEROS observations, are summarized. In Section 7.2 the basic characteristics of the debris disk model are summarized. In Section 7.3 the results of SED modeling of debris disks to constrain the physical parameters and properties are discussed. The findings in this work are summarized in Section 7.4.

7.1 Observations of the η Chamaeleon Association

7.1.1 APEX/LABOCA observations and data reduction

The **L**arge **A**pex **BO**lometer **CA**mera (LABOCA) is a multi-channel bolometer array for submillimeter continuum observations (Siringo et al., 2009), which was installed at **A**tacama **P**athfinder **EX**periment Instrumentation (APEX). The 12 out of 20 sources of the η Cha star cluster has been observed with this APEX/LABOCA between the end of October and December 2010 to trace the emission from different parts of protoplanetary disks and debris disks. The observations have been carried out in on-off mode with an integration time of 600 seconds, which were calibrated and reduced using the pipeline reduction of LABOCA data within the BoA package, in particular, developed for APEX bolometer data (Siringo et al., 2009). Four debris disks have been newly detected for the first time with APEX/LABOCA around three M stars, apart of RECX 1 that is a K7 source. The final fluxes are reported in Table 7.1. The associated error, σ, is the actual statistical uncertainty, measured on the data. This is computed as the standard deviation of all measurements, divided by the square root of the number of measurements. When a source was not detected one reports the upper limit computed as $3\,\sigma$. The beam size of APEX/LABOCA is ~ 19" (Siringo et al., 2009). The SEDs are classified (Sicilia-Aguilar et al., 2009) as Class II (comparable to Taurus), flattened disks (flat; $\lambda F_\lambda \sim \lambda^{-\frac{4}{3}}$), TO (zero or very small near-IR-excess), and Class III (no IR-excess over the stellar photosphere or second-generation of dust).

7.1.2 Cluster members on the Gaia/DR2 and FEROS instrument

The membership of the η Cha cluster was first confirmed by a radio continuum survey of X-ray sources with the Australia Telescope Compact Array (Mamajek, Lawson, and Feigelson, 1999). Successively Murphy, Lawson, and Bessell (2010) found seven more new probable members in this cluster using optical and near-IR photometry, astrometry (e.g., the Naval Observatory Merged Astrometric Catalogue), and a spectroscopic follow-up campaign. To confirm the membership of η Cha cluster, the Gaia/DR2 data (Gaia Collaboration et al., 2018) together with the radial velocity computed from the high-resolution spectra publicly available in the archive have been used. In particular, a maximization of the total likelihood function of a multivariate Gaussians model, where each gaussian characterize the distribution of each astrometric parameter, is applied. This approach (Roccatagliata et al., 2018; Franciosini et al., 2018) allows us to take into account the errors and the correlations between the parameters.

To complete the kinematic picture from the Gaia data with more precise radial velocity measurements, archival high-resolution spectroscopy with the ESO/MPG 2.2m telescope using the FEROS instrument (Kaufer et al., 1999) is used. Several η Cha members, e.g., RECX-1, RECX-3, RECX-4, RECX-6, RECX-10, RECX-12, η Cha, HD75505,

Table 7.1: LABOCA fluxes, detections, and marginal detections. The rms of the observation is given in the column σ while the calibration error, is given in the column σ_{CAL}. The upper limits is computed as $3\,\sigma$. Note that two of them are only marginal detection. See the text for more details in Sect. 7.1.1

Source	Flux at 870 µm [mJy]	σ [mJy]	σ_{CAL} [mJy]	SED type (Sicilia-Aguilar et al., 2009)
Detections				
J0843	5.42	0.83	1.28	class II
J0844	4.96	0.83	1.56	flat
RECX-5	20.01	2.45	4.78	TO
RECX-6	8.38	0.54	1.15	class III
RECX-8 (RS Cha)	18.62	2.63	4.09	class III
RECX-9	5.71	1.29	2.43	TO
RECX-11	12.74	1.68	2.11	class II
J0801[a]	7.58	0.86	1.27	
J0820[a]	8.12	1.1	1.58	
RX J1005.3-7749 8[a]	7.75	0.56	0.92	(class III)
Marginal detections				
η Cha	3.37	1.86	3.53	class III
J0841	2.88	0.97	1.69	TO/flat
Upper limits				
RECX-3	< 1.65			TO
RECX-4	< 3.03			TO
RECX-7	< 4.02			class III
HD 75505	< 7.86			class III
RECX-12	< 2.01			class III
RECX-16	< 40.4			
RECX-17	< 9.10			
RECX-18	< 29.8			

[a] candidate members from the work of Murphy et al. (2011)

and RECX-8, have been observed with FEROS as part of program 084.A-9003 (PI J. Setiawan) and 082.A-9008 (PI V. Roccatagliata).

7.2 Debris disk modeling with DMS

In this section, SEDs of the η Cha cluster members were compiled using SIMBAD and include several optical filters and 2MASS JHKs data (Sicilia-Aguilar et al., 2009), near-IR data (AKARI-IRC and WISE; Ishihara et al., 2010; Simon et al., 2012), mid-IR data (Spitzer-MIPS; Sicilia-Aguilar et al., 2009), far-IR data (Herschel-PACS; Riviere-Marichalar et al., 2015), and new submillimeter photometric points from the APEX/LABOCA survey at 870 µm and/or its upper limits (this work) to carry out the modeling of debris disks.

In the following, the basic characteristics of the debris disk model are summarized in brief (see also Table 7.2 & 7.3). Recent observational results particularly emphasizing disks that have been imaged at a wide range of wavelengths found that many debris disks are well described as a narrow ring (e.g., Kalas, Graham, and Clampin, 2005; Milli et al., 2017; Schneider et al., 2018; Sect 3.3.1). Furthermore, the dust re-emission in the disk is reproduced by varying the location of the ring, as well as the total dust mass, quantities that are related in the optically thin case. Therefore, one considers using the debris disks model of a very narrow ring (with a fixed extent of the narrow ring 20 au; see Fig. 7.1) to constrain the range of possible radial locations and the total dust mass based on an IR-excess detection and its upper limits. For the considered a range of possible ring locations one considers from 10 to 700 au. A typical debris disk systems around various stars as provided (see Table 7.3) is considered.

Astrosilicates (with bulk density 3.5 g cm^{-3}; Draine, 2003) is considered as a dust material. A steady-state grain size distribution that follows the power-law $n(a) \propto a^{-3.5}$ (Dohnanyi, 1969) from 1 to 1000 µm is assumed.

TABLE 7.2: Model stellar parameters for simulation of the debris disk model and references. As such, the process of finding a well-fitting model without any reference is always subject to some educated guesses. This means that, although a well-fitting model may be found, other solutions might be possible.

Object	SpT	T_{eff} [K]	R_* [R$_\odot$]	Distance [pc]
RECX-1	K7[1]	4115[1]	1.9[1]	100[2]
RECX-3	M3[1]	3300[1]	0.98[1]	98.8[2]
RECX-6	K7[1]	3410[1]	0.93[1]	98.1[2]
RECX-8 (RS cha)	A7[1]	7650[3]	3.04[3]	100.1[2]
RX J1005.3-7749	M1[4]	3640[2]	1.09	100.3[2]
2MASS J08014860 - 8058052	M4[4]	3100	0.72	100.1[2]

[1] Rugel, Fedele, and Herczeg (2018)
[2] Gaia Collaboration et al. (2018)
[3] van Leeuwen (2007)
[4] Murphy, Lawson, and Bessell (2010)

For the simulation of observables (e.g., the continuum SED) of debris disks, a software tool *DMS* (Kim et al., 2018; Kim et al., 2019; see also Sect. 4.1.1), which is optimized for optically thin systems, is used. The optical properties of the dust grains are computed using the tool *miex* (Wolf and Voshchinnikov, 2004).

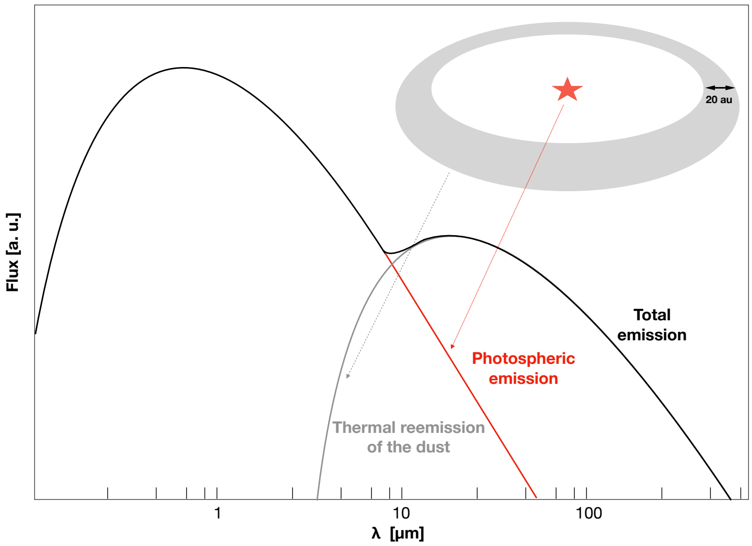

FIGURE 7.1: Fixed extent of the 20 au narrow ring description with flux (in arbitrary units). Figure credit: Roccatagliata et al. in preparation.

TABLE 7.3: Model parameters for simulation of debris disk model.

Parameter	Value
Stellar type	As provided in Table 7.2 with blackbody assumption
Considered a range of possible ring locations	[10 au, 700 au]
Extent of the narrow ring	20 au
Total disk mass	[9.0×10^{-8}M$_\odot$, 1.6×10^{-5}M$_\odot$]
Dust composition	Astrosilicate (Draine, 2003)
Size range modeling $n(a)$	[1 μm, 1000 μm] with $n(a) \propto s^{-3.5}$ (Dohnanyi, 1969)
Number of grain size bins	100

7.3 Results

7.3.1 Well-constrained narrow ring locations

2MASS J08014860 - 8058052 The first case is represented by 2MASS J08014860 - 8058052, which is one of the M4 sources classified by Murphy, Lawson, and Bessell (2010) as possible halo member of η Cha, and maybe a binary system due to its position in the color-magnitude diagram and the different high-velocity measurements they carried out in Murphy, Lawson, and Bessell (2010). Their dynamical simulations suggested the system was ejected from the cluster. This is a very well constrained case because of two data points (at 22.1 and 869 μm) from the dust emission. If the dust ring is located inside 17 au or outside 20 au, its dust emission will exceed at 22 μm or not enough, respectively. Consequently, 2MASS J08014860 - 8058052 is the only source with a massive narrow ring of 1.6-1.7 × 10^{-6} $M_\odot$ close to the central star (see Fig. 7.2).

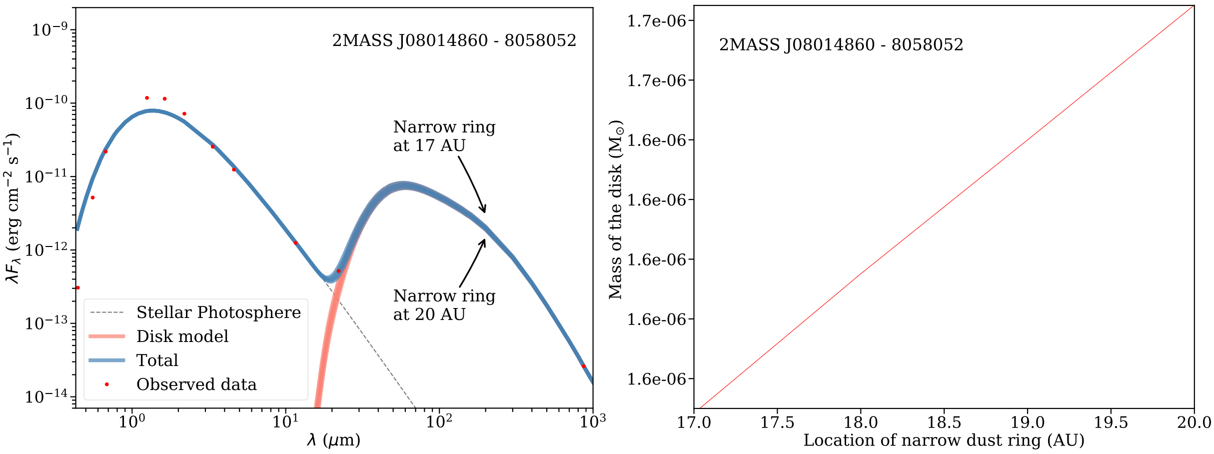

FIGURE 7.2: *Left*: SED models for the debris disks around 2MASS J08014860. The photometry data are marked by red circles (red triangles are upper limits). The various disk models are represented by blue and red lines (see Table 7.2 & 7.3 for details on individual models). *Right*: Results of the SED modeling of the debris disks around 2MASS J08014860 showing the mass of the disk as a function of the location the narrow dust ring. Figure credit: Roccatagliata et al. in preparation.

RECX3 The second most well-constrained case is represented by RECX-3, an M3 star, where the infrared photometry already suggested the presence of cold material around the star. For a similar reason with 2MASS J08014860 - 8058052 debris disk modeling, the dust ring should be located anywhere between 10-170 au. If the ring is located outside 170 au, the dust emission will exceed the maximum fluxes around Far-IR ranges. Thus, this modeling allows us to define a range in distance between 10 and 170 au of a ring with a mass of 1-9 × 10^{-7} $M_\odot$ (see Fig. 7.3).

7.3.2 Ring locations constrained within the considered parameter space

RX J1005.3-7749 8 The M1 object, RX J1005.3-7749 8, was first classified as a candidate member by Covino et al. (1997) and then Murphy, Lawson, and Bessell (2010) as a possible dynamical member. Basically, dust cannot be located inside 590 au. Thus, it harbors the most massive ring (1.0-1.5 × 10^{-5} $M_\odot$) at a location far from the central star between 590 and 680 au (see Fig. 7.4).

RECX-1 In the case of RECX-1, a K7 star, where two detections in the far-IR lie above the stellar photosphere, the missing LABOCA observation shows the poor fitting of the SED which led to a poor constraint of the location of a 0.2-1.2 × 10^{-7} $M_\odot$ disk. Basically, dust cannot be located inside 50 au, but it can be located out to 500 au and

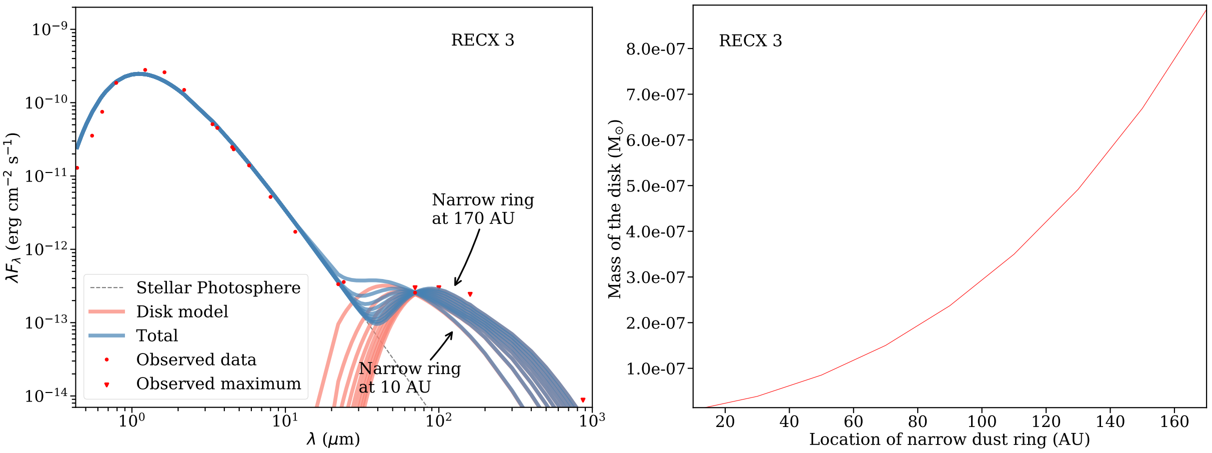

FIGURE 7.3: *Left*: SED models for the debris disks around RECX-3. The photometry data are marked by red circles (red triangles are upper limits). The various disk models are represented by blue and red lines (see Table 7.2 & 7.3 for details on individual models). *Right*: Results of the SED modeling of the debris disks around RECX-3 showing the mass of the disk as a function of the location the narrow dust ring. Figure credit: Roccatagliata et al. in preparation.

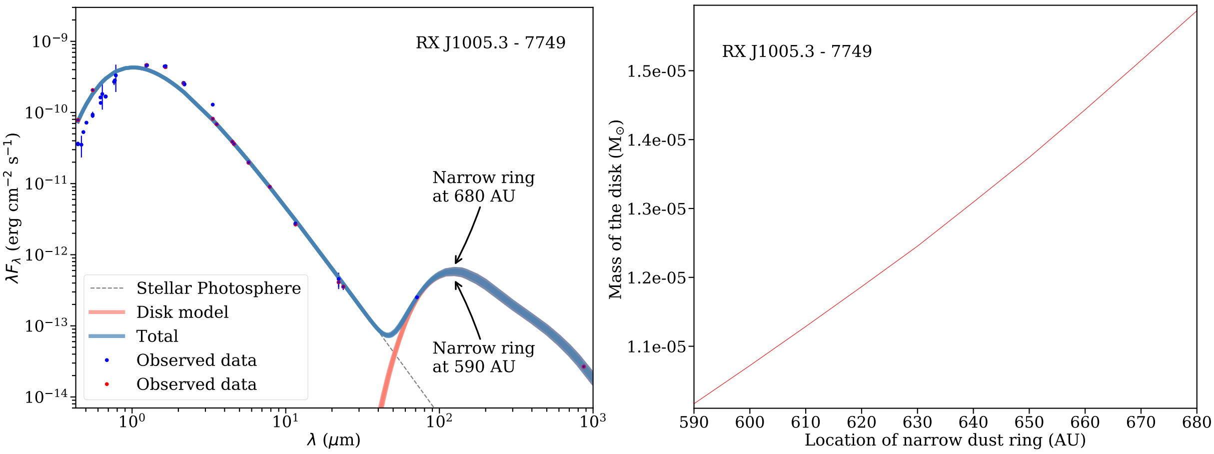

FIGURE 7.4: *Left*: SED models for the debris disks around RX J1005.3-7749 8. The photometry data are marked by red and blue circles (red triangles are upper limits). The various disk models are represented by blue and red lines (see Table 7.2 & 7.3 for details on individual models). *Right*: Results of the SED modeling of the debris disks around RX J1005.3-7749 8 showing the mass of the disk as a function of the location the narrow dust ring. Figure credit: Roccatagliata et al. in preparation.

further out. Based on the considered assumption with the ring-like structure debris disks, it is hardly possible to further constrain (see Fig. 7.5).

7.3.3 Extreme cases: the tentative interpretation of the SEDs

Here the results of the tentative interpretation of the SEDs of RECX-6 and RECX-8 are shown. Both sources are well detected with LABOCA at 870 µm above 3 σ.

RECX-6 There are two upper limits and one real detection around Far-IR. Because of the flux at 870 µm (which is not the maximum, but the real detection) it is hardly constraining. This modeling allows us to define an expected range of dust ring outside 1500 au, which is not in the reasonable ranges, of a ring with a mass of above 6×10^{-5} M$_\odot$ (see the left panel of Fig. 7.6).

RECX-8 (RS Cha) It shows the black body radiation of the star even at 70 µm probably without dust emission. In addition, due to the real detection at 870 µm (corresponding to a low temperature), dust would have to be located

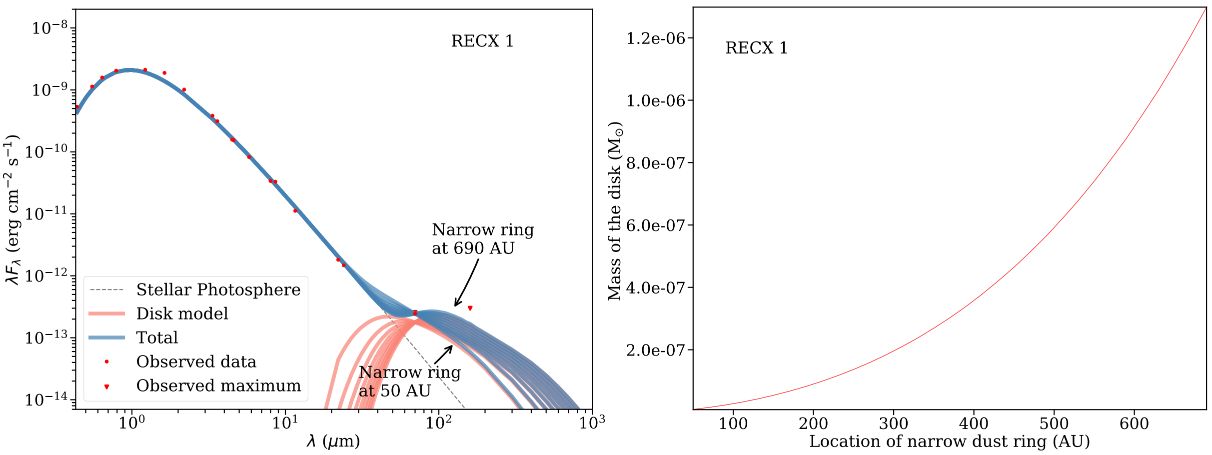

FIGURE 7.5: *Left*: SED models for the debris disks around RECX-1. The photometry data are marked by red circles (red triangles are upper limits). The various disk models are represented by blue and red lines (see Table 7.2 & 7.3 for details on individual models). *Right*: Results of the SED modeling of the debris disks around RECX-1 showing the mass of the disk as a function of the location the narrow dust ring. Figure credit: Roccatagliata et al. in preparation.

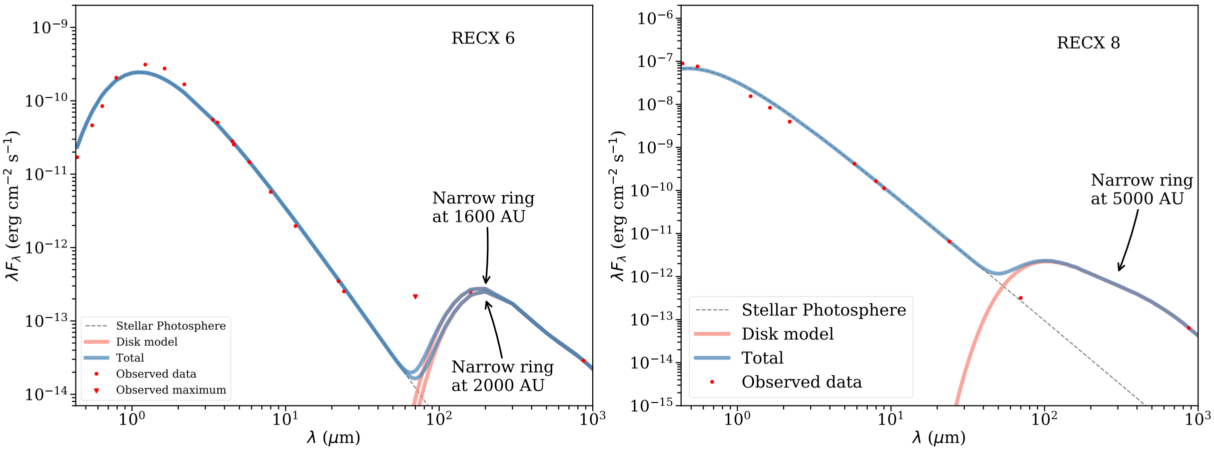

FIGURE 7.6: *Left*: SED models for the debris disks around RECX-6. The photometry data are marked by red circles (red triangles are upper limits). The various disk models are represented by blue and red lines. *Right*: SED models for the debris disks around RECX-8. The photometry data are marked by red circles (red triangles are upper limits). The various disk models are represented by blue and red lines (see Table 7.2 & 7.3 for details on individual models). Figure credit: Roccatagliata et al. in preparation.

outside 5000 au (i.e., already close to the arcminute scale; see the right panel of Fig. 7.6). The underlying debris disk model does not allow to explain the observations, i.e., the IR-excess flux must have another origin. However, Sicilia-Aguilar et al. (2009) indicated that RECX-8 is an eclipsing binary object, i.e., a disk around RECX-8 is a circumbinary ring or disk. Furthermore, they indicated that the low-mass companions are speculative, based on the X-ray emission from these stars having roughly the properties of a roughly ≈ 0.5 M$_\odot$ T Tauri star (spectral type $\sim$ M1).

7.4 Summary

The disks of η Cha are found with characteristics size too small still to be resolved by ALMA. However, thanks to its proximity, the detection of the sources has been done with APEX/LABOCA. The 12 out of 20 sources of the η Cha star cluster has been observed to trace the emission from different parts of protoplanetary disks and debris disks. In particular, four debris disks have been detected for the first time around three M stars and one K7 star. To carry out the debris disks modeling, SEDs of the η Cha cluster members were compiled using SIMBAD and includes several optical filters and 2MASS JHKs data, near-IR, mid-IR, far-IR data, and LABOCA observations and/or its upper limits of this work. The modeling of debris disks is assumed to be distributed as a ring to constrain the range of possible radial locations and total dust mass based on an IR-excess detection and its upper limits. The rings are found to be massive (1.0×10^{-7}-1.5×10^{-5} $M_\odot$) and at a distance from the central star between tens of au and a few hundreds of au. However, no relation between spectral types and the total dust mass is found.

Chapter 8

NIKA2 Observations of the debris disk around HD 107146

This chapter presents the results in Lestrade, J-F., Kim, M., Wolf, S., NIKA2 core team et al. in preparation, which is a follow-up study of Lestrade et al. (2020). The author of this dissertation performed the simulated observations and made major contributions to the write-up and interpretation of the results. Major contributions to the write-up and interpretation of the NIKA2 Observations are done by Jean-François Lestrade. Other parts of this study were done in collaboration with Sebastian Wolf and NIKA2 core team members.

The debris disk around HD 107146, an ~ 80-200 Myr old (Williams et al., 2004; Roccatagliata et al., 2009, and references therein) solar analogue G2 V star with 0.993 $R_\odot$ and 5820 K (Williams et al., 2004; Watson et al., 2011) at a distance of 28.5 pc (Perryman et al., 1997; Williams et al., 2004; Ardila et al., 2004) is of particularly great interest in many respects. For example, the disk is extending from ~ 40 to 140 au and is characterized by a circular gap (Marino et al., 2018), suggesting that the existence of a planet on a wide circular orbit opening a gap in a disk through a scattering process (Sect. 2.1.5). To date, this system is the only gas-poor system showing multiple rings of the mm-sized dust particle distribution (Marino et al., 2018). Furthermore, the coronagraphic observation can be well applied to this system because of its large inner hole (~ 40 au) without masking large parts of the disk. This disk system around HD 107146 is well studied (e.g., Ardila et al., 2004; Ertel et al., 2011; Marino et al., 2018). In particular, Ertel et al. (2011) provided the best fit of the SED with a single power-law for dust grain size distribution (Eq. 2.11) to the photometric data available extending into the mm wavelength domain with the Australian Telescope Compact Array (ATCA). The resulting fit of the SED showed large post-fit residuals between their best model and the data in the long-wavelength domain.

Furthermore, the SCUBA-2 Observations of Nearby Stars (SONS) JCMT legacy survey of debris disks (Panić et al., 2013; Holland et al., 2017) detected 48 debris disks in the (sub-)mm wavelength range (i.e., 450 μm and 850 μm) and found a large range of spectral slopes with β within the range of [-2.7, 0] in $S_\nu \propto \lambda^{-(2+\beta)}$, where S_ν is radiative flux density at given frequency ν. This corresponds to an index q_d in the size distribution $n\left(a\right) \propto a^\gamma$, where γ = 2-3q_d (see Eq. 2.11; Dohnanyi, 1969; Tanaka, Inaba, and Nakazawa, 1996; Wyatt and Dent, 2002), possibly larger than 2 for the collisional cascade. This result shows opposite trend to the deduced size distribution by SMA and ALMA observations (Hughes et al., 2011; MacGregor et al., 2016) at 850 μm and 1.3mm with an index q_d within the range of [1.61, 1.88]. Additionally, debris disks around HD 107146 is one of the systems showing the largest flux densities at 2mm predicted in extrapolating from these data (Holland et al., 2017), meaning that its spectral index is shallower, and thus becomes close to the Rayleigh-Jeans regime for mm wavelength region.

Dust emission with IR-excess of photospheric emission can be used to constrain the physical and dynamical properties of planetesimals through the grain size distribution (see Sect. 3.2.1; Wyatt and Dent, 2002; MacGregor et al., 2016). Furthermore, previous numerical studies with the kinetic approach (e.g., Krivov, Löhne, and Sremčević, 2006; Löhne, Krivov, and Rodmann, 2008; Kim et al., 2018) found that the dust grain size distribution significantly departs from the classical power-law model (Dohnanyi, 1969). In particular, the stellar radiation pressure perturbs the collisional cascade in imprinting "a wavy pattern" to the mass and size distribution (Thébault and Augereau, 2003; Thébault and Augereau, 2007; Kim et al., 2018; see Sect. 2.1.5 & Chapter 5). This is because the mass and grain size distribution depends strongly on the material strength, which is characterized by the catastrophic disruption threshold Q^*_{D} (Eq. 2.12; Sect. 2.1.5). Consequently, constraining the SED observationally is key to characterize the type of collisional cascade at the root of the dust production in debris disks.

The main aim of this chapter is to discuss the flattening of the SED of HD 107146 debris disks system that becomes close to the Rayleigh-Jeans regime for mm wavelength region. This chapter is organized as follows: In Section 8.1 the new NIKA2 observation at the 30m IRAM telescope in the mm wavelength domain at 1mm and 2mm is introduced and summarized. In Section 8.2 and 8.3 a model based on a planetesimal mass distribution function that includes the perturbed pattern (Thébault and Augereau, 2007; Krivov, Löhne, and Sremčević, 2006; Löhne et al., 2017; Kim et al., 2018) is proposed and discussed. The findings in this work are summarized in Section 8.4.

8.1 NIKA2 Observations

To constrain the SED of their dust emission in the mm wavelength domain, the observation with a new NIKA2 camera at the IRAM 30m radiotelescope was conducted to observe three known debris disks (Lestrade et al., 2020). They found that two out of three disks, e.g., around the stars HD 107146 and Vega, which are older, the spectral index between the two NIKA2 bands (e.g., 1154 μm and 2000 μm) is consistent with the Rayleigh-Jeans regime (λ^{-2}), unlike the steeper spectra (λ^{-3}) measured in the (sub-)mm wavelength range. The total flux densities are 12.9 ± 1.3 mJy and 4.1 ± 0.3 mJy at 1154 μm and 2000μm, respectively (see Fig. 8.1).

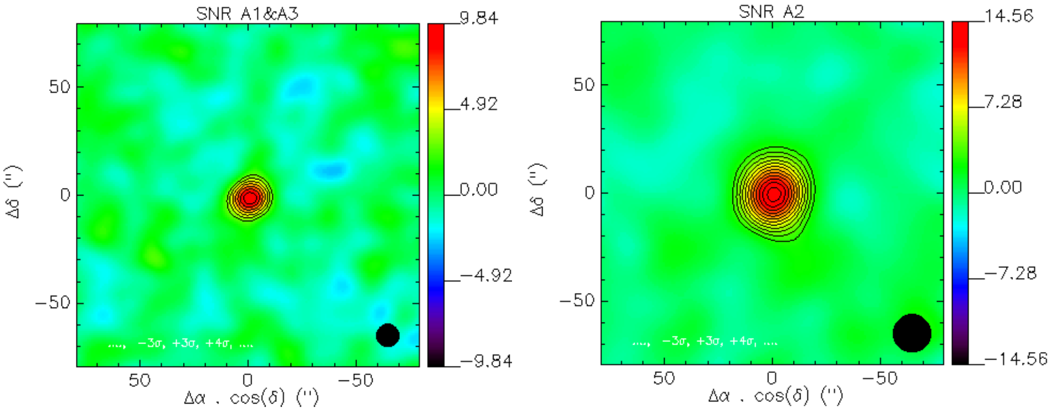

FIGURE 8.1: NIKA2 S/N images of HD 107146 with lower contours $+2\sigma$ at 260GHz (left) and 150GHz (right). The beams are shown in black. Figure credit: Lestrade et al. (2020) & Lestrade et al. in preparation.

Specifically, the NIKA2 flux density at 1154μm is statistically consistent with the ALMA flux density measured at 1100 μm by Marino et al. (2018) and 1250 μm by Ricci et al. (2015b). Furthermore, the two JCMT flux densities measured at 850 μm with SCUBA (20 ± 1 mJy) by Najita and Williams (2005) and SCUBA2 (20.6 ± 2.1 mJy) by Holland et al. (2017) agree to better than 1σ level. However, these are statistically inconsistent with ALMA at 860 μm (34 ± 3.5 mJy) in Marino et al. (2018), differing by 3.6 times the quadratically combined uncertainties, and even by 4.7 times with SMA at 880 μm (36 ± 1 mJy) in Hughes et al. (2011). These discrepancies are currently not understood.

TABLE 8.1: Photometry VERIFIER AVEC HD 107146

λ (μm)	S_ν [mJy]	σ_S [mJy]	references
0.44	3850		
0.55	5716		
0.64	6435		
0.79	7023		
1.26	7200	152	
1.60	6152	111	
2.22	4075	60	
11.7	175	10	
13	138	8.5	
17.8	85	8	
24	59.8	2.5	Hillenbrand (2008)
24	61.4	0.3	
33	86.7	5.7	
60	705.7	56	Moór et al. (2006)
70	669.0	47.8	Hillenbrand (2008)
70	785.1	6	Herschel Satellite [a]
100	698.1	7.5	Herschel Satellite [b]
100	910	15.5	Moór et al. (2006)
160	834.1	7.9	Herschel Satellite [a]
250	449.1	11.3	Herschel Satellite PSCv1 [c]
350	263.4	13.1	Herschel Satellite PSCv1 [c]
350	319	45	Corder et al. (2009)
450	130	12	Najita and Williams (2005)
500	129.7	11.6	Herschel Satellite PSCv1 [c]
850	20.6	2.1	Holland et al. (2017)
850	20	3.2	Najita and Williams (2005)
850	20	4	Williams et al. (2004)
860	34	3.5	Marino et al. (2018)
880	36	1	Hughes et al. (2011)
1100	16.1	1.6	Marino et al. (2018)
1154	12.9	0.93	This work
1250	12.5	1.3	Ricci et al. (2015b)
2000	4.1	0.24	This work
3100	1.42	0.25	Carpenter et al. (2005)
6800	0.166	0.025	Ricci et al. (2015c)

[a] 2017b.HSA-GMK
[b] 2017arXiv170505693M
[c] Herschel SPIRE Point Source Catalogue, Version 1.0. https://doi.org/10.5270/esa-6gfkpzh

Retaining the two consistent JCMT flux densities of HD 107146 at 850 μm (SCUBA and SCUBA2) and the NIKA2 and SMA observations at ~ 1200 μm rather than the higher ALMA and SMA flux densities around 850 μm leads to the finding of a change in the spectral index of dust emission in a debris disk between the (sub-)mm and radio wavelength ranges, i.e., the spectral index α in ν^α change from ~ 3 to ~ 2 (Rayleigh-Jeans) between the two wavelength domains. This finding leads us to investigate the cause of such a spectral change and model it in Sect. 8.3.2. However, the more typical SED obtained when the ALMA and SMA flux densities around 850 μm are retained is also discussed in Sect. 8.3.1. In the context of the present work, combined multi-wavelength SED modeling of the system has been carried out after collecting all photometric data available for HD 107146 (Table 8.1), mostly based on the HST/ACS data in the far-IR domain and up to the ATCA including the data from the NIKA2 observation.

8.2 Model parameters of SED analysis

The basic characteristics of the debris disk model are briefly summarized in Table 8.2. Motivated by ALMA observations of HD 107146 (Marino et al., 2018), the model consists of an inner and an outer belt with a central radial distance of 42/120 au from the star, respectively, and a radial extent of 20 au each. Although the blow out size for HD 107146 is ~ 0.5 µm (Brunngräber et al., 2017), the minimum grain radius adopted in the model is 2.5 µm constrained by fitting spatially resolved scattered light images observed with HST/NICMOS image by Ertel et al. (2011). If one assumes a steep slope of the grain size distribution following an ideal collisional cascade $n(a) \propto a^{-3.5}$, the contribution of grains with radii larger than 10 cm (assumed maximum grain size) to the considered observables is negligible. The stellar photospheric emission corresponding to the chosen stellar parameters for HD 107146 ($T_{\mathrm{eff}} = 5820\,\mathrm{K}$) are taken from the **NextGen** database (Allard, Homeier, and Freytag, 2012). For the simulation of the SED, the software tool *DMS* (Kim et al., 2018; Kim et al., 2019; see also Sect. 4.1.1), which is optimized for optically thin systems, is used. The dust grains are compact, a homogenous sphere with radius a, purely composed of astronomical silicate, with a bulk density of 3.5 g m^{-3} (Draine, 2003) are assumed. The optical properties of dust grains are calculated by the tool *miex* (Wolf and Voshchinnikov, 2004) using standard Mie theory.

8.3 Results

As discussed in Sect. 8.1, the constraints derived on the dust strongly depend on the selection of observed fluxes. In the following, two different fitting solutions to the observed SED, corresponding to two different shapes of SED in the sub-mm/mm wavelength range: with and without the observed local minimum of 850 and 1154 µm are discussed.

8.3.1 Model 1: SED with a single power-law grain size distribution

To model SED with the least number of parameters, particularly concerning the grain size distribution, first a classical single power-law grain size distribution $n(a) \propto a^{-3.5}$ (Dohnanyi, 1969; see the light blue line in Fig. 8.2), which assumes collisionally dominated debris disks with size-independent impact energy (Q^{*}_{D}) in a steady-state is considered. The Rayleigh-Jeans slope of the SED is a strong function of the dust opacity and thus the grain size distribution (Gáspár et al., 2012). As the absorption efficiency Q_{abs} is gradually decreasing towards longer wavelengths, increasing with the grain size of the dust grain, this model is expected to reproduce the SED with the continuous far-IR/(sub-)mm decrease.

One finds that this simple model provides a good fit to the interferometric total flux densities in the sub-mm/mm wavelength range, but fails to reproduce the local decrease observed with NIKA2. Moreover, it fails to produce the far-IR fluxes (~ 60 µm) of the SED. To provide a better fit, either (a) closer and thus warmer dust is required or (b) the relative amount of warm dust at a given radial location has to be increased (see Fig. 8.2 & 8.3). As the first solution would be in contradiction to the spatially resolved images, the second one is considered in the following.

8.3.2 Model 2: SED with a broken power-law grain size distribution

Motivated by the finding that a single power-law grain size distribution consisting of compact spherical grain does neither allow to reproduce far-IR fluxes (~ 60 µm) nor to create the local dip around the 1154 µm (NIKA2), now the influence of further dust parameters on the resulting SED is investigated. One finds that neither the change of the chemical composition (e.g., by substituting the composition into water ice/graphite) nor of the dust structure (e.g., by introducing porosity) allows us to achieve a good fit of the observed spectral inversion of the SED. This is because these models are still based on the assumption of a continuous distribution of the wavelength-dependent absorption

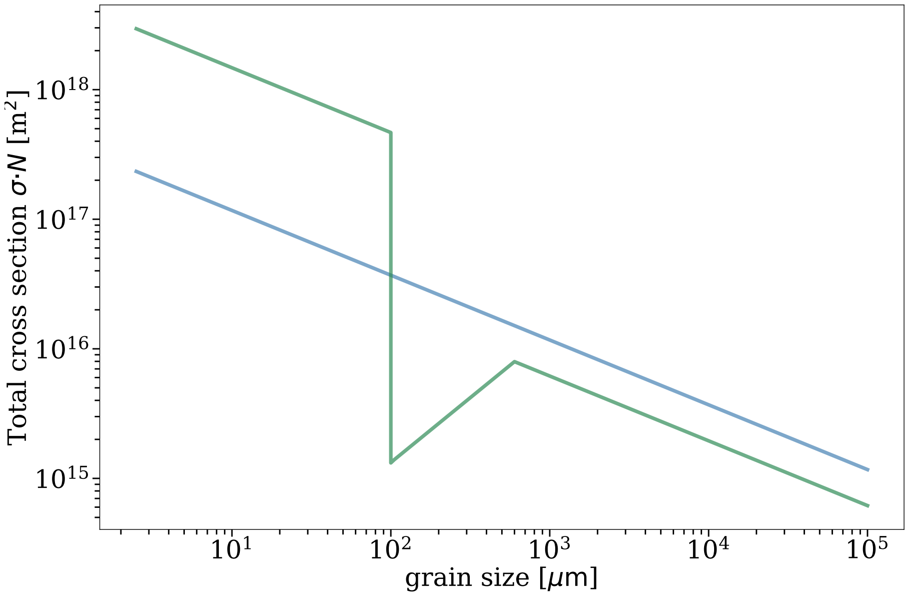

FIGURE 8.2: Different grain size distributions of the debris disk around HD 107146. As the geometrical cross-section of the dust grain is a proxy for the emitted and scattered light, it is shown as a function of the grain size. The blue line and the green line represent that the grain size distributions following the classical single power-law (Model 1, Sect. 8.3.1) and the broken power-law (Model 2, Sect. 8.3.2), respectively. Figure credit: Lestrade et al. in preparation.

efficiencies Q_{abs}. Consequently, the remaining solution is a discontinuous grain size distribution. The existence of such a more complex distribution has been investigated in previous studies by the perturbation of the bottom of the collisional cascade due to stellar radiation pressure. For example, when smaller grains are removed, the excess of slightly larger grains develops due to reduced collisional erosion. However this excess, in turn, produces a deficit of yet larger bodies, which alters excesses and deficits, eventually washing out towards increasing grain size (Thébault and Augereau, 2007; Löhne et al., 2017; Kim et al., 2018). This translates into a wavy pattern in the wavelength-dependent dust opacity and thus the corresponding shape of the thermal re-emission SED at far-IR/(sub-) mm wavelengths. The goal is to mimic such a discontinuous grain size distribution (e.g., Fig. 1 in Kim et al., 2018) to achieve following goals: (a) a higher abundance of the small (i.e., warmer) grains and (b) the depletion of SED around 850 to 1154 µm wavelength of JCMT and NIKA2 observations. In this context, a broken power-law grain size distribution $n(a) \propto a^{\gamma}$ with three different exponents γ assigned to three distinct intervals of grain sizes is considered (see Fig. 8.2 & Table 8.2). The model includes an over-density of smaller grains (e.g., 2.5 - 100 µm) and a strong depletion of the mid-sized grains (e.g., 100 - 600 µm), which is motivated by the characteristic grain size a_{c} ($\approx \lambda_{\text{obs}} / 2\pi$; Backman and Paresce, 1993) around a local decrease in the emission at 650 - 3000 µm of the SED. This wavy pattern of the grain size distribution is scaled by the total dust mass M_{total} for each of the three intervals of the grain size distribution separately (see Table 8.2).

One finds that the broken power-law grain size distribution allows us to explain the local minimum of 1154 µm (see Fig. 8.4). Moreover, the far-IR flux density is also well-fit by the model with the broken power-law grain size distribution. The observed signature in the SED can be expected to be a more common feature of collisional debris disks (Thébault and Augereau, 2007). In turn, this type of observation allows constraining not only the modifying grain size distribution but - based on this - the collisional activity in debris disks.

This model results in an inferred inner belt mass of $\sim 1.19 \times 10^{-8}$ $\text{M}_{\odot}$ based on the mid-infrared photometry, which shows a minor discrepancy with the result from the model with the single power-law grain size distribution (factor of 0.7). One also finds that the inner belt does not affect the spectral inversion of the SED, which is in agreement with the previous study (e.g., Marino et al., 2018; Ertel et al., 2011).

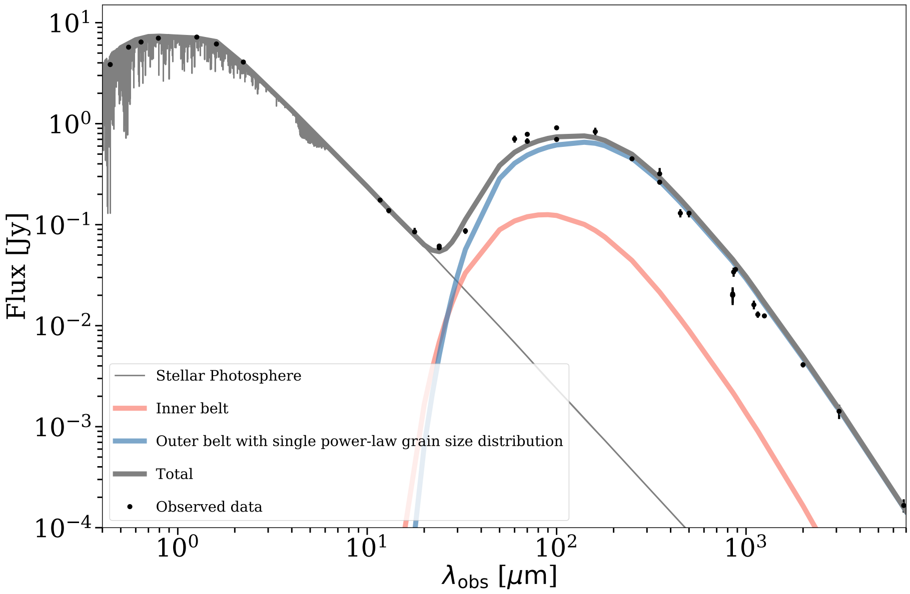

FIGURE 8.3: Model 1: Observed and modeled SED of HD 107146, its inner, and outer component with the single power-law grain size distribution in the model. The black dot, thin grey, salmon, and light green line represent the observed data, the stellar, inner component, and outer disks contribution to the total flux (thick grey line), respectively. See Sect. 8.3.1 for details. Figure credit: Lestrade et al. in preparation.

8.4 Summary

To constrain the SED of the dust emission of the debris disk around HD 107146 in the mm wavelength domain, the observation with a new NIKA2 camera at the IRAM 30m radiotelescope was conducted. Retaining the two consistent JCMT flux densities at 850 µm and the NIKA2 and SMA observations at ~ 1200 µm leads to the finding of a change in the spectral index of SED between the (sub-)mm and radio wavelength ranges, i.e., from ~ 3 to ~ 2 (close to the Rayleigh-Jeans regime). The long-wavelength slope of the SED can be directly related to the grain size distribution in the disk. Thus, a broken power-law grain size distribution model based on a planetesimal mass distribution function that includes the perturbed pattern is proposed to explain the spectral index inversion. The broken power-law grain size distribution model allows us to explain the local minimum of 1154 µm. Furthermore, the far-IR flux density is also well-fit by this model. Additionally, retaining the ALMA/SMA at 860/880 µm leads to the finding of the SED having a standard grey body shape with a steep spectral index ~ 3. Thus, the more typical SED obtained with a single power-law grain size distribution is also discussed.

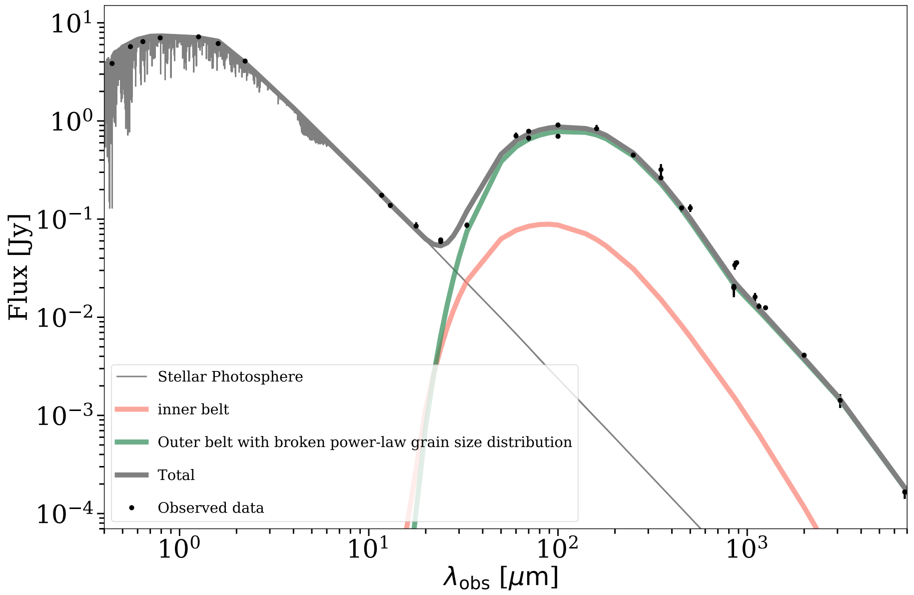

FIGURE 8.4: Model 2: Observed and modeled SED of HD 107146, its inner, and outer component with the broken power-law grain size distribution in the model. The black dot, thin grey, salmon, and light green line represent the observed data, the stellar, inner component, and outer disks contribution to the total flux (thick grey line), respectively. See Sect. 8.3.2 for details. Figure credit: Lestrade et al. in preparation.

TABLE 8.2: Model parameters for the simulation of the debris disk model

Parameter		Value
Stellar type		G2 V (Williams et al., 2004)
Radius of the star R_*		$0.993\,R_\odot$ (Watson et al., 2011)
Effective temperature $T_{\rm eff}$		5820 K (Watson et al., 2011)
Distance d		28.5 pc (Ardila et al., 2004)
Disk inclination i		25 ° (Ardila et al., 2004)
Radial density distribution $n(r)$		$n(r) \propto r^{-1.5}$ (Krivov, Löhne, and Sremčević, 2006)
Inner belt	$R_{\rm in}$	42 au with a width of 20 au
	Size range modeling $n(a)$ with $M_{\rm total}$ [a]	$n(a) \propto a^{-3.5}$ for [2.5 µm, 10 cm] with $1.69 \times 10^{-8}\,M_\odot$
	Size range modeling $n(a)$ with $M_{\rm total}$ [b]	$n(a) \propto a^{-3.5}$ for [2.5 µm, 10 cm] with $1.19 \times 10^{-8}\,M_\odot$
Outer belt	$R_{\rm out}$	120 au with a width of 20 au
	Size range modeling $n(a)$ with $M_{\rm total}$ [a]	$n(a) \propto a^{-3.5}$ for [2.5 µm, 10 cm] with $4.48 \times 10^{-6}\,M_\odot$
	Size range modeling $n(a)$ with $M_{\rm total}$ [b]	$n(a) \propto a^{-3.5}$ for [2.5, 100 µm] with $1.63 \times 10^{-7}\,M_\odot$ $n(a) \propto a^{-2.0}$ for [100, 600 µm] with $0.3 \times 10^{-10}\,M_\odot$ $n(a) \propto a^{-3.5}$ for [600 µm, 10 cm] with $4.6 \times 10^{-6}\,M_\odot$
Dust composition & bulk density		Astrosilicate (Draine, 2003) & 3.5 g m^{-3}

[a] with the single power-law
[b] with the broken power-law

Chapter 9

Conclusive Remarks

9.1 Summary & Outlook

In the present work, the observational appearance of debris disks has been studied through detailed modeling with multi-wavelength/spatially resolved observations. In this context, specialized simulation tools with analytical/collisional modeling of debris disks have been developed and used to constrain the appearance of the disk system with physical properties and phenomena. These allow the verification of predictions made concerning the spatial structure, underlying dynamical processes, and optical dust properties in the debris disk system. In detail, the results and outlooks of the present dissertation are as follows:

- The basic introduction of stellar/planetary and dust evolutions were discussed in Chapter 1. The comprehensive physics of dust in debris disks and the general context of debris disks observations were discussed in Chapter 2 and Chapter 3. The simulation tools used in this work were discussed in Chapter 4.
- In Chapter 5, impacts of collisional parameters, for instance, belt eccentricity e_{b}, dynamical excitation Δe_{b}, and the material strength Q_{s}, on the observational appearance of eccentric debris disks, were investigated. Surface brightness asymmetries caused by the combined effects of collisions and radiation pressure were found. For example, the wavelength-dependent apocenter-to-pericenter flux ratio at short wavelengths was increased in the case of higher efficiency of destructive collisions, caused by increasing dynamical excitation of the belt or decreasing material strengths. For very low material strengths, the pericenter glow phenomenon was reduced and eventually even replaced by the opposite effect, the apocenter glow, at shorter wavelength regimes, e.g., in the near to mid-IR wavelength range. This effect was less pronounced at sub-mm wavelengths. Within the considered parameter space, the impact of the material strength Q_{D}^{*} on the appearance of the disk was stronger than that of dynamical excitation of the belt. The SED alone does not provide unique constraints on the collisional parameters considered.

  This study motivates the need to have a closer look at the specific impacts/roles of specific types of dust, e.g., crystalline ice, amorphous ice, astrosilicates, PAH, and graphite, with various internal structure type (e.g., compact/porous and single component/multi-layer), on the observational appearance. Furthermore, future observations with a high spatial resolution for collision-dominated debris disks at short wavelength regime (e.g., optical to mid-infrared wavelengths) are necessary to confirm the apocenter glow phenomenon, and thus the verify predictions made concerning underlying collisional processes in the debris disk system.
- In Chapter 6, the feasibility of detecting water ice in typical debris disk systems, assuming ice destruction mechanisms, e.g., sublimation of ice, dust production through planetesimal collisions, and photosputtering by UV bright central stars, and dust mixtures with various shapes consisting of amorphous ice, crystalline ice, astrosilicate, and vacuum inclusions, was investigated. The scattered radiation at near-IR to mid-IR

wavelengths and the thermal radiation at far-IR wavelengths were significantly decreased by the destruction of ice grains by UV photosputtering or collisions even far beyond the ice survival line, while the effect of UV photosputtering or collision was weaker at sub-mm wavelengths. Furthermore, UV photosputtering and collisions determine the strength of the ice features. The optical properties of dust grains depend on size, shape, and physical states (amorphous vs. crystalline) of the dust grains, which were hardly noticeable in the surface brightness scale of spatially resolved observations at near-IR observation. However, the abrupt transition of surface brightness as a consequence of ice sublimation, which depends on the fractional ratio of ice $\mathcal{F}_{\rm ice}$, was found at 10 µm. Furthermore, the location of the ice survival line as a strong function of these parameters was estimated and analyzed. Finally, the feasibility of detecting ice in debris disks in future observations, e.g., approaches to detect water ice/ice-dust aggregates with future observations with instruments operating in the near- to mid-IR and far-IR, was discussed.

For further study, the effect of water ice on the analysis of debris disk observations and parameters needs to be investigated (T. Stuber et al. in preparation) to verify the sensitivity of parameter estimations to the presence of water ice/ice aggregate, as Brunngräber et al. (2017) showed that neglecting porosity leads to a deviate determination of blow-out size by a factor of ~ 2. Furthermore, future observations (e.g., JWST, ELT, and SPICA) are necessary to verify the models considered to simulate various ice destruction mechanisms in debris disks and quantitative estimates from this study.

- In Chapter 7, the combined multi-wavelength modeling of debris disks in η Chameleontis cluster was investigated. A continuum sub-millimeter survey of the η Chameleontis cluster member had been carried out with APEX/LABOCA. This had been combined with the photometric data available from the archive to compile a complete SED. The modeling of debris disks was assumed to be distributed as a ring to constrain the range of possible radial locations and total dust mass based on multi-wavelength observation. Debris disks in the η Chameleontis cluster were found to be massive (1.0×10^{-7}-1.5×10^{-5} $M_{\odot}$) and at a distance from the central star between tens of au and a few hundreds of au. However, no relation between spectral types and the total dust mass was found.

  For further study, derived and constrained possible radial locations of the ring and total dust mass should be verified via spatially resolved observations. Furthermore, these will further constrain extreme cases of debris disks for SED modeling, e.g., RECX-6 and RECX-8 (RS Cha). Additionally, distinguishing groups of stars according to their formation and/or disk survival might be helpful to connect the observations and the cluster structure. This may explain potential differences in star formation and disk evolution between sparse and dense clusters (e.g., Fang et al., 2013). These all motivate the need for further follow-up observations.

- In Chapter 8, the observation with a new NIKA2 camera at the IRAM 30m radiotelescope was conducted to constrain the SED of the dust emission of the debris disk around HD 107146 in the mm wavelength domain. The flattening of the SED of HD107146 that becomes close to the Rayleigh-Jeans regime at millimeter wavelength domain was discussed. In particular, a model based on a grain size distribution model that includes the perturbed pattern (e.g., a broken power-law grain size distribution model), found theoretically by Thébault and Augereau (2007) and by simulations with full treatment of planetesimal collisions (Kim et al., 2018), was proposed. This model explains well the local minimum of 1154 µm. Additionally, the more typical SED by retaining the ALMA/SMA at 860/880 µm obtained with a single power-law grain size distribution was discussed. This model explains the finding of the SED having a standard grey body shape with a steep spectral index ~ 3.

  A more sophisticated collisional modeling of debris disks (e.g., material strength should be an important parameter) with a more detailed spatial structure will be helpful to verify the proposed model in this chapter, and thus understand more natural outcomes of the collisional activity in debris disks. Furthermore, the discrepancies between the interferometric total flux density (e.g., ALMA or SMA) and single-dish flux density (e.g., JCMT) found in the debris disk around HD107146, though not the aim of this project, should be understood with further follow-up observations. Future observations are expected to reveal the complexity of these systems hidden from previous observations. This will help to confirm the spectral inversion with a local dip around the ~ mm wavelength NIKA2 observation as well.

Appendix A

Current/future observations of debris disks

Here, the general description of the current and (near) future observations of debris disks, depending on the wavelength, i.e., from visual to mm, will be briefly summarized.

A.1 Visual and near-IR observation

The dust in a debris disk scatters stellar radiation at visible to near-IR wavelengths, which highlights regions of disks where small grains dominate. Thus, this is a very useful method for identifying disk structures. Longer exposures for coronagraphic high-contrast imaging are used to suppress much of the starlight, which overwhelms the light scattered by the dust in debris disks at these wavelengths (see Sect. 3.1.2), with a possible small inner working angle, e.g., Hubble Space Telescope/Near-Infrared Camera and Multiobject Spectrometer (Kalas, Graham, and Clampin, 2005); Gemini Planet Imager/Exoplanet Survey (Esposito et al., 2018); Keck/NIRC2 (Esposito et al., 2011); Subaru Coronagraphic Extreme Adaptive Opticsto (Currie et al., 2017); James Webb Space Telescope/Near-Infrared Camera (Perrin et al., 2018).

The polarimetric observation at visible to near-IR wavelengths can be used as well to study and constrain the size distribution and chemical composition of dust (Krivova, Krivov, and Mann, 2000; see Sect. 3.2.2). Although these were done successfully only for a few of the brightest debris disks, such as β Pictoris and AU Mic (e.g., Hubble Space Telescope/Advanced Camera for Surveys coronagraph; Graham, Kalas, and Matthews, 2007).

To spatially resolve the hot exozodi from the central star, one promising method is near-IR interferometry at K band, measuring the visibility with a suitable set of baseline configurations (see also Sect. 3.3.2; Kral et al., 2017; Ertel et al., 2020), e.g., IOTA/IONIC (Defrère et al., 2011); VLTI/PIONIER (Ertel et al., 2014; Marion et al., 2014); PTI (Ciardi et al., 2001) at H band and VLTI/VINCI (Absil et al., 2009); CHARA/FLUOR (Absil et al., 2013; Nuñez et al., 2017); VLTI/GRAVITY (Defrère et al., 2018); PFN (Mennesson et al., 2011).

A.2 Mid-IR observation

Since various lines are located in the mid-IR regime (e.g., aromatic + aliphatic hydrocarbons at ~ 8-9 µm, broad 10-15 µm astrosilicate features due to the Si-O bond stretch/bend mode, and atomic H and molecular H_2 at ~ 10 µm), the presence and shape of spectral features help to constrain the dust composition and size, e.g., Spitzer/Infrared Array Camera and Multiband Imaging Photometer and Infrared Spectrograph (Chen, 2006; Beichman et al., 2005; Chen, Fitzgerald, and Smith, 2008; Morales et al., 2009); Subaru/COoled Mid-Infrared Camera and Spectrometer (Sako et al., 2003); AKARI (ASTRO-F[1])/IRC Mid-Infrared All-Sky Survey data (Fujiwara et al., 2012); VLT/SPHERE (Sissa et al., 2018); JWST/MIRI (Brande et al., 2020).

An alternative way to get meaningful information in the mid-IR regime is to use the (coronagraphic) scattered light/thermal emission images, e.g., Keck II imaging Mid-Infrared Large-well Imager (Ressler et al., 1994); Gemini/T-ReCS (Telesco et al., 1998); SPICA/SMI (Kaneda et al., 2016). The mid-IR high-resolution images extrasolar Kuiper belts and mid-planetary system belts, which reveal features that signal the presence of gravitational interactions between unseen planetesimals (and/or planets), i.e., dust grains are indicative of the physical processes occurring by collisions or orbital resonances. Also, these show the dynamical importance of various disk features with non-axisymmetric, azimuthal asymmetries, and inclination offsets (see also Sect. 3.3.1).

Furthermore, the detection of warm exozodi in the habitable zones (HZ) of Sun-like stars is also of particular interest at these wavelengths because this can be a potential indicator of (ongoing) terrestrial planet formation. The temperature ~ 300 K blackbody peaks near 10-15 µm, and thus mid-IR observation is also another proper source for understanding exozodi around the star (see 3.2). To detect warm dust with mid-IR interferometry at N band, several observational data, e.g., VLTI/MIDI (Smith, Wyatt, and Haniff, 2012); MMT/BLINC (Liu et al., 2005; Stock et al., 2010); KIN (Mennesson et al., 2014); LBTI/NOMIC (Defrère et al., 2015), were obtained.

A.3 Far-IR observation

Dust is cold, typically ranging from 50-120K, meaning it peaks at a few tens to a hundred µm of their thermal re-emission of absorbed stellar radiation, which is much brighter than their host stars at this region. This is the main reason that most debris disks are easily detected in far-IR observations, e.g., The Infrared Astronomical Satellite (IRAS; Aumann, 1984); The Infrared Space Observatory (ISO; de Muizon, 2005); Wide-field Infrared Survey Explorer (WISE; Maldonado et al., 2017); Herschel Space Observatory/PACS and SPIRE (HSO; Morales et al., 2016); Spitzer/Infrared Spectrograph (Houck et al., 2004); SPICA/SAFARI (Jellema et al., 2017).

In particular, the higher sensitivity and angular resolution of HSO, superior to previous far-infrared telescopes, can help us measure the actual location of the dust, and thus provide many resolved debris disks. HSO has two key programs dedicated to searching for debris disks: Disc Emission via a Bias-free Reconnaissance in the Infrared/Submillimetre (DEBRIS; Matthews et al., 2010; Booth et al., 2013) and DUst around NEarby Stars (DUNES; Eiroa et al., 2010).

A.4 Sub-mm/mm observation

Observations at longer wavelengths are the proper method for observing the emitting grains large enough to trace the larger solids. Thus, these observations have revealed a diversity of debris disks, e.g., debris disks with a narrow/broad ring with/without halos and evidence for interactions with the interstellar medium/planet(s). The advent of interferometers in the sub-mm/mm (e.g. ALMA Partnership et al., 2015; MacGregor et al., 2017; Hughes et al., 2017) with the very long baseline, which provide sufficient angular resolution (i.e., 0.03-3.4" ALMA Partnership et al., 2015), revealed the spatial distribution of large dust grains that are not significantly affected by radiation pressure. Also, sub-mm/mm wavelength observations with sufficient angular resolution are complementary to observations at shorter wavelengths that probe the spatial distribution of smaller dust grains. More than a few dozen debris disks have been spatially resolved using (sub)millimeter interferometry already, and this will be increasing rapidly, e.g., Submillimeter Array (SMA; Hughes et al., 2011; MacGregor et al., 2015); Atacama Large Millimeter/sub-millimeter Array (ALMA; Kóspál et al., 2013; Moór et al., 2013; MacGregor, 2014; Ricci et al.,

---

[1] ASTRO-F was launched on 21 February 2006. After its launch, it was named AKARI

2015a; Moór et al., 2019); Combined Array for Millimeter-wave Astronomy (CARMA; Corder et al., 2009); James Clerk Maxwell Telescope/SCUBA and SCUBA2 (JCMT; Holland et al., 2017); Caltech Submillimeter Observatory (CSO; Backman et al., 2009).

In particular, JCMT has a key program dedicated to searching for debris disks: SCUBA-2 Observations of Nearby Stars (SONS; Holland et al., 2017).

Appendix B

Spatially resolved disks considering different collisional parameters

In this section, simulated observations of spatially resolved disks considering different collisional parameters, e.g., belt eccentricities e_b and the material strength Q_s are present. The panels in Fig. B.1 (see Fig. 5.8 for the radial profile) show simulated observations of spatially resolved disks at different belt eccentricities ($e_\mathrm{b} = 0.2$ and 0.4), different levels of dynamical excitation ($\Delta e_\mathrm{b} = 0.05$, 0.1, and 0.2) for the reference material strength Q_s at wavelengths $\lambda_\mathrm{obs} = 2.2\,\mu\mathrm{m}$, 21 µm, 160 µm, 850 µm, and 3000 µm.

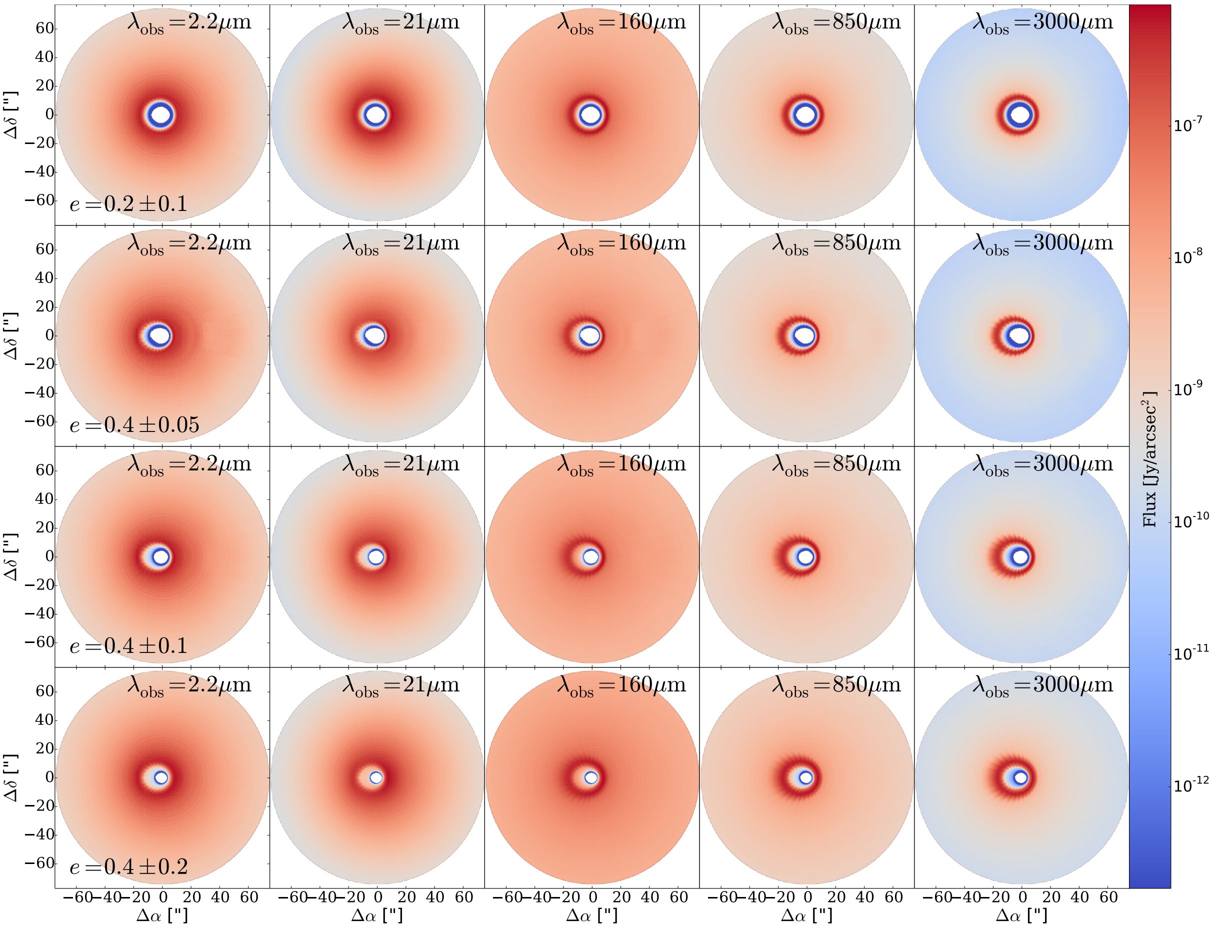

FIGURE B.1: The simulated surface brightness from near-IR to sub-mm wavelengths (λ_{obs} = 2.2 µm, 21 µm, 160 µm, 850 µm, and 3000 µm), for different belt eccentricities (e_{b} = 0.2 and 0.4) and dynamical excitations (Δe_{b} = 0.05, 0.1, and 0.2) for the reference material strength. Both scattered and thermal re-emission are considered.

The panels in Fig. B.2 (see Fig. 5.9 for the radial profile) show simulated observations of spatially resolved disks as a function of the material strength Q_s at wavelengths λ_obs = 2.2 µm, 21 µm, 160 µm, 850 µm, and 3000 µm ($e_\mathrm{b} = 0.4$).

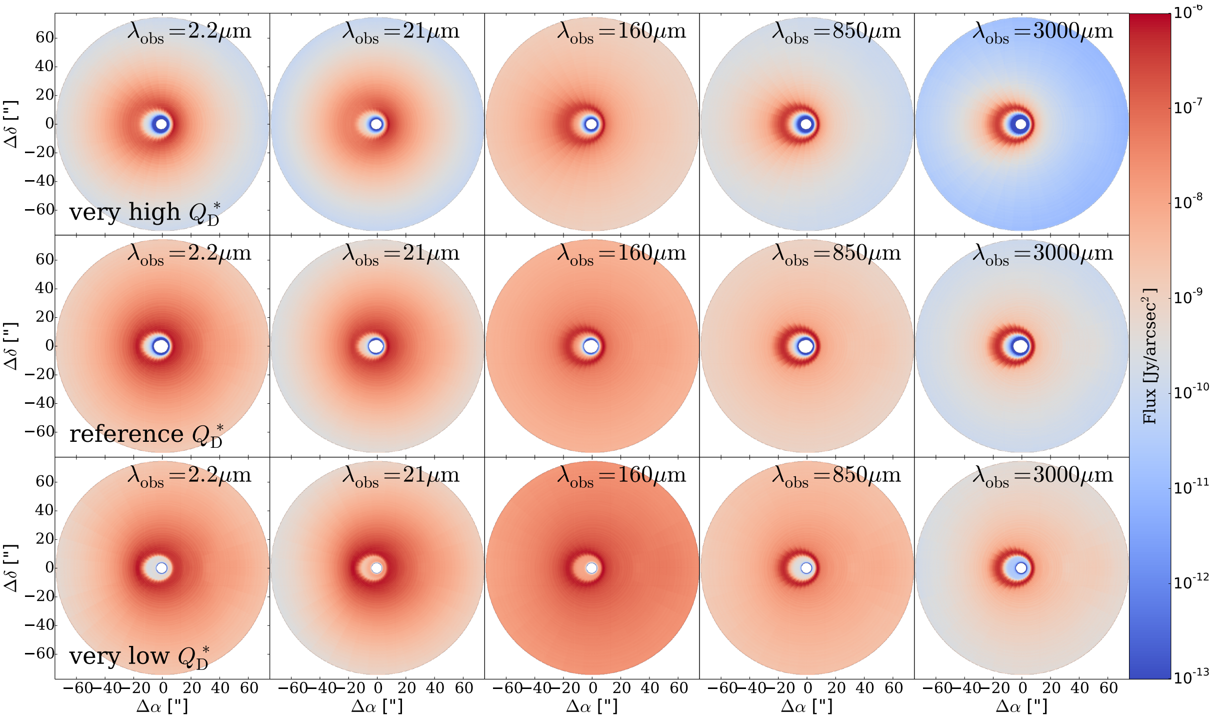

Figure B.2: The simulated surface brightness from near-IR to sub-mm wavelengths at λ_obs = 2.2 µm, 21 µm, 160 µm, 850 µm, and 3000 µm (different material strengths Q_s, fixed belt eccentricities e_b = 0.4). Both scattered and thermal re-emission are considered.

Appendix C

Spatially resolved disks considering different ice dust parameters

In this section, simulated observations of spatially resolved disks considering different ice dust parameters are present. The panels in Fig. C.1 show simulated observations of spatially resolved disks considering different destructive mechanisms of crystalline and amorphous ice, that is, sublimation, collisions, and UV photosputtering (see Fig. 6.11 for the radial profile). The panels in Fig. C.2 show simulated observations of spatially resolved disks considering different fractional ratios of crystalline and amorphous ice $\mathcal{F}_{\text{ice}}$ in the icy-astrosilicate dust aggregates (see Fig. 6.12 for the radial profile). The panels in Fig. C.3 show radial profiles of simulated observations of spatially resolved disks considering different shapes of dust aggregates, that is, inclusion-matrix particles and core-mantle particles with spherical shapes, and inclusion-matrix particles with platelet shapes with the same fractional ratio as ice, that is, $\mathcal{F}_{\text{ice}} = 0.5$ (see Fig. 6.13 for the radial profile).

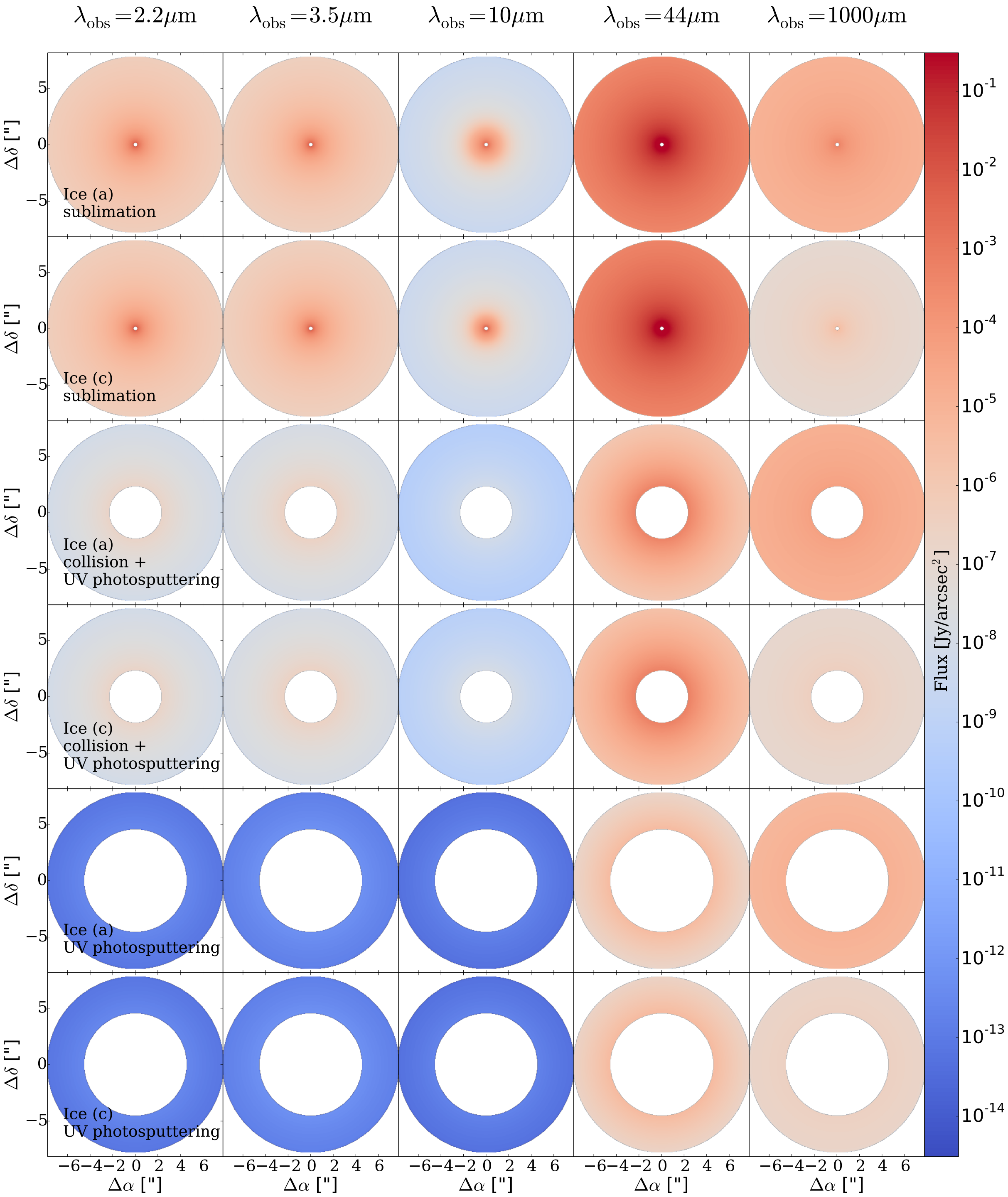

FIGURE C.1: Simulated surface brightness with debris disks composed of pure ice from near-IR to submm wavelengths at $\lambda_{\rm obs}$ = 2.2 µm, 3.5 µm, 10 µm, 44 µm, and 1000 µm. Different mechanisms of ice destruction are considered (indicated in each row). Ice (a) and ice (c) indicate amorphous and crystalline ice, respectively.

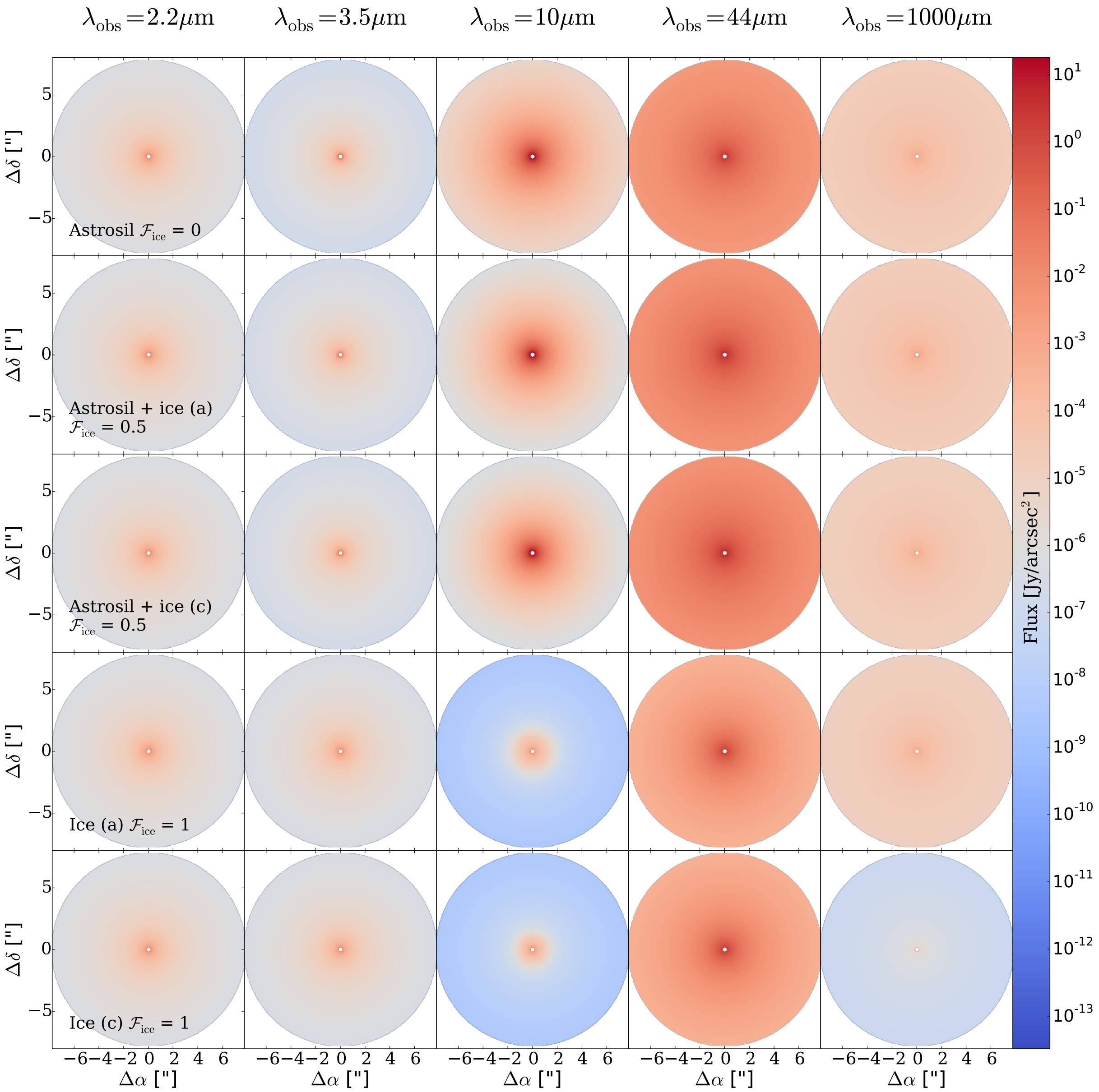

FIGURE C.2: Simulated surface brightness with debris disks composed of the icy dust mixture from near-IR to submm wavelengths at $\lambda_{\rm obs}$ = 2.2 µm, 3.5 µm, 10 µm, 44 µm, and 1000 µm. Different fractional ratios of ice $\mathcal{F}_{\rm ice}$ are considered (indicated in each row). Ice (a), ice (c), and astrosil indicate amorphous ice, crystalline ice, and astrosilicate, respectively.

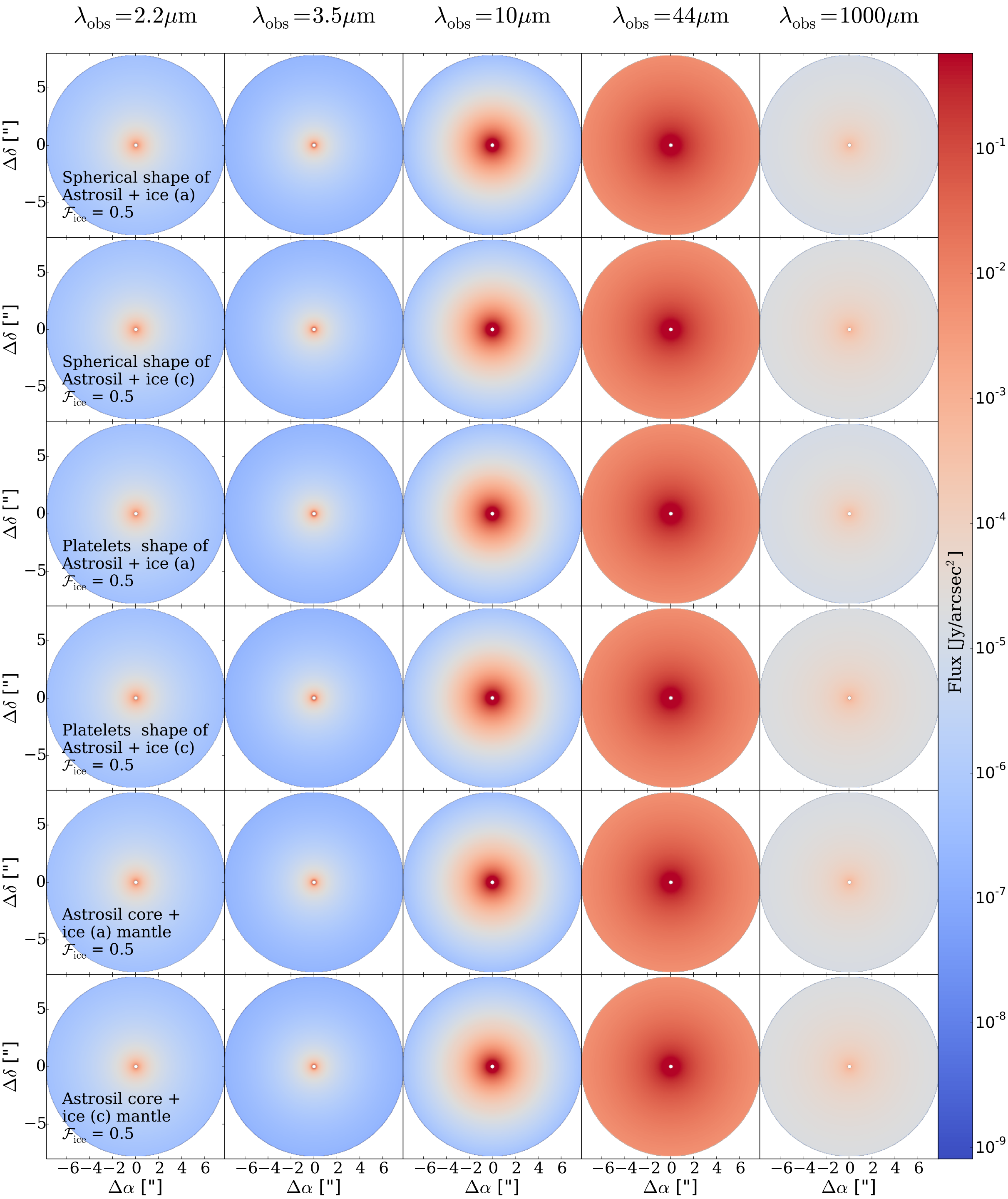

FIGURE C.3: Simulated surface brightness with debris disks composed of the icy dust mixture from near-IR to submm wavelengths at λ_{obs} = 2.2 µm, 3.5 µm, 10 µm, 44 µm, and 1000 µm. Different shapes of icy dust aggregates with the same $\mathcal{F}_{ice}$ = 0.5 are considered (indicated in each row). Ice (a), ice (c), and astrosil indicate amorphous ice, crystalline ice, and astrosilicate, respectively.

Bibliography

Absil, O. et al. (2010). “Do we Need to Solve the Exozodi Question? If Yes, How to Best Solve It?” In: *Pathways Towards Habitable Planets*. Ed. by Vincent Coudé du Foresto, Dawn M. Gelino, and Ignasi Ribas. Vol. 430. Astronomical Society of the Pacific Conference Series, p. 293.

Absil, O. et al. (Nov. 2013). “Searching for companions down to 2 AU from β Pictoris using the L’-band AGPM coronagraph on VLT/NACO”. In: *A&A* 559, L12, p. L12. DOI: `10.1051/0004-6361/201322748`. arXiv: `1311.4298 [astro-ph.SR]`.

Absil, Olivier et al. (Oct. 2009). “An Interferometric Study of the Fomalhaut Inner Debris Disk. I. Near-Infrared Detection of Hot Dust with VLTI/VINCI”. In: *ApJ* 704.1, pp. 150–160. DOI: `10.1088/0004-637X/704/1/150`. arXiv: `0908.3133 [astro-ph.SR]`.

Aikawa, Y. et al. (Feb. 2012). “AKARI observations of ice absorption bands towards edge-on young stellar objects”. In: *A&A* 538, A57, A57. DOI: `10.1051/0004-6361/201015999`.

Alexander, R. et al. (Jan. 2014). “The Dispersal of Protoplanetary Disks”. In: *Protostars and Planets VI*. Ed. by Henrik Beuther et al., p. 475. DOI: `10.2458/azu_uapress_9780816531240-ch021`. arXiv: `1311.1819 [astro-ph.EP]`.

Alexander, R. D. and P. J. Armitage (2007). “Dust dynamics during protoplanetary disc clearing”. In: *MNRAS* 375.2, pp. 500–512. DOI: `10.1111/j.1365-2966.2006.11341.x`. arXiv: `astro-ph/0611821 [astro-ph]`.

Alibert, Y. et al. (2005). “Formation of (exo)planets”. In: *SF2A-2005: Semaine de l’Astrophysique Francaise*. Ed. by F. Casoli et al., p. 173.

Allard, F., D. Homeier, and B. Freytag (2012). “Models of very-low-mass stars, brown dwarfs and exoplanets”. In: *Philosophical Transactions of the Royal Society of London Series A* 370.1968, pp. 2765–2777. DOI: `10.1098/rsta.2011.0269`. arXiv: `1112.3591 [astro-ph.SR]`.

Allen, D. A. and M. V. Penston (Jan. 1973). “Dust temperatures around hot stars.” In: *MNRAS* 165, pp. 121–131. DOI: `10.1093/mnras/165.2.121`.

ALMA Partnership et al. (July 2015). “The 2014 ALMA Long Baseline Campaign: An Overview”. In: *ApJ* 808.1, L1, p. L1. DOI: `10.1088/2041-8205/808/1/L1`. arXiv: `1504.04877 [astro-ph.IM]`.

Andre, Philippe and Thierry Montmerle (1994). “From T Tauri Stars to Protostars: Circumstellar Material and Young Stellar Objects in the rho Ophiuchi Cloud”. In: *ApJ* 420, p. 837. DOI: `10.1086/173608`.

Andre, Philippe, Derek Ward-Thompson, and Mary Barsony (1993). “Submillimeter Continuum Observations of rho Ophiuchi A: The Candidate Protostar VLA 1623 and Prestellar Clumps”. In: *ApJ* 406, p. 122. DOI: `10.1086/172425`.

Ardila, D. R. et al. (2004). “A Resolved Debris Disk around the G2 V Star HD 107146”. In: *ApJ* 617.2, pp. L147–L150. DOI: `10.1086/427434`. arXiv: `astro-ph/0411422 [astro-ph]`.

Armitage, Philip J. (Sept. 2011). “Dynamics of Protoplanetary Disks”. In: *ARA&A* 49.1, pp. 195–236. DOI: `10.1146/annurev-astro-081710-102521`. arXiv: `1011.1496 [astro-ph.SR]`.

Artymowicz, Pawel, Christopher Burrows, and Francesco Paresce (Feb. 1989). “The Structure of the Beta Pictoris Circumstellar Disk From Combined IRAS and Coronagraphic Observations”. In: *ApJ* 337, p. 494. DOI: `10.1086/167118`.

Artymowicz, Pawel and Mark Clampin (Dec. 1997). “Dust around Main-Sequence Stars: Nature or Nurture by the Interstellar Medium?” In: *ApJ* 490.2, pp. 863–878. DOI: 10.1086/304889.

Arzoumanian, D. et al. (2011). “Characterizing interstellar filaments with Herschel in IC 5146”. In: *A&A* 529, L6, p. L6. DOI: 10.1051/0004-6361/201116596. arXiv: 1103.0201 [astro-ph.GA].

Augereau, J. C. et al. (Aug. 1999). “On the HR 4796 A circumstellar disk”. In: *A&A* 348, pp. 557–569. arXiv: astro-ph/9906429 [astro-ph].

Aumann, H. H. (1984). “IRAS Observations of Nearby Main-Sequence Dwarfs”. In: 16, p. 483.

Aumann, Hartmut H. and Ronald G. Probst (Feb. 1991). “Search for Vega-like Nearby Stars with 12 Micron Excess”. In: *ApJ* 368, p. 264. DOI: 10.1086/169690.

Backman, D. et al. (Jan. 2009). “Epsilon Eridani’s Planetary Debris Disk: Structure and Dynamics Based on Spitzer and Caltech Submillimeter Observatory Observations”. In: *ApJ* 690.2, pp. 1522–1538. DOI: 10.1088/0004-637X/690/2/1522. arXiv: 0810.4564 [astro-ph].

Backman, Dana E. and Francesco Paresce (1993). “Main-Sequence Stars with Circumstellar Solid Material - the VEGA Phenomenon”. In: ed. by Eugene H. Levy and Jonathan I. Lunine, p. 1253.

Ballering, Nicholas P. et al. (Sept. 2013). “A Trend between Cold Debris Disk Temperature and Stellar Type: Implications for the Formation and Evolution of Wide-orbit Planets”. In: *ApJ* 775.1, 55, p. 55. DOI: 10.1088/0004-637X/775/1/55. arXiv: 1308.2223 [astro-ph.EP].

Ballering, Nicholas P. et al. (June 2016). “A Comprehensive Dust Model Applied to the Resolved Beta Pictoris Debris Disk from Optical to Radio Wavelengths”. In: *ApJ* 823.2, 108, p. 108. DOI: 10.3847/0004-637X/823/2/108. arXiv: 1605.01731 [astro-ph.EP].

Banzatti, A. and K. M. Pontoppidan (Aug. 2015). “An Empirical Sequence of Disk Gap Opening Revealed by Rovibrational CO”. In: *ApJ* 809.2, 167, p. 167. DOI: 10.1088/0004-637X/809/2/167. arXiv: 1507.06650 [astro-ph.EP].

Beck, P. et al. (Feb. 2011). “Goethite as an alternative origin of the 3.1 μm band on dark asteroids”. In: *A&A* 526, A85, A85. DOI: 10.1051/0004-6361/201015851.

Beichman, C. A. et al. (June 2005). “An Excess Due to Small Grains around the Nearby K0 V Star HD 69830: Asteroid or Cometary Debris?” In: *ApJ* 626.2, pp. 1061–1069. DOI: 10.1086/430059. arXiv: astro-ph/0504491 [astro-ph].

Benz, Willy and Erik Asphaug (Nov. 1999). “Catastrophic Disruptions Revisited”. In: *Icarus* 142.1, pp. 5–20. DOI: 10.1006/icar.1999.6204. arXiv: astro-ph/9907117 [astro-ph].

Bertie, J. E. and E. Whalley (Feb. 1967). “Optical Spectra of Orientationally Disordered Crystals. II. Infrared Spectrum of Ice Ih and Ice Ic from 360 to 50 cm^{-1}”. In: *J. Chem. Phys.* 46.4, pp. 1271–1284. DOI: 10.1063/1.1840845.

Besla, Gurtina and Yanqin Wu (Jan. 2007). “Formation of Narrow Dust Rings in Circumstellar Debris Disks”. In: *ApJ* 655.1, pp. 528–540. DOI: 10.1086/509495. arXiv: astro-ph/0609248 [astro-ph].

Beust, H. and P. Valiron (Apr. 2007). “High latitude gas in the <ASTROBJ>β Pictoris</ASTROBJ> system. A possible origin related to falling evaporating bodies”. In: *A&A* 466.1, pp. 201–213. DOI: 10.1051/0004-6361:20053425. arXiv: astro-ph/0701241 [astro-ph].

Beust, H. et al. (Jan. 2014). “An independent determination of Fomalhaut b’s orbit and the dynamical effects on the outer dust belt”. In: *A&A* 561, A43, A43. DOI: 10.1051/0004-6361/201322229. arXiv: 1311.5035 [astro-ph.SR].

Blum, J. and G. Wurm (Sept. 2008). “The growth mechanisms of macroscopic bodies in protoplanetary disks.” In: *ARA&A* 46, pp. 21–56. DOI: 10.1146/annurev.astro.46.060407.145152.

Blum, Jürgen et al. (2006). “The Physics of Protoplanetesimal Dust Agglomerates. I. Mechanical Properties and Relations to Primitive Bodies in the Solar System”. In: *ApJ* 652.2, pp. 1768–1781. DOI: 10.1086/508017.

Bodenheimer, P. and J. B. Pollack (1986). “Calculations of the accretion and evolution of giant planets: The effects of solid cores”. In: *Icarus* 67.3, pp. 391–408. DOI: `10.1016/0019-1035(86)90122-3`.

Bohren, Craig F. and Donald R. Huffman (1983). *Absorption and scattering of light by small particles*.

Bonnefoy, M. et al. (Jan. 2017). “Belt(s) of debris resolved around the Sco-Cen star HIP 67497”. In: *A&A* 597, L7, p. L7. DOI: `10.1051/0004-6361/201628929`. arXiv: `1609.05638 [astro-ph.EP]`.

Bonnell, I. A., C. J. Clarke, and M. R. Bate (May 2006). “The Jeans mass and the origin of the knee in the IMF”. In: *MNRAS* 368.3, pp. 1296–1300. DOI: `10.1111/j.1365-2966.2006.10214.x`. arXiv: `astro-ph/0603444 [astro-ph]`.

Bonsor, A. and M. C. Wyatt (Mar. 2012). “The scattering of small bodies in planetary systems: constraints on the possible orbits of cometary material”. In: *MNRAS* 420.4, pp. 2990–3002. DOI: `10.1111/j.1365-2966.2011.20156.x`. arXiv: `1111.1858 [astro-ph.EP]`.

Booth, Mark et al. (Jan. 2013). “Resolved debris discs around A stars in the Herschel DEBRIS survey”. In: *MNRAS* 428.2, pp. 1263–1280. DOI: `10.1093/mnras/sts117`. arXiv: `1210.0547 [astro-ph.EP]`.

Booth, Mark et al. (Aug. 2017). “The Northern arc of ϵ Eridani’s Debris Ring as seen by ALMA”. In: *MNRAS* 469.3, pp. 3200–3212. DOI: `10.1093/mnras/stx1072`. arXiv: `1705.01560 [astro-ph.EP]`.

Booth, Mark et al. (Jan. 2019). “Deep ALMA search for CO gas in the HD 95086 debris disc”. In: *MNRAS* 482.3, pp. 3443–3452. DOI: `10.1093/mnras/sty2993`. arXiv: `1811.00412 [astro-ph.EP]`.

Borucki, William and David Koch (2010). “Kepler Mission Status, Results, and Plans”. In: EGU General Assembly Conference Abstracts, p. 3890.

Boss, A. P. (1997). “Giant Planet Formation and Wobbling Stars”. In: *American Astronomical Society Meeting Abstracts*. Vol. 191. American Astronomical Society Meeting Abstracts, p. 27.05.

Boulanger, F. et al. (Aug. 1996). “The dust/gas correlation at high Galactic latitude.” In: *A&A* 312, pp. 256–262.

Brande, Jonathan et al. (Jan. 2020). “The Feasibility of Directly Imaging Nearby Cold Jovian Planets with MIRI/JWST”. In: *AJ* 159.1, 18, p. 18. DOI: `10.3847/1538-3881/ab5444`. arXiv: `1911.02022 [astro-ph.EP]`.

Brandeker, A. et al. (2004). “The Gas Disk of β Pictoris”. In: *Debris Disks and the Formation of Planets*. Ed. by Larry Caroff et al. Vol. 324. Astronomical Society of the Pacific Conference Series, p. 228.

Brandl, Bernhard R. et al. (July 2018). “Status of the mid-IR ELT imager and spectrograph (METIS)”. In: *Proc. SPIE*. Vol. 10702. Society of Photo-Optical Instrumentation Engineers (SPIE) Conference Series, 107021U. DOI: `10.1117/12.2311492`.

Brauer, F., C. P. Dullemond, and Th. Henning (Mar. 2008). “Coagulation, fragmentation and radial motion of solid particles in protoplanetary disks”. In: *A&A* 480.3, pp. 859–877. DOI: `10.1051/0004-6361:20077759`. arXiv: `0711.2192 [astro-ph]`.

Breiter, S. and A. A. Jackson (Aug. 1998). “Unified analytical solutions to two-body problems with drag”. In: *MNRAS* 299.1, pp. 237–243. DOI: `10.1046/j.1365-8711.1998.01768.x`.

Briggs, Robert E. (Dec. 1962). “Symposium: Astrometry I: The steady-state space distribution of meteoric particles under the operation of the Poynting-Robertson Effect”. In: *AJ* 67, p. 710. DOI: `10.1086/108799`.

Brown, Robert H. et al. (Mar. 2006). “Composition and Physical Properties of Enceladus’ Surface”. In: *Science* 311.5766, pp. 1425–1428. DOI: `10.1126/science.1121031`.

Brown, W. L., L. J. Lanzerotti, and R. E. Johnson (Nov. 1982). “Fast Ion Bombardment of Ices and its Astrophysical Implications”. In: *Science* 218.4572, pp. 525–531. DOI: `10.1126/science.218.4572.525`.

Brown, Wendy A. and Amandeep S. Bolina (Jan. 2007). “Fundamental data on the desorption of pure interstellar ices”. In: *MNRAS* 374.3, pp. 1006–1014. DOI: `10.1111/j.1365-2966.2006.11216.x`.

Bruggeman, D. A. G. (Jan. 1936). “Berechnung verschiedener physikalischer Konstanten von heterogenen Substanzen. II. Dielektrizitätskonstanten und Leitfähigkeiten von Vielkristallen der nichtregulären Systeme”. In: *Annalen der Physik* 417.7, pp. 645–672. DOI: `10.1002/andp.19364170706`.

Brunngräber, Robert (2018). “Beobachtbarkeit von ausgewählten Strukturen und Staubeigenschaften zirkumstellarer Scheiben in verschiedenen Entwicklungsstadien”. PhD thesis. Faculty of Mathematics and Natural Sciences of the University of Kiel, Germany.

Brunngräber, Robert et al. (Feb. 2017). “The influence of dust grain porosity on the analysis of debris disc observations”. In: *MNRAS* 464.4, pp. 4383–4389. doi: `10.1093/mnras/stw2675`. arXiv: `1610.06372 [astro-ph.SR]`.

Bryden, G. and D. N. C. Lin (Sept. 1999). “The Effects of Gap Formation and Orbital Migration on Planetary Systems”. In: *AAS/Division for Planetary Sciences Meeting Abstracts #31*. AAS/Division for Planetary Sciences Meeting Abstracts, p. 36.06.

Bryden, G. et al. (Sept. 2000). “On the Interaction between Protoplanets and Protostellar Disks”. In: *ApJ* 540.2, pp. 1091–1101. doi: `10.1086/309363`.

Bryden, G. et al. (Nov. 2009). “Planets and Debris Disks: Results from a Spitzer/MIPS Search for Infrared Excess”. In: *ApJ* 705.2, pp. 1226–1236. doi: `10.1088/0004-637X/705/2/1226`.

Buenzli, E. and H. M. Schmid (Sept. 2009). “A grid of polarization models for Rayleigh scattering planetary atmospheres”. In: *A&A* 504.1, pp. 259–276. doi: `10.1051/0004-6361/200911760`. arXiv: `0907.1862 [astro-ph.EP]`.

Bukhari Syed, M. et al. (Jan. 2017). “The Role of Pebble Fragmentation in Planetesimal Formation. I. Experimental Study”. In: *ApJ* 834.2, 145, p. 145. doi: `10.3847/1538-4357/834/2/145`. arXiv: `1609.06914 [astro-ph.EP]`.

Bulger, J. et al. (Aug. 2013). “Submillimeter observations of IRAS and WISE debris disk candidates”. In: *A&A* 556, A119, A119. doi: `10.1051/0004-6361/201321726`. arXiv: `1307.4015 [astro-ph.SR]`.

Burns, J. A., P. L. Lamy, and S. Soter (1979). “Radiation forces on small particles in the solar system”. In: *Icarus* 40.1, pp. 1–48. doi: `10.1016/0019-1035(79)90050-2`.

Butler, R. P. et al. (2006). “Catalog of Nearby Exoplanets”. In: *ApJ* 646.1, pp. 505–522. doi: `10.1086/504701`. arXiv: `astro-ph/0607493 [astro-ph]`.

Campo Bagatin, A. et al. (Dec. 1994). “Wavy size distributions for collisional systems with a small-size cutoff”. In: *Planet. Space Sci.* 42.12, pp. 1079–1092. doi: `10.1016/0032-0633(94)90008-6`.

Carpenter, John M. et al. (2005). “Evolution of Cold Circumstellar Dust around Solar-type Stars”. In: *AJ* 129.2, pp. 1049–1062. doi: `10.1086/427131`. arXiv: `astro-ph/0411020 [astro-ph]`.

Cavallius, M. et al. (Aug. 2019). “Upper limits on the water vapour content of the β Pictoris debris disk”. In: *A&A* 628, A127, A127. doi: `10.1051/0004-6361/201935655`. arXiv: `1906.11106 [astro-ph.EP]`.

Chen, C. H. (2006). “Dust and Gas Debris around Main Sequence Stars”. In: *New Horizons in Astronomy: Frank N. Bash Symposium*. Ed. by Sheila J. Kannappan et al. Vol. 352. Astronomical Society of the Pacific Conference Series, p. 63.

Chen, C. H. et al. (Dec. 2005). “A Spitzer Study of Dusty Disks around Nearby, Young Stars”. In: *ApJ* 634.2, pp. 1372–1384. doi: `10.1086/497124`.

Chen, C. H. et al. (June 2007). “The Dust and Gas Around Beta Pictoris”. In: *In the Spirit of Bernard Lyot: The Direct Detection of Planets and Circumstellar Disks in the 21st Century*, p. 33.

Chen, Christine H., Michael P. Fitzgerald, and Paul S. Smith (Dec. 2008). “A Possible Icy Kuiper Belt around HD 181327”. In: *ApJ* 689.1, pp. 539–544. doi: `10.1086/592567`. arXiv: `0808.2273 [astro-ph]`.

Chiang, E. I. and A. B. Jordan (Dec. 2002). “On the Plutinos and Twotinos of the Kuiper Belt”. In: *AJ* 124.6, pp. 3430–3444. doi: `10.1086/344605`. arXiv: `astro-ph/0210440 [astro-ph]`.

Ciardi, David R. et al. (Oct. 2001). “On the Near-Infrared Size of Vega”. In: *ApJ* 559.2, pp. 1147–1154. doi: `10.1086/322345`. arXiv: `astro-ph/0105561 [astro-ph]`.

Clampin, M. et al. (July 2003). “Hubble Space Telescope ACS Coronagraphic Imaging of the Circumstellar Disk around HD 141569A”. In: *AJ* 126.1, pp. 385–392. DOI: `10.1086/375460`. arXiv: `astro-ph/0303605 [astro-ph]`.

Clarke, C. J., A. Gendrin, and M. Sotomayor (2001). “The dispersal of circumstellar discs: the role of the ultraviolet switch”. In: *MNRAS* 328.2, pp. 485–491. DOI: `10.1046/j.1365-8711.2001.04891.x`.

Collings, Mark P. et al. (Nov. 2004). “A laboratory survey of the thermal desorption of astrophysically relevant molecules”. In: *MNRAS* 354.4, pp. 1133–1140. DOI: `10.1111/j.1365-2966.2004.08272.x`.

Collins, Gareth S. et al. (2019). “Planetary Impact Processes in Porous Materials”. In: *Shock Phenomena in Granular and Porous Materials*. Ed. by Tracy J. Vogler and D. Anthony Fredenburg. Cham: Springer International Publishing, pp. 103–136. DOI: `10.1007/978-3-030-23002-9_4`. URL: `https://doi.org/10.1007/978-3-030-23002-9_4`.

Corder, Stuartt et al. (Jan. 2009). “A Resolved Ring of Debris Dust around the Solar Analog HD 107146”. In: *ApJ* 690.1, pp. L65–L68. DOI: `10.1088/0004-637X/690/1/L65`. arXiv: `0811.2713 [astro-ph]`.

Coupeaud, A. et al. (Dec. 2010). “Dust silicate emission in FIR/submm”. In: *SF2A-2010: Proceedings of the Annual meeting of the French Society of Astronomy and Astrophysics*. Ed. by S. Boissier et al., p. 205.

Covino, E. et al. (Dec. 1997). “A study of the Chamaeleon star-forming region from the ROSAT all-sky survey. III. High resolution spectroscopic study”. In: *A&A* 328, pp. 187–202.

Crifo, F. et al. (Aug. 1997). “Beta Pictoris: Back to the ZAMS”. In: *Hipparcos - Venice ’97*. Ed. by R. M. Bonnet et al. Vol. 402. ESA Special Publication, pp. 437–440.

Currie, Thayne et al. (July 2015). “Direct Imaging and Spectroscopy of a Young Extrasolar Kuiper Belt in the Nearest OB Association”. In: *ApJ* 807.1, L7, p. L7. DOI: `10.1088/2041-8205/807/1/L7`. arXiv: `1505.06734 [astro-ph.EP]`.

Currie, Thayne et al. (Feb. 2017). “Subaru/SCExAO First-light Direct Imaging of a Young Debris Disk around HD 36546”. In: *ApJ* 836.1, L15, p. L15. DOI: `10.3847/2041-8213/836/1/L15`. arXiv: `1701.02314 [astro-ph.EP]`.

Curtis, Daniel B. et al. (July 2005). “Measurement of the temperature-dependent optical constants of water ice in the 15-200 μm range”. In: *Appl. Opt.* 44.19, pp. 4102–4118. DOI: `10.1364/AO.44.004102`.

Czechowski, A. and I. Mann (May 2007). “Collisional Vaporization of Dust and Production of Gas in the β Pictoris Dust Disk”. In: *ApJ* 660.2, pp. 1541–1555. DOI: `10.1086/512965`.

D’Angelo, G., R. H. Durisen, and J. J. Lissauer (2010). “Giant Planet Formation”. In: *Exoplanets*. Ed. by S. Seager, pp. 319–346.

Dartois, E. et al. (Oct. 1998). “Detection of the “44 MU m” band of water ice in absorption in combined ISO SWS-LWS spectra”. In: *A&A* 338, pp. L21–L24.

Davies, M. B. et al. (Jan. 2014). “The Long-Term Dynamical Evolution of Planetary Systems”. In: *Protostars and Planets VI*. Ed. by Henrik Beuther et al., p. 787. DOI: `10.2458/azu_uapress_9780816531240-ch034`. arXiv: `1311.6816 [astro-ph.EP]`.

Davis, M. et al. (May 1985). “The evolution of large-scale structure in a universe dominated by cold dark matter”. In: *ApJ* 292, pp. 371–394. DOI: `10.1086/163168`.

de Boer, J. et al. (Nov. 2016). “Multiple rings in the transition disk and companion candidates around RX J1615.3-3255. High contrast imaging with VLT/SPHERE”. In: *A&A* 595, A114, A114. DOI: `10.1051/0004-6361/201629267`. arXiv: `1610.04038 [astro-ph.EP]`.

de Muizon, Marie Jourdain (Aug. 2005). “Debris Discs Around Stars: The 2004 ISO Legacy”. In: *Space Sci. Rev.* 119.1-4, pp. 201–214. DOI: `10.1007/s11214-005-8063-0`.

de Vries, B. L. et al. (Oct. 2012). “Comet-like mineralogy of olivine crystals in an extrasolar proto-Kuiper belt”. In: *Nature* 490.7418, pp. 74–76. DOI: `10.1038/nature11469`. arXiv: `1211.2626 [astro-ph.EP]`.

Debes, John H., Alycia J. Weinberger, and Marc J. Kuchner (Sept. 2009). “Interstellar Medium Sculpting of the HD 32297 Debris Disk”. In: *ApJ* 702.1, pp. 318–326. doi: `10.1088/0004-637X/702/1/318`. arXiv: `0908.4368 [astro-ph.SR]`.

Defrère, D. et al. (Oct. 2011). “Hot exozodiacal dust resolved around Vega with IOTA/IONIC”. In: *A&A* 534, A5, A5. doi: `10.1051/0004-6361/201117017`. arXiv: `1108.3698 [astro-ph.EP]`.

Defrère, D. et al. (2015). “Exoplanet science with the LBTI: instrument status and plans”. In: *Proc. SPIE*. Vol. 9605. Society of Photo-Optical Instrumentation Engineers (SPIE) Conference Series, 96051G. doi: `10.1117/12.2188912`.

Defrère, D. et al. (July 2018). “Hi-5: a potential high-contrast thermal near-infrared imager for the VLTI”. In: *Proc. SPIE*. Vol. 10701. Society of Photo-Optical Instrumentation Engineers (SPIE) Conference Series, 107010U. doi: `10.1117/12.2313700`. arXiv: `1807.07467 [astro-ph.IM]`.

Deirmendjian, D. (1969). *Electromagnetic scattering on spherical polydispersions.*

Dent, W. et al. (Jan. 2000). “HARP and ACSIS on the JCMT”. In: *Imaging at Radio through Submillimeter Wavelengths*. Ed. by Jeffrey G. Mangum and Simon J. E. Radford. Vol. 217. Astronomical Society of the Pacific Conference Series, p. 33.

Dent, W. R. F. et al. (Mar. 2014). “Molecular Gas Clumps from the Destruction of Icy Bodies in the β Pictoris Debris Disk”. In: *Science* 343.6178, pp. 1490–1492. doi: `10.1126/science.1248726`. arXiv: `1404.1380 [astro-ph.SR]`.

Di Folco, E. et al. (Nov. 2004). “VLTI near-IR interferometric observations of Vega-like stars. Radius and age of α PsA, β Leo, β Pic, $\in$ Eri and τ Cet”. In: *A&A* 426, pp. 601–617. doi: `10.1051/0004-6361:20047189`.

Dohnanyi, J. S. (May 1969). “Collisional Model of Asteroids and Their Debris”. In: *J. Geophys. Res.* 74, pp. 2531–2554. doi: `10.1029/JB074i010p02531`.

Dominik, C. and G. Decin (2003). “Age Dependence of the Vega Phenomenon: Theory”. In: *ApJ* 598.1, pp. 626–635. doi: `10.1086/379169`. arXiv: `astro-ph/0308364 [astro-ph]`.

Dominik, C. et al. (Dec. 2005). “Gas-Phase Water in the Surface Layer of Protoplanetary Disks”. In: *ApJ* 635.1, pp. L85–L88. doi: `10.1086/498942`. arXiv: `astro-ph/0510635 [astro-ph]`.

Dominik, C. et al. (2007). “Growth of Dust as the Initial Step Toward Planet Formation”. In: ed. by Bo Reipurth, David Jewitt, and Klaus Keil, p. 783. arXiv: `astro-ph/0602617 [astro-ph]`.

Dong, Ruobing, Zhaohuan Zhu, and Barbara Whitney (Aug. 2015). “Observational Signatures of Planets in Protoplanetary Disks I. Gaps Opened by Single and Multiple Young Planets in Disks”. In: *ApJ* 809.1, 93, p. 93. doi: `10.1088/0004-637X/809/1/93`. arXiv: `1411.6063 [astro-ph.EP]`.

Draine, B. T. (Jan. 2003). “Interstellar Dust Grains”. In: *ARA&A* 41, pp. 241–289. doi: `10.1146/annurev.astro.41.011802.094840`. arXiv: `astro-ph/0304489 [astro-ph]`.

— (Jan. 2006). “On the Submillimeter Opacity of Protoplanetary Disks”. In: *ApJ* 636.2, pp. 1114–1120. doi: `10.1086/498130`. arXiv: `astro-ph/0507292 [astro-ph]`.

Draine, B. T. and H. M. Lee (Oct. 1984). “Optical Properties of Interstellar Graphite and Silicate Grains”. In: *ApJ* 285, p. 89. doi: `10.1086/162480`.

Dullemond, C. P. and C. Dominik (July 2004). “The effect of dust settling on the appearance of protoplanetary disks”. In: *A&A* 421, pp. 1075–1086. doi: `10.1051/0004-6361:20040284`. arXiv: `astro-ph/0405226 [astro-ph]`.

— (2005). “Dust coagulation in protoplanetary disks: A rapid depletion of small grains”. In: *A&A* 434.3, pp. 971–986. doi: `10.1051/0004-6361:20042080`. arXiv: `astro-ph/0412117 [astro-ph]`.

Duquennoy, A. and M. Mayor (1991). “Multiplicity among solar-type stars in the solar neighbourhood. II - Distribution of the orbital elements in an unbiased sample.” In: *A&A* 500, pp. 337–376.

Durda, Daniel D. and Stanley F. Dermott (Nov. 1997). “The Collisional Evolution of the Asteroid Belt and Its Contribution to the Zodiacal Cloud”. In: *Icarus* 130.1, pp. 140–164. DOI: `10.1006/icar.1997.5803`.

Durda, Daniel D., Richard Greenberg, and Robert Jedicke (Oct. 1998). “Collisional Models and Scaling Laws: A New Interpretation of the Shape of the Main-Belt Asteroid Size Distribution”. In: *Icarus* 135.2, pp. 431–440. DOI: `10.1006/icar.1998.5960`.

Dutrey, A. et al. (Jan. 2014). “Physical and Chemical Structure of Planet-Forming Disks Probed by Millimeter Observations and Modeling”. In: *Protostars and Planets VI*. Ed. by Henrik Beuther et al., p. 317. DOI: `10.2458/azu_uapress_9780816531240-ch014`. arXiv: `1402.3503 [astro-ph.GA]`.

Eiroa, C. and Dunes Consortium (2013). “DUNES: DUst around NEarby Stars. A Herschel Open Time Key Programme.” In: *New Quests in Stellar Astrophysics III: A Panchromatic View of Solar-Like Stars, With and Without Planets*. Ed. by M. Chavez et al. Vol. 472. Astronomical Society of the Pacific Conference Series, p. 23.

Eiroa, C. et al. (July 2010). “Cold DUst around NEarby Stars (DUNES). First results. A resolved exo-Kuiper belt around the solar-like star ζ^2 Ret”. In: *A&A* 518, L131, p. L131. DOI: `10.1051/0004-6361/201014594`. arXiv: `1005.3151 [astro-ph.SR]`.

Eisner, J. A. (May 2007). “Water vapour and hydrogen in the terrestrial-planet-forming region of a protoplanetary disk”. In: *Nature* 447.7144, pp. 562–564. DOI: `10.1038/nature05867`. arXiv: `0706.1239 [astro-ph]`.

Ertel, S., S. Wolf, and J. Rodmann (Aug. 2012). “Observing planet-disk interaction in debris disks”. In: *A&A* 544, A61, A61. DOI: `10.1051/0004-6361/201219236`. arXiv: `1206.3154 [astro-ph.IM]`.

Ertel, S. et al. (Sept. 2011). “Multi-wavelength modeling of the spatially resolved debris disk of HD 107146”. In: *A&A* 533, A132, A132. DOI: `10.1051/0004-6361/201015910`. arXiv: `1107.1057 [astro-ph.SR]`.

Ertel, S. et al. (Oct. 2014). “A near-infrared interferometric survey of debris-disk stars. IV. An unbiased sample of 92 southern stars observed in H band with VLTI/PIONIER”. In: *A&A* 570, A128, A128. DOI: `10.1051/0004-6361/201424438`. arXiv: `1409.6143 [astro-ph.EP]`.

Ertel, Steve (Jan. 2012). “Modeling the spatial structure of debris disks”. PhD thesis. Faculty of Mathematics and Natural Sciences of the University of Kiel, Germany.

Ertel, Steve et al. (Mar. 2020). “The HOSTS survey for exozodiacal dust: Observational results from the complete survey”. In: *arXiv e-prints*, arXiv:2003.03499, arXiv:2003.03499. arXiv: `2003.03499 [astro-ph.SR]`.

Esposito, Thomas et al. (Jan. 2011). “Keck Adaptive Optics Imaging of the HD 32297 Debris Disk”. In: *American Astronomical Society Meeting Abstracts #217*. Vol. 217. American Astronomical Society Meeting Abstracts, p. 339.03.

Esposito, Thomas M. et al. (Oct. 2016). “Bringing “The Moth” to Light: A Planet-sculpting Scenario for the HD 61005 Debris Disk”. In: *AJ* 152.4, 85, p. 85. DOI: `10.3847/0004-6256/152/4/85`. arXiv: `1605.06161 [astro-ph.EP]`.

Esposito, Thomas M. et al. (Aug. 2018). “Direct Imaging of the HD 35841 Debris Disk: A Polarized Dust Ring from Gemini Planet Imager and an Outer Halo from HST/STIS”. In: *AJ* 156.2, 47, p. 47. DOI: `10.3847/1538-3881/aacbc9`. arXiv: `1806.02904 [astro-ph.EP]`.

Fang, M. et al. (Jan. 2013). “Young stars in ϵ Chamaleontis and their disks: disk evolution in sparse associations”. In: *A&A* 549, A15, A15. DOI: `10.1051/0004-6361/201118528`. arXiv: `1209.5832 [astro-ph.SR]`.

Faramaz, V. et al. (Mar. 2014). “Can eccentric debris disks be long-lived?. A first numerical investigation and application to ζ^2 Reticuli”. In: *A&A* 563, A72, A72. DOI: `10.1051/0004-6361/201322469`. arXiv: `1312.5146 [astro-ph.EP]`.

Faramaz, Virginie et al. (2019). “From Scattered-light to Millimeter Emission: A Comprehensive View of the Gigayear-old System of HD 202628 and its Eccentric Debris Ring”. In: *AJ* 158.4, 162, p. 162. DOI: `10.3847/1538-3881/ab3ec1`. arXiv: `1909.04162 [astro-ph.EP]`.

Fedele, D. et al. (Feb. 2010). “Timescale of mass accretion in pre-main-sequence stars”. In: *A&A* 510, A72, A72. doi: 10.1051/0004-6361/200912810. arXiv: 0911.3320 [astro-ph.SR].

Feistel, Rainer and Wolfgang Wagner (Jan. 2007). “Sublimation pressure and sublimation enthalpy of H $_2$O ice Ih between 0 and 273.16 K”. In: *Geochim. Cosmochim. Acta* 71.1, pp. 36–45. doi: 10.1016/j.gca.2006.08.034.

Feldt, M. et al. (May 2017). “SPHERE/SHINE reveals concentric rings in the debris disk of HIP 73145”. In: *A&A* 601, A7, A7. doi: 10.1051/0004-6361/201629261. arXiv: 1612.07621 [astro-ph.SR].

Fitzgerald, Michael P. et al. (Nov. 2007). “The AU Microscopii Debris Disk: Multiwavelength Imaging and Modeling”. In: *ApJ* 670.1, pp. 536–556. doi: 10.1086/521344. arXiv: 0705.4196 [astro-ph].

Franciosini, E. et al. (Aug. 2018). “The Gaia DR2 view of the Gamma Velorum cluster: resolving the 6D structure”. In: *A&A* 616, L12, p. L12. doi: 10.1051/0004-6361/201833815. arXiv: 1807.03621 [astro-ph.SR].

Fraser, Helen J. et al. (Nov. 2001). “Thermal desorption of water ice in the interstellar medium”. In: *MNRAS* 327.4, pp. 1165–1172. doi: 10.1046/j.1365-8711.2001.04835.x. arXiv: astro-ph/0107487 [astro-ph].

Fujiwara, Hideaki et al. (Nov. 2012). “The Absence of Cold Dust around Warm Debris Disk Star HD 15407A”. In: *ApJ* 759.1, L18, p. L18. doi: 10.1088/2041-8205/759/1/L18. arXiv: 1210.0587 [astro-ph.EP].

Gaia Collaboration et al. (Aug. 2018). “Gaia Data Release 2. The celestial reference frame (Gaia-CRF2)”. In: *A&A* 616, A14, A14. doi: 10.1051/0004-6361/201832916. arXiv: 1804.09377 [astro-ph.GA].

Gammie, Charles F. (2001). “Nonlinear Outcome of Gravitational Instability in Cooling, Gaseous Disks”. In: *ApJ* 553.1, pp. 174–183. doi: 10.1086/320631. arXiv: astro-ph/0101501 [astro-ph].

Gáspár, András et al. (July 2012). “Modeling Collisional Cascades in Debris Disks: Steep Dust-size Distributions”. In: *ApJ* 754.1, 74, p. 74. doi: 10.1088/0004-637X/754/1/74. arXiv: 1111.0296 [astro-ph.SR].

Goertz, C. K. (May 1989). “Dusty plasma in the solar system”. In: *Reviews of Geophysics* 27.2, pp. 271–292. doi: 10.1029/RG027i002p00271.

Goicoechea, J. et al. (2011). In: *SPICA Yellow book* 3.

Goldreich, Peter, Yoram Lithwick, and Re’em Sari (2004). “Final Stages of Planet Formation”. In: *ApJ* 614.1, pp. 497–507. doi: 10.1086/423612. arXiv: astro-ph/0404240 [astro-ph].

Golimowski, D. A. et al. (June 2006). “Hubble Space Telescope ACS Multiband Coronagraphic Imaging of the Debris Disk around β Pictoris”. In: *AJ* 131.6, pp. 3109–3130. doi: 10.1086/503801. arXiv: astro-ph/0602292 [astro-ph].

Gor’kavyi, N. et al. (Dec. 1997). “The Zodiacal Emission at Different Places of the Solar System and the Choice of a Site for the NGST”. In: *American Astronomical Society Meeting Abstracts*. Vol. 191. American Astronomical Society Meeting Abstracts, p. 64.02.

Graham, James R., Paul G. Kalas, and Brenda C. Matthews (Jan. 2007). “The Signature of Primordial Grain Growth in the Polarized Light of the AU Microscopii Debris Disk”. In: *ApJ* 654.1, pp. 595–605. doi: 10.1086/509318. arXiv: astro-ph/0609332 [astro-ph].

Gray, Richard O. et al. (Dec. 2006). “Results from the Nearby Stars (NStars) Program: Candidate Solar Twinsand Chromospheric Diversity in G and K dwarfs”. In: *American Astronomical Society Meeting Abstracts*. Vol. 209. American Astronomical Society Meeting Abstracts, p. 89.02.

Greaves, J. S. and W. S. Holland (1999). “Ambipolar diffusion in magnetized cloud cores”. In: *MNRAS* 302.3, pp. L45–L48. doi: 10.1046/j.1365-8711.1999.02243.x.

Greaves, J. S., M. C. Wyatt, and G. Bryden (Aug. 2009). “Debris discs around nearby solar analogues”. In: *MNRAS* 397.2, pp. 757–762. doi: 10.1111/j.1365-2966.2009.15048.x. arXiv: 0907.3677 [astro-ph.GA].

Greaves, J. S. et al. (Oct. 1998). “A Dust Ring around $\in$ Eridani: Analog to the Young Solar System”. In: *ApJ* 506.2, pp. L133–L137. doi: 10.1086/311652. arXiv: astro-ph/9808224 [astro-ph].

Greaves, J. S. et al. (Feb. 2005). “Structure in the $\in$ Eridani Debris Disk”. In: *ApJ* 619.2, pp. L187–L190. doi: 10.1086/428348.

Greenberg, J. M. and C. E. P. M. Vandebult (Jan. 1984). “The 3 micron ice band.” In: *Occasional Reports of the Royal Observatory Edinburgh* 12, pp. 70–81.

Grigorieva, A., P. Artymowicz, and Ph. Thébault (Jan. 2007). “Collisional dust avalanches in debris discs”. In: *A&A* 461.2, pp. 537–549. doi: `10.1051/0004-6361:20065210`. arXiv: `astro-ph/0609025 [astro-ph]`.

Grigorieva, A. et al. (Nov. 2007). “Survival of icy grains in debris discs. The role of photosputtering”. In: *A&A* 475.2, pp. 755–764. doi: `10.1051/0004-6361:20077686`. arXiv: `0709.0811 [astro-ph]`.

Gustafson, B. A. S. (Jan. 1994). “Physics of Zodiacal Dust”. In: *Annual Review of Earth and Planetary Sciences* 22, pp. 553–595. doi: `10.1146/annurev.ea.22.050194.003005`.

Güttler, C. et al. (2010). “Collisional Evolution of Many-Particle Systems in Astrophysics”. In: *Next-Generation Suborbital Researchers Conference*. Vol. 1534, pp. 36–37.

Haisch Karl E., Jr., Elizabeth A. Lada, and Charles J. Lada (2001). “Disk Frequencies and Lifetimes in Young Clusters”. In: *ApJ* 553.2, pp. L153–L156. doi: `10.1086/320685`. arXiv: `astro-ph/0104347 [astro-ph]`.

Harwit, Martin (Apr. 1963). “Origins of the Zodiacal Dust Cloud”. In: *J. Geophys. Res.* 68.8, pp. 2171–2180. doi: `10.1029/JZ068i008p02171`.

Häßner, Denny et al. (Dec. 2018). “Laboratory measurements of the sub-millimetre opacity of amorphous and micro-particulate H_2O ices for temperatures above 80 K”. In: *MNRAS* 481.4, pp. 5022–5033. doi: `10.1093/mnras/sty2664`.

Hatzes, Artie P. et al. (Dec. 2000). “Evidence for a Long-Period Planet Orbiting ϵ Eridani”. In: *ApJ* 544.2, pp. L145–L148. doi: `10.1086/317319`. arXiv: `astro-ph/0009423 [astro-ph]`.

Hauschildt, Peter H. et al. (Nov. 1999). “The NEXTGEN Model Atmosphere Grid. II. Spherically Symmetric Model Atmospheres for Giant Stars with Effective Temperatures between 3000 and 6800 K”. In: *ApJ* 525.2, pp. 871–880. doi: `10.1086/307954`. arXiv: `astro-ph/9907194 [astro-ph]`.

Henning, T. and F. Salama (Dec. 1998). “Carbon in the Universe”. In: *Science* 282, p. 2204. doi: `10.1126/science.282.5397.2204`.

Higuchi, Aya E. et al. (Apr. 2017). “Detection of Submillimeter-wave [C I] Emission in Gaseous Debris Disks of 49 Ceti and β Pictoris”. In: *ApJ* 839.1, L14, p. L14. doi: `10.3847/2041-8213/aa67f4`. arXiv: `1703.06661 [astro-ph.SR]`.

Hildebrand, R. H. (Sept. 1983). “The determination of cloud masses and dust characteristics from submillimetre thermal emission.” In: *QJRAS* 24, pp. 267–282.

Hillenbrand, Lynne (2008). *The Association of Dust Disks and Planets*. Keck Observatory Archive HIRES.

Hinkley, Sasha et al. (Aug. 2009). “Speckle Suppression Through Dual Imaging Polarimetry, and a Ground-based Image of the HR 4796A Circumstellar Disk”. In: *ApJ* 701.1, pp. 804–810. doi: `10.1088/0004-637X/701/1/804`. arXiv: `0906.3010 [astro-ph.IM]`.

Holland, W. et al. (2010). “Debris Disks: Signposts to planetary systems Prospects for the next decade”. In: *A White Paper for the Astro2010 Decadal Survey Submitted to the "Planetary and Star Formation" Panel*.

Holland, W. S. et al. (Jan. 2003). “Submillimeter Observations of an Asymmetric Dust Disk around Fomalhaut”. In: *ApJ* 582.2, pp. 1141–1146. doi: `10.1086/344819`.

Holland, Wayne S. et al. (Apr. 1998). “Submillimetre images of dusty debris around nearby stars”. In: *Nature* 392.6678, pp. 788–791. doi: `10.1038/33874`.

Holland, Wayne S. et al. (Sept. 2017). “SONS: The JCMT legacy survey of debris discs in the submillimetre”. In: *MNRAS* 470.3, pp. 3606–3663. doi: `10.1093/mnras/stx1378`. arXiv: `1706.01218 [astro-ph.SR]`.

Hollenbach, D. and F. C. Adams (2004). “Dispersal of Disks Around Young Stars: Constraints on Kuiper Belt Formation”. In: *Debris Disks and the Formation of Planets*. Ed. by Larry Caroff et al. Vol. 324. Astronomical Society of the Pacific Conference Series, p. 168.

Holsapple, K. et al. (2002). “Asteroid Impacts: Laboratory Experiments and Scaling Laws”. In: *Asteroids III*, pp. 443–462.

Holsapple, K. A. (Dec. 1994). “Catastrophic disruptions and cratering of solar system bodies: a review and new results”. In: *Planet. Space Sci.* 42.12, pp. 1067–1078. DOI: `10.1016/0032-0633(94)90007-8`.

Honda, M. et al. (Jan. 2009). “Detection of Water Ice Grains on the Surface of the Circumstellar Disk Around HD 142527”. In: *ApJ* 690.2, pp. L110–L113. DOI: `10.1088/0004-637X/690/2/L110`.

Honda, M. et al. (Apr. 2016). “Water Ice at the Surface of the HD 100546 Disk”. In: *ApJ* 821.1, 2, p. 2. DOI: `10.3847/0004-637X/821/1/2`. arXiv: `1603.09512 [astro-ph.EP]`.

Houck, James R. et al. (2004). “The infrared spectrograph on the Spitzer Space Telescope”. In: *Proc. SPIE*. Ed. by John C. Mather. Vol. 5487. Society of Photo-Optical Instrumentation Engineers (SPIE) Conference Series, pp. 62–76. DOI: `10.1117/12.550517`.

Hough, J. H. et al. (Nov. 1989). “Spectropolarimetry of the 3-μm ice feature in molecular clouds. II. GL 2591, GL 2136, W33A and Elias 29 (ρ Ophiuchi dark cloud).” In: *MNRAS* 241, pp. 71–88. DOI: `10.1093/mnras/241.1.71`.

Hubickyj, Olenka, Peter Bodenheimer, and Jack J. Lissauer (2005). “Accretion of the gaseous envelope of Jupiter around a 5 10 Earth-mass core”. In: *Icarus* 179.2, pp. 415–431. DOI: `10.1016/j.icarus.2005.06.021`.

Hudgins, D. M. et al. (June 1993). “Mid- and Far-Infrared Spectroscopy of Ices: Optical Constants and Integrated Absorbances”. In: *ApJS* 86, p. 713. DOI: `10.1086/191796`.

Hughes, A. Meredith, Gaspard Duchêne, and Brenda C. Matthews (Sept. 2018). “Debris Disks: Structure, Composition, and Variability”. In: *ARA&A* 56, pp. 541–591. DOI: `10.1146/annurev-astro-081817-052035`. arXiv: `1802.04313 [astro-ph.EP]`.

Hughes, A. Meredith et al. (Oct. 2011). “Resolved Submillimeter Observations of the HR 8799 and HD 107146 Debris Disks”. In: *ApJ* 740.1, 38, p. 38. DOI: `10.1088/0004-637X/740/1/38`. arXiv: `1107.3153 [astro-ph.EP]`.

Hughes, A. Meredith et al. (Apr. 2017). “Radial Surface Density Profiles of Gas and Dust in the Debris Disk around 49 Ceti”. In: *ApJ* 839.2, 86, p. 86. DOI: `10.3847/1538-4357/aa6b04`. arXiv: `1704.01972 [astro-ph.EP]`.

Ida, Shigeru and Junichiro Makino (1993). “Scattering of Planetesimals by a Protoplanet: Slowing Down of Runaway Growth”. In: *Icarus* 106.1, pp. 210–227. DOI: `10.1006/icar.1993.1167`.

Ishihara, D. et al. (May 2010). “The AKARI/IRC mid-infrared all-sky survey”. In: *A&A* 514, A1, A1. DOI: `10.1051/0004-6361/200913811`. arXiv: `1003.0270 [astro-ph.IM]`.

Jellema, W. et al. (Nov. 2017). “Safari: instrument design of the far-infrared imaging spectrometer for spica”. In: *Proc. SPIE*. Vol. 10563. Society of Photo-Optical Instrumentation Engineers (SPIE) Conference Series, 105631K. DOI: `10.1117/12.2304105`.

Jewitt, David C., Chadwick A. Trujillo, and Jane X. Luu (Aug. 2000). “Population and Size Distribution of Small Jovian Trojan Asteroids”. In: *AJ* 120.2, pp. 1140–1147. DOI: `10.1086/301453`. arXiv: `astro-ph/0004117 [astro-ph]`.

Johnson, R. E. (Nov. 1989). “Effect of irradiation on the surface of Pluto”. In: *Geophys. Res. Lett.* 16.11, pp. 1233–1236. DOI: `10.1029/GL016i011p01233`.

Jura, M. et al. (Oct. 1998). “A Protocometary Cloud around HR 4796A?” In: *ApJ* 505.2, pp. 897–902. DOI: `10.1086/306184`.

Jura, M. et al. (2007). “Infrared Emission from the Dusty Disk Orbiting GD 362, an Externally Polluted White Dwarf”. In: *AJ* 133.5, pp. 1927–1933. DOI: `10.1086/512734`. arXiv: `astro-ph/0701469 [astro-ph]`.

Kalas, Paul, James R. Graham, and Mark Clampin (2005). “A planetary system as the origin of structure in Fomalhaut’s dust belt”. In: *Nature* 435.7045, pp. 1067–1070. DOI: `10.1038/nature03601`. arXiv: `astro-ph/0506574 [astro-ph]`.

Kalas, Paul and David Jewitt (Aug. 1995). “Asymmetries in the Beta Pictoris Dust Disk”. In: *AJ* 110, p. 794. DOI: 10.1086/117565.

Kalas, Paul et al. (Dec. 2007). “Discovery of an Extended Debris Disk around the F2 V Star HD 15745”. In: *ApJ* 671.2, pp. L161–L164. DOI: 10.1086/525252. arXiv: 0712.0378 [astro-ph].

Kalas, Paul et al. (Nov. 2008). “Optical Images of an Exosolar Planet 25 Light-Years from Earth”. In: *Science* 322.5906, p. 1345. DOI: 10.1126/science.1166609. arXiv: 0811.1994 [astro-ph].

Kalas, Paul G. et al. (Nov. 2015). “Direct Imaging of an Asymmetric Debris Disk in the HD 106906 Planetary System”. In: *ApJ* 814.1, 32, p. 32. DOI: 10.1088/0004-637X/814/1/32. arXiv: 1510.02747 [astro-ph.EP].

Kamp, I. et al. (Sept. 2018). “Diagnostic value of far-IR water ice features in T Tauri disks”. In: *A&A* 617, A1, A1. DOI: 10.1051/0004-6361/201732368. arXiv: 1804.05324 [astro-ph.EP].

Kaneda, Hidehiro et al. (2016). “SPICA Mid-infrared Instrument (SMI): technical concepts and scientific capabilities”. In: *Proc. SPIE*. Vol. 9904. Society of Photo-Optical Instrumentation Engineers (SPIE) Conference Series, p. 99042I. DOI: 10.1117/12.2232442.

Kant, Immanuel (1755). *Allgemeine Naturgeschichte und Theorie des Himmels*.

Kaufer, A. et al. (Mar. 1999). “Commissioning FEROS, the new high-resolution spectrograph at La-Silla.” In: *The Messenger* 95, pp. 8–12.

Kennedy, G. M. and M. C. Wyatt (June 2010). “Are debris discs self-stirred?” In: *MNRAS* 405.2, pp. 1253–1270. DOI: 10.1111/j.1365-2966.2010.16528.x. arXiv: 1002.3469 [astro-ph.EP].

Kenyon, S. J. and B. C. Bromley (June 2010). “Variations on debris disks. II. (Kenyon+, 2010)”. In: *VizieR Online Data Catalog*, J/ApJS/188/242, J/ApJS/188/242.

Kenyon, Scott J. and Benjamin C. Bromley (Sept. 2002). “Dusty Rings: Signposts of Recent Planet Formation”. In: *ApJ* 577.1, pp. L35–L38. DOI: 10.1086/344084. arXiv: astro-ph/0208155 [astro-ph].

— (2004). “The Size Distribution of Kuiper Belt Objects”. In: *AJ* 128.4, pp. 1916–1926. DOI: 10.1086/423697. arXiv: astro-ph/0406556 [astro-ph].

— (July 2005). “Prospects for Detection of Catastrophic Collisions in Debris Disks”. In: *AJ* 130.1, pp. 269–279. DOI: 10.1086/430461. arXiv: astro-ph/0503551 [astro-ph].

— (2006). “Terrestrial Planet Formation. I. The Transition from Oligarchic Growth to Chaotic Growth”. In: *AJ* 131.3, pp. 1837–1850. DOI: 10.1086/499807. arXiv: astro-ph/0503568 [astro-ph].

— (2008). “Variations on Debris Disks: Icy Planet Formation at 30-150 AU for 1-3 $M_\odot$ Main-Sequence Stars”. In: *ApJS* 179.2, pp. 451–483. DOI: 10.1086/591794. arXiv: 0807.1134 [astro-ph].

Kervella, Pierre et al. (Jan. 2003). “Modeling of Alpha CEN and Procyon Using Vlti Observations”. In: *IAU Joint Discussion*. Vol. 25. IAU Joint Discussion, E57. arXiv: astro-ph/0312068 [astro-ph].

Kim, M. et al. (Oct. 2018). “Impact of planetesimal eccentricities and material strength on the appearance of eccentric debris disks”. In: *A&A* 618, A38, A38. DOI: 10.1051/0004-6361/201833061. arXiv: 1806.02391 [astro-ph.EP].

Kim, M. et al. (Sept. 2019). “Constraining the detectability of water ice in debris disks”. In: *A&A* 629, A141, A141. DOI: 10.1051/0004-6361/201936014. arXiv: 1908.07354 [astro-ph.EP].

Kippenhahn, Rudolf and Alfred Weigert (1994). *Stellar Structure and Evolution*.

Kirchschlager, F. and S. Wolf (Apr. 2013). “Porous dust grains in debris disks”. In: *A&A* 552, A54, A54. DOI: 10.1051/0004-6361/201220486. arXiv: 1302.5275 [astro-ph.SR].

Kirchschlager, Florian et al. (Jan. 2018). “Modelling of mid-infrared interferometric signature of hot exozodiacal dust emission”. In: *MNRAS* 473.2, pp. 2633–2638. DOI: 10.1093/mnras/stx2515. arXiv: 1709.08514 [astro-ph.SR].

Kley, W. (2000). “The Orbital Evolution of Planets in Disks”. In: *Disks, Planetesimals, and Planets*. Ed. by G. Garzón et al. Vol. 219. Astronomical Society of the Pacific Conference Series, p. 69.

Kobayashi, H. et al. (Jan. 2010). "Ice sublimation of dust particles and their detection in the outer solar system". In: *Earth, Planets, and Space* 62.1, pp. 57–61. doi: `10.5047/eps.2009.03.001`.

Kobayashi, H. et al. (Oct. 2011). "Sublimation temperature of circumstellar dust particles and its importance for dust ring formation". In: *Earth, Planets, and Space* 63.10, pp. 1067–1075. doi: `10.5047/eps.2011.03.012`. arXiv: `1104.5627 [astro-ph.EP]`.

Kobayashi, Hiroshi et al. (June 2008). "Dust ring formation due to ice sublimation of radially drifting dust particles under the Poynting Robertson effect in debris disks". In: *Icarus* 195.2, pp. 871–881. doi: `10.1016/j.icarus.2008.02.005`.

Kokubo, Eiichiro and Shigeru Ida (1998). "Oligarchic Growth of Protoplanets". In: *Icarus* 131.1, pp. 171–178. doi: `10.1006/icar.1997.5840`.

Konishi, Mihoko et al. (Feb. 2016). "Discovery of an Inner Disk Component around HD 141569 A". In: *ApJ* 818.2, L23, p. L23. doi: `10.3847/2041-8205/818/2/L23`. arXiv: `1601.06560 [astro-ph.EP]`.

Kóspál, Á. et al. (Oct. 2013). "ALMA Observations of the Molecular Gas in the Debris Disk of the 30 Myr Old Star HD 21997". In: *ApJ* 776.2, 77, p. 77. doi: `10.1088/0004-637X/776/2/77`. arXiv: `1310.5068 [astro-ph.SR]`.

Kral, Q., P. Thébault, and S. Charnoz (Oct. 2013). "LIDT-DD: A new self-consistent debris disc model that includes radiation pressure and couples dynamical and collisional evolution". In: *A&A* 558, A121, A121. doi: `10.1051/0004-6361/201321398`. arXiv: `1308.6502 [astro-ph.EP]`.

Kral, Q. et al. (Jan. 2015). "Signatures of massive collisions in debris discs. A self-consistent numerical model". In: *A&A* 573, A39, A39. doi: `10.1051/0004-6361/201424309`. arXiv: `1409.7609 [astro-ph.EP]`.

Kral, Quentin et al. (Apr. 2017). "Exozodiacal clouds: hot and warm dust around main sequence stars". In: *The Astronomical Review* 13.2, pp. 69–111. doi: `10.1080/21672857.2017.1353202`. arXiv: `1703.02540 [astro-ph.EP]`.

Krause, M. et al. (July 2011). "Thermal conductivity measurements of porous dust aggregates: I. Technique, model and first results". In: *Icarus* 214.1, pp. 286–296. doi: `10.1016/j.icarus.2011.04.024`. arXiv: `1101.2586 [astro-ph.EP]`.

Krist, John E. et al. (Aug. 2012). "Hubble Space Telescope Observations of the HD 202628 Debris Disk". In: *AJ* 144.2, 45, p. 45. doi: `10.1088/0004-6256/144/2/45`. arXiv: `1206.2078 [astro-ph.SR]`.

Krivov, A. V., T. Löhne, and M. Sremčević (Aug. 2006). "Dust distributions in debris disks: effects of gravity, radiation pressure and collisions". In: *A&A* 455.2, pp. 509–519. doi: `10.1051/0004-6361:20064907`.

Krivov, A. V., I. Mann, and N. A. Krivova (Oct. 2000). "Size distributions of dust in circumstellar debris discs". In: *A&A* 362, pp. 1127–1137.

Krivov, A. V. et al. (Jan. 2007). "On the nature of clumps in debris disks". In: *A&A* 462.1, pp. 199–210. doi: `10.1051/0004-6361:20065584`. arXiv: `astro-ph/0610871 [astro-ph]`.

Krivov, A. V. et al. (Dec. 2009). "Can gas in young debris disks be constrained by their radial brightness profiles?" In: *A&A* 507.3, pp. 1503–1516. doi: `10.1051/0004-6361/200912917`. arXiv: `0909.4225 [astro-ph.EP]`.

Krivov, Alexander V. (2010). "Debris disks: seeing dust, thinking of planetesimals and planets". In: *Research in Astronomy and Astrophysics* 10.5, pp. 383–414. doi: `10.1088/1674-4527/10/5/001`. arXiv: `1003.5229 [astro-ph.EP]`.

Krivov, Alexander V. and Mark Booth (Sept. 2018). "Self-stirring of debris discs by planetesimals formed by pebble concentration". In: *MNRAS* 479.3, pp. 3300–3307. doi: `10.1093/mnras/sty1607`. arXiv: `1806.05431 [astro-ph.EP]`.

Krivov, Alexander V., Miodrag Sremčević, and Frank Spahn (Mar. 2005). "Evolution of a Keplerian disk of colliding and fragmenting particles: a kinetic model with application to the Edgeworth Kuiper belt". In: *Icarus* 174.1, pp. 105–134. doi: `10.1016/j.icarus.2004.10.003`.

Krivov, Alexander V. et al. (Nov. 2008). “Collisional and Thermal Emission Models of Debris Disks: Toward Planetesimal Population Properties”. In: *ApJ* 687.1, pp. 608–622. DOI: `10.1086/591507`. arXiv: `0807.0603 [astro-ph]`.

Krivova, Natalia A., Alexander V. Krivov, and Ingrid Mann (Aug. 2000). “The Disk of β Pictoris in the Light of Polarimetric Data”. In: *ApJ* 539.1, pp. 424–434. DOI: `10.1086/309214`.

Kruegel, Endrik (2003). *The physics of interstellar dust*.

Krumholz, Mark R. (2017). *Star Formation*. DOI: `10.1142/10091`.

Kuchner, Marc J. and Matthew J. Holman (May 2003). “The Geometry of Resonant Signatures in Debris Disks with Planets”. In: *ApJ* 588.2, pp. 1110–1120. DOI: `10.1086/374213`. arXiv: `astro-ph/0209261 [astro-ph]`.

Kuchner, Marc J. and Christopher C. Stark (Oct. 2010). “Collisional Grooming Models of the Kuiper Belt Dust Cloud”. In: *AJ* 140.4, pp. 1007–1019. DOI: `10.1088/0004-6256/140/4/1007`. arXiv: `1008.0904 [astro-ph.EP]`.

Lada, C. J. and B. A. Wilking (1984). “The nature of the embedded population in the rho Ophiuchi dark cloud : mid-infrared observations.” In: *ApJ* 287, pp. 610–621. DOI: `10.1086/162719`.

Lagrange, A. and G. Chauvin (Dec. 2012). “β Pictoris, a Laboratory for Planetary Formation Studies”. In: *The Messenger* 150, pp. 39–43.

Lagrange, A. M. et al. (July 2010). “A Giant Planet Imaged in the Disk of the Young Star β Pictoris”. In: *Science* 329.5987, p. 57. DOI: `10.1126/science.1187187`. arXiv: `1006.3314 [astro-ph.EP]`.

Laplace, Pierre Simon (1808). *Exposition Du Systme Du Monde. Paris, Courcier*.

Lawler, S. M. et al. (Nov. 2009). “Explorations Beyond the Snow Line: Spitzer/IRS Spectra of Debris Disks Around Solar-type Stars”. In: *ApJ* 705.1, pp. 89–111. DOI: `10.1088/0004-637X/705/1/89`. arXiv: `0909.0058 [astro-ph.SR]`.

Lebreton, J. et al. (Mar. 2012). “An icy Kuiper belt around the young solar-type star HD 181327”. In: *A&A* 539, A17, A17. DOI: `10.1051/0004-6361/201117714`. arXiv: `1112.3398 [astro-ph.EP]`.

Lecar, M. et al. (Apr. 2006). “On the Location of the Snow Line in a Protoplanetary Disk”. In: *ApJ* 640.2, pp. 1115–1118. DOI: `10.1086/500287`. arXiv: `astro-ph/0602217 [astro-ph]`.

Lecavelier Des Etangs, A., A. Vidal-Madjar, and R. Ferlet (Mar. 1996). “Dust distribution in disks supplied by small bodies: is the β Pictoris disk a gigantic multi-cometary tail?” In: *A&A* 307, pp. 542–550. arXiv: `astro-ph/9508035 [astro-ph]`.

Lee, Eve J. and Eugene Chiang (Aug. 2016). “A Primer on Unifying Debris Disk Morphologies”. In: *ApJ* 827.2, 125, p. 125. DOI: `10.3847/0004-637X/827/2/125`. arXiv: `1605.06118 [astro-ph.EP]`.

Lestrade, J. F. et al. (June 2020). “Debris disks around stars in the NIKA2 era”. In: *European Physical Journal Web of Conferences*. Vol. 228. European Physical Journal Web of Conferences, p. 00015. DOI: `10.1051/epjconf/202022800015`. arXiv: `1911.06250 [astro-ph.EP]`.

Lestrade, Jean-François and Elodie Thilliez (Apr. 2015). “MAMBO image of the debris disk around ϵ Eridani: robustness of the azimuthal structure”. In: *A&A* 576, A72, A72. DOI: `10.1051/0004-6361/201425422`. arXiv: `1503.03097 [astro-ph.EP]`.

Levison, Harold F. and Martin J. Duncan (May 1997). “From the Kuiper Belt to Jupiter-Family Comets: The Spatial Distribution of Ecliptic Comets”. In: *Icarus* 127.1, pp. 13–32. DOI: `10.1006/icar.1996.5637`.

Li, Aigen (Aug. 2008). “Optical Properties of Dust”. In: *arXiv e-prints*, arXiv:0808.4123, arXiv:0808.4123. arXiv: `0808.4123 [astro-ph]`.

Li, Aigen and J. Mayo Greenberg (Mar. 1998). “A comet dust model for the beta Pictoris disk”. In: *A&A* 331, pp. 291–313.

Li, M. P., G. Zhao, and Aigen Li (Nov. 2007). “On the crystallinity of silicate dust in the interstellar medium”. In: *MNRAS* 382.1, pp. L26–L29. DOI: `10.1111/j.1745-3933.2007.00382.x`. arXiv: `0808.4129 [astro-ph]`.

Lieman-Sifry, Jesse et al. (Sept. 2016). “Debris Disks in the Scorpius-Centaurus OB Association Resolved by ALMA”. In: *ApJ* 828.1, 25, p. 25. DOI: `10.3847/0004-637X/828/1/25`. arXiv: `1606.07068 [astro-ph.EP]`.

Lissauer, J. J. (1987). “Timescales for planetary accretion and the structure of the protoplanetary disk”. In: *Icarus* 69.2, pp. 249–265. DOI: `10.1016/0019-1035(87)90104-7`.

Lisse, C. M. et al. (Feb. 2008). “Circumstellar Dust Created by Terrestrial Planet Formation in HD 113766”. In: *ApJ* 673.2, pp. 1106–1122. DOI: `10.1086/523626`. arXiv: `0710.0839 [astro-ph]`.

Liu, Qiong, Tinggui Wang, and Peng Jiang (July 2014). “Bright Debris Disk Candidates Detected with the AKARI/Far-infrared Surveyor”. In: *AJ* 148.1, 3, p. 3. DOI: `10.1088/0004-6256/148/1/3`. arXiv: `1308.5593 [astro-ph.EP]`.

Liu, Wilson M. et al. (Jan. 2005). “Resolved Mid-Infrared Emission around AB Aurigae and V892 Tauri with Adaptive Optics Nulling Interferometric Observations”. In: *ApJ* 618.2, pp. L133–L136. DOI: `10.1086/427922`. arXiv: `astro-ph/0412337 [astro-ph]`.

Löhne, T. et al. (Jan. 2012). “Modelling the huge, Herschel-resolved debris ring around HD 207129”. In: *A&A* 537, A110, A110. DOI: `10.1051/0004-6361/201117731`.

Löhne, T. et al. (Aug. 2017). “Collisions and drag in debris discs with eccentric parent belts”. In: *A&A* 605, A7, A7. DOI: `10.1051/0004-6361/201630297`. arXiv: `1704.08085 [astro-ph.EP]`.

Löhne, Torsten, Alexander V. Krivov, and Jens Rodmann (Feb. 2008). “Long-Term Collisional Evolution of Debris Disks”. In: *ApJ* 673.2, pp. 1123–1137. DOI: `10.1086/524840`. arXiv: `0710.4294 [astro-ph]`.

Lynden-Bell, D. and J. E. Pringle (1974). “The evolution of viscous discs and the origin of the nebular variables.” In: *MNRAS* 168, pp. 603–637. DOI: `10.1093/mnras/168.3.603`.

MacGregor, Meredith (Jan. 2014). “A Resolved Millimeter Emission Belt in the AU Mic Debris Disk”. In: *Exploring the Formation and Evolution of Planetary Systems*. Ed. by Mark Booth, Brenda C. Matthews, and James R. Graham. Vol. 299. IAU Symposium, pp. 313–317. DOI: `10.1017/S1743921313008752`.

MacGregor, Meredith A. et al. (Mar. 2015). “Resolved Millimeter Emission from the HD 15115 Debris Disk”. In: *ApJ* 801.1, 59, p. 59. DOI: `10.1088/0004-637X/801/1/59`. arXiv: `1501.05962 [astro-ph.SR]`.

MacGregor, Meredith A. et al. (Sept. 2016). “ALMA Observations of the Debris Disk of Solar Analog τ Ceti”. In: *ApJ* 828.2, 113, p. 113. DOI: `10.3847/0004-637X/828/2/113`. arXiv: `1607.02513 [astro-ph.SR]`.

MacGregor, Meredith A. et al. (2017). “A Complete ALMA Map of the Fomalhaut Debris Disk”. In: *ApJ* 842.1, 8, p. 8. DOI: `10.3847/1538-4357/aa71ae`. arXiv: `1705.05867 [astro-ph.EP]`.

Maldonado, Raul F. et al. (Nov. 2017). “Infrared excesses in stars with and without planets using revised WISE photometry”. In: *MNRAS* 471.3, pp. 3419–3427. DOI: `10.1093/mnras/stx1766`. arXiv: `1707.04037 [astro-ph.SR]`.

Malfait, K. et al. (May 1999). “The ISO spectrum of the young star HD 142527”. In: *A&A* 345, pp. 181–186.

Mamajek, Eric E., Warrick A. Lawson, and Eric D. Feigelson (Dec. 1999). “A Radio Survey of Older T Tauri Stars in the η Chamaeleontis Cluster”. In: *PASA* 16.3, pp. 257–261. DOI: `10.1071/AS99257`.

Mamajek, Eric E. et al. (Mar. 2012). “Planetary Construction Zones in Occultation: Discovery of an Extrasolar Ring System Transiting a Young Sun-like Star and Future Prospects for Detecting Eclipses by Circumsecondary and Circumplanetary Disks”. In: *AJ* 143.3, 72, p. 72. DOI: `10.1088/0004-6256/143/3/72`. arXiv: `1108.4070 [astro-ph.SR]`.

Mandell, Avi M. (2014). “Oligarchic Growth”. In: *Encyclopedia of Astrobiology*. Ed. by Ricardo Amils et al. Berlin, Heidelberg: Springer Berlin Heidelberg, pp. 1–1. ISBN: 978-3-642-27833-4. DOI: `10.1007/978-3-642-27833-4_1102-4`. URL: `https://doi.org/10.1007/978-3-642-27833-4_1102-4`.

Maness, H. L. et al. (Dec. 2009). “Hubble Space Telescope Optical Imaging of the Eroding Debris Disk HD 61005”. In: *ApJ* 707.2, pp. 1098–1114. DOI: `10.1088/0004-637X/707/2/1098`. arXiv: `0910.5223 [astro-ph.EP]`.

Marino, S. et al. (Oct. 2018). “A gap in the planetesimal disc around HD 107146 and asymmetric warm dust emission revealed by ALMA”. In: *MNRAS* 479.4, pp. 5423–5439. DOI: `10.1093/mnras/sty1790`. arXiv: `1805.01915 [astro-ph.EP]`.

Marion, L. et al. (Oct. 2014). “Searching for faint companions with VLTI/PIONIER. II. 92 main sequence stars from the Exozodi survey”. In: *A&A* 570, A127, A127. DOI: `10.1051/0004-6361/201424780`. arXiv: `1409.6105 [astro-ph.SR]`.

Marsh, K. A. et al. (Feb. 2005). “Image of Fomalhaut Dust Ring at 350 Microns: The Relative Column Density Map Shows Pericenter-Apocenter Asymmetry”. In: *ApJ* 620.1, pp. L47–L50. DOI: `10.1086/428401`. arXiv: `astro-ph/0501140 [astro-ph]`.

Marsh, K. A. et al. (July 2006). “Images of the Vega Dust Ring at 350 and 450 μm: New Clues to the Trappingof Multiple-Sized Dust Particles in Planetary Resonances”. In: *ApJ* 646.1, pp. L77–L80. DOI: `10.1086/506520`. arXiv: `astro-ph/0606347 [astro-ph]`.

Matthews, B. C. et al. (July 2010). “Resolving debris discs in the far-infrared: Early highlights from the DEBRIS survey”. In: *A&A* 518, L135, p. L135. DOI: `10.1051/0004-6361/201014667`. arXiv: `1005.5147 [astro-ph.SR]`.

Matthews, Brenda et al. (Jan. 2014). “Resolved Imaging of the HR 8799 Debris Disk with Herschel”. In: *ApJ* 780.1, 97, p. 97. DOI: `10.1088/0004-637X/780/1/97`. arXiv: `1311.2977 [astro-ph.SR]`.

Maxwell Garnett, J. C. (Jan. 1904). “Colours in Metal Glasses and in Metallic Films”. In: *Philosophical Transactions of the Royal Society of London Series A* 203, pp. 385–420.

Mayor, Michel and Didier Queloz (1995). “A Jupiter-mass companion to a solar-type star”. In: *Nature* 378.6555, pp. 355–359. DOI: `10.1038/378355a0`.

McClure, M. K. et al. (Nov. 2012). “Probing Dynamical Processes in the Planet-forming Region with Dust Mineralogy”. In: *ApJ* 759.1, L10, p. L10. DOI: `10.1088/2041-8205/759/1/L10`. arXiv: `1209.5671 [astro-ph.SR]`.

McClure, M. K. et al. (Feb. 2015). “Detections of Trans-Neptunian Ice in Protoplanetary Disks”. In: *ApJ* 799.2, 162, p. 162. DOI: `10.1088/0004-637X/799/2/162`. arXiv: `1411.7618 [astro-ph.EP]`.

Melis, C. et al. (2010). “The Age of the HD 15407 System and The Epoch of Final Catastrophic Mass Accretion onto Terrestrial Planets Around Sun-like Stars”. In: *ApJ* 717.1, pp. L57–L61. DOI: `10.1088/2041-8205/717/1/L57`. arXiv: `1005.2451 [astro-ph.SR]`.

Mennesson, B. et al. (Dec. 2011). “High-contrast Stellar Observations within the Diffraction Limit at the Palomar Hale Telescope”. In: *ApJ* 743.2, 178, p. 178. DOI: `10.1088/0004-637X/743/2/178`.

Mennesson, B. et al. (Dec. 2014). “Constraining the Exozodiacal Luminosity Function of Main-sequence Stars: Complete Results from the Keck Nuller Mid-infrared Surveys”. In: *ApJ* 797.2, 119, p. 119. DOI: `10.1088/0004-637X/797/2/119`.

Mestel, L. and Jr. Spitzer L. (1956). “Star formation in magnetic dust clouds”. In: *MNRAS* 116, p. 503. DOI: `10.1093/mnras/116.5.503`.

Mie, Gustav (Jan. 1908). “Beiträge zur Optik trüber Medien, speziell kolloidaler Metallösungen”. In: *Annalen der Physik* 330.3, pp. 377–445. DOI: `10.1002/andp.19083300302`.

Milli, J. et al. (Mar. 2017). “Near-infrared scattered light properties of the HR 4796 A dust ring. A measured scattering phase function from 13.6° to 166.6°”. In: *A&A* 599, A108, A108. DOI: `10.1051/0004-6361/201527838`. arXiv: `1701.00750 [astro-ph.EP]`.

Min, M. et al. (Mar. 2011). “The thermal structure and the location of the snow line in the protosolar nebula: Axisymmetric models with full 3-D radiative transfer”. In: *Icarus* 212.1, pp. 416–426. DOI: `10.1016/j.icarus.2010.12.002`. arXiv: `1012.0727 [astro-ph.EP]`.

Mishima, O., D. D. Klug, and E. Whalley (June 1983). “The far-infrared spectrum of ice Ih in the range 8-25 cm^{-1}. Sound waves and difference bands, with application to Saturn’s rings$^{a)}$”. In: *J. Chem. Phys.* 78.11, pp. 6399–6404. DOI: 10.1063/1.444700.

Mittal, Tushar et al. (Jan. 2015). “The Spitzer Infrared Spectrograph Debris Disk Catalog. II. Silicate Feature Analysis of Unresolved Targets”. In: *ApJ* 798.2, 87, p. 87. DOI: 10.1088/0004-637X/798/2/87.

Mizuno, H., K. Nakazawa, and C. Hayashi (1980). “Dissolution of the primordial rare gases into the molten Earth’s material”. In: *Earth and Planetary Science Letters* 50.1, pp. 202–210. DOI: 10.1016/0012-821X(80)90131-4.

Moerchen, Margaret Marie (Jan. 2008). “Location and origin of dust in circumstellar debris disks: A mid-infrared imaging study”. PhD thesis. University of Florida.

Mölders, N. and G Kramm (2014). *Atmospheric Radiation. In: Lectures in Meteorology*.

Molinari, Sergio et al. (Aug. 1999). “Detection of the 62 Micron Crystalline H_2O Ice Feature in Emission toward HH 7 with the Infrared Space Observatory Long-Wavelength Spectrometer”. In: *ApJ* 521.1, pp. L71–L74. DOI: 10.1086/312178.

Monnier, John D. et al. (Feb. 2019). “Multiple Spiral Arms in the Disk around Intermediate-mass Binary HD 34700A”. In: *ApJ* 872.2, 122, p. 122. DOI: 10.3847/1538-4357/aafe87. arXiv: 1901.02467 [astro-ph.EP].

Moór, A. et al. (2006). “Nearby Debris Disk Systems with High Fractional Luminosity Reconsidered”. In: *ApJ* 644.1, pp. 525–542. DOI: 10.1086/503381. arXiv: astro-ph/0603729 [astro-ph].

Moór, A. et al. (Oct. 2011). “Molecular Gas in Young Debris Disks”. In: *ApJ* 740.1, L7, p. L7. DOI: 10.1088/2041-8205/740/1/L7. arXiv: 1109.2299 [astro-ph.SR].

Moór, A. et al. (Nov. 2013). “ALMA Continuum Observations of a 30 Myr Old Gaseous Debris Disk around HD 21997”. In: *ApJ* 777.2, L25, p. L25. DOI: 10.1088/2041-8205/777/2/L25. arXiv: 1310.5069 [astro-ph.SR].

Moór, Attila et al. (Nov. 2017). “Molecular Gas in Debris Disks around Young A-type Stars”. In: *ApJ* 849.2, 123, p. 123. DOI: 10.3847/1538-4357/aa8e4e. arXiv: 1709.08414 [astro-ph.SR].

Moór, Attila et al. (Oct. 2019). “New Millimeter CO Observations of the Gas-rich Debris Disks 49 Cet and HD 32297”. In: *ApJ* 884.2, 108, p. 108. DOI: 10.3847/1538-4357/ab4272. arXiv: 1908.09685 [astro-ph.EP].

Morales, F. Y. et al. (Nov. 2016). “Herschel-resolved Outer Belts of Two-belt Debris Disks—Evidence of Icy Grains”. In: *ApJ* 831.1, 97, p. 97. DOI: 10.3847/0004-637X/831/1/97.

Morales, Farisa Y. et al. (July 2009). “Spitzer Mid-IR Spectra of Dust Debris Around A and Late B Type Stars: Asteroid Belt Analogs and Power-Law Dust Distributions”. In: *ApJ* 699.2, pp. 1067–1086. DOI: 10.1088/0004-637X/699/2/1067.

Morbidelli, A., V. V. Emel’yanenko, and H. F. Levison (Dec. 2004). “Origin and orbital distribution of the trans-Neptunian scattered disc”. In: *MNRAS* 355.3, pp. 935–940. DOI: 10.1111/j.1365-2966.2004.08372.x.

Morbidelli, A. et al. (Nov. 2000). “Source regions and time scales for the delivery of water to Earth”. In: *Meteoritics and Planetary Science* 35.6, pp. 1309–1320. DOI: 10.1111/j.1945-5100.2000.tb01518.x.

Moro-Martín, A. et al. (Jan. 2005). “Signatures of planets in debris disks”. In: *ESA Special Publication*. Ed. by A. Wilson. Vol. 577. ESA Special Publication, pp. 163–166.

Mouschovias, T. Ch. and Jr. Spitzer L. (1976). “Note on the collapse of magnetic interstellar clouds.” In: *ApJ* 210, p. 326. DOI: 10.1086/154835.

Movshovitz, N. et al. (Sept. 2016). “Impact disruption of gravity-dominated bodies: New simulation data and scaling”. In: *Icarus* 275, pp. 85–96. DOI: 10.1016/j.icarus.2016.04.018.

Mukai, T. and T. Yamamoto (Jan. 1979). “A Model of the Circumsolar Dust Cloud”. In: *PASJ* 31, pp. 585–596.

Müller, S., T. Löhne, and A. V. Krivov (Jan. 2010). “The Debris Disk of Vega: A Steady-state Collisional Cascade, Naturally”. In: *ApJ* 708.2, pp. 1728–1747. DOI: 10.1088/0004-637X/708/2/1728. arXiv: 0912.1190 [astro-ph.EP].

Murphy, Simon J., Warrick A. Lawson, and Michael S. Bessell (July 2010). “First detection of a low-mass stellar halo around the young open cluster η Chamaeleontis”. In: *MNRAS* 406.1, pp. L50–L54. DOI: `10.1111/j.1745-3933.2010.00879.x`. arXiv: `1005.3308 [astro-ph.SR]`.

— (July 2012). “RX J0942.7-7726AB: an isolated pre-main-sequence wide binary”. In: *MNRAS* 424.1, pp. 625–634. DOI: `10.1111/j.1365-2966.2012.21243.x`. arXiv: `1205.1510 [astro-ph.SR]`.

Murphy, Simon J. et al. (Feb. 2011). “Episodic disc accretion in the halo of the ‘old’ pre-main-sequence cluster η Chamaeleontis”. In: *MNRAS* 411.1, pp. L51–L55. DOI: `10.1111/j.1745-3933.2010.00992.x`. arXiv: `1011.3816 [astro-ph.SR]`.

Murray, C. D. and S. F. Dermott (1999). *Solar system dynamics*.

Mustill, Alexander J. and Mark C. Wyatt (Nov. 2009). “Debris disc stirring by secular perturbations from giant planets”. In: *MNRAS* 399.3, pp. 1403–1414. DOI: `10.1111/j.1365-2966.2009.15360.x`. arXiv: `0907.1389 [astro-ph.EP]`.

Nagasawa, M. et al. (Jan. 2007). “The Diverse Origins of Terrestrial-Planet Systems”. In: *Protostars and Planets V*. Ed. by Bo Reipurth, David Jewitt, and Klaus Keil, p. 639.

Najita, Joan and Jonathan P. Williams (Dec. 2005). “An 850 μm Survey for Dust around Solar-Mass Stars”. In: *ApJ* 635.1, pp. 625–635. DOI: `10.1086/497159`. arXiv: `astro-ph/0508165 [astro-ph]`.

Nesvold, Erika R. and Marc J. Kuchner (Dec. 2015a). “A SMACK Model of Colliding Planetesimals in the β Pictoris Debris Disk”. In: *ApJ* 815.1, 61, p. 61. DOI: `10.1088/0004-637X/815/1/61`. arXiv: `1506.07187 [astro-ph.EP]`.

— (Jan. 2015b). “Gap Clearing by Planets in a Collisional Debris Disk”. In: *ApJ* 798.2, 83, p. 83. DOI: `10.1088/0004-637X/798/2/83`. arXiv: `1410.7784 [astro-ph.EP]`.

Nesvold, Erika R. et al. (Nov. 2013). “SMACK: A New Algorithm for Modeling Collisions and Dynamics of Planetesimals in Debris Disks”. In: *ApJ* 777.2, 144, p. 144. DOI: `10.1088/0004-637X/777/2/144`. arXiv: `1309.2289 [astro-ph.EP]`.

Nuñez, P. D. et al. (Dec. 2017). “A near-infrared interferometric survey of debris-disc stars. VI. Extending the exozodiacal light survey with CHARA/JouFLU”. In: *A&A* 608, A113, A113. DOI: `10.1051/0004-6361/201730859`. arXiv: `1709.01655 [astro-ph.SR]`.

O’Brien, David P. and Richard Greenberg (Nov. 2005). “The collisional and dynamical evolution of the main-belt and NEA size distributions”. In: *Icarus* 178.1, pp. 179–212. DOI: `10.1016/j.icarus.2005.04.001`.

Oka, Akinori et al. (Mar. 2012). “Effect of Photodesorption on the Snow Lines at the Surface of Optically Thick Circumstellar Disks around Herbig Ae/Be Stars”. In: *ApJ* 747.2, 138, p. 138. DOI: `10.1088/0004-637X/747/2/138`. arXiv: `1201.1961 [astro-ph.EP]`.

Olofsson, Göran, René Liseau, and Alexis Brandeker (Dec. 2001). “Widespread Atomic Gas Emission Reveals the Rotation of the β Pictoris Disk”. In: *ApJ* 563.1, pp. L77–L80. DOI: `10.1086/338354`. arXiv: `astro-ph/0111206 [astro-ph]`.

Olofsson, J. et al. (Nov. 2012). “Transient dust in warm debris disks (Corrigendum). Detection of Fe-rich olivine grains”. In: *A&A* 547, C1, p. C1. DOI: `10.1051/0004-6361/201118735e`.

Olofsson, J. et al. (2016). “Azimuthal asymmetries in the debris disk around HD 61005. A massive collision of planetesimals?” In: *A&A* 591, A108, A108. DOI: `10.1051/0004-6361/201628196`. arXiv: `1601.07861 [astro-ph.SR]`.

Omont, A. et al. (May 1990). “Observations of 40–70 Micron Bands of Ice in IRAS 09371+1212 and Other Stars”. In: *ApJ* 355, p. L27. DOI: `10.1086/185730`.

Ossenkopf, V. (Nov. 1991). “Effective-medium theories for cosmic dust grains”. In: *A&A* 251.1, pp. 210–219.

Pan, Margaret, Erika R. Nesvold, and Marc J. Kuchner (2016). “Apocenter Glow in Eccentric Debris Disks: Implications for Fomalhaut and ∊ Eridani”. In: *ApJ* 832.1, 81, p. 81. doi: `10.3847/0004-637X/832/1/81`. arXiv: `1607.06798 [astro-ph.EP]`.

Panić, O. et al. (Oct. 2013). “First results of the SONS survey: submillimetre detections of debris discs”. In: *MNRAS* 435.2, pp. 1037–1046. doi: `10.1093/mnras/stt1293`.

Pantin, E., P. O. Lagage, and P. Artymowicz (Nov. 1997). “Mid-infrared images and models of the beta Pictoris dust disk”. In: *A&A* 327, pp. 1123–1136.

Paolicchi, P., A. Verlicchi, and A. Cellino (May 1996). “An Improved Semi-Empirical Model of Catastrophic Impact Processes. I: Theory and Laboratory Experiments”. In: *Icarus* 121.1, pp. 126–157. doi: `10.1006/icar.1996.0075`.

Patel, Rahul I., Stanimir A. Metchev, and Aren Heinze (May 2014). “A Sensitive Identification of Warm Debris Disks in the Solar Neighborhood through Precise Calibration of Saturated WISE Photometry”. In: *ApJS* 212.1, 10, p. 10. doi: `10.1088/0067-0049/212/1/10`. arXiv: `1403.3435 [astro-ph.SR]`.

Pawellek, Nicole and Alexander V. Krivov (Dec. 2015). “The dust grain size-stellar luminosity trend in debris discs”. In: *MNRAS* 454.3, pp. 3207–3221. doi: `10.1093/mnras/stv2142`. arXiv: `1509.04032 [astro-ph.SR]`.

Pawellek, Nicole et al. (Sept. 2014). “Disk Radii and Grain Sizes in Herschel-resolved Debris Disks”. In: *ApJ* 792.1, 65, p. 65. doi: `10.1088/0004-637X/792/1/65`. arXiv: `1407.4579 [astro-ph.SR]`.

Payne, Matthew J. et al. (Mar. 2009). “Dynamical simulations of the planetary system HD69830”. In: *MNRAS* 393.4, pp. 1219–1234. doi: `10.1111/j.1365-2966.2008.14338.x`. arXiv: `0812.2475 [astro-ph]`.

Pearce, Tim D., Mark C. Wyatt, and Grant M. Kennedy (Jan. 2014). “Imaged substellar companions: not as eccentric as they appear? The effect of an unseen inner mass on derived orbits”. In: *MNRAS* 437.3, pp. 2686–2701. doi: `10.1093/mnras/stt2080`. arXiv: `1310.7427 [astro-ph.EP]`.

Perri, F. and A. G. W. Cameron (1974). “Hydrodynamic Instability of the Solar Nebula in the Presence of a Planetary Core”. In: *Icarus* 22.4, pp. 416–425. doi: `10.1016/0019-1035(74)90074-8`.

Perrin, Marshall D. et al. (Aug. 2018). “Updated optical modeling of JWST coronagraph performance contrast, stability, and strategies”. In: *Proc. SPIE.* Vol. 10698. Society of Photo-Optical Instrumentation Engineers (SPIE) Conference Series, p. 1069809. doi: `10.1117/12.2313552`.

Perryman, M. A. C. et al. (July 1997). “The Hipparcos Catalogue.” In: *A&A* 500, pp. 501–504.

Pessah, Martin and Oliver Gressel (2017). *Formation, Evolution, and Dynamics of Young Solar Systems*. Vol. 445. doi: `10.1007/978-3-319-60609-5`.

Planck Collaboration et al. (Oct. 2015). “Planck intermediate results. XXV. The Andromeda galaxy as seen by Planck”. In: *A&A* 582, A28, A28. doi: `10.1051/0004-6361/201424643`. arXiv: `1407.5452 [astro-ph.GA]`.

Plavchan, Peter, M. Jura, and S. J. Lipscy (Oct. 2005). “Where Are the M Dwarf Disks Older Than 10 Million Years?” In: *ApJ* 631.2, pp. 1161–1169. doi: `10.1086/432568`. arXiv: `astro-ph/0506132 [astro-ph]`.

Pollack, James B. et al. (Feb. 1994). “Composition and Radiative Properties of Grains in Molecular Clouds and Accretion Disks”. In: *ApJ* 421, p. 615. doi: `10.1086/173677`.

Pollack, James B. et al. (1996). “Formation of the Giant Planets by Concurrent Accretion of Solids and Gas”. In: *Icarus* 124.1, pp. 62–85. doi: `10.1006/icar.1996.0190`.

Pontoppidan, K. M. and S. M. Blevins (May 2014). “The chemistry of planet-forming regions is not interstellar”. In: *Faraday Discussions* 168, pp. 49–60. doi: `10.1039/C3FD00141E`. arXiv: `1406.1457 [astro-ph.EP]`.

Pontoppidan, K. M. and C. P. Dullemond (May 2005). “Projection of circumstellar disks on their environments”. In: *A&A* 435.2, pp. 595–610. doi: `10.1051/0004-6361:20042059`. arXiv: `astro-ph/0502103 [astro-ph]`.

Poppe, Torsten, Jürgen Blum, and Thomas Henning (Apr. 2000). “Experiments on Collisional Grain Charging of Micron-sized Preplanetary Dust”. In: *ApJ* 533.1, pp. 472–480. doi: `10.1086/308631`.

Potapov, Alexey, Cornelia Jäger, and Thomas Henning (Sept. 2018). “Temperature Programmed Desorption of Water Ice from the Surface of Amorphous Carbon and Silicate Grains as Related to Planet-forming Disks”. In: *ApJ* 865.1, 58, p. 58. DOI: `10.3847/1538-4357/aad803`. arXiv: `1806.07673 [astro-ph.GA]`.

— (July 2019). “Photodesorption of Water Ice from Dust Grains and Thermal Desorption of Cometary Ices Studied by the INSIDE Experiment”. In: *ApJ* 880.1, 12, p. 12. DOI: `10.3847/1538-4357/ab25e7`. arXiv: `1905.13465 [astro-ph.IM]`.

Potapov, Alexey et al. (July 2018). “Low-temperature Optical Properties of Interstellar and Circumstellar Icy Silicate Grain Analogs in the Mid-infrared Spectral Region”. In: *ApJ* 861.2, 84, p. 84. DOI: `10.3847/1538-4357/aac6d3`. arXiv: `1803.05810 [astro-ph.GA]`.

Poulton, C. J., J. S. Greaves, and A. Collier Cameron (Oct. 2006). “Detecting a rotation in the ϵ Eridani debris disc”. In: *MNRAS* 372.1, pp. 53–59. DOI: `10.1111/j.1365-2966.2006.10708.x`. arXiv: `astro-ph/0606588 [astro-ph]`.

Poynting, J. H. (Dec. 1903). “Radiation Pressure”. In: *Proceedings of the Physical Society of London* 19.1, pp. 475–490. DOI: `10.1088/1478-7814/19/1/341`.

Pringle, J. E. (1981). “Accretion discs in astrophysics”. In: *ARA&A* 19, pp. 137–162. DOI: `10.1146/annurev.aa.19.090181.001033`.

Queck, Martina et al. (Nov. 2007). “Collisional velocities and rates in resonant planetesimal belts”. In: *Celestial Mechanics and Dynamical Astronomy* 99.3, pp. 169–196. DOI: `10.1007/s10569-007-9095-4`. arXiv: `0707.3369 [astro-ph]`.

Quirrenbach, A. et al. (2016). “CARMENES: an overview six months after first light”. In: *Proc. SPIE*. Vol. 9908. Society of Photo-Optical Instrumentation Engineers (SPIE) Conference Series, p. 990812. DOI: `10.1117/12.2231880`.

Raymond, S. N., T. Quinn, and J. I. Lunine (May 2004). “Making other Earths: Simulations of Terrestrial Planet Formation and Water Delivery”. In: *AAS/Division of Dynamical Astronomy Meeting #35*. AAS/Division of Dynamical Astronomy Meeting, p. 05.03.

Raymond, Sean N. et al. (Oct. 2009). “Building the terrestrial planets: Constrained accretion in the inner Solar System”. In: *Icarus* 203.2, pp. 644–662. DOI: `10.1016/j.icarus.2009.05.016`. arXiv: `0905.3750 [astro-ph.EP]`.

Reche, R. et al. (Mar. 2008). “On the observability of resonant structures in planetesimal disks due to planetary migration”. In: *A&A* 480.2, pp. 551–561. DOI: `10.1051/0004-6361:20077934`. arXiv: `0801.2691 [astro-ph]`.

Reidemeister, M. et al. (Mar. 2011). “The cold origin of the warm dust around ϵ Eridani”. In: *A&A* 527, A57, A57. DOI: `10.1051/0004-6361/201015328`. arXiv: `1011.4882 [astro-ph.EP]`.

Reinert, C. et al. (Jan. 2015). “Absorption of crystalline water ice in the far infrared at different temperatures”. In: *A&A* 573, A29, A29. DOI: `10.1051/0004-6361/201424276`. arXiv: `1409.5651 [astro-ph.EP]`.

Reissl, S., S. Wolf, and R. Brauer (Sept. 2016). “Radiative transfer with POLARIS. I. Analysis of magnetic fields through synthetic dust continuum polarization measurements”. In: *A&A* 593, A87, A87. DOI: `10.1051/0004-6361/201424930`. arXiv: `1604.05305 [astro-ph.IM]`.

Ressler, Michael E. et al. (Mar. 1994). “The JPL deep-well mid-infrared array camera”. In: *Experimental Astronomy* 3.1-4, pp. 277–280. DOI: `10.1007/BF00430176`.

Ricci, L. et al. (2015a). “ALMA Observations of the Debris Disk around the Young Solar Analog HD 107146”. In: *ApJ* 798.2, 124, p. 124. DOI: `10.1088/0004-637X/798/2/124`. arXiv: `1410.8265 [astro-ph.EP]`.

Ricci, L. et al. (2015b). “An ATCA Survey of Debris Disks at 7 Millimeters”. In: *ApJ* 813.2, 138, p. 138. DOI: `10.1088/0004-637X/813/2/138`. arXiv: `1510.03513 [astro-ph.EP]`.

Ricci, L. et al. (2015c). “Highlighting the Dynamical Interaction Between Planets and Planetesimal Belts with ALMA”. In: *Revolution in Astronomy with ALMA: The Third Year*. Ed. by D. Iono et al. Vol. 499. Astronomical Society of the Pacific Conference Series, p. 269.

Riviere-Marichalar, P. et al. (Dec. 2015). “Herschel-PACS observations of discs in the η Chamaeleontis association”. In: *A&A* 584, A22, A22. DOI: `10.1051/0004-6361/201526584`. arXiv: `1510.01594 [astro-ph.SR]`.

Roberge, A. et al. (Aug. 2000). “High-Resolution Hubble Space Telescope STIS Spectra of C I and CO in theβ Pictoris Circumstellar Disk”. In: *ApJ* 538.2, pp. 904–910. DOI: `10.1086/309157`. arXiv: `astro-ph/0003446 [astro-ph]`.

Robertson, H. P. (Apr. 1937). “Dynamical effects of radiation in the solar system”. In: *MNRAS* 97, p. 423. DOI: `10.1093/mnras/97.6.423`.

Robinson, G., R. G. Smith, and A. R. Hyland (June 1992). “A spherical circumstellar dust model for IRAS 09371+1212.” In: *MNRAS* 256, pp. 437–448. DOI: `10.1093/mnras/256.3.437`.

Roccatagliata, V. et al. (Apr. 2009). “Long-wavelength observations of debris discs around sun-like stars”. In: *A&A* 497.2, pp. 409–421. DOI: `10.1051/0004-6361/200811018`. arXiv: `0902.0338 [astro-ph.SR]`.

Roccatagliata, V. et al. (Sept. 2018). “The double population of Chamaeleon I detected by Gaia DR2”. In: *A&A* 617, L4, p. L4. DOI: `10.1051/0004-6361/201833890`. arXiv: `1808.06931 [astro-ph.SR]`.

Roccatagliata, Veronica et al. (June 2011). “Disk Evolution in OB Associations: Deep Spitzer/IRAC Observations of IC 1795”. In: *ApJ* 733.2, 113, p. 113. DOI: `10.1088/0004-637X/733/2/113`. arXiv: `1103.5770 [astro-ph.SR]`.

Rodigas, Timothy J. et al. (Jan. 2015). “On the Morphology and Chemical Composition of the HR 4796A Debris Disk”. In: *ApJ* 798.2, 96, p. 96. DOI: `10.1088/0004-637X/798/2/96`. arXiv: `1410.7753 [astro-ph.SR]`.

Rodmann, Jens (2006). “Dust in circumstellar disks”. PhD thesis. Combined Faculties for the Natural Sciences and for Mathematics of the University of Heidelberg, Germany.

Roelfsema, P. R. et al. (Aug. 2018). “SPICA-A Large Cryogenic Infrared Space Telescope: Unveiling the Obscured Universe”. In: *PASA* 35, e030, e030. DOI: `10.1017/pasa.2018.15`. arXiv: `1803.10438 [astro-ph.IM]`.

Rosotti, Giovanni P. et al. (July 2016). “The minimum mass of detectable planets in protoplanetary discs and the derivation of planetary masses from high-resolution observations”. In: *MNRAS* 459.3, pp. 2790–2805. DOI: `10.1093/mnras/stw691`. arXiv: `1603.02141 [astro-ph.EP]`.

Rugel, Michael, Davide Fedele, and Gregory Herczeg (Jan. 2018). “X-shooter observations of low-mass stars in the η Chamaeleontis association”. In: *A&A* 609, A70, A70. DOI: `10.1051/0004-6361/201630111`. arXiv: `1709.03414 [astro-ph.SR]`.

Safronov, V. S. and E. V. Zvjagina (1969). “Relative Sizes of the Largest Bodies during the Accumulation of Planets”. In: *Icarus* 10.1, pp. 109–115. DOI: `10.1016/0019-1035(69)90013-X`.

Sako, Shigeyuki et al. (Mar. 2003). “Developing new data acquisition devices for COMICS”. In: *Proc. SPIE*. Ed. by Masanori Iye and Alan F. M. Moorwood. Vol. 4841. Society of Photo-Optical Instrumentation Engineers (SPIE) Conference Series, pp. 1211–1218. DOI: `10.1117/12.461916`.

Schegerer, A. A. and S. Wolf (July 2010). “Spatially resolved detection of crystallized water ice in a T Tauri object”. In: *A&A* 517, A87, A87. DOI: `10.1051/0004-6361/200911849`. arXiv: `1005.3719 [astro-ph.EP]`.

Schneider, Glenn et al. (Oct. 2006). “Discovery of an 86 AU Radius Debris Ring around HD 181327”. In: *ApJ* 650.1, pp. 414–431. DOI: `10.1086/506507`. arXiv: `astro-ph/0606213 [astro-ph]`.

Schneider, Glenn et al. (Jan. 2009). “HST/STIS High-Resolution Imaging Of The Hr 4796A Circumstellar Debris Ring”. In: *American Astronomical Society Meeting Abstracts #213*. Vol. 213. American Astronomical Society Meeting Abstracts, p. 409.05.

Schneider, Glenn et al. (Oct. 2014). “Probing for Exoplanets Hiding in Dusty Debris Disks: Disk Imaging, Characterization, and Exploration with HST/STIS Multi-roll Coronagraphy”. In: *AJ* 148.4, 59, p. 59. DOI: `10.1088/0004-6256/148/4/59`. arXiv: `1406.7303 [astro-ph.IM]`.

Schneider, Glenn et al. (Feb. 2018). “The HR 4796A Debris System: Discovery of Extensive Exo-ring Dust Material”. In: *AJ* 155.2, 77, p. 77. DOI: `10.3847/1538-3881/aaa3f3`. arXiv: `1712.08599 [astro-ph.SR]`.

Schwarz, Hugo E. (Jan. 1986). “Polarimetry of cool giants and supergiants”. In: *Vistas in Astronomy* 29.3, pp. 253–280. DOI: `10.1016/0083-6656(86)90016-4`.

Sende, J. A. and T. Löhne (Nov. 2019). “Twisted debris: how differential secular perturbations shape debris disks”. In: *A&A* 631, A141, A141. DOI: `10.1051/0004-6361/201935199`. arXiv: `1911.07120 [astro-ph.EP]`.

Shu, Frank H. and Fred C. Adams (1987). “Star formation and the circumstellar matter of young stellar objects.” In: *Circumstellar Matter*. Ed. by I. Appenzeller and C. Jordan. Vol. 122. IAU Symposium, p. 7.

Sibthorpe, B. et al. (Apr. 2018). “Analysis of the Herschel DEBRIS Sun-like star sample”. In: *MNRAS* 475.3, pp. 3046–3064. DOI: `10.1093/mnras/stx3188`. arXiv: `1803.00072 [astro-ph.EP]`.

Sicilia-Aguilar, Aurora et al. (Aug. 2009). “The Long-Lived Disks in the η Chamaeleontis Cluster”. In: *ApJ* 701.2, pp. 1188–1203. DOI: `10.1088/0004-637X/701/2/1188`. arXiv: `0906.3365 [astro-ph.SR]`.

Simon, M. et al. (June 2012). “WISE Detection of the Circumstellar Disk Associated with 2MASS J0820-8003 in the η Cha Cluster”. In: *ApJ* 751.2, 114, p. 114. DOI: `10.1088/0004-637X/751/2/114`. arXiv: `1203.3202 [astro-ph.GA]`.

Siringo, G. et al. (Apr. 2009). “The Large APEX BOlometer CAmera LABOCA”. In: *A&A* 497.3, pp. 945–962. DOI: `10.1051/0004-6361/200811454`. arXiv: `0903.1354 [astro-ph.IM]`.

Sissa, E. et al. (May 2018). “New disk discovered with VLT/SPHERE around the M star GSC 07396-00759”. In: *A&A* 613, L6, p. L6. DOI: `10.1051/0004-6361/201832740`. arXiv: `1804.02882 [astro-ph.EP]`.

Smith, B. A. and R. J. Terrile (1984). “A Circumstellar Disk around β Pictoris”. In: *Science* 226.4681, pp. 1421–1424. DOI: `10.1126/science.226.4681.1421`.

Smith, R., M. C. Wyatt, and C. A. Haniff (May 2012). “Resolving the terrestrial planet forming regions of HD 113766 and HD 172555 with MIDI”. In: *MNRAS* 422.3, pp. 2560–2580. DOI: `10.1111/j.1365-2966.2012.20816.x`. arXiv: `1202.5487 [astro-ph.SR]`.

Smith, R. G. et al. (Nov. 1994). “Molecular ices as temperature indicators for interstellar dust: the 44- and 62-μm lattice features of H_2O ice.” In: *MNRAS* 271, pp. 481–489. DOI: `10.1093/mnras/271.2.481`.

Soummer, Rémi et al. (May 2014). “Five Debris Disks Newly Revealed in Scattered Light from the Hubble Space Telescope NICMOS Archive”. In: *ApJ* 786.2, L23, p. L23. DOI: `10.1088/2041-8205/786/2/L23`. arXiv: `1404.5614 [astro-ph.SR]`.

Stapelfeldt, K. R. et al. (Sept. 2004). “First Look at the Fomalhaut Debris Disk with the Spitzer Space Telescope”. In: *ApJS* 154.1, pp. 458–462. DOI: `10.1086/423135`.

Stark, Christopher C. and Marc J. Kuchner (Oct. 2008). “The Detectability of Exo-Earths and Super-Earths Via Resonant Signatures in Exozodiacal Clouds”. In: *ApJ* 686.1, pp. 637–648. DOI: `10.1086/591442`. arXiv: `0810.2702 [astro-ph]`.

— (Dec. 2009). “A New Algorithm for Self-consistent Three-dimensional Modeling of Collisions in Dusty Debris Disks”. In: *ApJ* 707.1, pp. 543–553. DOI: `10.1088/0004-637X/707/1/543`. arXiv: `0909.2227 [astro-ph.SR]`.

Stark, Christopher C. et al. (July 2014). “Revealing Asymmetries in the HD 181327 Debris Disk: A Recent Massive Collision or Interstellar Medium Warping”. In: *ApJ* 789.1, 58, p. 58. DOI: `10.1088/0004-637X/789/1/58`. arXiv: `1405.7055 [astro-ph.SR]`.

Stevenson, D. J. (Aug. 1982). “Formation of the giant planets”. In: *Planet. Space Sci.* 30.8, pp. 755–764. DOI: `10.1016/0032-0633(82)90108-8`.

Stewart, Sarah T. and Zoë M. Leinhardt (Feb. 2009). “Velocity-Dependent Catastrophic Disruption Criteria for Planetesimals”. In: *ApJ* 691.2, pp. L133–L137. doi: `10.1088/0004-637X/691/2/L133`.

Stock, Nathan D. et al. (Dec. 2010). “The Structure of the β Leonis Debris Disk”. In: *ApJ* 724.2, pp. 1238–1255. doi: `10.1088/0004-637X/724/2/1238`. arXiv: `1010.0003 [astro-ph.EP]`.

Strubbe, Linda E. and Eugene I. Chiang (2006). “Dust Dynamics, Surface Brightness Profiles, and Thermal Spectra of Debris Disks: The Case of AU Microscopii”. In: *ApJ* 648.1, pp. 652–665. doi: `10.1086/505736`. arXiv: `astro-ph/0510527 [astro-ph]`.

STScI (2017). In: *Space Telescope Science Institute Article, JWST User Documentation, Baltimore, MD* Updated July 13, 2017.

Su, K. Y. L. et al. (Dec. 2004). “MIPS Observations of the Fabulous Four Debris Disks”. In: *American Astronomical Society Meeting Abstracts*. Vol. 205. American Astronomical Society Meeting Abstracts, p. 17.09.

Su, K. Y. L. et al. (2006). “Debris Disk Evolution around A Stars”. In: *ApJ* 653.1, pp. 675–689. doi: `10.1086/508649`. arXiv: `astro-ph/0608563 [astro-ph]`.

Su, Kate (Oct. 2005). “The Vega Debris Disk - A Surprise from Spitzer”. In: *Nearby Resolved Debris Disks*. Ed. by I. Kamp and M. Meixner, p. 36.

Su, Kate et al. (Dec. 2014). *Debris Disk Variability: Observational Test Bed for Probing Terrestrial Planet Formation*. Spitzer Proposal.

Sylvester, R. J., S. K. Dunkin, and M. J. Barlow (Oct. 2001). “SCUBA photometry of candidate Vega-like sources”. In: *MNRAS* 327.1, pp. 133–140. doi: `10.1046/j.1365-8711.2001.04672.x`.

Tanaka, Hidekazu, Satoshi Inaba, and Kiyoshi Nakazawa (Oct. 1996). “Steady-State Size Distribution for the Self-Similar Collision Cascade”. In: *Icarus* 123.2, pp. 450–455. doi: `10.1006/icar.1996.0170`.

Telesco, C. M. et al. (Feb. 2000). “Deep 10 and 18 Micron Imaging of the HR 4796A Circumstellar Disk: Transient Dust Particles and Tentative Evidence for a Brightness Asymmetry”. In: *ApJ* 530.1, pp. 329–341. doi: `10.1086/308332`. arXiv: `astro-ph/9909363 [astro-ph]`.

Telesco, Charles M. et al. (Aug. 1998). “GatirCam: Gemini mid-infrared imager”. In: *Proc. SPIE*. Ed. by Albert M. Fowler. Vol. 3354. Society of Photo-Optical Instrumentation Engineers (SPIE) Conference Series, pp. 534–544. doi: `10.1117/12.317279`.

Terada, Hiroshi et al. (Sept. 2007). “Detection of Water Ice in Edge-on Protoplanetary Disks: HK Tauri B and HV Tauri C”. In: *ApJ* 667.1, pp. 303–307. doi: `10.1086/520951`.

Thalmann, C. et al. (Dec. 2011). “Images of the Extended Outer Regions of the Debris Ring around HR 4796 A”. In: *ApJ* 743.1, L6, p. L6. doi: `10.1088/2041-8205/743/1/L6`. arXiv: `1110.2488 [astro-ph.SR]`.

Thébault, P. (Oct. 2009). “Vertical structure of debris discs”. In: *A&A* 505.3, pp. 1269–1276. doi: `10.1051/0004-6361/200912396`. arXiv: `0906.5524 [astro-ph.EP]`.

— (Jan. 2012). “A new code to study structures in collisionally active, perturbed debris discs: application to binaries”. In: *A&A* 537, A65, A65. doi: `10.1051/0004-6361/201117899`. arXiv: `1110.3648 [astro-ph.EP]`.

Thébault, P. and J. C. Augereau (May 2003). “Collisional dust production in extrasolar discs: a new dynamical and photometric model”. In: *AAS/Division for Planetary Sciences Meeting Abstracts #35*. AAS/Division for Planetary Sciences Meeting Abstracts, p. 18.13.

— (Sept. 2007). “Collisional processes and size distribution in spatially extended debris discs”. In: *A&A* 472.1, pp. 169–185. doi: `10.1051/0004-6361:20077709`. arXiv: `0706.0344 [astro-ph]`.

Thebault, P., Q. Kral, and J. C. Augereau (Jan. 2014). “Grain size segregation in debris discs”. In: *A&A* 561, A16, A16. doi: `10.1051/0004-6361/201322052`. arXiv: `1310.1584 [astro-ph.EP]`.

Thébault, P. and Y. Wu (Apr. 2008). “Outer edges of debris discs. How sharp is sharp?” In: *A&A* 481.3, pp. 713–724. doi: `10.1051/0004-6361:20079133`. arXiv: `0801.3724 [astro-ph]`.

Thi, W. F. et al. (Jan. 2014). “Gas lines from the 5-Myr old optically thin disk around HD 141569A . Herschel observations and modeling”. In: *A&A* 561, A50, A50. DOI: `10.1051/0004-6361/201322150`. arXiv: `1309.5098 [astro-ph.GA]`.

Thommes, Edward W. and Martin J. Duncan (2006). “The accretion of giant-planet cores”. In: *Planet Formation*. Ed. by Hubert Klahr and Wolfgang Brandner, p. 129.

Toomre, A. (1981). “What amplifies the spirals”. In: *Structure and Evolution of Normal Galaxies*. Ed. by S. M. Fall and D. Lynden-Bell, pp. 111–136.

Torres, Rubén Asensio (2017). “Dust in circumstellar disks”. PhD thesis. Department of Astronomy of Stockholm University, Sweden.

Van de Hulst, H. C. and V. Twersky (Jan. 1957). “Light Scattering by Small Particles”. In: *Physics Today* 10.12, p. 28. DOI: `10.1063/1.3060205`.

van Leeuwen, F. (Nov. 2007). “Validation of the new Hipparcos reduction”. In: *A&A* 474.2, pp. 653–664. DOI: `10.1051/0004-6361:20078357`. arXiv: `0708.1752 [astro-ph]`.

van Lieshout, R. et al. (Nov. 2014). “Near-infrared emission from sublimating dust in collisionally active debris disks”. In: *A&A* 571, A51, A51. DOI: `10.1051/0004-6361/201322090`. arXiv: `1404.3271 [astro-ph.EP]`.

Voshchinnikov, N. V. and E. Krügel (Dec. 1999). “Circumstellar disc of begin {equation}ta Pictoris: constraints on grain properties from polarization”. In: *A&A* 352, pp. 508–516. arXiv: `astro-ph/9909292 [astro-ph]`.

Voshchinnikov, N. V. and D. A. Semenov (Oct. 2000). “The Temperature of Nonspherical Circumstellar Dust Grains”. In: *Astronomy Letters* 26.10, pp. 679–690. DOI: `10.1134/1.1316114`. arXiv: `astro-ph/0009149 [astro-ph]`.

Warren, S. G. (Apr. 1984). “Optical constants of ice from the ultraviolet to the microwave”. In: *Appl. Opt.* 23, pp. 1206–1225. DOI: `10.1364/AO.23.001206`.

Watson, C. A. et al. (2011). “On the alignment of debris discs and their host stars’ rotation axis - implications for spin-orbit misalignment in exoplanetary systems”. In: *MNRAS* 413.1, pp. L71–L75. DOI: `10.1111/j.1745-3933.2011.01036.x`. arXiv: `1009.4132 [astro-ph.EP]`.

Weidenschilling, S. J. et al. (1997). “Accretional Evolution of a Planetesimal Swarm”. In: *Icarus* 128.2, pp. 429–455. DOI: `10.1006/icar.1997.5747`.

Wetherill, G. W. (1980). “Formation of the terrestrial planets”. In: *ARA&A* 18, pp. 77–113. DOI: `10.1146/annurev.aa.18.090180.000453`.

Wetherill, G. W. and G. R. Stewart (1989). “Accumulation of a swarm of small planetesimals”. In: *Icarus* 77.2, pp. 330–357. DOI: `10.1016/0019-1035(89)90093-6`.

— (1993). “Formation of Planetary Embryos: Effects of Fragmentation, Low Relative Velocity, and Independent Variation of Eccentricity and Inclination”. In: *Icarus* 106.1, pp. 190–209. DOI: `10.1006/icar.1993.1166`.

Whittet, D. C. B. et al. (Nov. 1996). “An ISO SWS view of interstellar ices: first results.” In: *A&A* 315, pp. L357–L360.

Whizin, Akbar D., Jürgen Blum, and Joshua E. Colwell (Feb. 2017). “The Physics of Protoplanetesimal Dust Agglomerates. VIII. Microgravity Collisions between Porous SiO_2 Aggregates and Loosely Bound Agglomerates”. In: *ApJ* 836.1, 94, p. 94. DOI: `10.3847/1538-4357/836/1/94`.

Wien, Willy (Jan. 1897). “Ueber geschlossene Unstetigkeitsflächen der Geschwindigkeit in einer incompressiblen reibungslosen Flüssigkeit”. In: *Annalen der Physik* 298.9, pp. 192–203. DOI: `10.1002/andp.18972980915`.

Williams, Jonathan P. et al. (2004). “Detection of Cool Dust around the G2 V Star HD 107146”. In: *ApJ* 604.1, pp. 414–419. DOI: `10.1086/381721`. arXiv: `astro-ph/0311583 [astro-ph]`.

Wilner, D. J. et al. (Apr. 2002). “Structure in the Dusty Debris around Vega”. In: *ApJ* 569.2, pp. L115–L119. DOI: `10.1086/340691`. arXiv: `astro-ph/0203264 [astro-ph]`.

Windmark, F. et al. (2012). “Planetesimal formation by sweep-up: how the bouncing barrier can be beneficial to growth”. In: *A&A* 540, A73, A73. doi: 10.1051/0004-6361/201118475. arXiv: 1201.4282 [astro-ph.EP].

Witt, A. (Jan. 1989). “Visible/uv Scattering by Interstellar Dust”. In: *Interstellar Dust*. Ed. by Louis J. Allamandola and A. G. G. M. Tielens. Vol. 135. IAU Symposium, p. 87.

Woitke, P., I. Kamp, and W. F. Thi (July 2009). “Radiation thermo-chemical models of protoplanetary disks. I. Hydrostatic disk structure and inner rim”. In: *A&A* 501.1, pp. 383–406. doi: 10.1051/0004-6361/200911821. arXiv: 0904.0334 [astro-ph.EP].

Woitke, P. et al. (July 2009). “Hot and cool water in Herbig Ae protoplanetary disks. A challenge for Herschel”. In: *A&A* 501.1, pp. L5–L8. doi: 10.1051/0004-6361/200912249. arXiv: 0906.0448 [astro-ph.EP].

Woitke, P. et al. (Oct. 2011). “The unusual protoplanetary disk around the T Tauri star ET Chamaeleontis”. In: *A&A* 534, A44, A44. doi: 10.1051/0004-6361/201116684. arXiv: 1103.5309 [astro-ph.EP].

Wolf, S. and L. A. Hillenbrand (Oct. 2005). “Debris disk radiative transfer simulation tool (DDS)”. In: *Computer Physics Communications* 171.3, pp. 208–218. doi: 10.1016/j.cpc.2005.04.014. arXiv: astro-ph/0506406 [astro-ph].

Wolf, S. and N. V. Voshchinnikov (Sept. 2004). “Mie scattering by ensembles of particles with very large size parameters”. In: *Computer Physics Communications* 162.2, pp. 113–123. doi: 10.1016/j.cpc.2004.06.070. arXiv: astro-ph/0406118 [astro-ph].

Wolf, Sebastian and Lynne A. Hillenbrand (Oct. 2003). “Model Spectral Energy Distributions of Circumstellar Debris Disks. I. Analytic Disk Density Distributions”. In: *ApJ* 596.1, pp. 603–620. doi: 10.1086/377638. arXiv: astro-ph/0306479 [astro-ph].

Wyatt, M. C. (Dec. 2003). “Resonant Trapping of Planetesimals by Planet Migration: Debris Disk Clumps and Vega’s Similarity to the Solar System”. In: *ApJ* 598.2, pp. 1321–1340. doi: 10.1086/379064. arXiv: astro-ph/0308253 [astro-ph].

— (Sept. 2005). “Spiral structure when setting up pericentre glow: possible giant planets at hundreds of AU in the HD 141569 disk”. In: *A&A* 440.3, pp. 937–948. doi: 10.1051/0004-6361:20053391. arXiv: astro-ph/0506208 [astro-ph].

— (2008). “Evolution of debris disks.” In: *ARA&A* 46, pp. 339–383. doi: 10.1146/annurev.astro.45.051806.110525.

Wyatt, M. C., C. J. Clarke, and M. Booth (Oct. 2011). “Debris disk size distributions: steady state collisional evolution with Poynting-Robertson drag and other loss processes”. In: *Celestial Mechanics and Dynamical Astronomy* 111.1-2, pp. 1–28. doi: 10.1007/s10569-011-9345-3. arXiv: 1103.5499 [astro-ph.EP].

Wyatt, M. C. and W. R. F. Dent (Aug. 2002). “Collisional processes in extrasolar planetesimal discs - dust clumps in Fomalhaut’s debris disc”. In: *MNRAS* 334.3, pp. 589–607. doi: 10.1046/j.1365-8711.2002.05533.x. arXiv: astro-ph/0204034 [astro-ph].

Wyatt, M. C. et al. (1999). “How Observations of Circumstellar Disk Asymmetries Can Reveal Hidden Planets: Pericenter Glow and Its Application to the HR 4796 Disk”. In: *ApJ* 527.2, pp. 918–944. doi: 10.1086/308093. arXiv: astro-ph/9908267 [astro-ph].

Wyatt, M. C. et al. (Mar. 2007). “Transience of Hot Dust around Sun-like Stars”. In: *ApJ* 658.1, pp. 569–583. doi: 10.1086/510999. arXiv: astro-ph/0610102 [astro-ph].

Wyatt, M. C. et al. (Feb. 2010). “Collisional evolution of eccentric planetesimal swarms”. In: *MNRAS* 402.1, pp. 657–672. doi: 10.1111/j.1365-2966.2009.15930.x. arXiv: 0910.4725 [astro-ph.EP].

Wyatt, M. C. et al. (Aug. 2012). “Herschel imaging of 61 Vir: implications for the prevalence of debris in low-mass planetary systems”. In: *MNRAS* 424.2, pp. 1206–1223. doi: 10.1111/j.1365-2966.2012.21298.x. arXiv: 1206.2370 [astro-ph.EP].

Wyatt, S. P. and F. L. Whipple (Jan. 1950). “The Poynting-Robertson effect on meteor orbits”. In: *ApJ* 111, pp. 134–141. doi: `10.1086/145244`.

Zagorovsky, Kyryl, Alexis Brandeker, and Yanqin Wu (Sept. 2010). “Gas Emission from Debris Disks Around A and F Stars”. In: *ApJ* 720.1, pp. 923–939. doi: `10.1088/0004-637X/720/1/923`. arXiv: `1007.3343 [astro-ph.EP]`.

Zook, H. A. and O. E. Berg (1975). “A source for hyperbolic cosmic dust particles”. In: *Planet. Space Sci.* 23.1, pp. 183–203. doi: `10.1016/0032-0633(75)90078-1`.

Zuckerman, B. (Jan. 2001). “Dusty Circumstellar Disks”. In: *ARA&A* 39, pp. 549–580. doi: `10.1146/annurev.astro.39.1.549`.

Zuckerman, B. and E. E. Becklin (Sept. 1993). “Submillimeter Studies of Main-Sequence Stars”. In: *ApJ* 414, p. 793. doi: `10.1086/173123`.

Zuckerman, B., Sungsoo S. Kim, and T. Liu (June 1995). “Luminosity Class III Stars with Excess Far-Infrared Emission”. In: *ApJ* 446, p. L79. doi: `10.1086/187935`.

Acknowledgements

The author of this dissertation acknowledges the DFG for financial support under contract WO 857/15-1 within the context of the Research Unit FOR 2285 “Debris Disks in Planetary Systems”.

It would have been impossible to complete my Ph.D. without the help of various people. They are all part of this thesis in one or the other way. I truly wanna thank them all here, and I sincerely apologize for anyone that I forget.

I would like to first say a very BIG thank you to my supervisor Prof. Dr. Sebastian Wolf. Thank you for your endless patience for my stupidity, guiding me through this long journey, exposing me to a lot of great people and topics, and always being available for questions and discussions. You are the best scientist ever in my life. The most important lesson I have learned from you is that science can be great fun.

I am also very grateful to all those in the Research Unit FOR 2285 members: Prof. Dr. A. V. Krivov, Fabian Geiler, Dr. Torsten Löhne, Jan Sende, Dr. Mark Booth, Dr. Nicole Pawellek, Patricia Luppe, Dr. Harald Mutschke, Jonas Greif, Prof. Dr. Jürgen Blum, Alexander Landeck, Prof. Dr. Falko Langenhorst, Dr. Cornelia Jäger, Dr. Alexey Potapov, and all FOR 2285 members. It was a great pleasure to have a discussion with all of you, which was always very useful for me. Thank you for your invaluable feedback on my research. The lesson I learned from you in this regard: "Plan less, explore more!".

A very special thank you to Mrs. Brigitte Kuhr and Dipl.-Geol. Holger Boll for all the genuine administrative and IT support throughout this research work. I can’t express how thankful I am for your supports.

I am indebted to all my friends in ITAP who were always so helpful in numerous ways. I would keep a lot of warm memories from Kiel. It was also great fun to have a scientific discussion sharing your wisdom. Please keep in mind that whenever you need me, I will be always on your sides. I owe you all, Anton Krieger, Dr. Florian Kirchschlager, Jannes Klee, Jubin Lirawi, Juila Kobus, Lars Bösch, Moritz Lietzow, Niko Zielinski, Dr. Robert Brauer, Dr. Robert Brunngräber, Roman Avramenko, Dr. Stefan Hesse, Dr. Tobias F. Illenseer, Tommy Breslein, Thomas Stuber, Prof. Dr. Wolfgang J. Duschl (*first name alphabetical order*), and my office mate Alexander A. Bensberg.

I specifically would like to thank everyone who has taken the time to read the draft of this dissertation and gave me a lot of invaluable feedback, Anton Krieger, Roman Avramenko, Julia Kobus, Niko Zielinski, Moritz Lietzow, Alexander A. Bensberg, Thomas Stuber, and our captain Dr. Robert Brunngräber.

I also would like to say a special thank you to my co-authors, Dr. Torsten Löhne, Dr. Florian Kirchschlager, Prof. Dr. A. V. Krivov, Dr. Alexey Potapov, Dr. Harald Mutschke, Dr. Cornelia Jäger, Dr. Veronica Roccatagliata, Dr. Jean-François Lestrade, and SPICA formation of planetary systems working group people. Working with you is an extremely exciting and inspiring experience for me.

Undertaking my Ph.D. has been a truly life-changing experience for me. I have to say that I am the happiest one in this world to do science, boulder, work out, sail, and spend my time, with you.

Declaration of Authorship

I, **Minjae Kim**, hereby declare that this thesis titled, "**Observational appearance of debris disks**" and the work presented in it are my own.

I declare that apart from the supervisor Prof. Dr. Sebastian Wolf's guidance the content and design of this dissertation are carried out by myself without improper external assistance and to the best of my knowledge.

I declare that I have identified all quotations of other authors and used none but the indicated sources.

I declare that this dissertation has not been submitted either partially or wholly as part of a doctoral degree to another examining body and whether it has not been published or submitted for publications.

I declare that parts of this work are published in Kim et al., 2018 (Chapter 5) and Kim et al., 2019 (Chapter 6), or will be submitted for publication in Roccatagliata et al. in preparation (Chapter 7) and Lestrade et al. in preparation (Chapter 8).

I declare that this dissertation has been prepared subject to the Rules of Good Scientific Practice of the German Research Foundation.

Kiel, 2020

Minjae Kim

Minjae Kim